



TECHNISCHE  
UNIVERSITÄT  
WIEN

Vienna University of Technology

# DISSERTATION

Monitoring and modelling of the urban micro-climate in  
Vienna

**ausgeführt zum Zwecke der Erlangung des akademischen Grades einer  
Doktorin/eines Doktors der technischen Wissenschaften unter der Leitung von**

(BetreuerIn) Univ. Prof. DI Dr. Ardeshir Mahdavi

E 259/3  
Abteilung für Bauphysik und  
Bauökologie

**eingereicht an der Technischen Universität Wien  
Fakultät für Architektur und Raumplanung**

von

(VerfasserIn) DI Aida Maleki Gavvani

0927242  
*Matrikelnummer*

.....  
*Anschrift*

**Wien, July 2014**

.....  
*Unterschrift*

*in the memory of my father*

*and*

*to my mother*

## Kurzfassung

Die vorliegende Arbeit befasst sich mit dynamischen Beobachtungen des urbanen Mikroklimas an den verschiedenen, morphologisch-unterschiedlichen Orten im Stadtgebiet Wien. Das Hauptziel dieser Studie besteht darin, ein besseres Verständnis für den Einfluss von städtebaulichen Parameter auf das Mikroklima zu entwickeln. Hierfür wurden Wetterdaten mit Hilfe einer mobilen Wetterstation an verschiedenen Orten in der Stadt gesammelt. Die gesammelten Daten wurden mit den allgemeinen Wetterbedingungen, die gleichzeitig über eine stationäre Wetterstation beobachtet wurden, verglichen. Die Ergebnisse zeigen, dass es große Unterschiede im Mikroklima an den verschiedenen Standorten gibt. Eine genaue Analyse der Daten lässt Tendenzen erkennen, die es ermöglichen, Charakteristika und ihren Einfluss auf das Mikroklima zu identifizieren. Besonders hohe Lufttemperaturen wurde an offenen Plätzen und Wiesen gemessen, wohingegen in verschatteten Innenhöfen und Straßenzügen niedrigere Temperaturen beobachtet wurden.

Zusätzlich zu den Messungen wurden mit Hilfe des Programms ENVI-met Simulationen von Teilbereichen der Stadt vorgenommen. Zur Kalibrierung des Modells wurden die Daten mehrerer Wetterstationen verwendet.

Mit Hilfe dieser Simulationsmodelle konnten Veränderungen der physikalischen und geometrischen Struktur der jeweiligen Umgebung untersucht werden. Unter anderem wurde der Einfluss von Gründächern, „Cool roofs“, Vegetation und unterschiedlichen Oberflächenmaterialien auf das umliegende Mikroklima untersucht. Die Ergebnisse zeigen vor allem bei erhöhter Vegetation auf Straßenniveau und bei wasserdurchlässigen Bodenbelägen eine klare Verbesserung des Mikroklimas.

Mit dieser Forschungsarbeit soll vor allem das Verständnis für das Mikroklima innerhalb des urbanen Raums verbessert werden. Vor allem in Angesicht des Klimawandels und der voranschreitenden Urbanisierung ist ein genaueres Verständnis von klimatischen Prozessen innerhalb kleinteiliger städtischer Strukturen wichtig. Stadtplaner, Architekten und Entscheidungsträger benötigen die notwendigen Grundlagen, um Entscheidungen in der Planung und Strukturierung des Urbanen Raumes treffen zu können. Der Lebensraum innerhalb der Städte gewinnt immer mehr an Bedeutung und soll auch für die Zukunft als lebenswerter Raum erhalten bleiben.

## Summary

The present work addresses a dynamic monitoring of micro-climatic conditions in various – morphologically distinct – locations in the city of Vienna. The main purpose of the study is to develop a deeper understanding of the urban design and planning parameters that lead to variance in micro-climatic conditions in large and densely populated cities such as Vienna. Thereby, weather information was collected with a mobile weather station at various locations within the city. Collected data from these – morphologically differentiated – locations were compared with the general weather conditions simultaneously monitored by a stationary weather station. The comparisons suggest that the microclimatic conditions at different locations vary considerably. Moreover, these variations appear to be related to certain characteristic features of the locations (e.g., sky view factor, vegetation, etc.). Highest temperatures were monitored at open plazas and parks, whereas shaded courtyards and streets displayed the lowest temperatures during the day. The readings of the air temperature and solar irradiance showed a significant congruence with sky view factors.

In addition to the measurements, a micro-climatic simulation model was made for a part of the area under study. To perform the simulation, a simulation software known as ENVI-met was utilized. Weather data collected from the existing weather stations were used to adjust and calibrate the simulation model. In general, the simulation results showed a relatively good agreement with the measurements. Furthermore, effects of the variation of physical and geometrical properties of the urban fabric (i.e. cool roofs including green and white roofs, perviousness of paving materials and aspect ratio), which could not be evaluated by measurements, were investigated. Based on the results, the modifications implemented within the urban canopy have more influence on urban micro-climate than those applied above the canopy. Also, increasing the amount of vegetation and permeable pavements can cool the air temperature down by up to 3 K. Likewise, the simulations confirmed the results of empirical inquiries, establishing the effect of the height of the buildings and canyon aspect ratio on urban micro-climate.

The results of this research are intended to improve the knowledge of the urban heat island phenomenon as well as urban micro-climate to support the development of micro-climatic models. These models can support architects, urban planners, and building automation experts to design and operate sustainable buildings in the future.

## Acknowledgments

This project was funded in part by Wirtschaftskammer Wien – Wirtschaftskammerpreis 2011- "Monitoring and modeling of the urban microclimate". Additional resources were made available within the framework of the Austrian building award "Planungsinstrumente für klimataugliche Gebäude der Zukunft". Further support was provided within the framework of the EU-Project "Development and application of mitigation and adaptation strategies and measures for counteracting the global Urban Heat Island phenomenon" (Central Europe Program, No 3CE292P3).

First and foremost, I would like to express my sincere gratitude to Prof. Ardeshir Mahdavi, for his supervision, the generous support and guidance throughout my thesis work. He spent much time supporting me and giving suggestions. Without his expertise and his patience and encouragement from the initial to the final level, this thesis wouldn't have begun nor been successfully finished.

I also wish to thank Prof. Michael Bruse whose advice while working with his model facilitated enormously my work and kept me going on during this study.

I would also like to express my gratitude to Dr. Nader Sanei for his endless patience to help me to learn and understand computational fluid dynamic.

Furthermore, my thanks go to a number of my past and present colleagues at the Department of Building physics and Building Ecology, including C. Pröglhöf, K. Orehounig, E. Finz, K. Kiesel, E. Krätschmer, G. Heilmann and M. Vuckovic.

My deepest appreciation goes to Zeinab Alameddine, Mino Gharabeiglou, Parisa kaveh, E. Ebrahimi, N. Ghiasi, M. taheri, M. Zamini helped me through the course of my journey and facilitated my life in Austria. Without your friendship, encouragement and understanding my experience in this country wouldn't be beautiful.

I would also like to thank all of my friends who supported me in writing, and incited me to strive towards my goal.

And at the end a special thanks to my family. Words cannot express how grateful I am to my mother, my sister, my aunt and my brothers-in-law the sacrifices that you've made on my behalf. Your prayer for me was what sustained me thus far.

# Table of Contents

KURZFASSUNG .....	I
SUMMARY.....	II
ACKNOWLEDGMENTS.....	III
TABLE OF CONTENTS .....	IV
LIST OF TABLES.....	VIII
LIST OF FIGURES.....	IX
ABBREVIATIONS.....	XVII
1. INTRODUCTION .....	1
1.1. Objective .....	1
1.2. Motivation .....	2
1.3. Structure .....	3
2. THEORETICAL BACKGROUND .....	4
2.1. Urban Micro-climate.....	4
2.2. The Urban Energy Balance.....	6
2.2.1. Radiation .....	7
2.2.2. Anthropogenic energy.....	9
2.2.3. Convective sensible heat flux .....	10
2.2.4. Latent heat flux .....	11
2.2.5. Thermal storage .....	12
2.3. Wind Flow in Urban Spaces .....	13
2.4. Urban Heat Island .....	14
2.5. Vegetation.....	15
2.6. Measuring methods.....	16
2.6.1. Fixed stations.....	16
2.6.2. Mobile traverses.....	17
2.6.3. Remote sensing .....	17
2.7. Modeling the urban micro-climate .....	18
2.7.1. Physical model.....	18
2.7.2. Mathematical model .....	19
2.8. CFD Modeling.....	20
2.8.1. Turbulence.....	22

3.	APPROACH .....	30
3.1.	Overview .....	30
3.2.	Empirical inquiry .....	30
3.2.1.	Site description .....	31
3.2.2.	Stationary weather station .....	45
3.2.3.	Mobile weather stations .....	49
3.3.	Computational inquiries .....	54
3.3.1.	Relevance of ENVI-met to the present study .....	55
3.3.2.	General structure of ENVI-met 3.1(4.0) .....	55
3.3.3.	Model layout .....	56
3.3.4.	Atmospheric model .....	57
3.3.5.	Soil model .....	62
3.3.6.	Vegetation model .....	63
3.3.7.	Ground surface model .....	66
3.3.8.	Building surface .....	67
3.3.9.	Forcing .....	69
3.3.10.	Required Input Data .....	70
3.3.11.	Shortcomings of ENVI-met .....	71
4.	EMPIRICAL INQUIRY RESULTS .....	72
4.1.	Overview .....	72
4.2.	Short measurements .....	73
4.2.1.	Reference day analysis .....	73
4.2.2.	Degree of dispersion for the measured data .....	77
4.2.3.	Correlational studies .....	80
4.2.4.	Regression Analysis .....	82
4.3.	Control studies .....	91
4.3.1.	Influence of air velocity, sky conditions, and diurnal pattern on temperature .....	91
4.3.2.	Influence of air velocity, sky conditions, and diurnal pattern on water vapor concentration .....	93
4.3.3.	Influence of air velocity, sky conditions, and diurnal pattern on CO <sub>2</sub> .....	94
4.3.4.	Influence of the wind speed above the urban canopy on that of inside the urban canopy .....	95

4.4.	Long time measurements .....	96
5.	COMPUTATIONAL INQUIRY RESULTS .....	99
5.1.	Adjusting the required input weather data .....	99
5.2.	Main Simulation Model Buildup .....	109
5.2.1.	Domain properties .....	110
5.2.2.	Model setting and sensitivity analysis .....	110
5.3.	Parametric Analysis.....	114
5.3.1.	Main Model, Base case.....	115
5.3.2.	V1: Vegetation change, trees .....	117
5.3.3.	V2: Vegetation change, green roof .....	119
5.3.4.	V3: Vegetation change, trees and green roof .....	123
5.3.5.	M1: Material properties change, permeable pavement .....	125
5.3.6.	VM: Combination of scenario V3 and M1 – increasing vegetation and applying impermeable materials.....	127
5.3.7.	M2: Material properties change, white roofs .....	129
5.3.8.	M3: Material properties change, light Walls.....	132
5.3.9.	H1: Aspect Ratio change, lower aspect ratio.....	135
5.3.10.	H2: Aspect Ratio change, higher aspect ratio .....	138
5.3.11.	Overview, differences among all scenarios .....	141
6.	CONCLUSION .....	149
7.	OUTLOOK.....	151
	REFERENCES.....	152
	APPENDICES.....	159
	Appendix A-1: Input data to run a simulation using ENVI-met 4.0.....	160
	Appendix A2: Required information to build an area input file .....	162
	Appendix A3: ENVI-met outputs, main data file (Atmosphere).....	163
	Appendix A4: ENVI-met outputs, main data file (Surface) .....	165
	Appendix A5: ENVI-met outputs, main data file (Buildings).....	166
	Appendix A6: ENVI-met outputs, main data file (Soil).....	166
	Appendix A7: ENVI-met outputs, 1D-Model Model Files (1D- inflow) .....	167
	Appendix A8: ENVI-met outputs, receptor files .....	168
	Appendix B: Sim file for the Base case.....	169
	Appendix C1: Simulated air temperaturefor the base case [K] .....	171



Appendix C2: Simulated air temperature for the V1 [K].....	172
Appendix C3: Simulated air temperature for the V2 [K].....	173
Appendix C4: Simulated air temperature for the V3 [K].....	174
Appendix C5: Simulated air temperature for the M1 [K] .....	175
Appendix C6: Simulated air temperature for the VM [K] .....	176
Appendix C7: Simulated air temperature for the M2 [K] .....	177
Appendix C8: Simulated air temperature for the M3 [K] .....	178
Appendix C9: Simulated air temperature for the H1 [K] .....	179
Appendix C10: Simulated air temperature for the H2 [K] .....	180
Appendix D1: Simulated specific humidity for the base case [g.kg <sup>-1</sup> ].....	181
Appendix D2: Simulated specific humidity for the V1 [g.kg <sup>-1</sup> ].....	182
Appendix D3: Simulated specific humidity for the V2 [g.kg <sup>-1</sup> ].....	183
Appendix D4: Simulated specific humidity for the V3 [g.kg <sup>-1</sup> ].....	184
Appendix D5: Simulated specific humidity for the M1 [g.kg <sup>-1</sup> ].....	185
Appendix D6: Simulated specific humidity for the VM [g.kg <sup>-1</sup> ].....	186
Appendix D7: Simulated specific humidity for the M2 [g.kg <sup>-1</sup> ].....	187
Appendix D8: Simulated specific humidity for the M3 [g.kg <sup>-1</sup> ].....	188
Appendix D9: Simulated specific humidity for the H1 [g.kg <sup>-1</sup> ].....	189
Appendix D10: Simulated specific humidity for the H2 [g.kg <sup>-1</sup> ].....	190
Appendix E1: Database of soil type in ENVI-met.....	191
Appendix E2: Database of soil profile in ENVI-met.....	193
Appendix E3: Database of materials in ENVI-met .....	195
Appendix E4: Database of wall/roof type in ENVI-met.....	197
Appendix E5: Database 3D plants in ENVI-met .....	199

## List of Tables

Table 3-1:	
Technical properties of the sensors used in BPI weather station.....	45
Table 3-2:	
The selected measurement spot with information regarding category, SVF, orientation, vegetation, surface properties, water body presence, intensity of traffic, H/W ratio (of streets).....	48
Table 3-3:	
Instruments used in mobile weather station.....	48
Table 3-4:	
Well-known available micro-climate simulation tools.....	54
Table 5-1 :	
$R^2$ and RMSE and CV (RMSE) in simulated calibration scenarios for BPI temperature .....	104
Table 5-2:	
$R^2$ and RMSE and CV (RMSE) in simulated calibration scenarios for BPI solar radiation .....	104
Table 5-3 :	
$R^2$ and RMSE and CV (RMSE) in simulated calibration scenarios for temperature...	104
Table 5-4:	
Simulation input data for calibration scenarios (0-I-II-III-IV) .....	105
Table 5-5:	
$R^2$ and RMSE and CV (RMSE) in simulated calibration scenarios for C2 air temperature .....	108
Table 5-6:	
$R^2$ and RMSE and CV (RMSE) in simulated calibration scenarios for S1 air temperature .....	108
Table 5-7:	
$R^2$ and RMSE and CV (RMSE) in simulated calibration scenarios for S5 air temperature .....	108
Table 5-8:	
$R^2$ and RMSE and CV (RMSE) in simulated calibration scenarios for P1 air temperature .....	108
Table 5-9:	
Indicators showing the of ENVI-met model performance for different input weather data forcing .....	113
Table 5-10:	
Indicators showing the ENVI-met model performance in comparison with observed data for different days .....	113
Table 5-11:	
The properties of the locations .....	115

## List of Figures

Figure 2-1: Schematic section of the urban atmosphere, showing UBL and UCL (top), and the homogeneous surface layer above the city and the heterogeneous urban canopy layer (bottom) .....	5
Figure 2-2: Schematic section showing urban surface energy balance components (Erell et al., 2011) .....	7
Figure 3-1: Urban plan showing the location of stops S1 and S2.....	32
Figure 3-2: Location S1.....	32
Figure 3-3: Fish eye picture of S1.....	32
Figure 3-4: Location S2:.....	33
Figure 3-5: Fish eye picture of S2.....	33
Figure 3-6: Urban plan showing the location of stops S3 and S4.....	34
Figure 3-7: Location S3.....	34
Figure 3-8: Fish eye picture of S3.....	34
Figure 3-9: Location S4.....	35
Figure 3-10: Fish eye picture of S4.....	35
Figure 3-11: Urban plan showing the location of stop S5.....	35
Figure 3-12: Location S5.....	36
Figure 3-13: Fish eye picture of S5.....	36
Figure 3-14: Urban plan showing the location of stop S6.....	37
Figure 3-15: Fish eye picture of S6.....	37
Figure 3-16: Location S6.....	37

Figure 3-17: Urban plan showing the location of stops G1 and G2 .....	38
Figure 3-18: Location G1 .....	38
Figure 3-19: Fish eye picture of G1 .....	38
Figure 3-20: Location G2 .....	39
Figure 3-21: Fish eye picture of G2 .....	39
Figure 3-22: Urban plan showing the location of stops P1 and P2 .....	39
Figure 3-23: Location P1 .....	40
Figure 3-24: Fish eye picture of P1.....	40
Figure 3-25: Location P2 .....	41
Figure 3-26: Fish eye picture of P2.....	41
Figure 3-27: Urban plan showing the location of stop P3.....	41
Figure 3-28: location P3 .....	42
Figure 3-29: Fish eye picture of P3.....	42
Figure 3-30: Urban plan showing the location of stops C1 and C2 .....	42
Figure 3-31: Location C1 .....	43
Figure 3-32: Fish eye picture of C1.....	43
Figure 3-33: Location C2 .....	44
Figure 3-34: Fish eye picture of C2.....	44
Figure 3-35: BPI stationary weather station .....	46
Figure 3-36: Schematic section showing BPI stationary weather station .....	46
Figure 3-37:	

Stationary weather station C* (Schuss, 2011) .....	47
Figure 3-38: Measurement locations and reference weather station (BPI) marked on an area map (www.wien.at, 2012) .....	47
Figure 3-39: First mobile weather station.....	50
Figure 3-40: Second mobile weather station.....	50
Figure 3-41: Fluctuation of temperature and wind speed at test measurement .....	51
Figure 3-42: Monitored air temperature at BPI and mobile weather station .....	52
Figure 3-43: Monitored relative humidity at BPI and mobile weather station.....	52
Figure 3-44: Regression analysis of temperature monitored by BPI and mobile weather station to calibrate the mobile weather station.....	53
Figure 3-45: Regression analysis of relative humidity monitored by BPI and mobile weather station to calibrate the mobile weather station.....	53
Figure 3-46: Graphical overview over the data flow within the ENVI-met.....	56
Figure 3 47: Schematic description of model lay-out. ....	57
Figure 3-48: Schematic of the 7-node model.....	68
Figure 4-1: Temperature differences (MW – BPI) for a reference day (from 11:00 h to 18:00 h) at all 13 measuring spots.....	74
Figure 4-2: Relative solar radiation differences for a reference day (from 11:00 h to 18:00 h) for all 13 measuring spots.....	75
Figure 4-3: Wind speed differences for a reference day (from 11:00 h to 18:00 h) for all 13 measuring spots.....	76
Figure 4-4: Water vapor concentration differences for a reference day (from 11:00 h to 18:00 h) for all 13 measuring spots .....	77
Figure 4-5: Box plot of temperature differences for all 13 measuring spots.....	78
Figure 4-6: Box plot of relative solar radiation difference (MW – BPI) for all 13 locations .....	78

Figure 4-7:	
Box plot of wind speed difference (MW – BPI) for all 13 locations .....	79
Figure 4-8:	
Box plot of absolute humidity difference (MW – BPI) for all 13 locations .....	80
Figure 4-9:	
Relationship between relative solar radiation and temperature difference .....	81
Figure 4-10:	
Relationship between temperature difference and SVF .....	81
Figure 4-11:	
Relationship between relative solar radiation difference and SVF .....	82
Figure 4-12:	
Measured air temperatures at the BPI and at the measuring spots (category: Street) .....	83
Figure 4-13:	
Measured air temperatures at the BPI and at the measuring spots (category: Plaza).....	83
Figure 4-14:	
Measured air temperatures at the BPI and at the measuring spots (category: Courtyard).....	84
Figure 4-15:	
Measured air temperatures at the BPI and at the measuring spots (category: Park).....	84
Figure 4-16:	
Measured solar radiation at the BPI and at the measuring spots (category: Street) .....	85
Figure 4-17:	
Measured solar radiation at the BPI and at the measuring spots (category: Plaza)...	85
Figure 4-18:	
Measured solar radiation at the BPI and at the measuring spots (category: Courtyard).....	86
Figure 4-19:	
Measured solar radiation at the BPI and at the measuring spots (category: Park)....	86
Figure 4-20:	
Relationship between wind speed at BPI and Streets .....	87
Figure 4-21:	
Relationship between wind speed at BPI and plazas.....	87
Figure 4-22:	
Relationship between wind speed at BPI and Courtyards.....	88
Figure 4-23:	
Relationship between wind speed at BPI and Parks.....	88
Figure 4-24:	
Relation between absolute humidity at BPI and streets .....	89
Figure 4-25:	

Relation between absolute humidity at BPI and plazas .....	89
Figure 4-26: Relation between absolute at BPI and courtyards .....	90
Figure 4-27: Relation between absolute humidity at BPI and parks .....	90
Figure 4-28: Mean temperature differences for all 13 measuring locations, classified by sky condition.....	92
Figure 4-29: Mean temperature differences for all 13 measuring locations, classified by wind speed at BPI .....	92
Figure 4-30: Mean temperature differences for all 13 measuring locations classified by the day time .....	93
Figure 4-31: Mean water vapor concentration differences (MW – BPI) for all 13 locations classified by sky condition .....	93
Figure 4-32: Mean water vapor concentration differences (MW – BPI) for all 13 locations classified by wind speed at BPI .....	94
Figure 4-33: Mean CO2 concentration for all 13 locations classified by wind sky condition.....	94
Figure 4-34: Mean CO2 concentration for all 13 locations classified by wind speed at BPI.....	95
Figure 4-35: Mean wind speed differences (MW-BPI) for all 13 locations classified by wind speed at BPI .....	96
Figure 4-36: The temperature difference (MW-BPI) for the locations S1, S5, P1, C2, and G1 during long measurements.....	97
Figure 4-37: Solar radiation differences (MW-BPI) for the locations S1, S5, P1, C2, and G1 during long measurements.....	97
Figure 4 38: Water vapor differences (MW-BPI) for the locations S1, S5, P1, C2, and G1 during long measurements.....	98
Figure 4 39: Wind speed differences (MW-BPI) for the locations S1, S5, P1, C2, and G1 during long measurements .....	98
Figure 5 1: Selected area as first model including BPI, C*, C2, S1 and P1 ( <a href="http://www.wien.at">www.wien.at</a> ) .....	100
Figure 5-2: Monitored and simulated air temperatures of BPI (scenarios: 0- I-II-III- IV), simulated time period from 03:00 h on 22.07.2010 to 05:00 h on 23.07.2010 .....	106

Figure 5-3: Monitored and simulated global radiation of BPI (scenarios: 0- I-II-III- IV), simulated time period from 03:00 h on 22.07.2010 to 05:00 h on 23.07.2010 .....	106
Figure 5-4: Monitored and simulated air temperatures of C* (scenarios: 0- I-II-III- IV), simulated time period from 03:00 h on 22.07.2010 to 05:00 h on 23.07.2010 .....	107
Figure 5-5: Map of the simulated area (www.wien.at) .....	109
Figure 5-6: Arial picture from the simulated area (google Map) .....	110
Figure 5-7: Observed and predicted air temperature at WIS, (simulated day: 13.07.2011) .....	111
Figure 5-8: Observed and predicted air temperature at BPI, (simulated day: 13.07.2011) .....	111
Figure 5-9: Different urban spaces used in the parametric analysis for the Main Model .....	115
Figure 5-10: Simulated air temperature for defined locations at 1.4 m above the ground level (the base case) .....	116
Figure 5-11: Simulated specific humidity for defined locations at 1.4 m above the ground level (the base case model) .....	117
Figure 5-12: 3D view of the model V1 .....	118
Figure 5-13: Air temperature differences between the base case and V1 at 1.4 m above the ground level .....	119
Figure 5-14: Water vapor concentration differences between the base case and the scenario V1 at 1.4 m above the ground level.....	119
Figure 5-15: 3D view of the scenario V2 .....	120
Figure 5-16: Air temperature differences between base case and V2 .....	121
Figure 5-17: Vertical view of wind distribution in the scenario V2 .....	122
Figure 5-18: Water vapor concentration differences between the base case and the scenario V2 .....	122
Figure 5-19: 3D view of the model after adding the trees and green roofs (scenario V3) .....	123
Figure 5-20: air temperature differences between the base case and the model after implementing additional trees and green roof (scenario V3).....	124



Figure 5-21:	
Water vapor concentration differences between the base case and the model after implementing additional trees and green roof (scenario V3).....	124
Figure 5-22:	
3D view of the model after adding the permeable pavements (scenario M1).....	125
Figure 5-23:	
Air temperature differences between the base case and the main model as defined by scenario M1 .....	126
Figure 5-24:	
Water vapor concentration differences the base case and the main model as defined by scenario M1 .....	127
Figure 5-25:	
3D View of the model after adding more trees and green roof as well as changing the sealing to the permeable pavement (scenario VM).....	128
Figure 5-26:	
Air temperature differences between the base case and the model after adding more trees and green roof as well as changing the sealing to the permeable pavement (scenario VM) .....	128
Figure 5-27:	
Water vapor concentration difference between the base case and the model after adding more trees and green roof as well as changing the sealing to the permeable pavement (scenario VM) .....	129
Figure 5-28:	
3D view of the model after increasing the roofs reflections (scenario M2) .....	130
Figure 5-29:	
Air temperature differences between the base case and the model after increasing roofs reflections (scenario M2) .....	131
Figure 5-30:	
Water vapor concentration difference between the base case and the model after increasing roofs reflections (scenario M2).....	132
Figure 5-31:	
3D view of the model after increasing the walls reflections (scenario M3) .....	133
Figure 5-32:	
Temperature difference between the base case and the model after increasing walls reflections (scenario M3).....	133
Figure 5-33:	
Global radiation difference between the base case and the model after increasing walls reflections (scenario M3).....	134
Figure 5-34:	
Water vapor concentration difference between the base case and the model after increasing walls reflections (scenario M3).....	135
Figure 5-35:	
3D view of the model after decreasing the height of buildings to 70% of their current condition (scenario H1).....	136

Figure 5-36: Air temperature differences between the base case and the model after decreasing the height of the buildings to 70% of its current condition (scenario H1) .....	137
Figure 5-37: Water vapor concentration differences between the base case and the model after decreasing the height of the buildings to 70% of its current condition (scenario H1).....	138
Figure 5-38: 3D view of the model after increasing the height of buildings up to 30% (scenario H2).....	138
Figure 5-39: Air temperature differences between base case and the model after decreasing the height of buildings to 70% of its current condition (scenario H2).....	139
Figure 5-40: Water vapor concentration difference between base case and the model after decreasing the height of buildings to 70% of its current condition (scenario H2) ...	140
Figure 5-41: Average air temperature differences between scenarios and the base case within the model domain .....	141
Figure 5-42: Average air temperature differences between scenarios and the base case within the streets.....	142
Figure 5-43: Average water vapor concentration differences between scenarios and the base case within the model domain .....	143
Figure 5-44: Average water vapor concentration differences between scenarios and the base case within the streets.....	144
Figure 5-45: Average cooling effect of the evaluated scenarios for every location during 24 hours.....	145
Figure 5-46: Average cooling effect of the evaluated scenarios for every location during the day .....	146
Figure 5-47: Average cooling effect of the evaluated scenarios for every location during the night.....	146
Figure 5-48: Average air specific humidity change for the evaluated scenarios for every location during 24 hours.....	147
Figure 5-49: Average cooling effect of evaluated scenarios for every location during the day ...	148
Figure 5-50: Average cooling effect of evaluated scenarios for every location during the day ...	148

## Abbreviations

Symbol	Description	Unit
A	proportion the catchment covered with the $i^{\text{th}}$ surface	-
a	average albedo of walls	-
AA	status of the soil moisture	-
ABL	Atmospheric Boundary Layer	-
$a_{c,f,s}$	albedo of clouds, leaf, soil	-
AH	absolute humidity	$\text{g.m}^{-3}$
C	heat capacity of air	$\text{J.K}^{-1}.\text{m}^{-3}$
$c_{1,2,3}$	$\epsilon$ -equation standard constant ( $c_1=1.44$ , $c_2=1.92$ , $c_3=1.44$ )	-
$C_{d,f}$	mechanical drag coefficient (=0.2)	-
$C_p$	specific heat capacity at constant pressure	$\text{J.kg}^{-1}.\text{K}^{-1}$
CV	coefficient of variation of root mean square deviation	%
$c_\mu$	constant for turbulence model (=0.09)	-
d	zero-plane displacement length	m
d	index of agreement	-
D	leaf diameter	m
$D_x$	distance between the facade and the center on next grid cell	m
$D_\eta$	hydraulic diffusivity of the soil	$\text{m}^2.\text{s}^{-1}$
e	vapor pressure	hPa
E	evapotranspiration	$\text{kg.m}^{-2}.\text{s}^{-1}$
E	local turbulence	$\text{m}^2.\text{s}^{-2}$
$e^*$	mean saturation pressure	Pa
$e_{2m}$	water vapor pressure in 2 m above ground level	hPa
$E_a$	drying power of air	-
$e_a$	ambient vapor pressure	Pa
f	Coriolis parameter ( $=10^{-4}$ )	$\text{s}^{-1}$
F	extinction coefficient	-
F	orientation of leaf toward sun(=0.5 for random orientation)	-

$f_w$	fraction of wet leaves	-
$g$	gravity	$m.s^{-2}$
$G(T0)$	soil heat flux	$W.m^{-2}$
$h$	convective heat transfer coefficient	$W.m^{-2}.K^{-1}$
$h$	sun height	°
$H(T0)$	turbulent sensible heat (for ground 0)	$W.m^{-2}$
$h_c$	convection heat transfer coefficient	$W.m^{-2}.K^{-1}$
$h_{c,i}$	inside heat transfer coefficient	$m^{-2}.K^{-1}$
$I_0$	radiation intensity of sun	$W.m^{-2}$
$i^{th}$	surface type	-
$J_{f,evap}$	evapotranspiration flux of liquid water on the leaves	$m.s^{-1}$
$J_{f,h}$	sensible heat flux	$m.K.s^{-1}$
$J_{f,trans}$	transpiration flux controlled by the leaf	$m.s^{-1}$
$K$	solid material thermal conductivity	$W.m^{-1}.K^{-1}$
$k$	von Karman constant =0.4	-
$k$	kinetic energy of turbulence, dilatation viscosity	$m^2.s^{-2}$
$k$	dilatation viscosity	$Kg.m^{-1}.s^{-1}$
$K_{(mobile, BPI)}$	shortwave radiation (measured by mobile weather station, measured by BPI)	$W.m^{-2}$
$K_{dif, dir}$	diffuse/ direct short wave radiation	$W.m^{-2}$
$K_E$	diffusion coefficient for local turbulence	$m^2.s^{-1}$
$K_h$	exchange coefficient for heat	$m^2.s^{-1}$
$K_{hw}$	air thermal diffusivity at the surface of wall/roof	$m^2.s^{-1}$
$K_m$	exchange coefficient	$m^2.s^{-1}$
$K_q$	exchange coefficient for vapor	$m^2.s^{-1}$
$K_{rel}$	relative short wave radiation	%
$K_s$	thermal diffusivity of the soil	$m^2.s^{-1}$
$K_e$	diffusion coefficient for local turbulence	$m^2.s^{-1}$
$K_\eta$	hydraulic conductivity	$m.s^{-1}$
$l$	amount of water vapor in a layer of air	g
$L$	latent heat of vaporization	$J.kg^{-1}$
$L$	length	m
$L_{clearsky\downarrow}$	incoming atmospheric infrared radiation	$W.m^{-2}$

$L\uparrow$	emitted long wave radiation	$W.m^{-2}$
$L\downarrow$	received long wave radiation	$W.m^{-2}$
LAD	Leaf Area density	$m^2.m^{-3}$
LAI	Leaf area Index	$m^3.m^{-3}$
LAI*	3D leaf area index including angle of incidence of sun rays	$m^3.m^{-3}$
$LE(T_0, q_0)$	turbulent latent heat density (for ground 0)	$W.m^{-2}$
$L_v$	latent heat of vaporization	$MJ.kg^{-1}$
m	optical air mass	-
m	mass	kg
$\bar{m}$	mass flow	$kg.s^{-1}$
$m_i$	measured data	-
$m_{trans}$	total mass of transpired water	$kg.m^{-2}.s^{-1}$
n	fraction of the sky covered by cloud (0-1)	-
N	cloud cover (in octas)	-
Nu	Nusselt number	-
$p_v$	water vapor partial pressure	Pa
$p'$	pressure perturbation	Pa
PBL	Planetary Boundary Layer	-
Pr	Prantal number	-
Pr	Production of turbulence energy due to wind shearing	$m^2.s^{-3}$
$P_{vs}$	saturation vapor pressure	Pa
q	specific humidity	$g.kg^{-1}$
$q''$	Heat flux	$W.m^{-2}$
$Q^*$	net all wave radiation	$W.m^{-2}$
$q^*$	saturation value at the leaf surface	$g.kg^{-1}$
$Q_A$	net horizontal heat advection	$W.m^{-2}$
$Q_E$	latent heat flux	$W.m^{-2}$
$Q_E$	additional turbulence produced by vegetation	$m^2.s^{-3}$
$Q_F$	anthropogenic heat flux	$W.m^{-2}$
$Q_H$	convective (or turbulent ) sensible heat flux	$W.m^{-2}$
$Q_h$	sink/source term due to heat	$K.s^{-1}$
$Q_q$	sink/source term due to vapor	$(g.kg^{-1}).s^{-1}$

$Q_s$	net storage heat flux	$W.m^{-2}$
$Q_\epsilon$	additional turbulence dissipated by vegetation	$m^2.s^{-4}$
$R$	radiation given off by an object	$W.m^{-2}$
$R$	individual gas content (=461.52)	$J.kg^{-1}.K^{-1}$
$r$	Radius	$m$
$R_{sw}^*$	incoming short wave radiation at the boundary	$W.m^{-2}$
$R_{sw,dif}^o$	diffuse short wave radiation	$W.m^{-2}$
$R_{sw,dir}^o$	absolute shortwave radiation	$W.m^{-2}$
$r_a$	aerodynamic resistance of leaf	$s.m^{-1}$
$RAD$	root area density	$m^2.m^{-3}$
$R_{lw,building}$	long wave radiation emitted from buildings	$W.m^{-2}$
$R_{lw,ground}$	long wave radiation emitted from ground	$W.m^{-2}$
$R_{lw,sky}$	long wave radiation emitted from sky	$W.m^{-2}$
$R_{lw}\downarrow$	incoming long wave radiation	$W.m^{-2}$
$R_{lw}\leftrightarrow$	horizontal longwave radiation flux	$W.m^{-2}$
$RMSE$	root mean square errore	-
$r_s$	stomatal resistance	$s.m^{-1}$
$R_{sw,abs}$	absorbed shortwave radiation	$W.m^{-2}$
$s$	slope of the saturation vapor pressure versus the temperature relationship	-
$Sc$	Schmidt-number	-
$s_i$	simulated data	-
$S_u$	loss of wind speed due to drag forced at the plants	$m.s^{-2}$
$S_v$	loss of wind speed due to drag forced at the plants	$m.s^{-2}$
$SVF$	Sky View Factor	-
$S_w$	loss of wind speed due to drag forced at the plants	$m.s^{-2}$
$S_\eta$	water uptake by the plant root	$s^{-1}$
$T$	absolute temperature/ Averaged Temperature	$K$
$T_a$	dry bulb temperature of air near the ground	$K$
$T_a$	temperature of ambient air	$K$
$T_f^{(+,-)}$	leaf temperature (+overlying side, - underlying side of the leaf	$K$
$Th$	dissipation of turbulence energy due to thermal	$m^2.s^{-3}$

	stratification	
$T_{rf}$	transmission factor	-
$T_s$	surface temperature, soil temperature	K
TU	Vienna University of Technology	-
$T_w$	temperature of wall	K
$u$	horizontal wind speed	$m.s^{-1}$
$u$	mean horizontal wind speed	$m.s^{-1}$
UCL	Urban Canopy Layer	-
$v$	wind speed	$m.s^{-1}$
$W$	mean wind speed	$m.s^{-1}$
$W_{dew}$	actual amount of dew on the leave surface	$kg.m^{-2}$
$W_{dew.max}$	maximum possible amount of dew on the leave surface (=0.2)	$kg.m^{-2}$
$x,y,z$	Cartesian coordinates	-
$X_s$	empirical parameters (=0.10 low land, =11.5 mountains)	-
$Y_s$	empirical parameters (=0.35 low land, =0.43 mountains)	$K.hPa^{-1}$
$Z_0$	micro scale roughness length of the surface	m
$z_{0m}$	momentum roughness length	m
$z_{0v}$	water vapor roughness length	m
$\alpha$	albedo	-
$\alpha$	ratio of evaporation from a wet surface	-
$\alpha'_i$	empirical coefficient	-
$\alpha_M$	Mie scattering coefficient (=0.00816. $\lambda^{-4}$ )	-
$\alpha_R$	Raileight scattering coefficient (=1.3 $\beta r t$ )	-
$\beta_{tr}$	opacity coefficient	-
$\gamma$	psychometric constant	Pa.K
$\delta$	Kronecker delta (=1 if $i=j$ , =0 if $i \neq j$ )	-
$\delta_c$	factor depending on evaporation and transpiration probability	-
$\Delta q$	leaf to air humidity deficit	$g.kg^{-1}$
$\Delta Q_s$	surface (net storage) heat flux density	$W.m^{-2}$

$\epsilon$	total hemispherical emissivity	-
$\epsilon$	dissipation rate	$m^2.s^{-3}$
$\epsilon$	emissivity of façade	-
$\epsilon$	turbulent dissipation	$m^2.s^{-3}$
$\epsilon_{sky, f, s}$	emissivity of sky, leaf, surface	-
$\epsilon_n$	emissivity of the layer n	-
$\eta$	volumetric water content	$m^3.m^{-3}$
$\theta$	potential temperature	K
$\theta_{ref}$	reference temperature at the see level	K
$\lambda$	wavelength range	$\mu m$
$\lambda$	Thermal conductivity	$W.K^{-1}.m^{-1}$
$\lambda_{s, w}$	thermal conductivity of the wall	$W.K^{-1}.m^{-1}$
$\lambda_w$	thermal conductivity of the wall	$W.K^{-1}.m^{-1}$
$\mu$	Viscosity (air)	$Kg.m^{-1}.s^{-1}$
$\rho$	Density (air)	$kg.m^{-3}$
$\rho$	Pressure	Pa
$\rho_w$	density of wall	$kg.m^{-3}$
$\sigma, \sigma_B$	Stefan-Boltzman constant ( $=5.67 \times 10^{-8}$ )	$W.m^{-2}.K^{-4}$
$\sigma_E$	constant for turbulence model (=1)	-
$\sigma_{Iw\uparrow}$	modification factor upwards long wave radiation	-
$\sigma_{Iw\downarrow}$	modification factor downwards long wave radiation	-
$\sigma_{SVF}$	Sky View Factor	-
$\sigma_{sw.dif}$	modification factor for diffuse short-wave radiation	-
$\sigma_{sw.dir}$	modification factor for direct short-wave radiation	-
$\sigma_E$	constant for turbulence model (=1.3)	-
$\tau$	Shear stress	$kg.m^{-1}.s^{-2}$
$\tau$	time	s
$\phi$	relative humidity	%
$\Psi$	Fluid flow parameter	-
$\omega$	minimum cutoff angle in spatial direction	°
$\Gamma$	turbulent diffusivity	$m^2.s^{-1}$



# 1. Introduction

## 1.1. Objective

The present work is derived by the wish to develop an efficient approach to dynamic monitoring of micro-climatic conditions in various – morphologically distinct – locations in the city of Vienna. This study tries to achieve a deeper understanding of those urban design and planning parameters that lead to variance in micro-climatic conditions in large and densely populated cities such as Vienna. It addresses the contribution of urban space design, i.e. aspect ratio, materials, wind speed, sky condition, surface protection and further more details towards predicting the variation of micro-climatic parameters in Vienna.

To do so, weather data, i.e. temperature, solar radiation, relative humidity, wind speed and CO<sub>2</sub> concentration in the air were measured at defined points at the height of pedestrians to develop a reliable database with high resolution. Using these data, the potential for the development of high resolution micro-climate boundary condition for the sustainable building design and operation through micro-climate modeling has to be studied. Furthermore, the influence of the geometrical parameters and urban material properties have to be surveyed using the collected weather data and by the aid of the results obtained through urban micro-climate modeling.

To realize the above mentioned goal the following features are investigated and discoursed within the context of this study:

- The effect of the urban geometry and materials properties on creating a different micro-climate within the urban canyon,
- The role of using vegetation and water in mitigating the thermal condition of the urban space.

Further, the importance and the effect of the following design parameters are evaluated:

- The street orientation, i.e. E-W, N-S, NE-SW, NW-SE,
- The height to width ratio: H/W.

## **1.2. Motivation**

According to the UN 2011 revision of world urbanization prospects the urban areas accommodate more than half of the world population and by the year 2050 this fraction will reach almost 70% of the world population (Department of Economic and Social Affairs, Population Division 2012). The effect of increasing urbanization on the urban micro-climate has been the subject of many research projects for quite some time (Arnfield 2003). Micro-climatic conditions can display a considerable variance, due to the differences in morphology and density of urban spaces as well as the thermal and radiative properties of surfaces, and thermal properties of materials (Oke 1982). Besides, the situation is different in rural areas than in urban areas, due to high anthropogenic heat emissions caused by people directly and indirectly due to air conditioning of buildings and traffic load (De la Flor and Dominguez 200; Rajagopalan et al. 2008).

Micro-climatic conditions are being modified through two main functions: the local weather condition and the urban fabric at the very location. In other words, in order to be able to precisely define the required boundary conditions (micro-climatic conditions) for the sustainable building design and operation (with respect to an optimized energy consumption and thermal comfort) within an urban area. Consideration of both the local weather condition and the urban fabric are of vital importance in urban micro-climate investigation. These two factors –in an interactive way- affect the micro-climate condition in a location within an urban area. Therefore, planning, retrofit, and mitigation measures for buildings cannot be based just on reliable local weather information (Maleki et al. 2012). It may be thus concluded that the lack of reliable micro-climatic data for cities lead to inappropriate building design and operation and thus, higher financial and ecological expenditures for the building owners and users.

To address this important issue, the data have been collected systematically, through this proposed research, in various locations within the city of Vienna to model the micro-climatic conditions for the immediate surroundings of the buildings. This information is essential to evaluate the performance issues relating to energy use improvement and thermal comfort requirements of the buildings, which accordingly contribute to the optimal coordination of the prevention, adaptation, and mitigation measures pertaining to the urban heat island phenomenon. The resulting micro-climatic models could also be integrated in planning tools such as the building performance simulation programs typically used to support the decision making in the design and retrofit process. These tools enable the engineering teams to conduct virtual experiments on building designs and to evaluate and optimize their expected performance before the actual building construction and operation, resulting in significant improvements concerning the cost-effectiveness and sustainability of the construction industry.

### **1.3. Structure**

This dissertation is structured in seven chapters including introduction.

**Chapter two:** the theoretical background of urban micro-climate studies, measuring and modeling methods are being reviewed.

**Chapter three:** this chapter delineates the approach in two main sections, i.e. empirical and computational inquiries. Empirical inquiries focus on the methodology used for monitoring and describing the case study, while computational inquiries provide the information about ENVI-met, the simulation tool used for the modeling in the particular framework relevant to this work.

**Chapter four:** The results of the empirical inquiries are shown and discussed in this chapter.

**Chapter five:** the results of numerical simulations are illustrated and discussed in this chapter;

**Chapter six:** conclude the empirical and computational inquiries done for this study.

**Chapter seven:** addresses the possibilities for future research in this topic.

## **2. Theoretical Background**

Man-made urban environment reforms the energy balance of the Earth surface and the composition of the atmosphere comparing with its intact natural terrains, even though these terrains are, in turn, affected by human activities such as agriculture and forestry. These changes result in formation of a district local climate in urban areas, which is known as urban micro-climate (Erell et al. 2011).

To have a better understanding of the urban micro-climate, the atmosphere above the urban area and the energy balance through it should be well comprehended. Owing to this aim, in this chapter the atmosphere layers above the cities as well as their characteristics will be shortly described. As well as the energy balance in the urban area, its components and modifying factors will be described and analyzed. At the end, the measuring and modeling methods of the urban microclimatic weather condition will be surveyed.

### **2.1. Urban Micro-climate**

The atmosphere of the earth is a layer of gases with an average thickness of 700 km surrounding the earth (Bishop 1976). It can be divided into several distinguishable layers with different characteristics concerning the temperature, composition, density, etc.

The lowest layer of atmosphere, named Troposphere, is the layer which we live in and is the one affected by the surfaces of the earth. Its thickness is 12 km in average, thinner in the polar region and thicker in the tropic. Its density and temperature decrease by increasing in the height (Geerts and Linacre 1997).

The Planetary Boundary Layer (PBL), also known as the Atmospheric Boundary Layer (ABL), is the lowest part of the troposphere and its behavior is directly influenced by its contact with the planetary surface (Encyclopaedia Britannica 2013). It usually responds to the changes in the surfaces in an hour or less. In an urbanized area this layer is also called as Urban Boundary Layer (UBL), which is further divided into a number of sub-layers. As it is illustrated in Figure 2-1, UBL grows from the upwind edge of the city and extends upwards to about ten times the height of the buildings in the urban area, and spreads beyond the urban area in the downwind direction. The upper portion of the UBL, 50 to 60% of its thickness, is known as the "Mixed Layer", which is influenced by the urban surface and the surrounding non-urban terrain. Another sub-layer of the UBL, known as the surface layer, extends normally to up to four to five times of the average building height in the urbanized area. Its

formation is entirely affected by the geometry and the morphology of the urban fabric, as well as by the characteristics of the buildings and the ground cover. Here, the holistic texture of the urban surface plays a key role by making the properties of this layer. The role of the single urban elements in this regard can normally be considered as minor. Within this layer the vertical velocity profile of the wind takes the shape of a logarithmic curve (Erell et al. 2011).

Also the vertical energy transfer between the urban surface and the atmosphere in this layer due to high degree of turbulence is assumed to be constant and uniform, which in turn eases the measurement of the heat flux (and the pollutants concentration) at any point above the surface within this layer. For this reason, the surface layer is also known as a constant flux layer, or alternately as the inertial sub-layer (Erell et al. 2011).

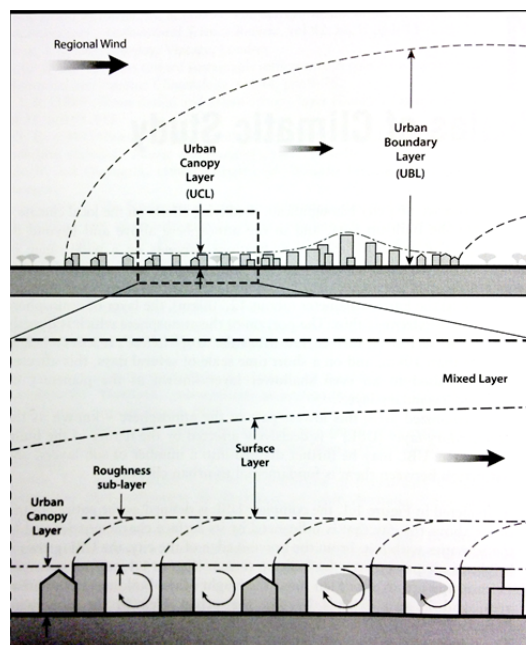


Figure 2-1: Schematic section of the urban atmosphere, showing UBL and UCL (top), and the homogeneous surface layer above the city and the heterogeneous urban canopy layer (bottom) (Erell et al. 2011)

Another sub-layer, starting directly below the surface layer, is known as the “roughness sub-layer”, whose thickness is assumed to be equal to about twice the average building height. In the urban area the characteristics of this layer are being determined and affected on one hand by the individual surface features, and on the other hand by the holistic of the urban fabric, as in the case of the surface layer. This layer is considered as a transition zone between the vertically homogenous surface layer and the so-called heterogeneous urban canopy-layer (UCL) (Florens et al. 2013).

Urban canopy layer (UCL) is the lowest sub-layer of the urban atmosphere, which forms from the ground level up to the height of the urban canopy (associated urban elements such as buildings and trees). This zone is mainly affected by the immediate single urban elements and the variation of conditions within the urban texture causing its properties to vary from point to point. The heterogeneity of the UCL establishes a unique micro-climate within any urban space, in which the climatic indicators of the urban micro-climate such as the air temperature and its relative humidity as well as the wind flow and the radiation balance are defined by physical properties of the very immediate surroundings as well as by the urban and the regional environment (Shashua-Bar et al. 2004; Erell et al. 2011).

## 2.2. The Urban Energy Balance

As mentioned, the micro-climate within the man-made area differs from its surrounding natural area. To understand this difference, the surface energy balance of this area should be analyzed.

The urban surface energy balance is based on the first law of thermodynamics (Shahmohamadi et al. 2011). Here, it means if the urban area is considered a closed system, the input energy will be equal to the output energy plus the stored energy. Therefore, the urban area is modeled as a box with an arbitrary height limitation within the surface sub-layer representing the overall urban climate, and with the physical and the transport properties representing the average properties of the urban texture. Within these boundaries, absorbed energy by the surface of the earth from the radiation or from anthropogenic heat either warms up the nearby air temperature, evaporates the existence moisture or heats the materials. This can be expressed in the following equation (Masson et al. 2002):

$$Q^* + Q_f = Q_h + Q_e + \Delta Q_s + \Delta Q_a \quad (2-1)$$

where  $Q^*$  is the net all-wave radiation,  $Q_f$  is the anthropogenic heat flux,  $Q_h$  is the convective (or turbulent) sensible heat flux,  $Q_e$  is the latent heat flux,  $\Delta Q_s$  is the net storage heat flux, and  $\Delta Q_a$  is the net horizontal heat advection.

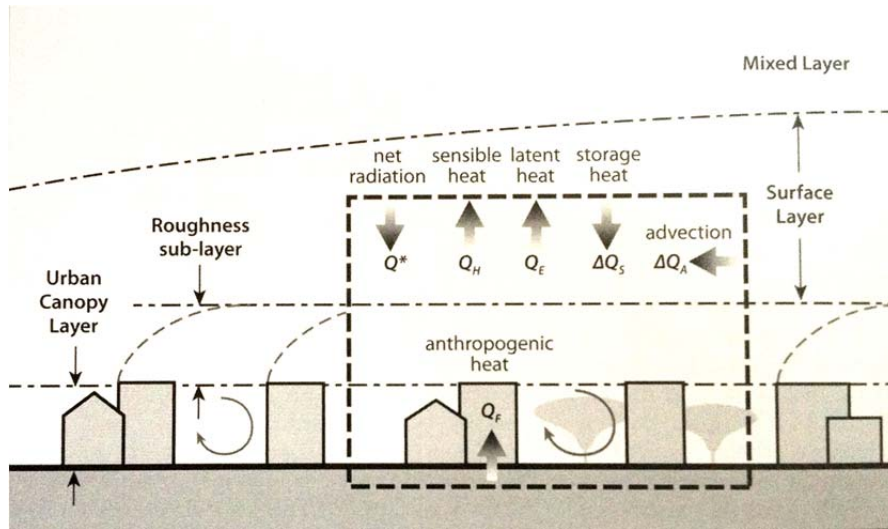


Figure 2-2: Schematic section showing urban surface energy balance components (Erell, Paarlmutter and Williamson 2011)

### 2.2.1. Radiation

Radiation is the major part of the input energy to the urban canopy model and is affected by several factors which will be explained later in this section. Radiation exchange in an outdoor surface is expressed by the following equation (Offerle et al. 2003):

$$Q^* = (K_{dir} + K_{dif})(1 - \alpha) + L \downarrow - L \uparrow \quad (2-2)$$

where  $Q^*$  is the net radiative balance,  $K_{dir}$  is the direct short-wave radiation,  $K_{dif}$  is the diffuse short-wave radiation,  $\alpha$  is the albedo of the surface, and  $L \downarrow$  and  $L \uparrow$  are respectively the long-wave radiation received by the surface from the sky and the long-wave emitted by the surface.

*Albedo* is defined as the hemispherical and wavelength-integrated reflectivity of a surface (Taha 1997). This definition is applied to two levels: (a) the individual urban facet (b) the three dimensional arrangement of the individual facets that comprise the urban surface.

In addition to the geographical condition of the urban area e.g. latitude, slope, the geometrical composition as well as the physical properties of the pertaining surface materials affect the absorption and the reflection of the incoming short-wave and long-wave radiation.

### 2.2.1.1. Geometrical factors affecting input radiation to urban canopy model

As mentioned, the geometrical characteristics of the urban elements can control the amount of the incident radiation to the urban surfaces, by shading or being open to the sky. To evaluate how and to which extent they might be effective, these properties shall be quantified to be capable of being analyzed (Mahdavi et al 2013). Owing to this aim, the following parameters are defined:

- *The height-width ratio or aspect ratio (H/W)*: it is the ratio of the average height of the adjacent vertical elements to the average width of the urban canyon (Mahdavi et al. 2013),
- *The canyon axis orientation ( $\vartheta$ )*: it represents the angle between a running line from the North to the South and the main axis of the urban canyon in degrees. Also, it can be described by the closer cardinal directions, e.g. N-S, E-W or the diagonal directions, i.e. NW-SE, NE-SW,
- *The Sky View Factor (SVF)*; is a geometric ratio that expresses the ratio of the solar radiation received by a planar surface compared to that received from the entire hemispheric radiating environment. Generally, the sky view factors are determined using either the analytical or photographic methods (Grimmond et al. 2001).

$$SVF = \left(\frac{1}{360}\right) \cdot \sum_{\pi=0}^{360} \cos \omega(\pi) \quad (2-3)$$

where  $\omega$  is the maximum cutoff angle in the spatial direction  $\pi$ .

- *Frontal area density*; which represents the ratio of the vertical surface area of all building facades facing to the prevailing wind direction to the overall horizontal plan area (Erell et al. 2011).
- *Plan area density*; which describes the density of the buildings, actually, can be considered a simple ratio of the area covered by the buildings to the total area available (Erell et al. 2011).
- *Vegetation Fraction*, used to quantify the density of the vegetated area in the city. It is the ratio of the area covered by the vegetation to the total existing area (Erell et al. 2011).

### 2.2.1.2. Long-wave radiation

According to the Stefan-Boltzmann law the radiation given off by an object can be calculated by the following equation (Offerle et al. 2003):

$$R = \varepsilon \cdot \sigma \cdot T^4 \quad (2-4)$$

where T is the absolute temperature in K and  $\sigma$ , known as Stefan-Boltzmann constant, is  $5.67 \times 10^{-8} \text{ W.m}^{-2} \cdot \text{K}^{-4}$  and  $\varepsilon$  is the total hemispherical emissivity.



*Emissivity* is the ability of a surface to re-radiate any absorbed energy to the sky. Surfaces with high emissivity release the heat faster. The higher the emissivity the larger the thermal radiation emitted from the surface. In case of the outgoing long-wave radiation  $L\uparrow$  this equation is expressed as following (Offerle et al. 2003):

$$L\uparrow = \varepsilon_s \cdot \sigma \cdot T_s^4 \quad (2-5)$$

where  $\varepsilon_s$  is the emissivity of the surface and  $T_s$  the temperature of the surface.

To calculate the incoming atmospheric infra-red radiation the equation 2-4 can be expressed in the following way (Offerle et al. 2003):

$$L_{clearsky}\downarrow = \varepsilon_{sky} \cdot \sigma \cdot T_a^4 \quad (2-6)$$

where  $T_a$  is the dry bulb temperature of the air near the ground (K) and  $\varepsilon_{sky}$  is the sky emissivity.

Different models were proposed to calculate the sky emissivity. In most of them the effect of the altitude on the long-wave radiation at the surface is indirectly incorporated. One of the proposed models which has incorporated the effect of the altitude in two empirical coefficients to calculate the incoming long-wave radiation ( $L\downarrow$ ), is (Erell et al. 2011):

$$L_{clearsky}\downarrow = \sigma \cdot T_a^4 \cdot (1 - X_s \cdot \exp(-Y_s \cdot e / T_a)) \quad (2-7)$$

for lowland sites  $X_s=0.35$  and  $Y_s=10 \text{ KhPa}^{-1}$  and for mountains these values are 0.43 and  $11.510 \text{ KhPa}^{-1}$ , respectively. And the term  $e$  stands for vapor pressure measured in hPa.

Another important effective parameter on the long-wave exchange in the atmosphere is the cloud cover. To compensate the cloud cover, the following modification is applied to the relationship between the incoming radiation from the clear and cloudy sky (Erell et al. 2011):

$$L\downarrow = (1 + 0.0224 n - 0.0035 n^2 + 0.00028 n^3) \cdot L_{clearsky}\downarrow \quad (2-8)$$

„n“ is the fraction of the sky covered by cloud, expressed in tenths on a scale from zero to unity.

### 2.2.2. Anthropogenic energy

In addition to the solar radiation, the anthropogenic heat in the urban areas causes heat flux too (Morvay and Gvozdenac 2008). The energy consumption due to the human activities in the industries, residences, transportation and commercial

activities cause anthropogenic heat discharge to the urban environment. Anthropogenic heat can affect the air temperature and the surface temperature in the downtown. The intensity of its impact alters temporally and spatially. Anthropogenic heating usually has the largest impact on the densely developed urban spaces in the winter time, due to intensive heating load during the season (Erell et al. 2011; Taha 1997; Hamilton et al. 2009). However in the hot climate, the waste heat from the refrigerative air-conditioning system can also cause a significant anthropogenic heat discharge. Additionally, the evaporative cooling of the building generates latent heat that can result in higher humidity and heat stress in the city (Erell et al. 2011). Taha (1997) reports the range of anthropogenic heat in the most major cities of US, between 20 and 40 W.m<sup>-2</sup> in the summer and between 70 and 210 W.m<sup>-2</sup> in the winter. Hamilton (2009) mentions the Ichinose et al's (1999) study of Tokyo quantified the increase in sensible temperatures within the urban environment to be up to 1.5 C within the areas of high anthropogenic daily heat emission (between 400 and 1540 W.m<sup>-2</sup>).

Taha (1997) and Hamilton (2009) declare that the effect of anthropogenic heat might be important in the urban centers but it is small and negligible in suburban areas.

### 2.2.3. Convective sensible heat flux

The convection is the transfer of the thermal energy by the means of a fluid or gas and is calculated by the following equation:

$$Q_h = h_c \cdot (T_s - T_a) \quad (2-9)$$

Where  $Q_h$  is the rate of convective heat exchange [W.m<sup>-2</sup>],  $h_c$  is the convection heat transfer coefficient [W.m<sup>-2</sup>.K<sup>-1</sup>],  $T_s$  is the temperature of the surface [K] and  $T_a$  is the temperature of ambient air [K].

The value of  $h_c$  is not a constant value since it is affected by the speed of the air velocity, the degree of turbulence as well as the surface properties due to its effects on the air flow pattern and the temperature difference between the surface and the air. The convection heat transfer coefficient,  $h_c$ , can be determined through evaluation of the so-called Nusselt number, Nu. Nusselt number for free-convection situation can be calculated by the following formulation (Bahrami 2011):

$$Nu = f(Gr, Pr) = C \cdot Gr^n \cdot Pr^m \quad (2-10)$$

where:

$$Nu = \left( \frac{h \cdot x}{K} \right) \quad (2-11)$$

$$Gr = \left( \frac{g \cdot \beta (T_s - T_o) x^3}{\mu^2} \right) \quad (\text{Grashof number}) \quad (2-12)$$

$$Pr = \left( \frac{C_p \cdot \mu}{K} \right) \quad (\text{Prandtl number}) \quad (2-13)$$

Where the experimental constants C and n depend on the geometry of the surface and the flow,  $\mu$  is viscosity [ $\text{kg} \cdot \text{m}^{-1} \cdot \text{s}^{-1}$ ],  $C_p$  is air specific heat capacity [ $\text{J} \cdot \text{kg}^{-1} \cdot \text{K}^{-1}$ ],  $h$  is convective heat transfer coefficient [ $\text{W} \cdot \text{m}^{-2} \cdot \text{K}^{-1}$ ],  $K$  is solid material thermal conductivity [ $\text{W} \cdot \text{m}^{-1} \cdot \text{K}^{-1}$ ],  $x$  is proper length representing the geometry under discussion,  $g$  is Earth's gravity [ $\text{m} \cdot \text{s}^{-2}$ ] and  $\beta$  is volumetric thermal expansion coefficient (equal to approximately  $1/T$ , for ideal fluids, where  $T$  is absolute temperature).

Since aforementioned effective factors on transfer coefficient are not homogeneously distributed within the urban canyon, the transfer coefficient is not spatially uniform either. This phenomenon is more considerable within the urban canyon on the vertical surfaces such as walls, and makes the detailed modeling of convective heat flux more complicated.

#### 2.2.4. Latent heat flux

The latent heat, generated via evapotranspiration, is another component of the energy balance equation in urban micro-climate, and which makes it different from its surrounding. A vast part of the urban ground surface is paved by impervious materials, so the water and the moist availability through the soil is less than the intact area. Additionally, less vegetation in the urban area reduces the magnitude of the transpiration from the plants.

The latent heat in the urban canopy model can be calculated by the following equation:

$$Q_\epsilon = L_v \cdot E \quad (2-14)$$

where  $Q_\epsilon$  is the latent heat flux,  $L_v$  is the latent heat of the vaporization, or the amount of energy required to evaporate a unit mass of a liquid. It varies with the temperature and the pressure, for the water at  $30^\circ\text{C}$  and  $100 \text{ kPa}$  it equals  $2.43 \text{ MJ} \cdot \text{kg}^{-1}$ . And  $E$  is the evapotranspiration.

$E$  is affected by the hydrological properties of the surface, here classified into three types:

1. Impervious surfaces: roads, parking lots, buildings
2. Pervious and unirrigated surfaces: open untended parks
3. Pervious and irrigated surfaces: gardens

Regarding to differences in the availability of the water and aforementioned hydrological properties of the surfaces, there are two possible conditions to calculate the evapotranspiration:

1. When the surface is wet or the soil moisture is at the field capacity (Erell et al. 2011):

$$E = (\alpha / L_v) \cdot [s / (s + \gamma)] \cdot (Q^* - \Delta Q_s) \quad (2-15)$$

where E is the evapotranspiration,  $L_v$  is the latent heat of vaporization, s is the slope of the saturation vapor pressure versus the temperature relationship,  $\gamma$  is the psychrometric constant,  $Q^*$  is the net all-wave radiation flux density and  $\Delta Q_s$  the surface (net storage) heat flux density. The (no dimensional) coefficient  $\alpha$  is the ratio of evaporation from a wet surface under conditions of minimal advection of equilibrium evaporation, which is the lowest limits to the evaporation from moist surface. The value of  $\alpha$  has been determined empirically and is about 1.2 to 1.3 in suburban areas.

2. if the surface is moist or dry (Erell et al. 2011):

$$E = \left( \frac{1}{L_v} \right) \cdot \left\{ \left[ (2\alpha - 1) \cdot (s / (s + \gamma)) \cdot (Q^* - \Delta Q_s) \cdot \sum_{i=2}^n A_i \alpha_i' \right] - [AA \cdot (\gamma / (\gamma + s)) \cdot E_a] \right\} \quad (2-16)$$

where A is the proportion the catchment covered with the  $i^{\text{th}}$  surface type,  $\alpha_i'$  is an empirical coefficient of the  $i^{\text{th}}$  surface type, defined as above and AA is the status of the soil moisture related to the area.  $E_a$  is related to the drying power of the air (Erell et al. 2011):

$$E_a = (C / \gamma) \cdot (\bar{e}^* - \bar{e}_a) \cdot \left\{ (\bar{u} / k^2) / [\ln(z_v - d + z_{Ov} / z_{Ov}) \cdot \ln(z_u - d + z_{Om} / z_{Om})] \right\} \quad (2-17)$$

where C is the heat capacity of the dry air;  $\bar{e}^*$  and  $\bar{e}_a$  are the mean saturation and the ambient vapor pressures at height  $z_v$ , respectively, u is the horizontal wind speed at height  $z_u$ , k is the von Karman constant (0.40), d is the zero-plane displacement length, and  $z_{Ov}$  and  $z_{Om}$  are the water vapor and the momentum roughness length, respectively.

### 2.2.5. Thermal storage

The thermal storage is one of the important components of the urban energy balance equation. The rest of the net radiation energy from the converted portion to the latent heat and sensible heat flux is stored in the surfaces defining the urban canyon. Therefore its magnitude fluctuates during the day by altering the radiative

energy. The stored heat during the day releases during the night when the net radiative energy is negative. Within the canopies with high sky view factor diurnal balance of heat storage is negligible. This circle repeats in the bigger temporal scale during the year. During the summer the body of the city absorbs and stores the heat and during the winter emits the stored heat. Therefore, its annual balance is zero unless the anthropogenic heat forced to the interested environment is considerably high.

The magnitude of the heat storage of incoming energy surplus is dependent on the thermal properties of the pertaining surface materials such as the heat capacity, thermal conductivity and density.

The heat capacity is the ability of the body to store the heat. The materials of the buildings in the urban fabric tend to have quit high thermal capacity. According to (Christen and Vogt 2004) the heat capacity of three-dimensional surface area in the city centers is nearly doubled compared with a plane surface. Due to this fact the energy received in the urban structure is stored in its mass during the day and released during the night when the ambient temperature is lower than the surface one (Alexandri and Jones 2006). For the given point on homogeneous and materially defined surface, calculating the stored heat is relatively easy but it is difficult to obtain a presentative value in an analytical way within the urban canopy with heterogeneous properties. So, in the models, that the other components of the urban energy balance equation are distinctive,  $\Delta Q_s$  can be found as the residual:

$$\Delta Q_s = Q^* + Q_f - Q_H - Q_E \quad (2-18)$$

### 2.3. Wind Flow in Urban Spaces

Air flow in the urban spaces has an important impact on the pedestrian comfort, the air pollutant dispersion and the building ventilation. Several studies have been done in order to understand how the artificial and the natural features affect the wind speed, its direction, and the intensity of the turbulence at any level of the UBL (Kitous, et al 2012; Erell et al. 2011; Niachou et al. 2008; Ghiaus et al. 2006).

Ghiaus et al (2006) report that the wind speed in the urban canyon is much lower than in the undisturbed area. And there is a correlation between them only when the speed of undisturbed wind is higher than  $2-4 \text{ m.s}^{-1}$ . They also report that when the wind direction is perpendicular to the street canyon and its speed is equal to or higher than  $2 \text{ m.s}^{-1}$ , a vortex develops in the canyon. When the wind direction is parallel to the canyon axis, the vertical velocity in the canyon is very low. Besides, their developed empirical model showed that when the speed of the oblique wind was less than  $4 \text{ m.s}^{-1}$  the temperature of the inside the street canyon was about  $5^\circ\text{C}$  lower than the canopy layer temperature.

Kitous et al (2012) explored the impact of the complex topography and the irregular compact urban forms on the wind environment and the air flow mechanisms at the street level. The results showed the horizontal movement of the air in the compact street canyon is related to the upwind conditions above the roofs. Also in the similar condition, the angle between the street axis and the prevailing wind direction is effective. The streets perpendicular to the prevailing wind direction had the highest reduction whereas the minimum reduction was observed in the streets parallel to the wind direction. The amount of reduction may reach 52% of the wind speed above the roof.

Niachou et al (2008) conducted an experimental study of the air flow distribution inside a SE-NW oriented urban street canyon in Athens. The results showed that the vertical wind speed profile in the center of the canyon had correlation with the ambient wind incident angles and the stability conditions. And its characteristic tends to be linear. But, in the same conditions for the horizontal wind speed, the vertical differentiation of the horizontal wind speed was negligible.

## **2.4. Urban Heat Island**

Under certain weather conditions a substantial difference in the air and surface temperature may be observed between a city and its surrounding rural areas. When the isotherms are drawn for the area in request, the city is apparent as a series of concentric, closed lines of higher temperature, with the maximum values recorded at or near the dense part of the urban area. This condition is known as the "Urban Heat Island" (Erell et al. 2011).

Urban Heat Island (UHI) first documented for the city of London by Luke Howard in 1818. The UHI effect can raise the air temperatures in a city by 2-5 K. In the evening, the differences can be even as high as 12 (Okeil 2010). It aggravates the air pollution in the cities and impacts the local climate by altering the wind patterns over the urban area, affecting the humidity and changing the precipitation rate within the cities (Mirzaei and Haghighat 2010).

The urban heat island has been observed both in the urban surfaces and the urban atmosphere above the city. Surface heat islands mostly form in the cities which are surrounded by moist soil or vegetation, cooled by the evaporation compared to the dry and impervious urban surfaces. Several researches investigated its spatiotemporal variation in the urban surfaces (Huang, Zhou and Cadenasso 2011), (Kantzioura et al. 2011; Buyantuyev and Wu 2010; Li and Roth 2009; Peterson 2003).

Atmospheric heat islands are observed both in the urban canopy-layer and the urban boundary-layer. The canopy-layer heat island occurs in the lowest layer of the atmosphere close to the surface of the city extended to the height of the buildings. It is more intensive during the night especially when the sky is cloudy to partly cloudy and the wind speed is low. And it is weaker during the day time. The boundary-layer

heat island which is larger during the day and it shrinks during the night, forms a dome of warmer air that extends downwind of the city. The formation of atmospheric urban heat islands, the factors affecting its intensity, its impact on the urban micro-climate, the outdoor thermal comfort, and the energy consumption of the affected areas were widely investigated by several researchers from different aspect of view (Priyadarsini 2009), (Kolokotroni and Giridharan 2008), (Kolokotsa, Psomas and Karapidakis 2009), (Yow and Carbone 2006), (Arnfield 2003).

## **2.5. Vegetation**

The interaction between the urban climate, the urban fabric, and the urban vegetation has been the subject of the researches in different climates and countries/cities: Osaka, Brazil, china, Greece, USA, and Montreal (Liu, Ma and Li 2011; Moriyama and Tanaka 2012; Ioannis X 2010). The results of the researches declare that besides the effect of the buildings, the most important control variable which affects the UCL micro-climate is the vegetation, especially shade trees. (Shashua-Bar et al. 2006)'s Studies show that the effect of vegetation on the urban micro-climate is related to several factors: the geometry of the urban canopy and the trees, the size of the green area, the prevailing climate, the season, the type of vegetation (e.g. tree, grass), the height of the sun, the ratio green/built-up area and the characteristics of the plant (species, density, shape size, volume, age. etc.) (Ali Toudert and Mayer 2006).

The urban green area mitigates the urban heat island (see section 2.4) by lowering the temperature and providing shading. Several investigations show that the greenery ratio of 30% reduces the temperature about 1 K. 50% can reduce it by nearly 2 K. And the temperature maximum difference between the inside and outside of the small green area can be 3 K. Other studies show that in deep urban canyons the heat lowering effect of the trees decreases. Also, the position of the trees influences their moderating effect. The effect of a single tree on the air temperature can be negligible, while a row of trees affects the micro-climate of their underneath, and a cluster of trees provides even cooler temperature, compared to the linear one.

(Hamada and Ohta 2010) show that in summer temperature difference between urban and green areas is larger than winter. Also during the day it was larger than night time, whereas in the winter the relationship was opposite. (Oliveira et al. 2011) show the difference is higher in hotter and sunny days.

In the warm climate, dense and deciduous trees may reduce the wind speed by 45% (Spangenberg et al. 2008) and that may reduce infiltration of the outside air, the effectiveness of the natural ventilation, and the convective cooling of the building surfaces (Robitu et al. 2006). Trees with large and dense crown also reduce the nocturnal cooling since they block some of the net outgoing long-wave radiation (Spangenberg et al. 2008). Additionally, Plants may increase the latent load for the

air conditioning by adding moisture to the air through evapotranspiration (Dimoudi and Nikolopoulou 2003; Ooka et al. 2008).

Green shades (trees, vines, etc.) reduce the incident solar radiation and accordingly, the surface temperature. Studies report that the shaded surfaces with green canopies are 5-20 K cooler than the sunlit surfaces (Robitu et al. 2006).

Green area reduces the run-off water (after rain) compared with the impervious surfaces of the urban areas or the bare ground. The run-off water drains quickly and in the long run, the less surface water remains available for the evapotranspiration. The lower evapotranspiration rate in the urban areas is the major effective factor in increasing the daytime temperatures. The evapotranspiration from vegetation system is another effective moderator of the near surface climates, particularly in the warm and dry, mid and low latitude (Priyadarsini 2009). It is estimated that 1460 kg water is evaporated from an average tree during a sunny summer day, consuming about 860MJ of energy. And this offers a cooling effect outside a building that is equal to five average air conditioners (Asimakopoulos et al. 2001).

The urban vegetation influences the urban micro-climate and consequently the outdoor pedestrian comfort levels along with the indoor ones (Dimoudi and Nikolopoulou 2003); (NREL 1995). The effect of the urban climate improvement on the indoor environment is, potentially, reducing the heat gains and the energy demands of the buildings (Akbari 2002; Givoni 1998; Huang et al. 1987). The urban trees not only help control the heat gain and mitigate the urban heat islands, (Huang et al. 2008); (Taha 1997)), but also reduce noise levels (Gidlof-Gunnarsson and Öhrström 2007; Lam et al. 2005).

Planting trees has the direct effect on reducing atmospheric CO<sub>2</sub> because; each individual tree sequesters carbon directly from the atmosphere through photosynthesis. However, planting trees in the cities has also an indirect effect on CO<sub>2</sub>, by reducing the demand for cooling energy thereby, indirectly reducing the emission of CO<sub>2</sub> from the power plants (Akbari et al. 2001).

## **2.6. Measuring methods**

There are different methods used by researchers to collect the microclimatic weather data within the cities. Here, three most applied approaches are described:

### **2.6.1. Fixed stations**

The most common and old method to monitor the climatic condition of an area is using the fixed weather stations. It has been used for several decades, and the collected data for most of the cities exist for quite some time (Gartland 2008).



The stationary weather stations record the climatic data continuously. Therefore, they are the most suitable tools to investigate the long-term trend of the climate change within an area. On the other hand, there are a few numbers of stationary weather stations, and they are mostly fixed on top of the buildings or towers, above the urban canyons, and do not reflect the urban canopy condition (Gartland 2008). Since the urban canopy weather conditions can vary dramatically, the data obtained from these weather stations are not reliable to investigate the urban micro-climate. Besides, it is too costly to install and protect a large number of fixed weather stations within the city in low levels, such as pedestrian level, to provide the high resolution database of the urban micro-climate.

### **2.6.2. Mobile traverses**

Stationary weather stations are not usually located in the needed places or height for the urban micro-climate research projects. And it can be difficult and very expensive to provide them in the required positions. Mobile traverses can be an economically good replacement for them. They can be adjusted to pedestrian level. Besides, they are portable and can present different urban spaces. This method has been used by several researchers (Spagnolo and Dear 2003; Giridharan et al. 2004; Krüger et al. 2011; Yang et al. 2010).

Vicente-Serrano et al. (2005) used digital thermometers mounted on 3 automobiles, at the height of 2 m above the ground, to define the shape and the temporal variability of the UHI intensity in Zaragoza. The vehicles were driving with a constant speed of  $30 \text{ km.h}^{-1}$  along all the 3 transects. The total length of the transects was 105 km, including 238 observation points distributed homogeneously within the city.

Rajasekar and Weng (2009) also used mobile traverse method for microclimatic modeling of the urban thermal environment of Singapore. They identified four routes within the city and equipped four vehicles with cylindrical observation tubes. Mobile surveys were conducted at midnight from 2:00 am to 4:00 am. All automobiles were driven along the highways at a speed of  $50 \text{ km.h}^{-1}$ . Ambient temperature and humidity were recorded by passing the locations at 2 min intervals.

Pinho and Orqaz (2000) also used passenger car to study the urban heat island in Aieiro, Portugal. Their measurements were taken during 48 nights to record the air temperature along the previously defined routes, covering diverse areas in the city and its surroundings.

### **2.6.3. Remote sensing**

In general, fixed stations and mobile traverses are used to monitor the air temperature in the urban area. Through remote sensing the surface temperature of roof tops, pavements, vegetation and bare soil can properly be recorded. Mostly, it

is used to investigate the urban heat islands phenomena within the cities (Fung et al. 2008).

In this method, using pictures taken by equipped airplanes or satellites, the energy radiating from the urban surfaces can be recorded. By using the taken pictures the surface temperature of a large area is visualized at once. But as they are bird eye pictures they just visualize two-dimensional images of horizontal surfaces. Another disadvantage here is that vertical surfaces, such as walls or surfaces under the upper surfaces like the ground under the trees cannot be taken into account. Additionally, they cannot record the surface conditions continuously. Satellites pass every location twice a day at a special time during the day and night (Gartland 2008). And only those pictures can be used that are taken in clear sky. On the other hand, although it can be conducted any time during the day, utilization of equipped airplanes is very expensive. So continuous surface monitoring to collect proper data would be too costly for a long time is too costly.

## **2.7. Modeling the urban micro-climate**

Equation (2-1) and its components as described in previous sections (see sections 2.3 to 2.5), set just a basis for the surface energy balance in the urban canopy layer. Detailed distribution of the climatic parameters such as the temperature distribution, the velocity components, magnitude of radiation and other needed climatic parameters within the urban canopy cannot be directly obtained out of this equation (Erell et al 2011). To do so, the interaction between the atmosphere and the urban fabric shall be properly modeled.

For urban micro-climate modeling each of the two existing approaches can be used, i.e. physical modeling and mathematical modeling. Above mentioned approaches are being explained in the next sections.

### **2.7.1. Physical model**

The physical scale models provide an alternative and powerful method in the urban design as well as in the climate-related researches, although they are usually highly simplified compared to real cities. They are usually used to study a particular environmental variable such as the solar radiation or the velocity within the urban area (Robinson 2011). Such studies are usually carried out under well-defined conditions to reflect a specific situation in laboratories. In some cases the scaled-down models are also exposed to the natural environment in order for being able to study the related effect.

The physical modeling has been used to be applied to the study of solar shading and overshadowing (Erell et al 2011). In a physical modeling, the scaled-down models are placed under a virtual sky or exposed to the natural sunlight, and its orientation can

be adjusted by the Heliodon in such a way that interested time of the day or year can be simulated.

Another benefit of the physical modeling in the building and the urban climatology is the use of wind tunnels in order to simulate and analyze the air-flow in the built area. In this context, in a wind tunnel experiment in addition to the simulation of the existing real environmental conditions on a scaled-down model (the physical model), to which the real object would be exposed, also the real air flow situation simulated. Another important issue which has to be considered here is the similarity of the mechanical and the thermal features of the model and those of the representative area. This means that following requirements shall be met: equality of 1) Richardson number, 2) a zero longitudinal pressure gradient and 3) Reynolds number. Wind tunnel modeling is used to investigate problems such as ground level pedestrian wind nuisance, air pollutant dispersion and wind driven rain exposure. For further details reference is made to (Erell et al 2011).

Because of the substantial simplifications which have to be implemented by a physical modeling. It can just be used to simulate specific conditions in a very limited manner. On the other hand, the development of the simulation software for visualizing the shadow cast by the buildings and the other urban elements, and its advantages e.g. accuracy, flexibility and saving time and cost saving potential compared with the physical models, have diminished the usage of the physical models (Robinson 2011).

### **2.7.2. Mathematical model**

The mathematical modeling of an urban fabric, the complete behavior of the fluid involved in conjunction with the surface energy balance -equation (2-1) has to be fully described and solved. This would mean a full description of the fluid behavior and movement from fluid dynamics point of view. All required micro-climatic parameters along with their associated fields can be described as a result of such modeling enabling researchers to properly define the micro-climatic conditions in an urban fabric under study.

Performing a micro-climate modeling in view of fluid dynamics, means a complete description of a non-isothermal Newtonian fluid movement. In other words, at each time point for each fluid element the following terms have to be matched (Robinson 2011):

- Conservation of mass (mass continuity);
- Conservation of momentum;
- Conservation of energy;

This, in turn, would mean utilization and setting up three non-linear partial differential equation systems in three dimensions (x,y,z), which have to be solved

simultaneously, at each single time point along with the surface energy balance equations (in accordance with all other associated sub-systems of equations).

But the very complex nature of such equation systems makes an analytical solution practically impossible. On one hand, the existing mathematical limitations for solving complicated partial differential equations pose an obstacle in this way. On the other hand – and the most important reason in this context- the existence of the very uncertainty and inabilities by describing the transport phenomena (momentum, heat and mass transfer) in a well-defined manner prohibit the achievement of an exact mathematical solutions (Robinson 2011).

That is why use of applied numerical analysis in this context has to be made. This leads to a revised approach known as Computational Fluid Dynamics (CFD). CFD modeling is being discussed in the next section.

## 2.8. CFD Modeling

Computational Fluid Dynamics (CFD) is a modeling technique that uses numerical methods to solve the problems that involve fluid flows. At first it was developed as a tool for mechanical engineering but latterly it was employed to the indoor and outdoor environment of buildings and its interacts with its envelope. CFD has been used to explore the issues related to air movement in and around the buildings, pollution dispersal, the pedestrian wind environment wind driven rain effects and the effect of vegetation on micro-climate (Erell et al 2011).

Following equations/ partial differential equation systems are utilized to fully describe a non-isothermal flow of a Newtonian fluid (Bird et al 1976):

- Conservation of mass (continuity equation):

$$\frac{\partial \rho}{\partial t} = -(\bar{\nabla} \cdot \rho \bar{v}) \quad (2-19)$$

- Momentum conservation:

$$\frac{\partial}{\partial t} \rho \bar{v} = -(\bar{\nabla} \cdot \rho \bar{v} \bar{v}) - \bar{\nabla} p - \left[ \bar{\nabla} \cdot \tau \right] + \rho \bar{g} \quad (2-20)$$

$$\left( \begin{array}{l} [\bar{\nabla} \cdot \tau] \quad \text{divergence of tensor } \tau \\ [\bar{\nabla} \cdot \rho \bar{v} \bar{v}] \quad \text{divergence of dyadic-multiplication } \rho \bar{v} \bar{v} \end{array} \right),$$

- Conservation of energy:

$$\rho c_p \frac{DT}{Dt} = -(\bar{\nabla} \cdot \bar{q}) - \left( \frac{\partial \ln \rho}{\partial \ln T} \right)_p \frac{D\rho}{Dt} - (\bar{\tau} : \bar{\nabla} \bar{v}) \quad (2-21)$$

$$\left( \frac{D}{Dt} = \frac{\partial}{\partial t} + \bar{v} \bar{\nabla} \quad : \quad \text{substantial derivative} \right),$$

- A suitable equation of state:

$$P = \Psi(\rho, T) \quad (2-22)$$

In addition one needs also suitable formulas for the change of density, viscosity, dilatation viscosity, thermal conductivity and heat capacity as a function of temperature. Moreover, depending on the flow situation proper boundary and initial conditions are necessary. The above-mentioned equation systems may be rewritten in Cartesian coordinate system:

- Conservation of mass (continuity equation):

$$\frac{\partial \rho}{\partial t} + \frac{\partial}{\partial x}(\rho v_x) + \frac{\partial}{\partial y}(\rho v_y) + \frac{\partial}{\partial z}(\rho v_z) = 0 \quad (2-23)$$

- Momentum conservation:

$$\rho \left( \frac{\partial v_x}{\partial t} + v_x \frac{\partial v_x}{\partial x} + v_y \frac{\partial v_x}{\partial y} + v_z \frac{\partial v_x}{\partial z} \right) = -\frac{\partial p}{\partial x} - \left[ \frac{\partial}{\partial x} \tau_{xx} + \frac{\partial}{\partial y} \tau_{yx} + \frac{\partial}{\partial z} \tau_{zx} \right] + \rho g_x, \quad (2-24)$$

$$\rho \left( \frac{\partial v_y}{\partial t} + v_x \frac{\partial v_y}{\partial x} + v_y \frac{\partial v_y}{\partial y} + v_z \frac{\partial v_y}{\partial z} \right) = -\frac{\partial p}{\partial y} - \left[ \frac{\partial}{\partial x} \tau_{xy} + \frac{\partial}{\partial y} \tau_{yy} + \frac{\partial}{\partial z} \tau_{zy} \right] + \rho g_y, \quad (2-25)$$

$$\rho \left( \frac{\partial v_z}{\partial t} + v_x \frac{\partial v_z}{\partial x} + v_y \frac{\partial v_z}{\partial y} + v_z \frac{\partial v_z}{\partial z} \right) = -\frac{\partial p}{\partial z} - \left[ \frac{\partial}{\partial x} \tau_{xz} + \frac{\partial}{\partial y} \tau_{yz} + \frac{\partial}{\partial z} \tau_{zz} \right] + \rho g_z, \quad (2-26)$$

- Conservation of energy:

$$\rho c_p \left( \frac{\partial T}{\partial t} + v_x \frac{\partial T}{\partial x} + v_y \frac{\partial T}{\partial y} + v_z \frac{\partial T}{\partial z} \right) = - \left[ \frac{\partial q_x}{\partial x} + \frac{\partial q_y}{\partial y} + \frac{\partial q_z}{\partial z} \right] - \left( \frac{\partial \ln \rho}{\partial \ln T} \right)_p \frac{DP}{Dt} - (\bar{\tau} : \bar{\nabla} \bar{v}) \quad (2-27)$$

Where:

$$\begin{aligned} (\bar{\tau} : \bar{\nabla} \bar{v}) = & \tau_{xx} \frac{\partial v_x}{\partial x} + \tau_{xy} \frac{\partial v_x}{\partial y} + \tau_{xz} \frac{\partial v_x}{\partial z} + \tau_{yx} \frac{\partial v_y}{\partial x} + \tau_{yy} \frac{\partial v_y}{\partial y} + \tau_{yz} \frac{\partial v_y}{\partial z} \\ & + \tau_{zx} \frac{\partial v_z}{\partial x} + \tau_{zy} \frac{\partial v_z}{\partial y} + \tau_{zz} \frac{\partial v_z}{\partial z}, \end{aligned} \quad (2-28)$$

$$\tau_{ij} = -\mu \left( \frac{\partial v_j}{\partial x_i} + \frac{\partial v_i}{\partial x_j} \right) + \left( \frac{2}{3} \mu - k \right) \left( \frac{\partial v_x}{\partial x} + \frac{\partial v_y}{\partial y} + \frac{\partial v_z}{\partial z} \right) \delta_{ij} \quad (\tau_{ij} = \tau_{ji}) \quad (2-29)$$

If the entire system of equations is solved, pressure, density, velocity, and temperature in each point in the system under consideration is defined at any time. But so that this objective can be achieved, detailed knowledge of the physical properties and the transport properties of the system considered at any time are necessary.

As long as a system under discussion can be considered – depending on the prevailing transport mechanisms - as a laminar system, all of the required system properties can be calculated based on the molecular properties (physical and transport properties) of the existing components in the system.

Should the flow condition in a system cannot be considered as laminar, then the flow system is either in a transition state or can be fully considered as turbulent. In both cases the required system properties cannot be calculated based on the molecular properties of the existing components anymore. In case of a turbulent flow condition by describing each of the physical and transport properties of the existing components in the system taking into account fluctuating time-dependent factors are of vital importance, the so-called turbulence quantities. In the following sections about the phenomenon of turbulence is discussed in detail (Sanei 2005).

### 2.8.1. Turbulence

The phenomenon of turbulence has played an important role in fluid mechanics and has been followed with great interest accordingly, especially since the Reynolds experiment showed that the flow in a pipe can be considered under certain conditions as turbulent (Sanei 2005). The chaotic nature of turbulence makes - until now - the precise quantitative description of a turbulent flow condition impossible. Historically, there are two approaches in dealing with turbulence: empiricism has been trying to describe the phenomenon by the temporary averages of flow variables. And through the statistical turbulence theory trials have been made to achieve better understanding concerning real mechanism of turbulence to get closer knowledge about the fluctuations in the flow parameters (Sanei 2005).

### 2.8.1.1. Reynolds Equations for incompressible, turbulent flows (Sanei 2005)

Even in the case of a turbulent flow the equations for conservation of mass, momentum and energy are still valid, if the instantaneous values for pressure, velocity and temperature are used. Reynold modified these three aforementioned equations as he replaced each of the required flow parameters with a combination of a time- averaged part and a fluctuating part, which means:

$$v_i = \bar{v}_i + v'_i \quad (2-30)$$

$$p_i = P + p'_i \quad (2-31)$$

$$T = T + T' \quad (2-32)$$

The time-averaged part of a flow parameter,  $\psi$  is calculated as follows (Bird, Stewart and Lightfoot 1976):

$$\bar{\psi}_i = \frac{1}{t_0} \int_{t-\frac{1}{2}t_0}^{t+\frac{1}{2}t_0} \psi_i dt \quad (2-33)$$

The time period  $t_0$  shall be long enough to be able to achieve an acceptable time-averaged function. Based on the equation (2-33):

$$\begin{aligned} \overline{\psi'_i} &= 0, \quad \overline{\bar{\psi}_i} = \bar{\psi}_i, \quad \overline{\psi_i \psi'_i} = 0, \\ \frac{\partial \bar{\psi}_i}{\partial x} &= \frac{\partial}{\partial x} \bar{\psi}_i, \quad \frac{\partial \bar{\psi}_i}{\partial t} = \frac{\partial}{\partial t} \bar{\psi}_i \end{aligned} \quad (2-34)$$

The term  $\overline{\psi_i'^2}$  (also  $\overline{\psi'_i \psi'_i}$ ) is not equal to zero and the ratio  $\sqrt{\overline{\psi_i'^2}} / \bar{\psi}_i$  is consider as the „turbulence intensity“ (normally it amounts to 1-10% in the bulk region and up to 25% or more close to the boundaries).

The continuity and momentum equations for an incompressible fluid flow (isothermal) can be re-written as follows, where  $\bar{v}$  is replaced with  $\bar{v} + v'$  (x-direction):

$$\frac{\partial}{\partial x} (\bar{v}_x + v'_x) + \frac{\partial}{\partial y} (\bar{v}_y + v'_y) + \frac{\partial}{\partial z} (\bar{v}_z + v'_z) = 0 \quad (2-35)$$

$$\begin{aligned} \frac{\partial}{\partial t} \rho (\bar{v}_x + v'_x) &= -\frac{\partial}{\partial x} (\bar{p} + p') - \left[ \frac{\partial}{\partial x} \rho (\bar{v}_x + v'_x) (\bar{v}_x + v'_x) + \frac{\partial}{\partial y} \rho (\bar{v}_y + v'_y) (\bar{v}_x + v'_x) \right. \\ &\quad \left. + \frac{\partial}{\partial z} \rho (\bar{v}_z + v'_z) (\bar{v}_x + v'_x) \right] + \mu \nabla^2 (\bar{v}_x + v'_x) + \rho g_x \end{aligned} \quad (2-36)$$

The relevant equations for the y- and the z-components can be obtained in the same way. In the next step equations (2-35) and (2-36) are converted to the time-averaged form using the rules described by (2-34), resulting in:

$$\frac{\partial}{\partial x} \bar{v}_x + \frac{\partial}{\partial y} \bar{v}_y + \frac{\partial}{\partial z} \bar{v}_z = 0 \quad (2-37)$$

$$\begin{aligned} \frac{\partial}{\partial t} \rho \bar{v}_x = & -\frac{\partial}{\partial x} \bar{p} - \left( \frac{\partial}{\partial x} \rho \bar{v}_x \bar{v}_x + \frac{\partial}{\partial y} \rho \bar{v}_y \bar{v}_x + \frac{\partial}{\partial z} \rho \bar{v}_z \bar{v}_x \right) \\ & - \left( \frac{\partial}{\partial x} \rho \overline{v'_x v'_x} + \frac{\partial}{\partial y} \rho \overline{v'_y v'_x} + \frac{\partial}{\partial z} \rho \overline{v'_z v'_x} \right) + \mu \nabla^2 (\bar{v}_x + v'_x) + \rho g_x \end{aligned} \quad (2-38)$$

The same procedure is also applied for the y- and the z-components. The equations (2-37) and (2-38) are the time-averaged form of the continuity and momentum conservation equations. A comparison with (2-23) to (2-26) results in:

- The continuity equation takes the same form in both cases, just  $\bar{v}$  has been replaced with  $\bar{v}$ ;
- The same is also valid for the momentum conservation equation ( $\bar{v}$  and  $\rho$  have been replaced with  $\bar{v}$  and  $\bar{\rho}$ ); but here there is an additional part (marked by the dashed underline), which describes the momentum-transport pertaining to the turbulent fluctuations, i.e. the turbulent momentum-tensor:

$$\bar{\tau}_{xx}^{(t)} = \rho \overline{v'_x v'_x}, \quad \bar{\tau}_{xy}^{(t)} = \rho \overline{v'_x v'_y}, \quad \bar{\tau}_{xz}^{(t)} = \rho \overline{v'_x v'_z} \quad (2-39)$$

These terms are known as „Reynolds stresses“. The time-averaged viscous momentum flux-tensor  $\bar{\tau}^{(v)}$  is defined as:

$$\bar{\tau}_{xx}^{(v)} = -2\mu \frac{\partial \bar{v}_x}{\partial x}, \quad \bar{\tau}_{xy}^{(v)} = -\mu \left( \frac{\partial \bar{v}_y}{\partial x} + \frac{\partial \bar{v}_x}{\partial y} \right), \quad \text{etc.} \quad (2-40)$$

This enables the vector form of the equations (2-37) and (2-38) to be shown as follows:

$$(\bar{\nabla} \cdot \bar{v}) = 0 \quad \text{and} \quad (\bar{\nabla} \cdot \bar{v}') = 0$$

(2-41, 2-42)

$$\frac{\partial}{\partial t} \rho \bar{v} = -\bar{\nabla} \bar{p} - [\bar{\nabla} \cdot \rho \bar{v} \bar{v}] - [\bar{\nabla} \cdot (\bar{\tau}^{(v)} + \bar{\tau}^{(t)})] + \rho \bar{g} \quad (2-43)$$



Equation (2-42) is derived from the subtraction of equation (2-41) from the original mass conservation equation.

The principal result of the performed above discussion is that for a time-averaged turbulent flow, the momentum conservation equation in the form of equation (2-20) may still be valid, if all  $\bar{v}$  are replaced with  $\bar{\bar{v}}$ , all  $\bar{\rho}$  are replaced with  $\bar{\bar{\rho}}$  and all  $\bar{\tau}_{ij}$  are replaced with  $\bar{\bar{\tau}}_{ij} = \bar{\bar{\tau}}_{ij}^{(v)} + \bar{\bar{\tau}}_{ij}^{(t)}$ . The main problem here is the "Reynolds stresses"  $\bar{\bar{\tau}}_{ij}^{(t)}$ , since these terms cannot be easily described/ formulated through the associated velocity gradients, as it is the case by the viscous stresses  $\bar{\bar{\tau}}_{ij}^{(v)}$  in the equation (2-40). This leads to the fact that in order to resolve the turbulent flow fields either experimental information on the respective Reynolds stresses are need, or one must rely on empirical or semi-empirical formulas in this context. This point is still one of the biggest challenges to the theory of turbulence, i.e. the striving for the development of an appropriate model and the resulting empirical or semi-empirical equations that describe the respective Reynolds stresses for a given flow condition with acceptable accuracy.

It is possible to drive equations describing the Reynolds stresses analytically, However, such equations would include terms like  $\bar{v}'_i \bar{v}'_j \bar{v}'_k$ , and an attempt to describe these terms analytically would result in formulas with higher-order terms such as  $\bar{v}'_i \bar{v}'_j \bar{v}'_k \bar{v}'_l$ , i.e. such an attempt would lead to an infinite number of systems of equations. To prevent this, there is no way other than depending on the empiricism. A direct attempt to describe the Reynolds stresses empirically would result in turbulence theory of the 1. Order. Accordingly any attempt to model  $\bar{v}'_i \bar{v}'_j \bar{v}'_k$  terms empirically would lead to the 2. Order turbulence theory, etc.

### 2.8.1.2. Turbulence models

The basic concept for turbulence modeling and modeling of the Reynolds stresses  $-\rho \cdot \bar{v}'_i \bar{v}'_j$  called "eddy viscosity concept," which was proposed in 1877 by Boussinesq. The "eddy viscosity concept" is based on the assumption that similar to the viscous stresses in laminar flow the turbulent (Reynolds) stresses can be brought also in relation to the time-averaged velocity gradients. In general, this approach is formulated as follows (Rodi 1980):

$$-\bar{v}'_i \bar{v}'_j = \nu_t \cdot \left( \frac{\partial \bar{v}_i}{\partial x_j} + \frac{\partial \bar{v}_j}{\partial x_i} \right) - \left( \frac{2k \cdot \delta_{ij}}{3} \right) \quad (\delta_{ij} = 1 \text{ for } i = j \text{ and } \delta_{ij} = 0 \text{ for } i \neq j) \quad (2-44)$$

$\nu_t$  denotes the turbulence or eddy viscosity, in contrast to molecular viscosity  $\nu$ , this term is not a material property, but depends in each case on the flow situation in a given system.  $\nu_t$  may change from point to point depending on the associated flow situation significantly. The equation (2-44) is not itself a turbulence model,

however, a turbulence model can be built based on this concept. Out of equation (45) the normal stresses (when  $i = j$ ) can be derived:

$$\overline{v_x'^2} = -2\nu_t \frac{\partial \overline{v_x}}{\partial x}, \quad \overline{v_y'^2} = -2\nu_t \frac{\partial \overline{v_y}}{\partial y}, \quad \overline{v_z'^2} = -2\nu_t \frac{\partial \overline{v_z}}{\partial z} \quad (2-45)$$

All normal stresses are, by definition, positive values and their sum is twice the kinetic energy of turbulence:

$$k = \frac{1}{2} (\overline{v_x'^2} + \overline{v_y'^2} + \overline{v_z'^2}) \quad (2-46)$$

The eddy viscosity concept is based on an analogy to the molecular movement. That means it is assumed that the turbulent eddies similar to those molecules collide with each other and thus between them a momentum and energy exchange takes place. The molecular viscosity is directly related to the average velocity components, and the mean free path in the observed control volume. Similarly, it can be assumed that the turbulent viscosity is also proportional to a velocity as well as to a turbulence motion length both characterizing the turbulence:

$$\nu_t \sim \overline{v} \cdot L \quad (2-47)$$

This characteristic length was named as "mixing-length" by Prandtl. The main success of the eddy viscosity concept lies in the fact that the two-dimensional shear stress,  $\tau = -\overline{\rho v_x' v_y'}$ , can be represented as follows:

$$\tau = \rho \nu_t \frac{\partial \overline{v_x}}{\partial y} \quad (2-48)$$

However, the basis for all discussions made above is the assumption of an isotropic eddy viscosity, which is considered as rare in the reality. In direct analogy to the turbulent momentum transport it is believed that the heat and mass transfer can be brought in connection with a gradient of a transported variable, which means:

$$-\overline{v_i' \phi'} = \Gamma \frac{\partial \phi}{\partial x_i} \quad (2-49)$$

The term  $\Gamma$  is referred to as turbulent diffusivity. The Reynolds analogy between heat and mass transfer and momentum transfer suggests that the terms  $\Gamma$  and  $\nu_t$  are closely related to each other. This would result:

$$\Gamma = \frac{\nu_t}{Pr^{(t)}} \quad (2-50)$$

$Pr^{(t)}$  is the turbulent Prandtl (for heat transfer) and Schmidt (for mass transport) number. Experimental results have shown that, in contrast to  $\Gamma$  and  $\nu_t$  in a flow field (in even in different flow layers in the same field),  $Pr^{(t)}$  stays somehow constant and does not change. For this reason, in many turbulence models a constant  $Pr^{(t)}$  is assumed.

### 2.8.1.3. Turbulence model classification

To date, many turbulence models have been developed by some of these no "Eddy (turbulent) viscosity concept" has been used, instead an attempt has been made to use differential transport equations for the calculation of the turbulent momentum and heat-/mass fluxes, i.e.  $\overline{v_i v_j'}$  and  $\overline{v_i \phi'}$ . However, there are many models that are based on the "eddy viscosity concept", among which there are major differences. The simplest model of this type is assumed a constant value for  $\nu_t$  and for  $\Gamma$ . The more developed the model, the more effort is invested to describe  $\nu_t$  and  $\Gamma$  accurately in the flow field under consideration in a more accurate way using several differential transport equations. Such differential transport equations contribute to better or more accurate results especially in situations, in which the turbulence in a point is highly dependent on the formation of turbulence at a different location in the flow field (the so-called history effect). In this way, one can classify the turbulence models in classes as follows:

#### A. Zero-Equation Models:

This type of turbulence models does not include transport equations to calculate the turbulent quantities. These relatively simple models all use the eddy viscosity concept. To determine the eddy viscosity either the experimental data can be used directly or by the trial-and-error approach derived empirical equations are utilized. The following models:

- Constant eddy viscosity / diffusivity models,
- Mixing length models (mixing-length models),
- Shear stress free layer models (Prandtl's Free-Shear-Layer Models)

belong to this group. For detailed descriptions of these models, reference is made to (Rodi 1980).

#### B. One-Equation Models:

Because of the relatively small mismatches generated by zero-equation models results with those from experiments (particularly in transitional cases) turbulence models have been developed, in which to determine the turbulent quantities

differential transport equations are used. A major step in this direction was that a direct connection between the fluctuating velocity scale and the time-averaged velocity is made. Here in the case of one-equation models a differential transport equation is used. Among these models:

- One equation models that directly use the eddy viscosity concept (k-models);
- One equation models that describe the distribution of the shear stress,  $\overline{v_i'v_j'}$  through a transport equation (e.g. Bradshaw et al model).

For detailed descriptions of this type of turbulence models, reference is made to (Rodi 1980).

### C. Two-Equation Models:

The reason for the development of two-equation models to determine the turbulent parameters is that in the one-equation models take into account only the velocity scale (equation (2-47)), which is described through a transport equation. But the length scale,  $L$ , in Equation (2-47) is subject to the variations (fluctuations) and is affected by transport processes existing in the flow system under consideration. Therefore the length scale,  $L$ , must also be described by a transport equation. All known two-equation models take in addition to k-equation (velocity-scale transport equation) another transport equation, which describes the length scale.

All these models are based on the eddy viscosity concept, as well. A transport equation for " $L$ " (equation (2-47) does not necessarily include " $L$ " as an independent variable. Each kind of the combination in the form ( $Z = k^m \cdot L^n$ ) would be of benefit, since " $k$ " (the kinetic energy of turbulence) out of the k-equation can be calculated. For this reason, Chou (Chou 1945; Davidov 1961; Harlow and Nakayama 1967; Jones and Launder 1972) have proposed an equation for the turbulent dissipation,  $\varepsilon$ , as follows:

$$\varepsilon \sim \left( k^{3/2} / L \right) \quad (2-51)$$

There are also some other proposals, which may be found in the literature. For the derivation of the exact k-transport equation, the original momentum conservation equation is used. This derivation is described in detail in (Jones and Launder 1972). For the  $\varepsilon$ -transport equation, similar to the k-equation, attempts are made to achieve an exact form starting from the momentum conservation equation. But such precise formulations contain very complicated correlations, which in practice do not allow the use of an exact form of the equation.

Taking into account the above-mentioned fact, fluid dynamics experts have accepted a predominantly empirical form for the  $\varepsilon$ -transport equation. In the international literature mainly the one proposed by Jones and Launder equation has been

presented as the best (Jones and Launder 1972). The so-called  $k - \varepsilon$  models are widely used by CFD calculation.

## **3. Approach**

### **3.1. Overview**

The main purpose of this study is to identify and develop a deeper understanding of those urban design and planning parameters that cause the variance in micro-climatic conditions in large and densely populated cities such as Vienna. Two approaches were employed to study important micro-climatic data, i.e. air temperature, solar radiation, relative humidity, wind speed, and CO<sub>2</sub> level. First, empirical inquiry, through which on-site measurements using the mobile traverse method were done to collect the required data; Second, the computational inquiry to simulate the micro-climatic situation in the urban fabric under the study was employed to analyze the effective parameters on urban micro-climate.

### **3.2. Empirical inquiry**

First to define the scope of the study, an area in the downtown of Vienna near the Vienna University of Technology was selected. To achieve a well spread measurement covering as many existing typological features in the city as possible, four kinds of urban spaces i.e. street, plaza, park and courtyard were defined as the major categories to collect weather data. Each of these categories was divided into proper subcategories as below.

- Street: Narrow, wide with heavy traffic load and vegetation and wide with heavy traffic load and without vegetation (street with heavy traffic here is considered as a street, through which vehicles are moving on a continuous basis).
- Park: grass field, water body
- Plaza: with vegetation, with water body, without vegetation nor water body
- Courtyard: with vegetation and without vegetation

All the categories along with the associated subcategories are being described in the following sections.

Since the measuring points were mostly located in public areas in the city, it is practically impossible to make use of fixed weather station to collect the required weather data, especially that the planned measurements had to be performed to the pedestrian level in order to be able to evaluate the micro-climatic condition in the subjected urban space, correctly.

For this reason, the mobile traverse methodology was used in this project. Accordingly a mobile weather station was designed and constructed (details given in section 3.2.3).

By the aid of this mobile instrument weather data, i.e. air temperature, relative humidity, global radiation, wind speed and CO<sub>2</sub> level in the air at the pedestrian level in the defined measuring spots were collected.

Gathered data were all compared with those through a fixed weather stations (known as BPI) collected. This fixed weather station (BPI) is mounted on the top of the VUT Vienna building and monitors continuously (24 h/day in a second basis) the weather condition and records the required data. This comparison set an appropriate basis for further evaluations by discussing the results pertaining to the micro-climatic conditions during the study. Details are given in chapter four.

### **3.2.1. Site description**

Meteorological measurements were conducted at 13 different locations, classified into 4 major categories, in downtown of the city of Vienna using a mobile weather station.

Vienna, the capital of Austria, is located at 48° N, 16°E and 151-542 m above the sea level. The area of the city is 414.87 km<sup>2</sup> with 1.731236 population and 4173 /km<sup>2</sup> density (Vienna City Administration n.d.). According to the Köppen classification, the climate of Vienna features a Cfb (oceanic) –climate and stands between the oceanic climate and the humid continental climate (Kottek et al. 2006). It has relatively warm summers with average high temperatures of 22 to 26 °C, with maximums exceeding 30 °C, and minimum around 15 °C. It has relatively cold winters with average temperatures at about 0 °C. Snowfall mainly occurs from December to March. Spring and autumn are cool to mild. And the average precipitation is about 620 mm.m<sup>-2</sup>, annually (ZAMG n.d.).

#### **3.2.1.1. Streets:**

Streets, as the most important urban spaces in the cities, have the major effect in modifying the urban micro-climate (Shishegar 2013). Used material, traffic load, their orientation and aspect ratio are some of the well-known factors which correspond with the urban canyon micro-climate in the cities (Ali Toudert and Mayer 2006). In this study, three types of streets (i.e. narrow type, wide type having heavy traffic load with vegetation and wide type having a heavy traffic load without vegetation) were selected for field measurements. Moreover each of the aforementioned types was investigated in two perpendicular orientations.

**Measuring spot S1 “Paniglgasse”:**

“Paniglgasse” is an almost narrow street with medium traffic load in forth district (one of the densest districts) of Vienna. Its axis is oriented in east-west direction. It is almost symmetric with an aspect ratio (H/W) of 1.29 and sky view factor (SVF) of 0.29. The surrounding buildings are almost in an equal height, typically 4-5 floor with pitched tile roofs. The street is made of asphalt and is 14.5 m wide, including a 2.5 m sidewalk on each sides. The facade of most of the buildings is made of plaster in light colors. About 32 % of the surface of the walls is covered by windows. The length of the street is 280 m. It ends, in the west, onto “Wiedner Hauptstrasse”, a medium wide street with heavy traffic, and in east, onto “Argantinnierstrasse”, a narrow street with a light traffic load. The street is crossed by two almost similar streets in the middle. The measurement station as it is seen in figure 3-1 was located 55 m from the east end in the southern sidewalk.



Figure 3-1: Urban plan showing the location of stops S1 and S2



Figure 3-2: Location S1



Figure 3-3: Fish eye picture of S1



**Measuring spot S2 on “Karlgasse”:**

“Karlgasse” shows very similar characteristics compared to “Paniglgasse”. Similarities in building materials used, SVF, H/W and the traffic load confirm this fact. It crosses “Paniglgasse” street in an almost perpendicular way and ends onto “Karlsplatz” in the north and “Gußhaus”, a medium wide street with heavier traffic, in the south. Its length is 210 m and the station was located 110 m from the north end, in the middle of the crossroads with “Paniglgasse” street and “Frankenberggasse” street on the east sidewalk. Other properties are the same as Paniglgasse. The configuration of these studied streets along with the exact position of the measuring spots S1 and S2 are shown in figures 3-1 to 3-5.



Figure 3-4: Location S2



Figure 3-5: Fish eye picture of S2

**Measuring spots S3 and S4 on “Schubertring” and “Kärntnerring”:**

These measuring spots are located on “Ring” as shown on figure 3-6. “Ring” is the widest street in downtown Vienna. It is flanked by tall trees. Two measuring spots i.e. “Schubertring”, S3 (oriented in Northeast-Southwest) and “Kärntnerring” S4, (orientated Northwest-Southeast), were picked as the samples for wide-street type with vegetation. Total width of the street is about 55 meters including: two asphalt cycle/pedestrian lines in the margin, along with two 2 m stone pavements in the inner sides, two 6 m asphalt roads next to them, and one 12 m road with a heavy traffic in the middle.

The surrounding buildings are almost the same in both measuring locations i.e. 6 floor buildings in light colors with a height of 25 m. Since most of the ground floors are commercial, the openings constitute 43% of the wall surfaces in the ground floors. But in the upper floors, 20% of the wall surfaces is covered by windows. The

summer Sky view factor in “Schubertring” (S3) is 0.55, and in “Kärtner Ring” (S4) is 0.20. These values increase to about 0.65 and 0.50 on “Schubertring” (S3) and “Kärtner Ring” (S4), respectively, due to the fallen tree leaves in the winter. Complementary pictures describing the measuring locations S3 and S4 are given in figures 3-6 to 3-10.



Figure 3-6: Urban plan showing the location of stops S3 and S4



Figure 3-7: Location S3



Figure 3-8: Fish eye picture of S3



Figure 3-9: Location S4



Figure 3-10: Fish eye picture of S4

**Measuring spot S5 on “Am Heumarkt” street:**

“Am Heumarkt” is a wide street with a heavy traffic load in the third district of Vienna city. Its width varies from 24 to 38 m along the street. Its main axis is oriented from the north east to the south west with 770 m length. The Northern part of it is next to the city park (known as Stadtpark), the middle part is without any vegetation and the southern part, which ends to “Schwarzenberg platz”, is flanked by trees. The station was located in middle part of the street to represent a wide street with a heavy traffic load and without any vegetation. The street texture is not symmetric. At the measuring spot, the western wall is 40 m height made of a dark gray stone. Windows and door are covering 20% of the façade. The exact location of this spot is mapped in figure 3-11.

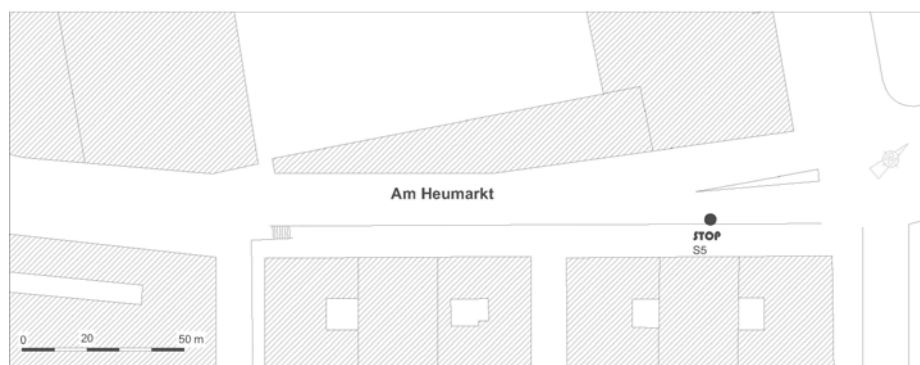


Figure 3-11: Urban plan showing the location of stop S5

Eastern buildings are residential 4 floor buildings with pitched roofs having the height of 20 m. The ground level of these buildings is about 1.2 m lower than the main street level. Here walls are made of stone and cement, painted in light colors with an opening fraction of about 40%. The height to width ratio at the measuring location is about 0.38 and the sky view factor here is estimated to be around 0.66. Street is made of asphalt including the sidewalks in both sides and in the middle. This measuring spot is shown in figures 3-12 to 3-13.



Figure 3-12: Location S5



Figure 3-13: Fish eye picture of S5

#### **Measuring spot S6 on “Favoritenstraße” street:**

“Favoritenstraße” is a Northwest-Southeast oriented street in the fourth district of Vienna. Its characteristics are similar to those of “Am Heumarkt” (see S5 description), while oriented perpendicularly to it. This street is selected, especially to observe the effect of orientation of a street on an urban micro-climate. The street is a long street that ends to “Wiedner Hauptstraße” in the north and “Südtirollerplatz” in the south. Its width varies from the north to the south so the station defined in the north part at a point which is almost similar to “Am Heumarkt” station.

In this spot the street is asymmetric. The east side building is a one floor building with 7 m height having white color painted walls. 80% of the walls are covered by windows. The West side building is a 7 floor building with stone Façade in white and purple color. The sky view factor in this spot is 0.5. The pavement of the street is made of asphalt with 31 m width. Details are shown in figures 3-14 to 3-16.



Figure 3-14: Urban plan showing the location of stop S6



Figure 3-15: Fish eye picture of S6



Figure 3-16: Location S6

### 3.2.1.2. Parks

Parks and city green areas as one of the defense lines of the cities against the artificial temperature increase are investigated in this study. For this reason, two measuring locations (G1 and G2) were selected in the City park (named as Stadtpark) located in the third district of Vienna to monitor the meteorological conditions. The total surface area of the park is about 65000 m<sup>2</sup>. The "Wienfluss" river flowing in 7 m lower than the park base level divides this park into two parts. A small lake in the western part is another considerable water body in the park. The park is vegetated by a wide variety of plants like deciduous trees, ever green trees with average height of 20 m, grass field and wide range of flora. Figure 3-17 reflects the configuration of the selected spots for the measurements in the city park.



Figure 3-17: Urban plan showing the location of stops G1 and G2

#### **Measuring spot G1 on “Stadtspark”:**

This spot is located near the Southern entrance of the park from the Parking street, in an open area surrounded by the grass fields having a summer SVF of about 0.89 and a winter one of about 0.91. The closest trees are in 20 m distance. Nearby trees are deciduous with an average height of 20 m. The paths are paved by asphalt. Figures 3-18 and 3-19 deliver more details.

#### **Measuring spot G2 on “Stadtspark”:**

The second measuring spot in the park was chosen at southwest shore of the lake. Its East side is a grass field. Tall trees in this spot are closer, i.e. 10 m westward. Comparing with the first spot the sky is less open here. The summer sky view factor is about 0.66 and the winter one is about 0.83. The road, on which the measuring spot is located, is made of asphalt in around 2 m wide. Figures 3-20 and 3-21 show more details.



Figure 3-18: Location G1



Figure 3-19: Fish eye picture of G1



Figure 3-20: Location G2



Figure 3-21: Fish eye picture of G2

### 3.2.1.3. Plaza

The third studied category is about plazas. During summer days, these spaces are used for outdoor activities by many people. Comprising to the total surface area of the city of Vienna considerable surfaces have been allocated to plazas, that is why they are assumed to affect the micro-climate of the city to a great extent.

The plaza category is divided into three subcategories, i.e. plaza with a water body, plaza with vegetation and plaza containing neither a water body nor vegetation.

Accordingly three measuring locations, each representing one of the above mentioned subcategories, are selected named here as P1, P2, and P3. Figure 3-22 displays the location of the measuring spots P1 and P2.

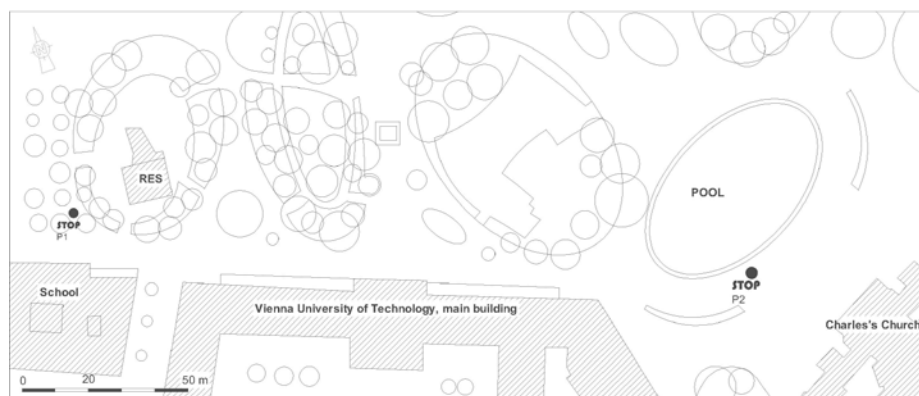


Figure 3-22: Urban plan showing the location of stops P1 and P2

#### **Measuring spots P1 and P2 on “Karlsplatz”:**

The measuring spots P1 and P2 were situated in the “Karlsplatz”. “Karlsplatz” with a surface area of about 30000 m<sup>2</sup> is located at the North of the fourth district. The

North border of it is “Lothringstrasse”, the west border touches the “Wiedner Hauptstraße”, in the south it is surrounded by a school building and the Vienna University of Technology, and on its east side the Vienna museum and a church are located. Almost 40% of the surface area is covered by green field and planted by average dense trees. The roads in the green area are made of asphalt, while these in the side part in front of the church, where there is no vegetation, are paved with gray stone. In this part there is a 2000 m<sup>2</sup> shallow pool. The measuring spot P1 is located in front of the school building within green area. It is in a place which is covered by 17 meter height trees and there is an open space restaurant, a one floor wooden building, in its east side. It is in 50 m distance from “Wiedner Hauptstraße” which has a heavy traffic load. The sky view factor of this spot in summer is about 0.15 and in winter 0.54.

The measuring spot P2 is located on the east side of the “Karlsplatz”. Because of fewer obstacles the sky view factor is higher, i.e. in summer it is equal to 0.87 and in winter around 0.89. Details pertaining to these measuring spots are shown in figures 3-23 to 3-26.



Figure 3-23: Location P1



Figure 3-24: Fish eye picture of P1





Figure 3-25: Location P2



Figure 3-26: Fish eye picture of P2

**Measuring spot P3 “Schwarzenbergplatz”:**

As it can be seen from the figure 3-27 the measuring spot P3 is located in “Schwarzenbergplatz”. “Schwarzenbergplatz” with an area of about 7000 m<sup>2</sup> is located on the border between the fourth and the third district of Vienna. Two 10 m wide streets, made of asphalt with a heavy traffic load, are drawn through this plaza. The area between these two streets, 18 m wide, is paved with stone. A 1 m asphalt bicycle way and a 2 m stone paved sidewalk are placed in outer sides of streets on both sides of plaza.



Figure 3-27: Urban plan showing the location of stopP3

“Schwarzenbergplatz” has a symmetric rectangular shape. The plaza is flanked by plastered buildings with around 6 floors. These buildings are in light color. The spot is almost in middle of the plaza and the SVF in that spot is around 0.81. Figures 3-28 and 3-29 show more details.



Figure 3-28: location P3



Figure 3-29: Fish eye picture of P3

#### 3.2.1.4. Courtyards

Courtyards are like lungs for the buildings to let them breathe. They provide an opportunity for natural ventilation and serve as a source of light for the inner spaces of buildings. Thus, improvement of climatic condition of these inner spaces can result in considerable savement in the energy consumption by using air conditioning systems for their contiguous closed spaces. In contemplation of having a better perspective of effective factors on the micro-climatic condition of courtyards the last category was specified to the courtyards. This category is divided to two subcategories, i.e. courtyards without vegetation and those with vegetation. Hence, 2 small courtyards in Vienna University of Technology (TU) complex (Hauptgebäude) in “Karlsplatz” area were chosen. The exact location of these two measuring points, named C1 and C2, is shown in figure 3-30.

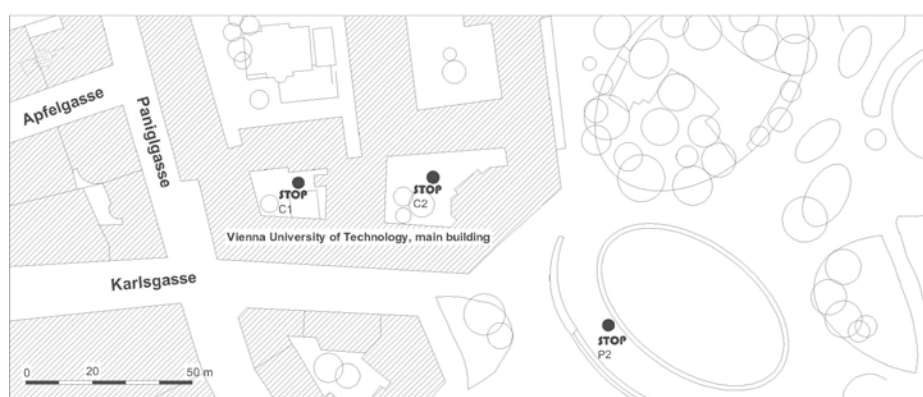


Figure 3-30: Urban plan showing the location of stops C1 and C2

**Measuring spot C1 at “TU4”:**

This spot is located in Courtyard 4, a small courtyard of VUT in the main building. Its area is about 270 m<sup>2</sup>. The surrounding buildings except the one in the east side are 5 floor buildings with 24 m total height in light color. The windows build 25% of the walls. The building in the eastern side is shorter than the other i.e. 12 m height and in 2 floors. The courtyard is sealed by asphalt and stone. On the northern side there is a sheltered parking place for the cars and the bicycles. The sky view factor of this spot is 0.19. Figures 3-31 and 3-32 show more detailed information about this measuring spot.



Figure 3-31: Location C1



Figure 3-32: Fish eye picture of C1

**Measuring spot C2 at “TU3”:**

This is located in the courtyard 3 in the same building area, as in the case for “C1”. It serves as an example for a courtyard with vegetation. Its surface area is about 600 m<sup>2</sup> including a small garden with 150 m<sup>2</sup> area, which has 3 average dense trees with about 17 m height. It is paved by stone and asphalt and surrounded by 5 floor buildings. The walls color is white and 12% of their surface area is made of windows. Its shape is rectangular with a cut in south-eastern corner. The sky view factor in this spot is 0.18.



*Figure 3-33: Location C2*



*Figure 3-34: Fish eye picture of C2*

### 3.2.2. Stationary weather station

BPI weather station, defined as the reference weather station (see section 4.1), belongs to the Building Physics and Building Ecology Institute of Vienna University of Technology (VUT). It is mounted on a tower on top of the main building of VUT. The height of the weather station is 42 m. The average height of the buildings in this area is about 27 m so it is located almost in the middle of the roughness layer in this area. SVF at this spot is 1 and there is no obstacle between short wave radiation sensor and sky.

The Sensors are manufactured by Thies Clima Company in Germany. It measures the illuminance, temperature, relative humidity, wind speed and direction, air pressure, precipitation and solar radiation with 1 second intervals. Details are given in table 3-1 and shown in figure 3-35 and 3-36.

*Table 3-1: Technical properties of the sensors used in BPI weather station*

<b>Item</b>	<b>Unit</b>	<b>Height</b>	<b>Accuracy</b>
Illuminance	Lx	42 m	<10%
Air Temperature	°C	42 m	±0.3 K
Relative Humidity	%	42 m	±2%
Air Pressure	hPa	42 m	±1 hPa
Global Radiation	W.m <sup>-2</sup>	42 m	±10%
Wind Direction	°	42 m	±5°
Wind Speed	m.s <sup>-1</sup>	42 m	±0.5m.s <sup>-1</sup> or 3% of measurement

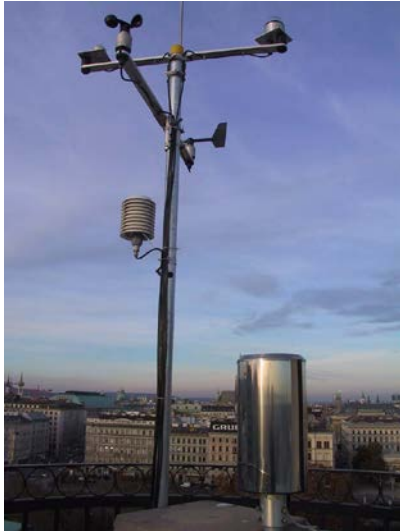


Figure 3-35: BPI stationary weather station

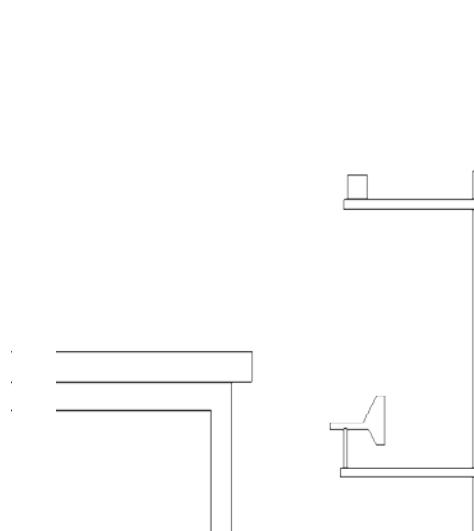


Figure 3-36: Schematic section showing BPI stationary weather station

### **C\*:**

Additionally, a second stationary weather station in the courtyard of the university old building, next to the main building was used to monitor weather data pertaining to the air temperature and pressure, the relative humidity, the global radiation, the wind speed and direction from 9.3.2010 to 31.12.2010 (Schuss 2011). The collected data were used for calibrating the simulation code used for micro-climate modeling (see section 5.1). This weather station, referred to as C\* here, was installed on an external wall next to a window in the first floor. The height was approximately 7 m from the ground level. The courtyard is relatively large with an area about 2245 m<sup>2</sup>. Out of that 1534 m<sup>2</sup> is a green area covered by grass and 11 dense trees. The ground is sealed by stone pavement. It is surrounded by buildings with 3 to 5 floors with gray and white facades.



Figure 3-37: Stationary weather station C\* (Schuss 2011)

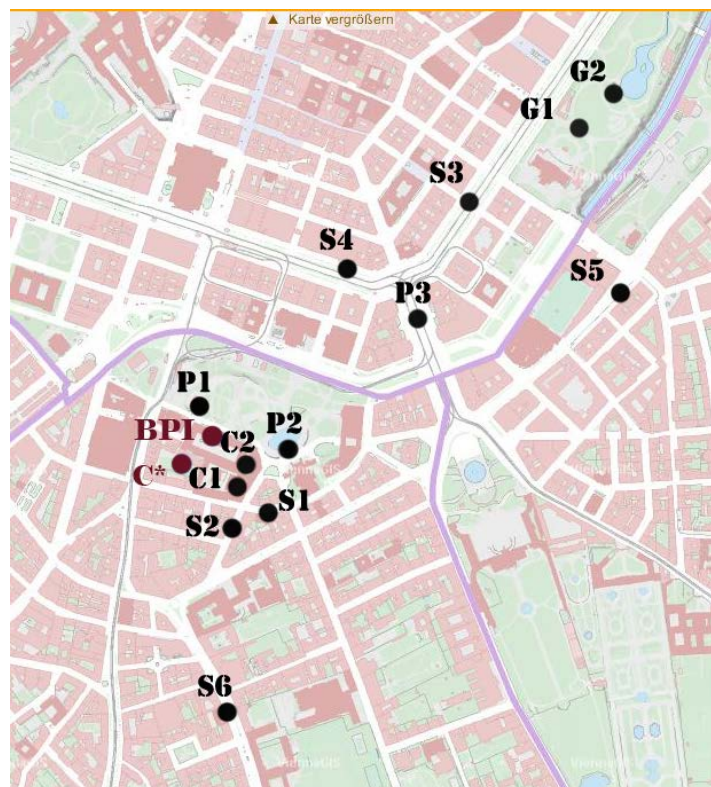


Figure 3-38: Measurement locations and reference weather station (BPI) marked on an area map (www.wien.at, 2012)

Table 3-2: The selected measurement spot with information regarding category, SVF, orientation, vegetation, surface properties, water body presence, intensity of traffic, H/W ratio (of streets).

Affiliation	Name of location	Category	SVF**	Orientation	Vegetation	Surface properties		Water body	Intensity of traffic	Streets' H/W ratio
						sealed	soil or green			
S1	Paniglgasse	street	0.30	E-W	no	100		no	medium	1.3
S2	Karlsgasse	street	0.29	N-S	no	100		no	medium	1.3
S3	schubert ring	street	0.59	NE-SW	heavy	86	14	no	heavy	0.5
S4	Kärntnerring	street	0.16	NW-SE	heavy	82	18	no	heavy	0.5
S5	Am Heumarkt	street	0.67	NE-SW	no	100		no	heavy	0.4
S6	Favoritenstraße	street	0.47	NW-SE	no	98	2	no	heavy	0.8
P1	Karlsplatz	plaza	0.16	n/a	heavy	75	25	no	no	n/a
P2	Karlsplatz	plaza	0.88	n/a	no	100		yes	no	n/a
P3	schwarzenbergplatz	plaza	0.82	NW-SE	no	100		no	heavy	n/a
C1	TU courtyard 4	courtyard	0.20	n/a	no	100	-	no	little	n/a
C2	TU courtyard 3	courtyard	0.18	n/a	medium	78	22	no	little	n/a
C*	TU Resselgasse	courtyard	0.45	n/a	heavy	35	65	no	no	n/a
G1	Stadtpark	park	0.90	n/a	medium	30	70	no	no	n/a
G2	Stadtpark	park	0.68	n/a	heavy	30	70	yes	no	n/a
BPI	Refrence point	n/a	1	n/a	n/a	n/a	n/a	n/a	n/a	n/a

\*\*The SVF was calculated using The SkyViewFactorCalculator, developed at University of Gothenburg. The equations used to derive SVF are based on the method presented in B. Holmer, U. Postgård, and M. Eriksson (2001). Sky view factors in forest canopies calculated with IDRISI. Theoretical and Applied Climatology 68, 33-40.



### 3.2.3. Mobile weather stations

The mobile weather station was mounted on a bike trailer at the height of about 1.6 m, recommended height is 1.5 m (Gartland 2008). It was equipped with a temperature sensor and as well as humidity sensor, a low power anemometer for wind speed (vector instruments type A100L2) and a pyranometer for solar radiation (Sky Instrument), all connected to the same logger (weather station DK-Stat1, Driesent Kern GmbH). The logger was carried in a trailer. The trailer was equipped with a camera tripod and an attached compass. The pulling bike was also equipped with a pair of bike bags to carry CO<sub>2</sub> sensors and camera. In outer net bags in the both sides which allow air ventilation, two Telaire 7001 CO<sub>2</sub>/temperature monitors connected to two Synotech onset HOBO data loggers were placed. Additionally a Nikon Coolpix 8400 camera with 8.0 Mega pixels with a Nikon UR-E16 Fisheye Lens was utilized in order to take pictures from the sky.

In the path of measurements due to some technical problems associated with the logger it was decided to replace the logger and the whole set of sensors with Onset HOBO loggers. The new data logger was H21-001, the temperature/humidity sensor was replaced by S-THA-M002, the wind speed sensor by S-WSA-M003 and for the solar radiation by Pyranometer, S-LIB-M003. The tripod which the sensors were mounted on was the same so the height did not change. The details pertaining to the loggers and the sensors used are given in table 3-3.

Table 3-3: Instruments used in mobile weather station

Item	Unit	Height	Instrument
Global radiation-1	W.m <sup>-2</sup>	1.6 m	pyranometer (Sky Instrument)
Air temperature-1	°C	1.6 m	low power anemometer
Wind speed-1	m.s <sup>-1</sup>	1.6 m	Vector instruments type A100L2
Relative humidity-1	%	1.6 m	low power anemometer
CO <sub>2</sub>	ppm	0.40 m	Telaire 7001
Global radiation-2	W.m <sup>-2</sup>	1.6 m	pyranometer S-LIB-M003
Air temperature-2	°C	1.6 m	S-THA-M002
Wind speed-2	m.s <sup>-1</sup>	1.6 m	S-WSA-M003
Relative humidity-2	%	1.6 m	S-THA-M002

Field measurements for the project started in June 2010 and continued till September 2011. Two types of measurements were done; short/regular as well as long ones. In terms of short/regular measurements several measuring spots were visited for a time span of 12 minutes. Long measurements took place at one location over a period of 12 h, from noon till midnight in order to record fluctuation of temperature and its decreasing trend during the evening. Unlike the other type of measurements the long one was carried out just at five measuring spots, i.e. at S1, S5, P1, C2 and G1. Depending on weather conditions to avoid precipitation, concerning each measuring spot short measurements were done about three times a week each time at a different time point during the day time scheduled on different times of the day.

### 3.2.3.1. Launching and reading out

The logger of the first mobile weather station was launched and read out using INFRALOG 301 software. The data was measured and recorded every 15 s. The data were saved in BIN format and were converted to ASC file by INFRALOG software. Thereafter the logger of the second mobile weather station was working using Hoboware software. The interval for measuring and recording the data was like before, 15 s. The data were saved as ONSET HOBO DATAFILE, which was converted to xls files (MS Excel) by Hoboware software later on.

The HOBO loggers used to record the CO<sub>2</sub> measurement results were using Onset GREENLINE software (measuring/recording every 15 s). The data were recorded under ONSET HOBO DATAFILE format, converted to the txt files during the reading out process. The HOBOs also recorded the air temperature and the relative humidity, but due to impropersness of this model of sensors for these types of measurements, the recorded air temperature and relative humidity here were ignored. Figures 3-39 and 3-40 show the first and second mobile weather station, respectively.



Figure 3-39: First mobile weather station



Figure 3-40: Second mobile weather station

### 3.2.3.2. Calibration of mobile weather station

A test measurement was conducted on June 6<sup>th</sup> 2010 to estimate the adaptation time of the sensors. For this test run, a measurement was done at S1 for around 17 minutes. The result showed that, when the average air velocity is about  $1-2 \text{ m.s}^{-1}$  the air temperature and relative humidity sensors need around 5 minutes to adapt to the environmental conditions (see figure 3-41). In the case of still air, the adaptation time can increase even up to 90 minutes, if the temperature difference between the two subsequent measuring spots is high. For this reason it was decided to have a 12 minutes measuring time for each measuring spot, every time

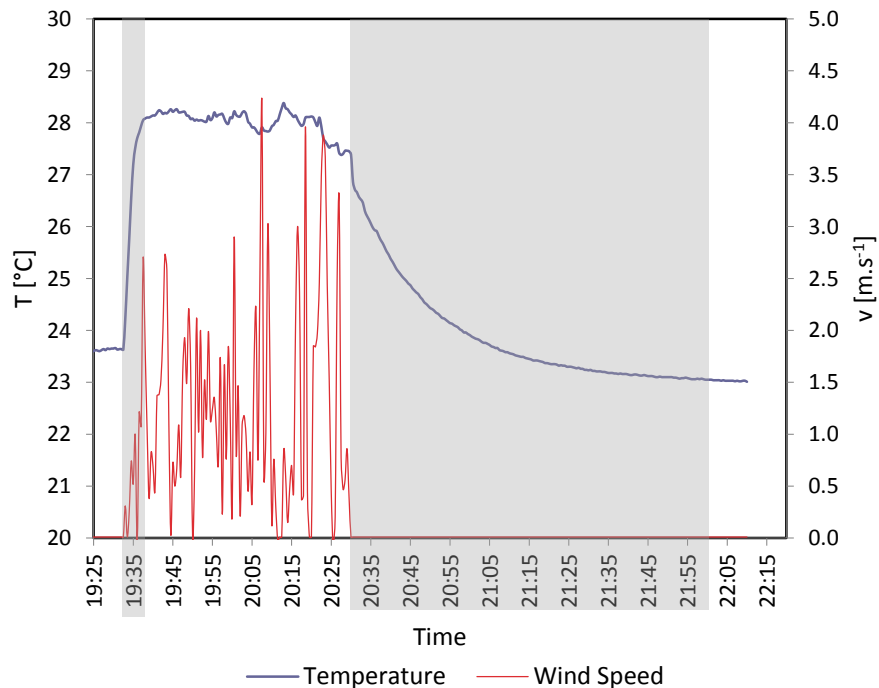


Figure 3-41: Fluctuation of temperature and wind speed at test measurement

To calibrate the first mobile weather station, it was mounted near the BPI weather station, for a time period of 4-5 days. The data collected by the BPI and those collected by the mobile station were compared. Taking BPI reading as the reference, through least square regression method, appropriate correlations were obtained for the correlation of the air temperature and air relative humidity read out of the mobile weather station. Details are shown in figures 3-42 to 3-45.

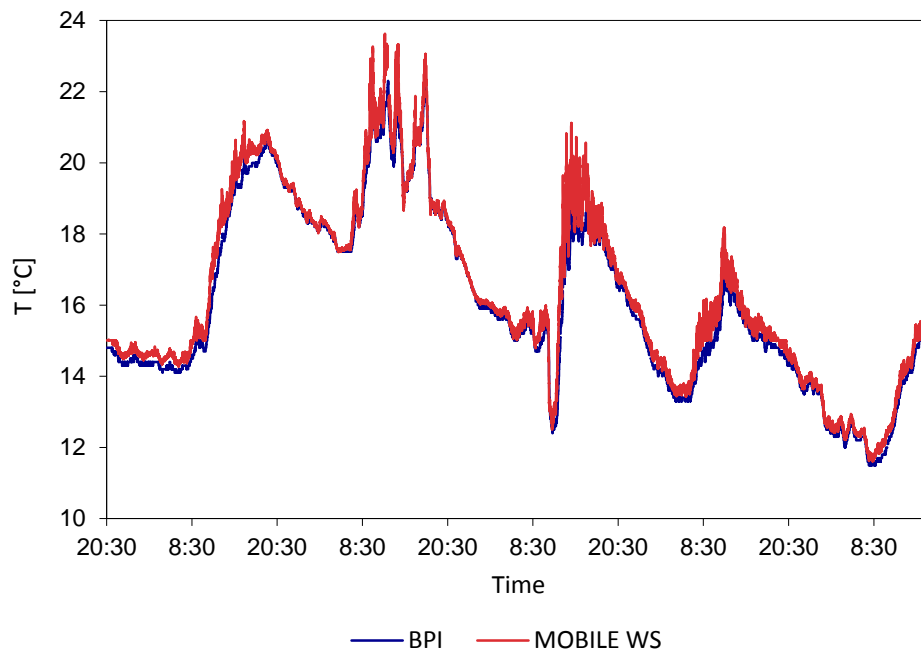


Figure 3-42: Monitored air temperature at BPI and first mobile weather station

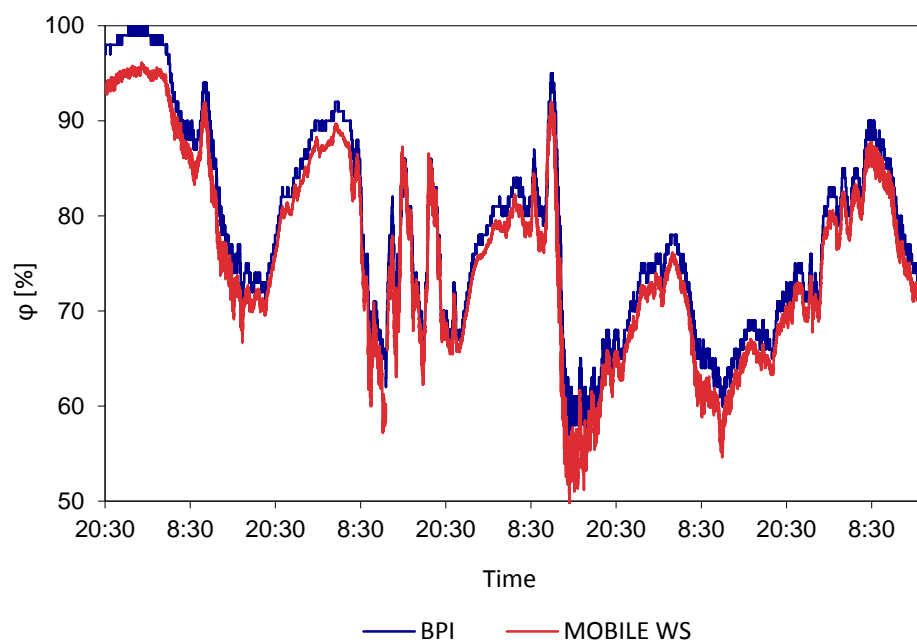


Figure 3-43: Monitored relative humidity at BPI and first mobile weather station

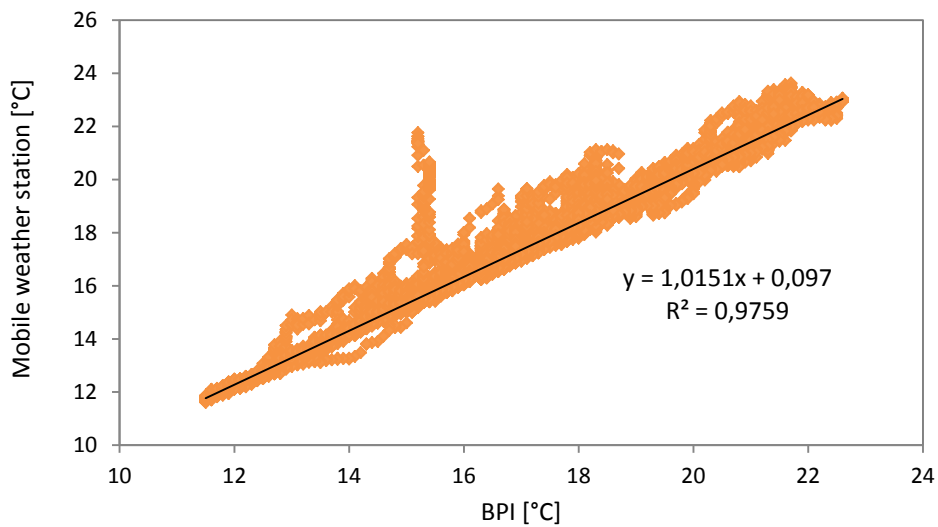


Figure 3-44: Regression analysis of temperature monitored by BPI and first mobile weather station to calibrate the mobile weather station

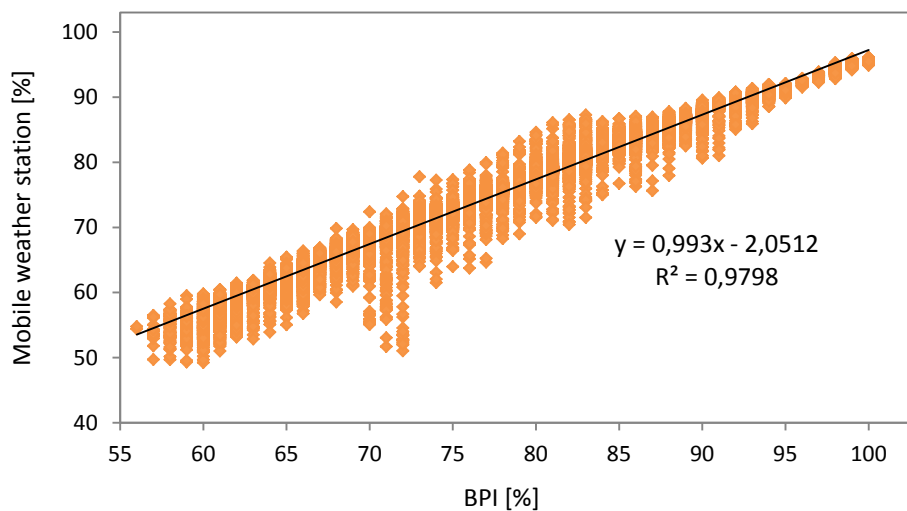


Figure 3-45: Regression analysis of relative humidity monitored by BPI and first mobile weather station to calibrate the mobile weather station

The same procedure was applied to calibrate the second mobile weather station. Since the difference between the data, obtained from both weather stations, was negligible in each case so no regression equation was applied to the data collected by the HOBO weather station (the second mobile weather station).

### 3.3. Computational inquiries

The uncontrollable and the unpredictable weather conditions and the wide variances in the urban geometry impose significant limitations to the empirical studies concerning the micro-climatic conditions (Ali Toudert and Mayer 2006). As a substitute, Numerical simulation perfectly fits to deal with the complexities and nonlinearities of the urban climate systems (Arnfield 2003). This method progressively is improving with computing power and sophisticated meteorological models that can integrate the effects of the urban configuration (Robinson 2011). Regarding to the physical foundation and the temporal / the spatial resolution, micro-scale climate models differ from each other. Most of them focus on one or two aspects of the urban micro-climate and neglect the other variables.

To find the most fitting simulation tool which can meet requirements of this project, existing micro-climate modeling tools were surveyed and summarized in the following table.

*Table 3-4: Well-known available micro-climate simulation tools*

<b>Name</b>	<b>Capability</b>
ENVI-met	Heat flux, radiation flux, air flow and aerosol desparation, and exchange processes of vapor at the ground surface and at the vegetation
MISKAM	airflow and the gas diffusion
RadTherm	temperature distribution of the product or system
Rayman	Radiation Flux and outdoor thermal comfort
OTC	Outdoor thermal comfort
RIAM-Compact	airflow and the gas diffusion
TownScope	Solar access and thermal comfort
LASAT	dispersion of atmospheric air pollutant
SOLWEIG	longwave and shortwave radiation Fluxes
SOLENE	Radiation flux

### **3.3.1. Relevance of ENVI-met to the present study**

Among the surveyed urban micro-climate simulation tools Envi-met is the most comprehensive tool. It is a freeware developed by Michael Bruse et. al. at the University of Mainz. It simulates the urban micro-climate with complex building shapes, vegetation and different types of pavements. Its input parameters are relatively few but it reproduces wide range of climatic parameters such as air, soil and surface temperature, air and soil humidity, wind speed and direction, short wave and long wave radiation fluxes, gas particles and many other important metrological factors which are being discussed in section 3.3.2 (Bruse 1999).

High spatial and temporal resolution of its outputs can provide deep understanding of the urban micro-climate variation within the urban fabric and can help to evaluate the findings of on-site measurements in this project. Therefore, Envi-met 3.1, which is officially released in the Internet, was employed for this project at the beginning of this research project. In July 2011 a preview version of ENVI-met 4.0 released for academic purposes. Due to its new features and improvements in some calculations, (see section 3.3.2 ) some other simulations were performed with this version and the results were compared with those obtained through version 3.1 to choose the best fitting tool and input assumption for this project.

### **3.3.2. General structure of ENVI-met 3.1(4.0)**

ENVI-met is a three-dimensional non-hydrostatic model for the simulation of surface-plant-air interactions within urban environments. It is a micro-scale model with a time step of 10 sec at maximum and with resolution from 0.5 to 10 m for the length (x) and the width (y) of the grids. Height of the grids (z) can be defined to increase by the height of the model and can be more than 10 m in upper grids. The model calculation includes (Bruse 1999):

- Shortwave and long-wave radiation fluxes considering absorption, reflection and re-radiation from buildings and ground surfaces and the plants,
- Transpiration, Evaporation and sensible heat flux from the vegetation into the air,
- Ground surface and wall temperature for each grid point and wall,
- Water and heat exchange inside the soil system,
- Calculation of biometeorological parameters like Mean Radiant Temperature or Fanger's Predicted Mean Vote (PMV) –Value,
- Dispersion of inert gases and particles including sedimentation of particles on leafs and surfaces,

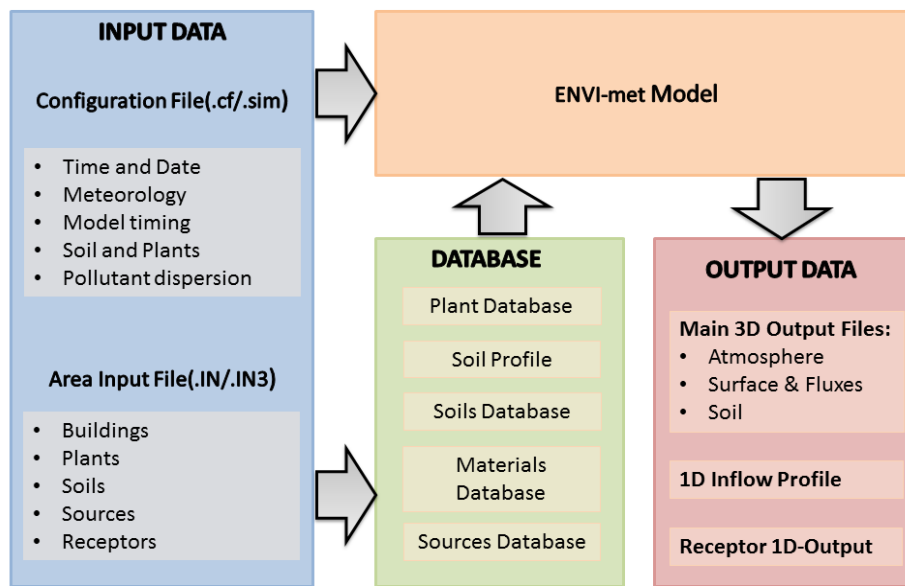


Figure 3-46: Graphical overview over the data flow within the ENVI-met

Buildings, vegetation, soils, surfaces and pollutant sources can be placed inside the model area. Besides of natural and artificial surfaces, the model is also able to handle water bodies but it cannot handle freezing and precipitation (Bruse 1999). An overview over the data flow within the ENVI-met is given in figure 3-46.

### 3.3.3. Model layout

The ENVI-met model consists of a 1D boundary model, a 3D atmospheric model and a 1D soil model. The 1D boundary model expands from the ground level to the height of 2500 m and calculates the values of the model boundary. The three-dimensional model incorporates rectangular grids with the dimension of x, y and z. Grid sizes can be defined from 0.5 to 10 meter.  $\Delta x$  and  $\Delta y$  are constant all over the model but  $\Delta z$  can be set to increase with the height. The objects inside the 3D model are squeezed into these grids parallel to the X, Y and Z axis. Every grid can be completely filled by an object or just by the air. The grids sizes of one dimensional boundary model is the same as 3D model but in the case of the 1D soil model, vertical size of the grids is defined by the model. The soil model consists of 19 grids and is extended down to the 4.50 m below the ground surface. A schematic overview over the model lay-out is shown in figure 3-47.



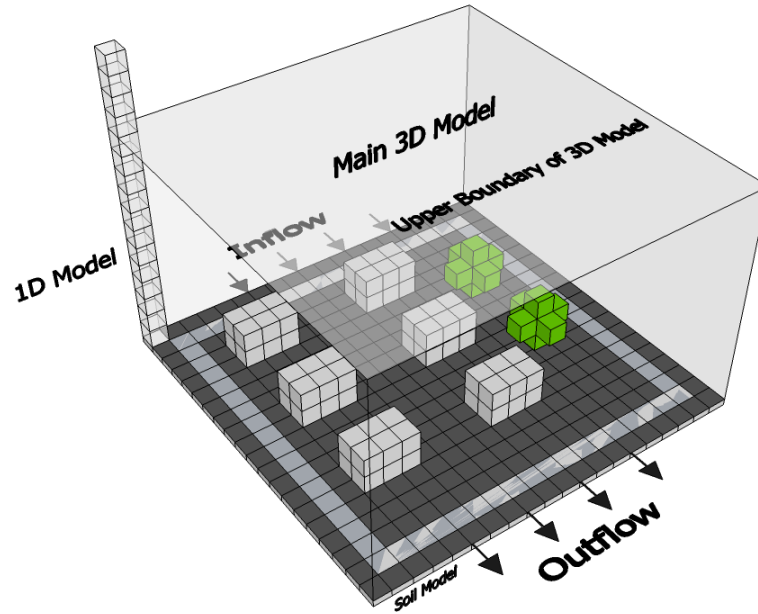


Figure 3-47: Schematic description of model lay-out.

### 3.3.4. Atmospheric model

The atmospheric model speculates changes in the air temperature and the air humidity, the air velocity and the turbulence and the radiation fluxes, based on the fluid dynamic laws (explained in section 2.8).

#### 3.3.4.1. Air flow

Calculation of the turbulent flow in ENVI-met is based on the non-hydrostatic incompressible Navier-Stokes equation (Bruse, 1999):

$$\frac{\partial u}{\partial t} + u_i \frac{\partial u}{\partial x_i} = -\frac{\partial p'}{\partial x} + K_m \left( \frac{\partial^2 u}{\partial x_i^2} \right) + f(v - v_g) - S_u \quad (3-1)$$

$$\frac{\partial v}{\partial t} + u_i \frac{\partial v}{\partial x_i} = -\frac{\partial p'}{\partial y} + K_m \left( \frac{\partial^2 v}{\partial x_i^2} \right) - f(u - u_g) - S_v \quad (3-2)$$

$$\frac{\partial w}{\partial t} + u_i \frac{\partial w}{\partial x_i} = -\frac{\partial p'}{\partial z} + K_m \cdot \left( \frac{\partial^2 w}{\partial x_i^2} \right) - g \cdot \left( \frac{\theta(z)}{\theta_{ref}(z)} \right) - S_w \quad (3-3)$$

$$\frac{\partial u}{\partial x} + \frac{\partial v}{\partial y} + \frac{\partial w}{\partial z} = 0 \quad (3-4)$$

where  $f=10^{-4}$  [s<sup>-1</sup>] is the Coriolis parameter,  $K_m$  is the exchange coefficient,  $p'$  is the local pressure perturbation,  $\theta$  is the potential temperature of the level  $z$  and  $\theta_{ref}$  a reference temperature at the same level. The terms  $u_g$  and  $v_g$  are denoted to geospheric wind components. Regarding to Boussinesq-Approximation (i.e.  $\Delta\rho=0$ ), the air density  $\rho$  is removed from the original equation.

Thus, an additional term  $g(\theta(z)/\theta_{ref}(z))$  is added to  $w$ -equation to include the thermal forced vertical motion. Nomenclature  $u_i$  stands for  $u, v, w, x_i$  for  $x, y, z$  and  $i$  for 1, 2, 3 to avoid expanding the equations.

Loss of the wind speed due to the drag, forced at the plants, is calculated via  $S_u, S_v$  and  $S_w$  according to Yamada (1982) and Liu(1996) by:

$$S_{u(i)} = \frac{\overline{\partial p'}}{\partial x_i} = c_{d,f} \cdot LAD(z) \cdot W \cdot u_i \quad (3-5)$$

$$W = \sqrt{u^2 + v^2 + w^2} \quad (3-6)$$

where  $W$  is the mean wind speed at level  $z$ ,  $LAD$  is the leaf area density of the plant at the same level and  $c_{d,f}$  is the mechanical drag coefficient set to 0.2.

### 3.3.4.2. Utilization of proper turbulence model

In ENVI-met a two equation turbulence model has been used to cope with turbulency. This model is known as Mellor and Yamada (1.5 order closure model 1975). Two equations for the local turbulence ( $E$ ) and its dissipation rate ( $\varepsilon$ ) are added to the original CFD two equation model. The main feature of this model is (Bruse, 1999):

$$\frac{\partial E}{\partial t} + u_i \frac{\partial E}{\partial x_i} = K_\varepsilon \cdot \left( \frac{\partial^2 E}{\partial x_i^2} \right) + Pr - Th + Q_\varepsilon - \varepsilon \quad (3-7)$$

$$\frac{\partial \varepsilon}{\partial t} + u_i \frac{\partial \varepsilon}{\partial x_i} = K_\varepsilon \cdot \left( \frac{\partial^2 \varepsilon}{\partial x_i^2} \right) + c_1 \frac{\varepsilon}{E} Pr - c_3 \frac{\varepsilon}{E} Th - c_2 \frac{\varepsilon^2}{E} + Q_\varepsilon \quad (3-8)$$

$\varepsilon$ -equation standard constants  $c_1=1.44, c_2=1.92$  and  $c_3=1.44$  are taken from Launder and Spalding (1974). The mechanical production and dissipation of the turbulent energy caused by the wind shearing ( $Pr$ ) and the thermal stratification ( $Th$ ) can be described as:

$$\begin{aligned} Pr = & 2K_m \cdot \left( \frac{\partial u}{\partial x} \right)^2 + K_m \cdot \left( \frac{\partial u}{\partial y} + \frac{\partial v}{\partial x} \right)^2 + K_m \cdot \left( \frac{\partial u}{\partial z} + \frac{\partial w}{\partial x} \right)^2 + 2K_m \cdot \left( \frac{\partial v}{\partial y} \right)^2 \\ & + K_m \cdot \left( \frac{\partial v}{\partial z} + \frac{\partial w}{\partial y} \right)^2 + 2K_m \cdot \left( \frac{\partial w}{\partial z} \right)^2 \end{aligned} \quad (3-9)$$

$$Th = \left( \frac{g}{\theta_{ref}(z)} \right) \cdot \left( K_h \frac{\partial \theta}{\partial z} \right) \quad (3-10)$$

According to Liu et al (1996) and Wilson (1988), the turbulence induced by vegetation  $Q_E$  and accelerated cascade of the turbulence energy from the large to the small scales near to the plant foliage elements  $Q_\epsilon$  can be expressed as:

$$Q_E = c_{d,f} \cdot LAD(z) \cdot W^3 - 4(c_{d,f} \cdot LAD(z) \cdot |W| \cdot E) \quad (3-11)$$

$$Q_\epsilon = 1.5(c_{d,f} \cdot LAD(z) \cdot W^3) - 6(c_{d,f} \cdot LAD(z) \cdot |W| \cdot \epsilon) \quad (3-12)$$

The turbulent exchange coefficients are derived from the calculated E-ε assuming the local turbulent isotropy by:

$$K_m = c_\mu \cdot \left( \frac{E^2}{\epsilon} \right) \quad (3-13)$$

$$K_h = K_q = (1.35K_m) \quad (3-14)$$

$$K_E = \left( \frac{K_m}{\sigma_E} \right) \quad (3-15)$$

$$K_\epsilon = \left( \frac{K_m}{\sigma_\epsilon} \right) \quad (3-16)$$

Where  $c_\mu = 0.09$  ,  $\sigma_E = 1$  and  $\sigma_\epsilon = 1.3$ .

### 3.3.4.3. Temperature and humidity

Distribution of the air temperature and the air humidity within the atmosphere is described and modeled by the combined advection-diffusion equation (Bruse 1999).

$$\frac{\partial \theta}{\partial t} + u_i \frac{\partial^2 \theta}{\partial x_i} = K_h \cdot \left( \frac{\partial^2 \theta}{\partial x_i^2} \right) + \left( \frac{1}{c_p \rho} \right) \cdot \left( \frac{\partial R_{lw}}{\partial z} \right) + Q_h \quad (3-17)$$

$$\frac{\partial q}{\partial t} + u_i \frac{\partial^2 q}{\partial x_i} = K_q \cdot \left( \frac{\partial^2 q}{\partial x_i^2} \right) + Q_q \quad (3-18)$$

where  $K_h$  and  $K_q$  are turbulent exchange coefficient for the heat and the humidity. The term  $(1/(c_p \cdot \rho)) \cdot (\partial R_{lw} / \partial z)$  describes the air temperature and the humidity changes, caused by the divergence of the long wave radiation.  $Q_h$  and  $Q_q$  are added to link the heat and the humidity flux between the plants and the atmosphere (see section 3.3.6).

#### 3.3.4.4. Radiation

The radiation budget of the atmosphere depends on the air temperature, the absorption and the emission coefficients of the atmosphere layers. Several factors such as water vapor concentration,  $CO_2$ , Ozone and content of other gasses as well as the number of existing aerosols define the emission and the absorption rate of the atmosphere. Due to the complexity of the process through which play their role to affect the absorption/the emission rate in the atmosphere as well as lack of the detailed information about the distribution of them in the atmosphere, ENVI-met just takes the water vapor effect into account (Huttner 2012).

The shortwave radiation flux at the upper boundary is calculated by integrating the radiation intensity of the sun  $I_0$  between the wavelength  $\lambda=0.29\mu\text{m}$  and  $\lambda=0.40\mu\text{m}$ :

$$R_{sw}^* = \int_{0.29}^{4.0} I_0(\lambda) \cdot \exp\{-\alpha_R \cdot (\lambda)m + \alpha_M \cdot (\lambda)m\} \cdot d\lambda \quad (3-19)$$

Where  $\alpha_R=0.00816 \cdot \lambda^{-4}$  and  $\alpha_M=\lambda^{-1.3} \beta_{t,r}$  are Raileight and Mie scattering coefficient, respectively with  $0.004 \leq \beta_{t,r} \leq 1$  as the opacity coefficient.  $m$  is the optical air mass and according to sun height is calculated by:

$$\text{If } h > 10 \text{ then: } m = \left( \frac{1}{\sin(h)} \right) \quad (3-20)$$

$$\text{If } h \leq 10 \text{ then: } m = 1.22 \left( \frac{1.0144}{\sin(h + 1.44)} - 0.49 \right) \quad (3-21)$$

The absorbed shortwave radiation by the water vapor should be subtracted from the incoming shortwave radiation at the boundary to calculate the absolute direct shortwave radiation.

$$R_{sw.dir}^0 = R_{sw}^* - R_{sw.abs} = R_{sw}^* - (70 + 2.8(e_{2m} \cdot m)) \quad (3-22)$$

$e_{2m}$  is the water vapor pressure in [hPa] in 2 m above ground level.

The diffuse shortwave radiation for the clear sky depends on the incoming direct shortwave radiation and the sun height,  $h$ , and is calculated after Brown and Islält (1974):

$$R_{sw,dif}^0 = R_{sw,dir}^0 \cdot \sin(h) \left( \frac{\Upsilon(h)}{1 - \Upsilon(h)} \right) \quad (3-23)$$

$$\Upsilon(h) = \frac{1}{1 + 8(\sin(h))^{0.7}} \quad (3-24)$$

In cloudy condition, the direct and the diffused radiation is reduced. Reduction rate is estimated after Taesler and Anderson (1984):

$$R_{sw,dir}^0(Clouds) = R_{sw,dir}^0 \cdot \left( 1 - \frac{N}{8} \right) \quad (3-25)$$

$$R_{sw,dif}^0(Clouds) = \left( \frac{R_{sw,dir}^0 \times \sin(h)}{1 - \Upsilon(h)} \right) \left( \frac{a_s - 1}{(a_s \times a_c) - 1} \right) - R_{sw,dir}^0(Clouds) \times \sin(h) \quad (3-26)$$

$N$  is the cloud cover in 1/8 (in octas),  $a_c$  the albedo of clouds and  $a_s$  albedo of the soil.

The incoming longwave radiation within a model with  $N$  layers, at the level of  $z$  can be estimated according to Paltridge and Platt (1976) by:

$$R_{lw}^\downarrow(z) = \sum_{n=1}^N \left( \sigma \cdot T^4(n) \cdot [\varepsilon_n(l + \Delta l) - \varepsilon_n(l)] \right) \quad (3-27)$$

where  $l$  is the amount of the water vapor between the height  $z$  and the lower boundary of the layer  $n$  and  $(l + \Delta l)$ , the amount of the water vapor between the height  $z$  and the upper boundary of the layer  $n$ . The term  $\varepsilon_n$  is the emissivity and  $T$  the absolute temperature of the layer  $n$ .

Radiation flux is significantly affected by the existing buildings and vegetation within the model. The reduction effect of these obstacles is taken into the account via introducing a number of coefficients. The modification effect of the buildings is described by  $\sigma_{SVF}$  explained in section 2.2.1.1. Other coefficients approximate the effect of the plants on the direct and the diffuse shortwave radiation ( $\sigma_{sw,dir}$  and  $\sigma_{sw,dif}$ ) as well as the upward and the downward long wave radiation ( $\sigma_{lw}^\uparrow$  and  $\sigma_{lw}^\downarrow$ ):

$$\sigma_{sw,dir} = \exp(F \cdot LAI^*(z)) \quad (3-28)$$

$$\sigma_{sw,dif} = \exp(F \cdot LAI(z, z_p)) \quad (3-29)$$

$$\sigma_{lw}^\uparrow = \exp(F \cdot LAI(0, z)) \quad (3-30)$$

$$\sigma_{lw}^{\downarrow} = \exp(F \cdot LAI(z, z_p)) \quad (3-31)$$

$F$  is the extinction coefficient and LAI is the one dimensional leaf area index of the plant from the height  $z$  up to the top of the plant  $z_p$  or down to the ground level ( $z=0$ ).

$$LAI(z, z + \Delta z) = \int_{z'}^{z'+\Delta z} LAD(z') \cdot dz' \quad (3-32)$$

For the shortwave solar radiation, LAI\* , is introduced instead of LAI to describe the effect of the angle of the incidence of the incoming sun rays.

The shortwave radiation budget can be summed up as:

$$R_{sw}(z) = (\sigma_{sw.dir}(z) \cdot R_{sw.dir}^0) + (\sigma_{sw.dif}(z) \cdot \sigma_{SVF}(z) \cdot R_{sw.dif}^0) + (1 - \sigma_{SVF}(z)) \cdot R_{sw.dir}^0 \cdot \bar{a} \quad (3-33)$$

Where  $R_{sw.dir}^0$  and  $R_{sw.dif}^0$  are the direct and the diffuse shortwave radiation at the upper boundary of the model respectively and  $\bar{a}$  is the average albedo of the walls within the domain. The long wave radiation flux within the model can be approximated by:

$$R_{lw}^{\downarrow}(z) = (\sigma_{lw}^{\downarrow}(z, z_p) \cdot R_{lw}^{\downarrow,0}) + (1 - \sigma_{lw}^{\downarrow}(0, z)) \cdot \varepsilon_f \cdot \sigma_B \cdot \bar{T}_{f+}^4 + (1 - \sigma_{SVF}(z)) \cdot R_{lw}^{\leftrightarrow} \quad (3-34)$$

$$R_{lw}^{\uparrow}(z) = (\sigma_{lw}^{\uparrow}(0, z) \cdot \varepsilon_s \cdot \sigma_B \cdot T_0^4) + (1 - \sigma_{lw}^{\uparrow}(0, z)) \cdot \varepsilon_f \cdot \sigma_f \cdot \bar{T}_{f-}^4 \quad (3-35)$$

$$R_{lw}^{\leftrightarrow}(z) = (1 - \sigma_{SVF}(z)) \cdot \varepsilon_w \cdot \sigma_B \cdot \bar{T}_w^4 \quad (3-36)$$

where  $\bar{T}_{f-}$  and  $\bar{T}_{f+}$  are the average foliage temperature of the underlying and overlying vegetation. The term  $\varepsilon_s$ ,  $\varepsilon_f$  and  $\varepsilon_w$  are the emissivity of the surface, foliage and wall, respectively.  $T_0$  is the surface temperature and  $R_{lw}^{\leftrightarrow}$  is the horizontal longwave radiation flux from the surrounding walls and the term  $\sigma_B$  refers to the Stefan\_Boltzman constant:  $\sigma_B = 5.97 \cdot 10^{-8} \text{ Wm}^{-2}\text{K}^{-4}$ .

### 3.3.5. Soil model

ENVI-met calculates the temperature and humidity of the soil by employing a one dimensional model. Every grid in the domain has a soil profile including 19 layers, extended from the ground level down to the 4.5 m. The thickness of the layers varies between 1 cm to 150 cm and increase from the upper layer to the deepest. The

temperature distribution and the soil volumetric moisture content within the model are approximated by (Bruse 1999):

$$\frac{\partial T_s}{\partial t} = K_s \cdot \left( \frac{\partial^2 T}{\partial z^2} \right) \quad (3-37)$$

$$\frac{\partial \eta}{\partial t} = D_\eta \cdot \left( \frac{\partial^2 \eta}{\partial z^2} \right) + \left( \frac{\partial K_\eta}{\partial z} \right) - S_\eta(z) \quad (3-38)$$

where  $K_s$  is the thermal diffusivity of the soil. It is constant for impermeable soils and a function of the soil moisture  $\eta$  for other types.  $S_\eta$  is the water uptake by the plant root, described in the section 3.3.6. And  $D_\eta$  is hydraulic diffusivity of soil layer.

### 3.3.6. Vegetation model

The plants inside the urban canopy as a biological body apart from influencing the air velocity and the radiation within the urban canopy interact with their surrounding environment by exchanging the heat and the vapor, as well (Ali Toudert 2005). In the present work, by the used CFD code the vegetation model is considered as a 1D column with height  $z_p$ . Along the plant height leaf area density (LAD) profile is used to describe the leaf distribution. The same pattern is used for the root distribution in the soil by the root area density (RAD) profile along the root depth, ( $-z_r$ ). To obtain suitable estimates for LAD and RAD values, which are supposed to be used in the simulation model, standard measurements/tables for different types of plants given in the literature should be used. In present work, in the most cases the proper default values in the ENVI-met code have been used.

#### 3.3.6.1. Turbulent heat flux through evaporation:

The heat transfer interactions between the plant leaves and the surrounding air are formulated in the following equations (Bruse 1999):

$$J_{f,h} = 1.1(r_a^{-1}) \cdot (T_f - T_a) \quad (3-39)$$

(sensible heat flux)

$$J_{f,evap} = (r_a^{-1} \cdot \Delta q \cdot \delta_c \cdot f_w) + (r_a^{-1} \cdot (1 - \delta_c) \cdot \Delta q) \quad (3-40)$$

(evaporation flux of liquid water on the leaves)

$$J_{f,trans} = \delta_c \cdot (r_a + r_s)^{-1} \cdot (1 - f_w) \cdot \Delta q \quad (3-41)$$

(transpiration flux controlled by the leaf stoma)

$$\Delta q = q^*(T_f) - q_a \quad (3-42)$$

where  $T_a$  and  $q_a$  are respectively the air temperature and specific humidity around the leaf.  $\Delta q$  is the leaf-to-air humidity deficit. The term  $T_f$  is the foliage temperature and  $q^*$  the saturation value of  $q$  at the leaf surface. The term  $\delta_c$  is set to 1 when evaporation and transpiration can occur ( $\Delta q \geq 0$ ) otherwise is 0.  $r_s$  is the stomatal resistance which depends on short-wave irradiance input and available soil water, and is calculated after Deardoff (1978) or alternatively after Jacobs (1994) which is a more dynamic description including the photosynthesis process.  $r_a$  is the aerodynamic resistance which is the function of the wind speed ( $W$ ). And the contribution of leaf geometry in terms of the leaf diameter,  $D$ , is considered. Through

$$r_a = A \cdot \sqrt{\frac{D}{\max(W, 0.05)}} \quad (3-43)$$

$A = 87 \text{ s}^{0.5} \text{ m}^{-1}$  for conifers and grass and  $A = 200 \text{ s}^{0.5} \text{ m}^{-1}$  for deciduous trees.  $D$  ranges from 0.02 m (for conifers) to 0.5 m (for tropical plants).

The term  $f_w$  refers to the fraction of wet leaves and is calculated as below:

$$f_w = \left( \frac{W_{dew}}{W_{dew,max}} \right)^{2/3} \quad (3-44)$$

where  $W_{dew}$  is the actual amount of dew on the leave surfaces and  $W_{dew,max}$  is the maximum possible value ( $0.2 \text{ kg} \cdot \text{m}^{-2}$ )

### 3.3.6.2. Leaf energy balance

By neglecting the internal energy storage inside a leaf the foliage temperature  $T_f$  can be obtained from the steady-state leaf energy balance energy balance equation (Bruse 2004):

$$0 = R_{sw,net}(z) + R_{lw,net}(z) - (c_p \cdot \rho \cdot J_{f,h}) - \rho \cdot L \cdot (J_{f,evap} + J_{f,tran}) \quad (3-45)$$

where  $c_p$  is the specific heat of the air and  $\rho$  the air density,  $L$  is the latent heat of vaporization. The terms  $J_{f,evap}$ , and  $J_{f,tran}$  are evaporation flux of liquid water on the leaves and transpiration flux controlled by the leaf stoma, calculated through equations (3-40) and (3-41), respectively.

$R_{sw,net}$  the net shortwave radiation absorbed by the leaf surface, is calculated through:

$$R_{sw,net}(z) = (F \cdot R_{sw,dir}(z) + R_{sw,dif}(z)) \cdot (1 - a_f - t_{rf}) \quad (3-46)$$



here,  $F$  is a non-dimensional parameter describing the orientation of the leaves towards the sun (0.5 for randomly orientated leaves),  $a_f$  is the albedo of the foliage and  $t_{rf}$  is a transmission factor (by default, 0.3).

The longwave radiation contribution in equation (3-45) is calculated using the following equation:

$$R_{lw,net}(z, T_f) = (\varepsilon_f \cdot R_{lw}^{\downarrow}(z)) + R_{lw}^{\leftrightarrow}(z) + (\varepsilon_f \cdot R_{lw}^{\uparrow}(z)) - (2\varepsilon_f \cdot \sigma_B \cdot T_f^4) - ((1 - \sigma_{svf}(z)) \cdot \sigma_B \cdot T_f) \quad (3-47)$$

The source/sink terms for the atmospheric model, used in equations (3-17) and (3-18), can finally be computed using equations (3-39) to (3-41) with  $T_f$  obtained by solving (3-45):

$$Q_h(z) = LAD(z) \cdot J_{f,h} \quad (3-48)$$

$$Q_q(z) = LAD(z) \cdot (J_{f,evapo} + J_{f,trans}) \quad (3-49)$$

where LAD is the leaf area density in height  $z$ . The equations assume that only one side of the leaf is participating in the exchange processes of the heat and the vapor (the luff side) and absorbs the shortwave radiation, whereas in the long wave radiation spectra, both sides of the leaf take part in the radiative exchange process.

To have more realistic simulation model the water balance of the plant/soil system must be taken into account. The transpired water by the plant is taken from the soil via its roots that results a decrease in the soil water content leading in turn to an increase in the stomatal resistance and the transpiration decrease.

The total mass of the transpired water ( $m_{trans}$ ) by the plant is given by the vertical integral over the transpiration fluxes in the different plant layers:

$$m_{trans} = \rho \times \int_0^{z_p} LAD(z) \times J_{f,trans}(z) \times dz \quad (3-50)$$

The amount of the taken water from the different soil layers inside the root zone of the plant depends on the amount of the roots in the layer ( $RAD(z)$  value) and the hydraulic diffusivity of the soil layer ( $D\eta(z)$ ):

$$S_{\eta}(-z) = \left( \frac{m_{trans}}{\rho_w} \right) \times (RAD(-z) \times D_{\eta}(-z)) \times \left( \int_{-z_r}^0 RAD(-z) \times D_{\eta}(-z) \times dz \right)^{-1} \quad (3-51)$$

### 3.3.7. Ground surface model

Ground surface temperature  $T_0$  can be computed via solving energy balance equation at the ground surface (Huttner 2012).

$$R_{sw.net} + R_{lw.net}(T_0) - G(T_0) - H(T_0) - LE(T_0, q_0) = 0 \quad (3-52)$$

where  $R_{sw.net}$  is the net short wave radiation and  $R_{lw.net}$  is the net longwave radiation at the ground surface.  $G, H$  and  $LE$  are the soil sensible and latent turbulent heat flux, respectively. Here  $R_{sw.net}$  is calculated as follow:

$$R_{sw.net} = [\cos \beta^* \cdot R_{sw.dir}(z=0) + R_{sw.dif}(z=0)] \cdot (1 - a_s) \quad (3-53)$$

Where  $\beta^*$  is the angle between the direct solar radiation and the surface exposition. The term  $a_s$  is the soil albedo, a constant value for the impermeable surfaces and a function of the sun angle and the soil water content for other types. The net long wave radiation at ground surface is divided into two parts:

$$R_{lw.net}(T_0) = (\sigma_{SVF} \cdot R_{lw.net}^{sky}(T_0)) + (1 - \sigma_{SVF}) \cdot R_{lw.net}^{screened}(T_0) \quad (3-54)$$

Where  $R_{lw.net}^{sky}$  is the part of the sky with unobstructed view and  $R_{lw.net}^{screened}$  is the part blocked by the buildings and the vegetation.

$$R_{lw.net}^{sky}(T_0) = \sigma_{lw}^\downarrow(0, z_p) \cdot (R_{lw}^{\downarrow,0} - \varepsilon_s \sigma_B T_0^4) + \left[ (1 - \sigma_{lw}^\downarrow(0, z_p)) \cdot \left( \frac{\varepsilon_v \varepsilon_s}{\varepsilon_v + \varepsilon_s - \varepsilon_v \varepsilon_s} \right) \cdot (\sigma_B \bar{T}_f^4 - \sigma_B \bar{T}_0^4) \right] \quad (3-55)$$

$$R_{lw.net}^{screened}(T_0) = \left( \frac{\varepsilon_w \varepsilon_s}{\varepsilon_w + \varepsilon_s - \varepsilon_w \varepsilon_s} \right) \cdot (\max(\sigma_B \bar{T}_w^4, \sigma_B \bar{T}_0^4) - \sigma_B \bar{T}_0^4) \quad (3-56)$$

where  $\varepsilon_s$ ,  $\varepsilon_v$ , and  $\varepsilon_w$  are the emissivity of the soil, the vegetation and the walls respectively,  $T_f$  and  $T_w$  are the surface temperature of the vegetation and the walls respectively.

The turbulent heat fluxes  $H$  and  $LE$  are a function of the calculated turbulent exchange coefficients,  $K_h^0$  and  $K_q^0$ , the temperature and the humidity of the ground surface, as described below:

$$H(T_0) = \rho \cdot c_p \cdot \left[ -K_h^0 \frac{\partial T}{\partial z} \Big|_{z=0} \right] = \rho \cdot c_p \cdot \left[ K_h^0 \left( \frac{T_0 - \theta_{k=1}}{0.5 \Delta z_{k=1}} \right) \right] \quad (3-57)$$

$$LE(T_0, q_0) = \rho \cdot L(T_0) \cdot \left[ -K_q^0 \frac{\partial q}{\partial z} \right] = \rho \cdot L(T_0) \cdot \left[ K_q^0 \left( \frac{q_0 - q_{k=1}}{0.5 \Delta z_{k=1}} \right) \right] \quad (3-58)$$

With

$$L(T_0) = (5.501 - 0.00237 (T_0 - 273.15)) \cdot 10^6 \quad (3-59)$$

and the soil heat flux G can be described as:

$$G(T_0) = -\lambda_s \frac{\partial T}{\partial z} = \lambda_s (k = -1) \cdot \left( \frac{T_0 - T_{k=-1}}{0.5 \Delta z_{k=-1}} \right) \quad (3-60)$$

where q is the specific humidity (q<sub>0</sub> at the surface), λ<sub>s</sub> is the soil heat conductivity, k = ± 1 corresponds to the first grid point over or under the ground surface, K<sub>h</sub><sup>0</sup> and K<sub>q</sub><sup>0</sup> are the exchange coefficient for heat and vapor between air and surface, calculated with respect to thermal stratification (Asaeda and Ca 1993).

### 3.3.8. Building surface

Up to version 4.0 by ENVI-met simulation code the buildings surface temperature was calculated based on a simple steady-state energy balance. Involved parameters were general thermal properties of materials (i.e. albedo, emissivity and U-value) as well as sensible heat transfer between the atmosphere and the facade and the heat conduction through the wall material. Since software could not assign an individual value for every single wall/roof, therefore an average value for the whole model was taken into account.

The steady-state energy balance on a building surface can be expressed by (Huttner 2012):

$$R_{sw.net}^{abs} + R_{lw.net}^{abs} - (\varepsilon_f \cdot \sigma_B \cdot T_w^4) - \left( c_p \cdot \rho_w \cdot K_h^w \frac{T_w - T_{w+1}}{D_x} \right) - \left( \frac{\lambda_w \cdot (T_w - T_{w,i})}{d} \right) = 0 \quad (3-61)$$

where  $R_{sw.net}^{abs}$  and  $R_{lw.net}^{abs}$  are absorbed shortwave and longwave radiation, respectively, ε<sub>f</sub> is the emissivity of the facade, σ<sub>B</sub> the Stefan-Boltzman constant, T<sub>w</sub> the wall temperature, c<sub>p</sub> the specific heat capacity of the air at the constant pressure [1200 J.kg<sup>-1</sup>.K<sup>-1</sup>], ρ<sub>w</sub> the density of the wall, K<sub>h</sub><sup>w</sup> [m<sup>2</sup>.s<sup>-1</sup>] refers to the air thermal diffusivity at the surface of the wall/roof, T<sub>w+1</sub> the air temperature at the grid cell next to the wall, D<sub>x</sub> the distance between the façade and the center of the next grid cell, λ<sub>w</sub> the thermal conductivity of the wall and T<sub>w,i</sub> the temperature of the inner surface of the wall and d describes the wall thickness.

As it is seen in the energy balance equation, heat storage within the building mass is neglected. Therefore absorbed shortwave radiation for the walls is set to the half of its actual value to achieve to the more realistic result. The absorbed long wave radiation for walls estimated by:

$$R_{lw.net}^{abs} = \varepsilon_f \cdot \left( (1 - \sigma_{SVF}) \cdot \left( \frac{1}{3} R_{lw,ground} + \frac{2}{3} R_{lw,buildings} \right) + \sigma_{SVF} \cdot \left( \frac{1}{2} R_{lw,sky} + \frac{1}{2} R_{lw,ground} \right) \right) \quad (3-62)$$

and for the roofs by:

$$R_{lw.net}^{abs} = \varepsilon_f \left( (1 - \sigma_{SVF}) \cdot R_{lw,buildings} + \sigma_{SVF} \cdot R_{lw,sky} \right) \quad (3-63)$$

Where  $R_{lw,ground}$ ,  $R_{lw,buildings}$ , and  $R_{lw,sky}$  are the long wave radiation emitted from the ground, building and coming from the sky respectively. The mean value of ground/walls temperatures within the domain were taken for calculation of the long wave emitted from the ground and buildings surfaces.

In version 4.0, to solve the problem of neglecting the heat capacity of the walls in calculation of the surface temperature, a new approach based on the multiple-node transient state model is taken. This model uses infinite numbers of nodes in calculation of the wall/roof temperature but for current version 7-nodes are used. Involved physical properties of the walls in this method are: transmission, emissivity, reflectivity, absorption, heat transfer coefficient, thermal conductivity specific heat capacity and the thickness of the wall.

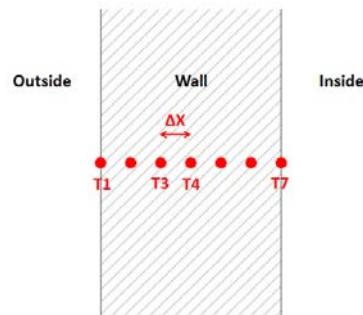


Figure 3-48: Schematic of the 7-node model

The energy balance for outer node can be expressed as:

$$R_{sw.net}^{abs} + R_{lw.net}^{abs} - (\varepsilon \cdot \sigma \cdot T_1^{*4}) + (h_{c,0} \cdot (T_{air} - T_1^*)) + \left( \frac{\lambda \cdot (T_2^* - T_1^*)}{\Delta x} \right) = \left( \frac{c_{wall} \cdot \rho_w \cdot \Delta x \cdot (T_1^* - T_1)}{2\Delta t} \right) \quad (3-64)$$

Where  $h_{c,0}$  is the heat transfer coefficient for the outside wall ( $\text{W}\cdot\text{m}^{-2}\cdot\text{K}^{-1}$ ),  $\lambda$  the thermal conductivity [ $\text{W}\cdot\text{m}^{-1}\cdot\text{K}^{-1}$ ],  $\Delta x$  the distance between two nodes,  $C_{\text{wall}}$  heat capacity of the wall,  $T_n$  the temperature at the node  $n$  at present or future time step  $T_n^*$ .

And  $h_{c,0}$  is calculated based on German DIN6446 [DIN 2005] as ( $h_{c,0}=4+4v$ ). The term  $v$  is the wind speed in front of the wall/roof [ $\text{m}\cdot\text{s}^{-1}$ ]. According to Fourier Equation:

$$\frac{\partial T}{\partial t} = \left( \frac{\lambda}{C_{\text{wall}} \cdot \rho} \right) \frac{\partial^2 T}{\partial x^2} \quad (3-65)$$

The energy flux at the middle node ( $T_n$ ) can be described as:

$$(P+2) \cdot T_n^* - T_{n+1}^* = P \cdot T_n + T_{n-1}^* \quad (3-66)$$

Where  $P = \left( \frac{\Delta x^2 \cdot C_{\text{wall}} \cdot \rho}{\lambda \cdot \Delta t} \right)$ . The energy balance for inner node sums up to:

$$-T_6^* + \left( \frac{P}{2} + \frac{h_c \cdot \Delta x}{\lambda} + 1 \right) \cdot T_7^* = \left( \frac{P}{2} \right) \cdot T_7 + \left( \frac{h_{c,i} \cdot \Delta x}{\lambda} \right) \cdot T_i \quad (3-67)$$

Where  $T_i$  is the inside temperature and  $h_{c,i}=7.7 \text{ W}\cdot\text{m}^{-2}\cdot\text{K}^{-1}$  is the heat transfer coefficient at the inside. Heat flux parallel to the surfaces is neglected.

### 3.3.9. Forcing

In contemplation of obtaining accurate results from simulation a specific meteorological development, it is necessary to use “forcing” for computing the interested variables at inflow boundaries (Huttner 2012). To achieve this goal the lateral boundary conditions type (LBC) shall be set to forced/closed. In this approach the values of the one dimensional model are copied to the grid cells at the inflow boundary of the model. Forcing allows the user to define a 1D profile every hour of the simulation time. By the used simulation software only the air temperature and the air relative humidity in one hour intervals for a 24 hour cycle or just minimum and maximum values and their respective times can be forced. A linear interpolation between time steps is used to calculate the 1D profile for the times in between (Huttner 2012).

$$\phi_t = \phi_{t_1} + (\phi_{t_2} - \phi_{t_1}) \cdot ((t - t_1) / (t_2 - t_1)) \quad (3-68)$$

Where  $t$  is the current simulation time,  $t_1$  and  $t_2$  are the previous/next time step for which the data is provided, and the term  $\phi$  is the variable at the respective time.

The height of the given data is assumed to be 2 m. A simple linear interpolation is used to develop the 1D-profile vertically (from the ground level up to 2500 m above the ground).

### 3.3.10. Required Input Data

The ability of a simulation software (a CFD code) in generating reliable results which can match the measured data in an optimized way at the same time, strongly depends on the accurate definition of the associated initial/boundary conditions, pertaining to an urban model area.

By mean of using ENVI-met, there are two possible modes to simulate a micro-climatic model, i.e. “none-forcing” and “forcing” (available from version 4.0) modes. For the “none-forcing” mode following minimum/basic inputs associated with initial/boundary conditions have to be provided:

- geographical position and time (solar radiation)
- $u_{10m}$ : horizontal wind speed in 10 m above ground
- wind direction
- $z_0$ : roughness length
- $T_{start}$ : initial air temperature
- $q$ : specific humidity at the top of the model (H=2500 m)
- $\phi_{2m}$ : relative humidity in 2 m above ground

In order to perform the simulation model via “forcing” mode, as basic inputs, instead of initial air temperature, specific humidity at the top of the model and relative humidity in 2 m above ground, hourly based air temperature and air relative humidity in 2 m above ground, shall be provided hourly based for a time span of 24 h.

In addition to above mentioned properties/conditions, which have to be provided as minimum inputs to the simulation software, there are also some more input parameters which can be adjusted to achieve a well-adapted software for a specific modeling. (default values are provided by ENVI-met). For more detailed explanations in this regards reference is made to appendix A.

To achieve a better software adaptation to match the simulation requirements, defined within the context of this work, the following input parameters in the ENVI-met software have been adjusted as follows:

- “Solar adjustment” value was set 0.82.
- “time step” was set to 1 s
- “The albedo of walls and roofs” for the runs performed by using version 3.1 was set to 0.4

By the rest of the input parameters default values, provided by the software, were used.

### **3.3.11. Shortcomings of ENVI-met**

ENVI-met is still considered as underdevelopment software, accordingly there are short-comings pertaining to its performance, some of which are mentioned below (Huttner 2012):

#### Atmosphere model:

- One of the characteristics of the standard k- $\epsilon$  (also named E- $\epsilon$ ) closure, used in ENVI-met, is over-prediction of the production of the turbulence, where anisotropic behavior of the turbulence dominates, such as flow around the obstacles. This behavior can be seen in ENVI-met too.
- ENVI-met is not able to simulate the precipitation and the temperature below freezing point.

#### Radiation model:

Results of the radiation model are not calculated accurately since:

- The scattering of the upward and the downward diffuse radiation is considered to be isotropic
- The effect of the plants is not considered in the calculation of diffuse shortwave radiation, neither the absorbed nor the created by plants.
- The emitted longwave radiation by the buildings and the plants are calculated based on the average temperature of surfaces within the model. Therefore the longwave radiation budget in the spaces with colder surfaces such as small inner courtyards is over-estimated.

#### Soil model:

- ENVI-met is not able to simulate the irrigation of the soil/plants.

#### Wall and roof model:

- For calculation of surface temperature, heat storage of walls and roofs is not taken into account. This leads to the release of energy from the building surfaces to the atmosphere during the night cannot be simulated.

## 4. Empirical Inquiry Results

### 4.1. Overview

As mentioned in chapter three, 13 measuring locations grouped into 4 categories and 13 subcategories were chosen as measuring spots. Air temperature and relative humidity, solar radiation, wind speed and CO<sub>2</sub> concentration level were measured in these measuring spots during different times of the day. Since there was only one mobile weather station and collecting the data simultaneously at all locations was impossible so BPI weather station was defined as the reference weather station and all the measuring spots were compared with this reference point; in order to be able to set a basis for comparing all these measuring spots with each other. To achieve this goal, for  $\Delta$ -variables were defined as follow:

$$\Delta T_a = T_{mobile} - T_{BPI} \quad [K] \quad (4-1)$$

$$\Delta \varphi = \varphi_{mobile} - \varphi_{BPI} \quad [\%] \quad (4-2)$$

$$\Delta v = v_{mobile} - v_{BPI} \quad [m \cdot s^{-1}] \quad (4-3)$$

$$\Delta K_{rel} = \left( \frac{K_{mobile} - K_{BPI}}{K_{BPI}} \right) \times 100 \quad [\%] \quad (4-4)$$

where  $\Delta T_a$ ,  $\Delta \varphi$  and  $\Delta v$  are the air temperature, the air relative humidity and the wind speed difference, respectively.  $T_{mobile}$  and  $T_{BPI}$  are the air temperature measured by the mobile weather station and the BPI,  $\varphi_{mobile}$  and  $\varphi_{BPI}$  the measured relative humidity by the mobile weather station and the BPI. The term  $\Delta K_{rel}$ , is the relative deviation of the solar radiation and  $K_{mobile}$  and  $K_{BPI}$  are the solar radiation monitored by the mobile weather station and the BPI, respectively.

Since the air relative humidity is a function of the air temperature, to analyze the water vapor concentration in the interested areas, the absolute humidity was calculated for every data point, by the following equations (Alduchov and Eskridge 1997):

$$p_{vs} = 611.2 \times \exp\left(\frac{17.502 \times T}{240.97 + T}\right) [Pa] \quad (4-5)$$



$$p_v = \left( \frac{\varphi \cdot p_{vs}}{100} \right) \text{ [Pa]} \quad (4-6)$$

$$AH = \left( \frac{p_v}{R \cdot (273.15 + T)} \right) \text{ [kg.m}^{-3}\text{]} \quad (4-7)$$

where  $p_{vs}$  is the saturation vapor pressure,  $T$  the air temperature in °C,  $p_v$  the water vapor partial pressure in the air,  $AH$  the absolute humidity and  $R=461.52 \text{ [J.kg}^{-1} \cdot \text{K}^{-1}\text{]}$  is the individual gas constant of the water.

## 4.2. Short measurements

In order to collect data as mentioned in previous chapter (3.2.3) two types of measurements were conducted, i.e. short measurements and long measurements. In terms of short measurements every measuring spot was measured about 10 minutes from 11:00 h to 18:00 h. Analyses associated with the collected data through short measurements are discussed all through this section. And all discussions related to the long measurements results are given in section 4.4.

### 4.2.1. Reference day analysis

Urban micro-climate is influenced by time due to the daily variation of the sun position in the sky. Therefore grouping the measured data, according to their measuring time can lead to a better understanding of their daily fluctuation and trend. Hence, a virtual day, hereafter named as the reference day, was defined. To form this concept, the mean value of the collected data at every hour, from 11:00 h to 18:00 h during a defined period was calculated for all of the previously mentioned 13 measuring spots as well as for the BPI. Due to seasonal variation of some effective factors on urban micro-climate such as length of the days and LAD of the trees, the time span of the used data to calculate the reference day cannot exceed a season. Thus, for this study only the data collected, during June to September, was used, and the rest was ignored due to the insufficient number of collected data points for other seasons. In figure 4-1 the temperature difference between the mobile and the reference weather station (BPI) during the calculated reference day for summer at all measuring spots for a time interval of 11:00 h to 18:00 h is shown.

As it can be seen in figure 4-1, higher temperatures were observed at around 14:00 h. E-W street (S1) shows the lowest values, which do not change much during the day. This may be due to the fact that this measuring location is shaded most of the day. Courtyards display tendentially lower values. At the spot C1 however an increase in temperature in the time period 14:00 h to 15:00 h was observed. It is a

small courtyard surrounded by relatively high buildings, without vegetation or pervious surfaces, direct solar radiation warm up the surfaces rapidly and consequently the ambient temperature rises. In the absence of direct solar radiation due to the high emissivity of used materials it cools down and returns to the previous condition. Parks show relatively high temperature values throughout the day. This might be due to the fact that although vegetation is present, SVF is very high at the measuring spots, on the other hand trees are considered as strong barrier against the air movement and accordingly avoid heat removal (less convective heat transfer) air from the area. In the category of plazas, the lowest temperatures were measured at location P1. This location has more vegetation and a significantly lower SVF, compared with the spots P2 and P3.

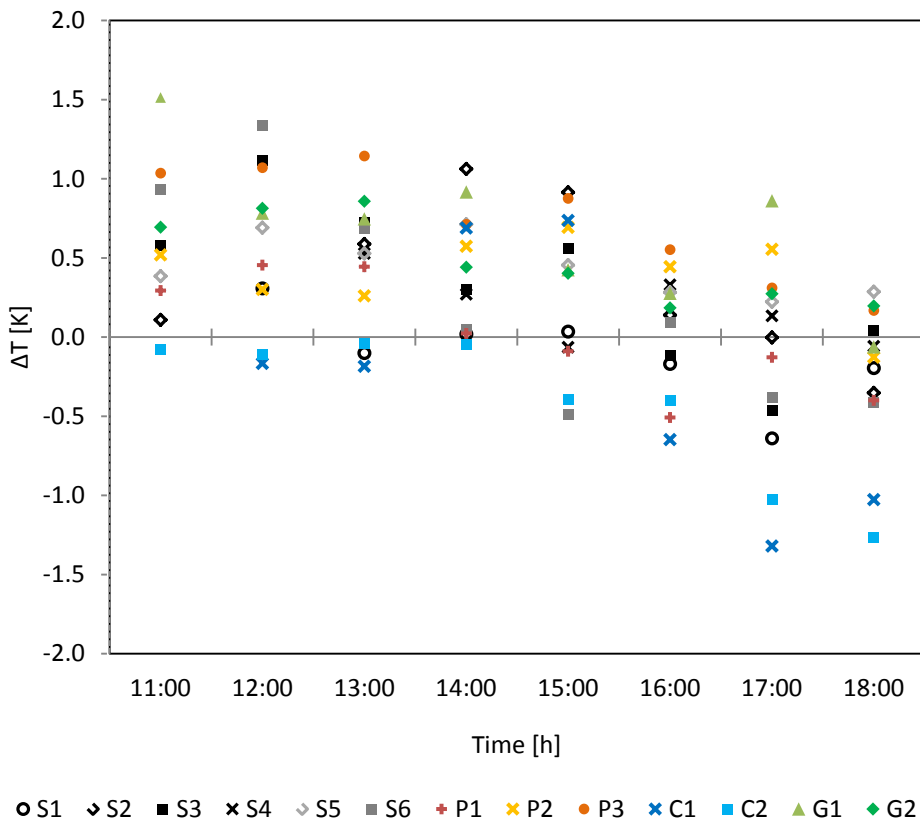


Figure 4-1: Temperature differences (MW – BPI) for a reference day (from 11:00 h to 18:00 h) at all 13 measuring spots

Figure 4-2 shows the relative solar radiation difference [%] during a reference day for all 13 measuring spots. Results of solar irradiance at the measurement locations appear to be consistent with the orientation of the streets or plazas. For example, at the spot S1 (located in E-W street) a small variance was observed, as it is mostly shaded. At S2 (located in a N-S oriented street) as expected, higher values were recorded around early afternoon, which can be traced back to the sun height and

the angle of incident solar spectrum in these hours. The NE-SW oriented S5 shows higher values in the afternoon, which is again consistent with increased solar exposure. The NW-SE oriented P3, on the other hand, shows the reverse tendency. The park locations G1 and G2 display high values, because of the associated high SVF values. Courtyards, on the other hand, show rather lower values, due to the lower SVF values.

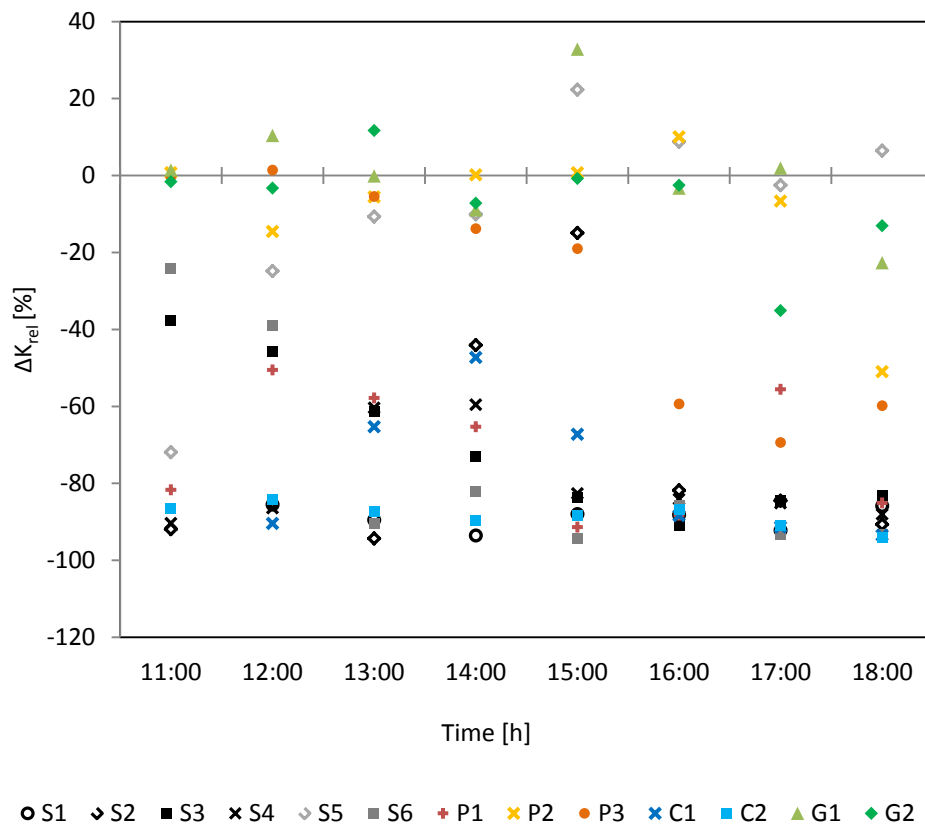


Figure 4-2: Relative solar radiation differences for a reference day (from 11:00 h to 18:00 h) for all 13 measuring spots

As discussed before, the observed  $\Delta T$  values are in logical correlation with the solar radiation during the day. Therefore the same daily trend for the wind velocity within the canyon may be expected due to the buoyancy force. Figure 4-3 illustrates a reference day for the wind speed difference [ $\text{m}\cdot\text{s}^{-1}$ ] for all 13 measuring spots. This figure shows a consistent reduction in the wind speed in different locations with the orientation and the vegetation (trees). S5 and S3 as NE-SW streets are windier than S6 and S3, they are similar in all properties except for orientation, (perpendicular streets). Meanwhile S5 is windier than its parallel street S3 which is flanked by the

trees. Likewise C2 compared to C1 and P2 and P3 compared to P1 display a low wind speed reduction due to the lack of trees.

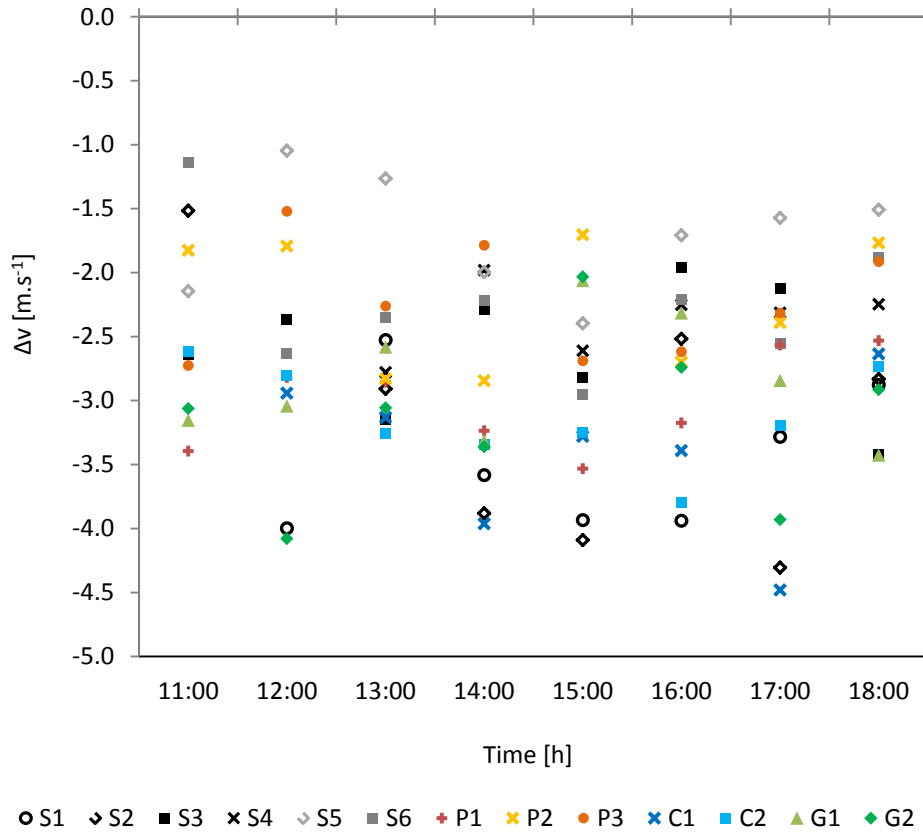


Figure 4-3: Wind speed differences for a reference day (from 11:00 h to 18:00 h) for all 13 measuring spots

The variation of absolute humidity differences between MW and BPI is investigated in figure 4-4. As it was expected green areas such as G1 and G2 contain more water vapor per air volume than other locations, while absolute humidity at P2 as a bare location with a water pool is not significantly higher than other locations. It is assumed that strong air volume movement due to higher air speed at P2 location causes more mixing with fresh air avoiding any increase in the absolute humidity. The aforementioned mechanism cannot be considered as valid at G2 location, where it is flanked by trees. So higher air humidity values were observed here.

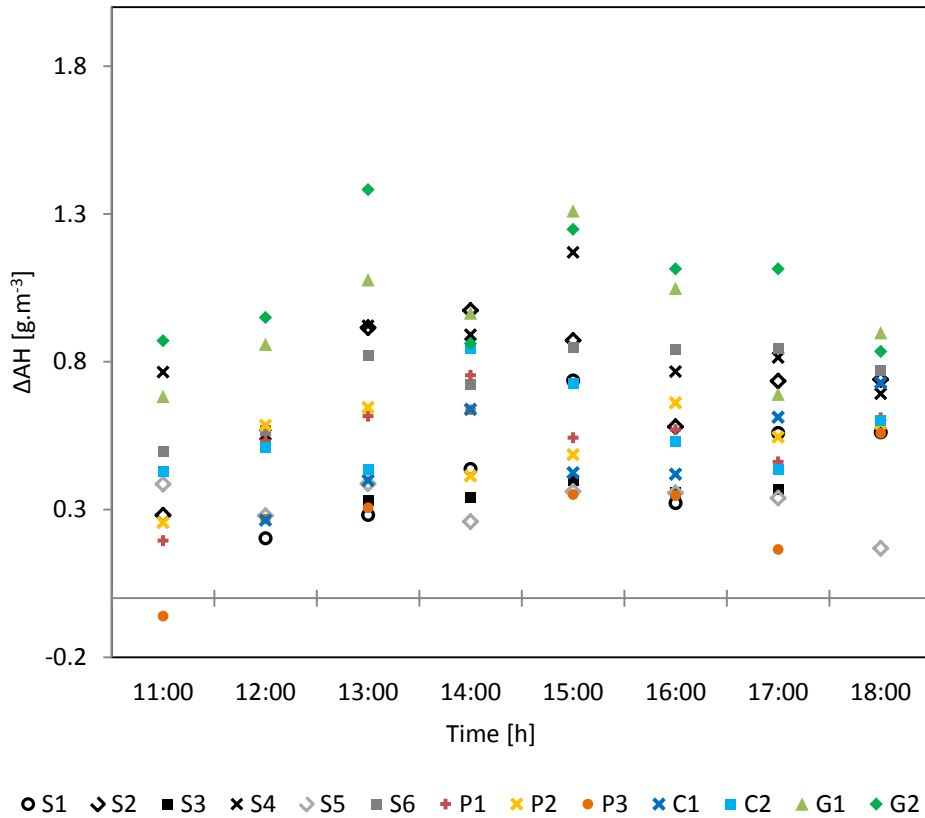


Figure 4-4: Water vapor concentration differences for a reference day (from 11:00 h to 18:00 h) for all 13 measuring spots

#### 4.2.2. Degree of dispersion for the measured data

In order to have an overview about the variation of urban-microclimatic parameters at measuring locations during the measuring period, all the data points for all 13 measuring spots were plotted using boxplots. These analysis help indicate the degree of dispersion/spread of data without making any assumptions of the underlying statistical distribution.

Figure 4-5 shows boxplots pertaining to temperature differences of MW and BPI for all 13 measuring locations (as per table 3-2). As expected, median temperatures of the MW are generally higher than the reference weather station, with 2 exceptions, namely C1 and C2, which are courtyards with low sky view factors. The temperatures at P2 and P3 (category plaza) show significantly higher values for the MW. P1 is also from the same category, but it has a lower SVF and more vegetation thereby its temperature pattern is different from P1 and P2 and is lower.

Figures 4-6 and 4-7 show relative differences for solar radiation [%] and wind speed [ $\text{m}\cdot\text{s}^{-1}$ ] respectively. The relative solar radiation difference in case of G1, G2, S5, P2, and P3 are rather similar, which is consistent with their relatively high SVF

(above 60%). The rest of the locations display a significantly higher relative solar radiation differences.

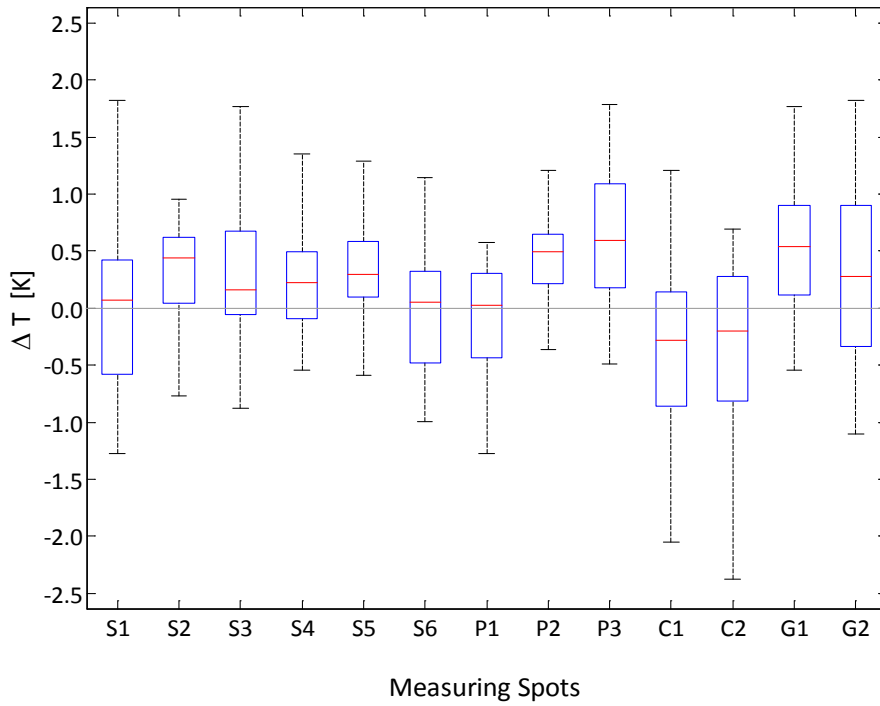


Figure 4-5: Dispersion of temperature differences (MW – BPI) for all 13 measuring spots

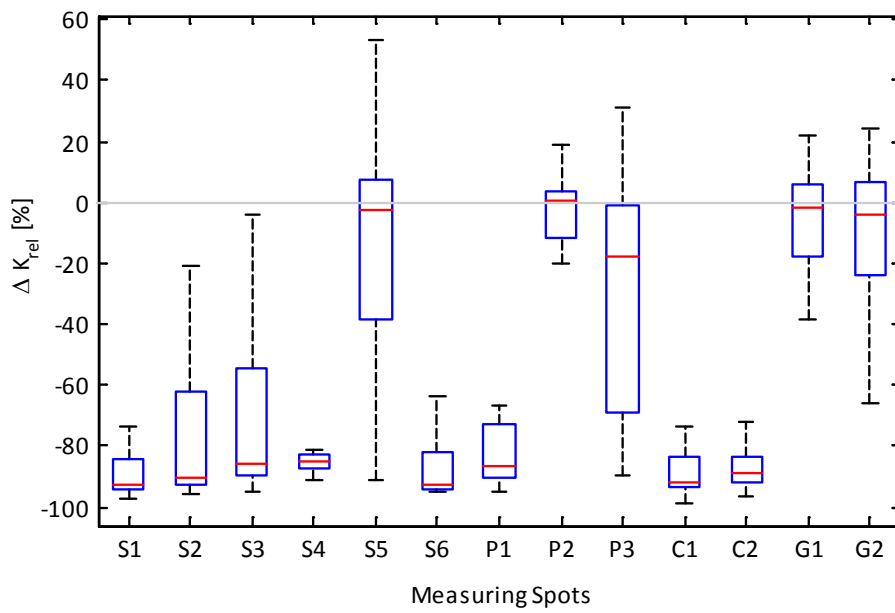


Figure 4-6: Dispersion of relative solar radiation difference (MW – BPI) for all 13 locations

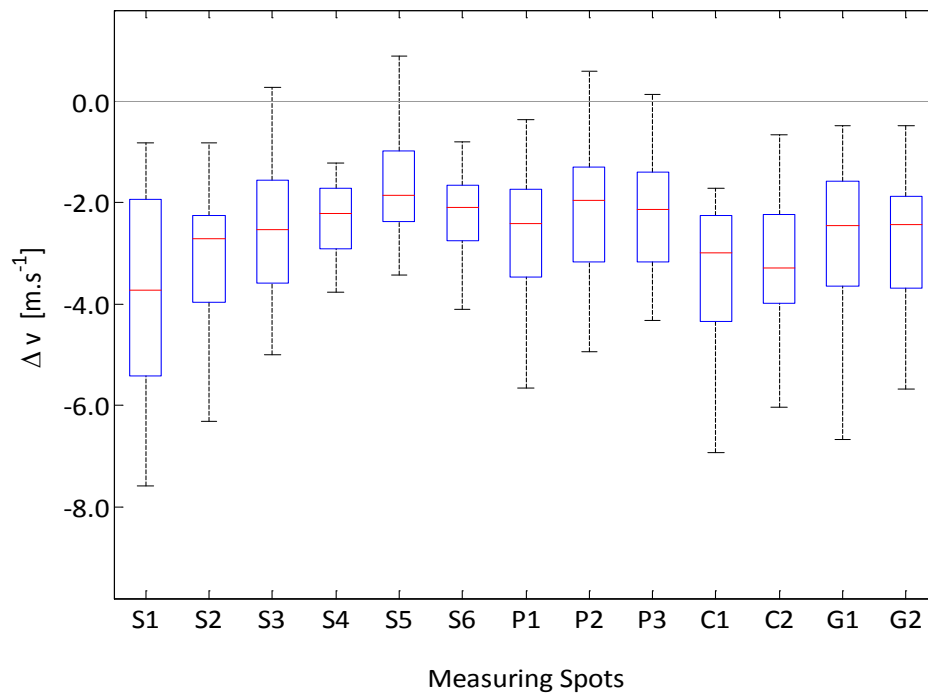


Figure 4-7: Dispersion of wind speed difference ( $MW - BPI$ ) for all 13 locations

Figure 4-8 shows the distribution of the water vapor concentration [ $\text{g}\cdot\text{m}^{-3}$ ]. Median values pertaining to the water vapor content are higher for G2 and G1, which have more vegetation (in case of G2 there is also a water body). The lowest values can be found for S1, S5 and P3, places with little or no vegetation and paved by impermeable materials. Locations with vegetation show more variation in humidity compared to their associated location in the same category without vegetation (P1 v.s. P2 and P3, C2 v.s. C1). It may be caused by irrigation and the variation of the soil humidity, which provides needed water for evapotranspiration through the leaves, as well as the variation of temperature that, can affect the amount of the evapotranspiration.

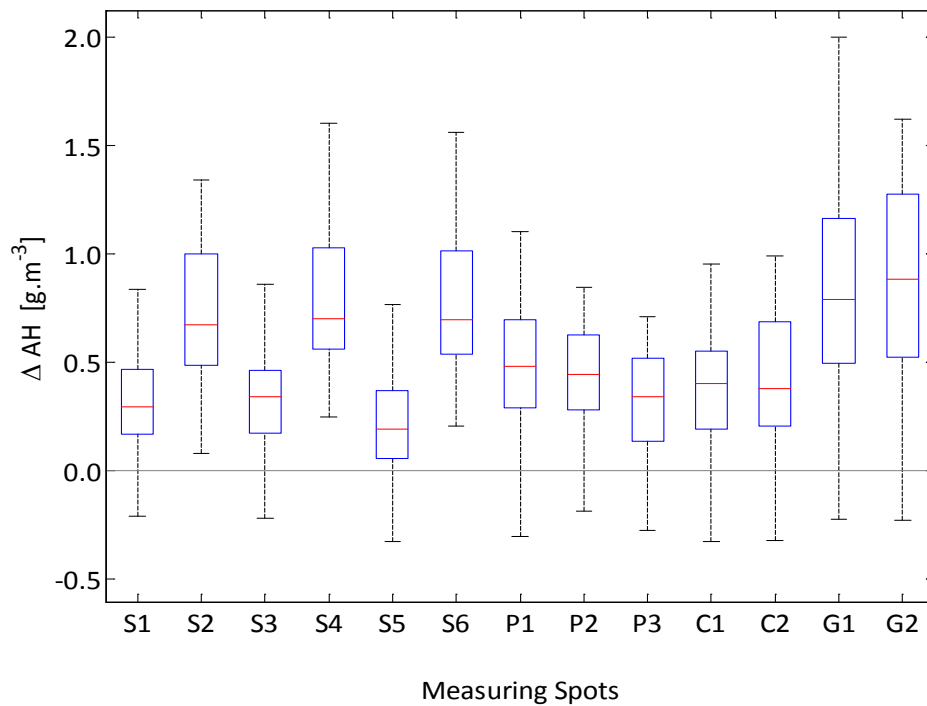


Figure 4-8: Dispersion of absolute humidity difference (MW – BPI) for all 13 locations

#### 4.2.3. Correlational studies

The results of previous analysis of the collected data showed, the air temperature at the measuring spots is consistent with incident solar radiation and accordingly SVF at that location. Hence, to evaluate this assumption correlation studies between these 3 parameters were performed.

Figure 4-9 shows the correlation between relative solar radiation and temperature differences (mean values), for all locations. Likewise, Figure 4-10 shows the correlation between sky view factor (SVF) and the temperature differences. Figure 4-11 shows the correlation between SVF and relative solar radiation differences (mean values) for the entire data set. In all cases, significant correlations ( $R^2$  between 0.59 and 0.79) are visible between the pertinent variables of the measurement locations (Figure 4-9 to 4-10).



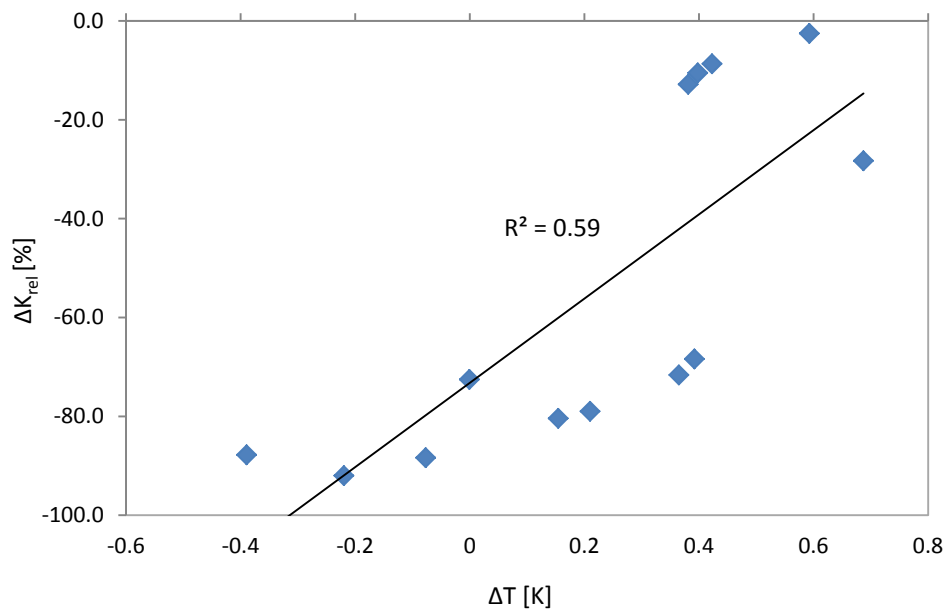


Figure 4-9: Relationship between relative solar radiation and temperature difference

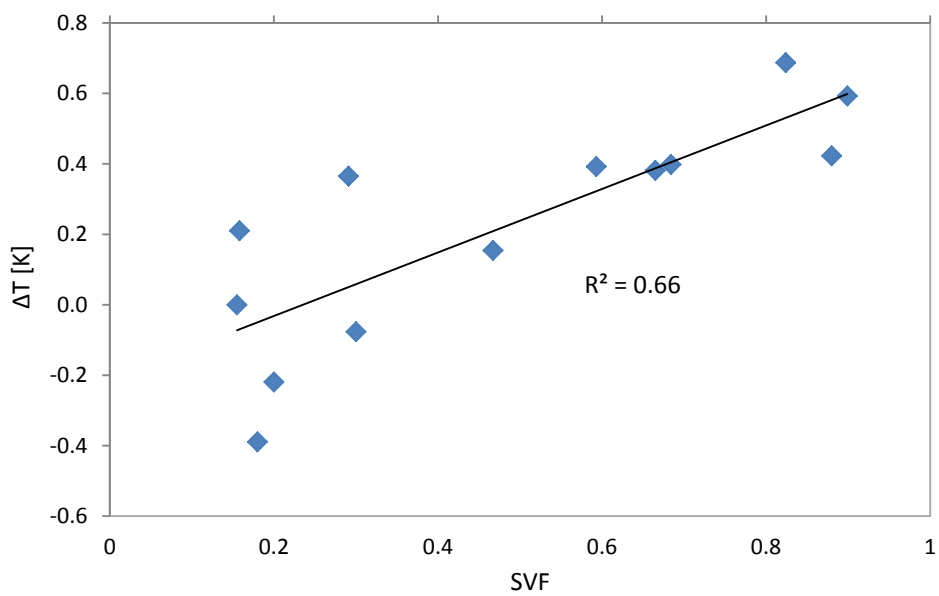


Figure 4-10: Relationship between temperature difference and SVF

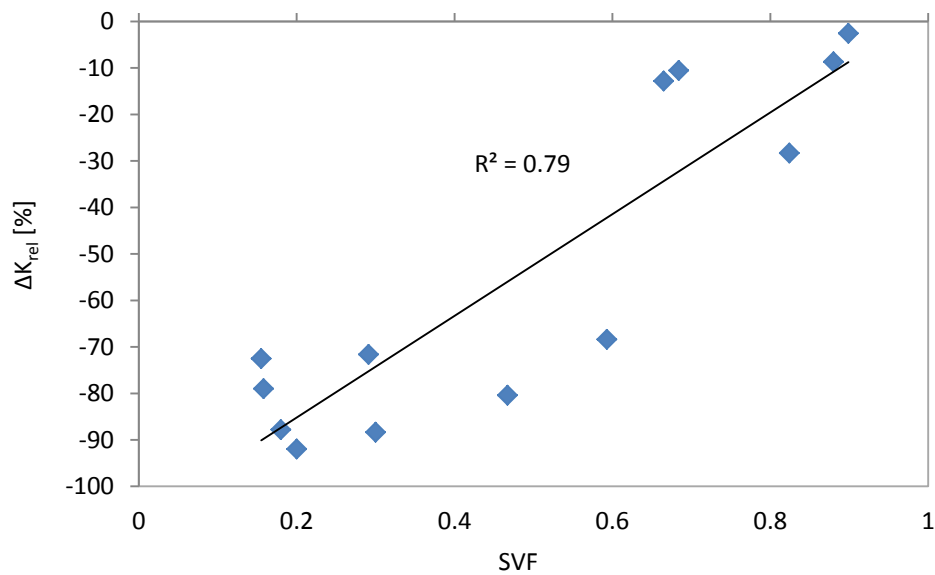


Figure 4-11: Relationship between relative solar radiation difference and SVF

#### 4.2.4. Regression Analysis

As it mentioned before, stationary weather stations are usually available at few points in the cities and mostly are mounted on top of the buildings above the urban canopy. Thus, studying the relation between the general weather condition, monitored by such fixed weather stations and urban micro-climate within the canopy layer can help modeling and predicting of the urban micro-climate based on the general weather data with lower resolution which is usually available for most of the cities. Regarding to this aim, regression analysis between the data obtained from BPI and all 13 measuring spots for the four measured parameters, i.e. air temperature and relative humidity, solar radiation and wind speed, was performed. The results and the associated graphs of analysis are illustrated below.

In figure 4-12 to 4-15 the collected air temperatures from measuring spots versus those obtained from the BPI are shown. Each measuring category is pertained in a separate figure. In all the cases there is a strong linear correlation ( $R^2 > 0.93$ ) between the collected data at the BPI and those obtained at the measuring spots.

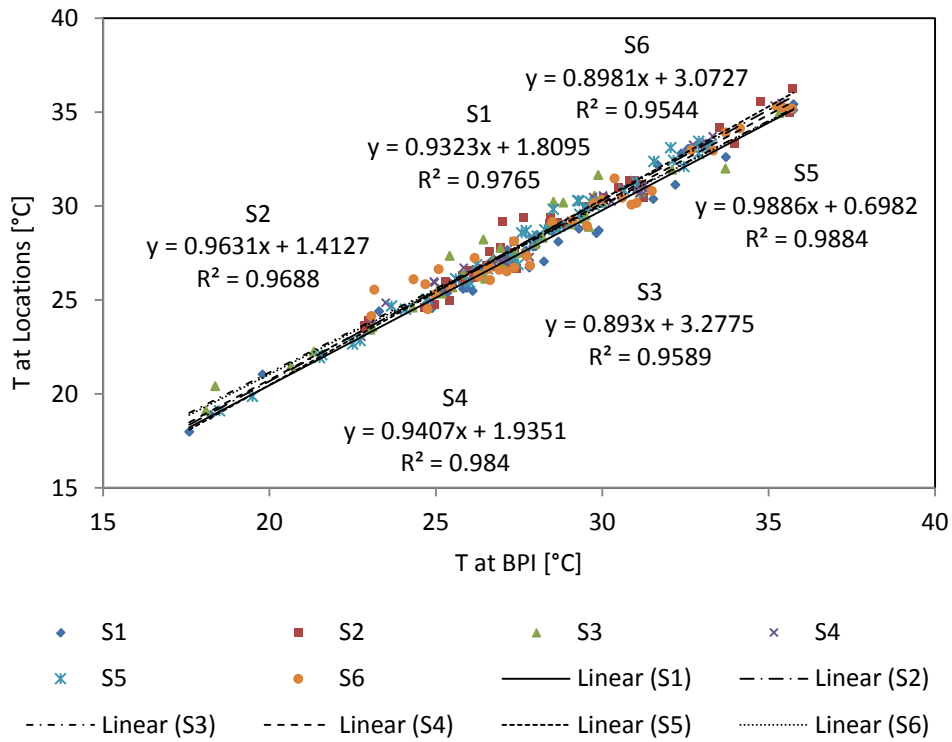


Figure 4-12: Measured air temperatures at the BPI and at the measuring spots (category: Street; S1, S2, S3, S4, S5 and S6)

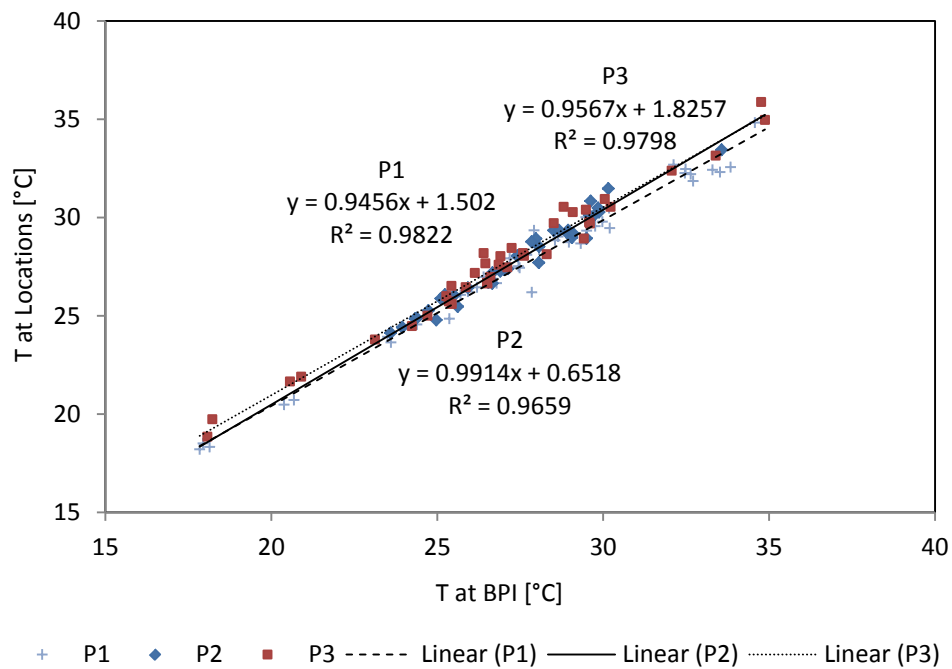


Figure 4-13: Measured air temperatures at the BPI and at the measuring spots (category: Plaza; P1, P2 and P3)

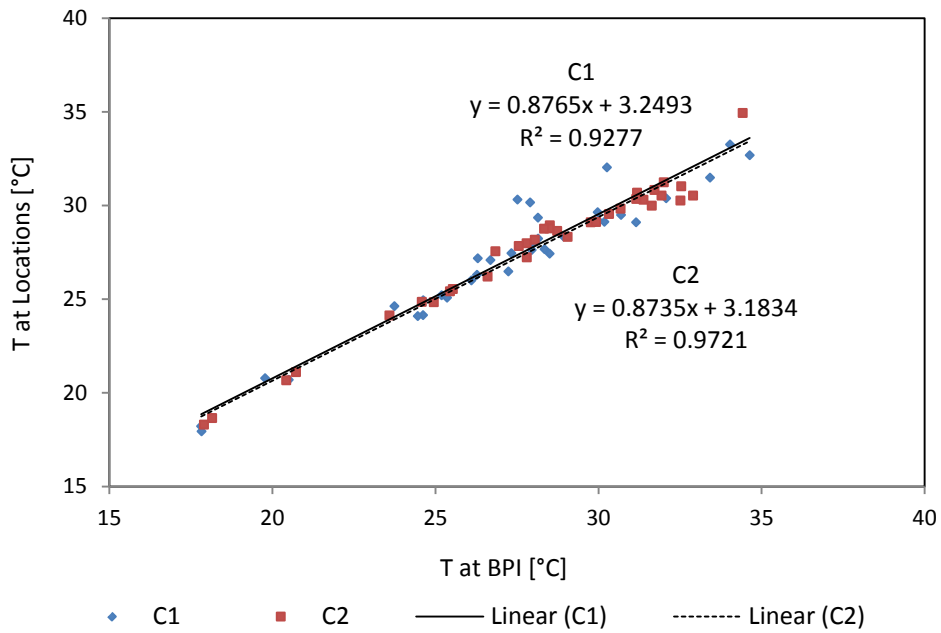


Figure 4-14: Measured air temperatures at the BPI and at the measuring spots (category: Courtyard; C1 and C2)

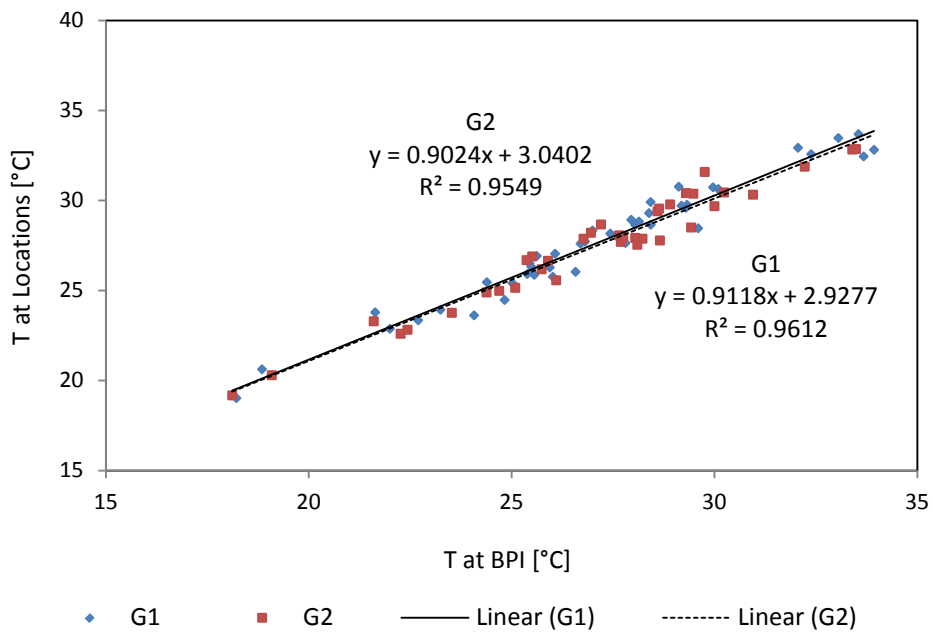


Figure 4-15: Measured air temperatures at the BPI and at the measuring spots (category: Park; G1 and G2)

Unlike the temperature, in the case of the solar radiation, figure 4-16 to 4-19 no logical correlation between the data sets can be observed. The reason could be that, the relationship between the incident radiation to the MW and BPI strongly depends

on the solar time (4.2.1) and the angel of incident spectrum. Thus regression analysis between them, regardless to the time, does not show significant correlation.

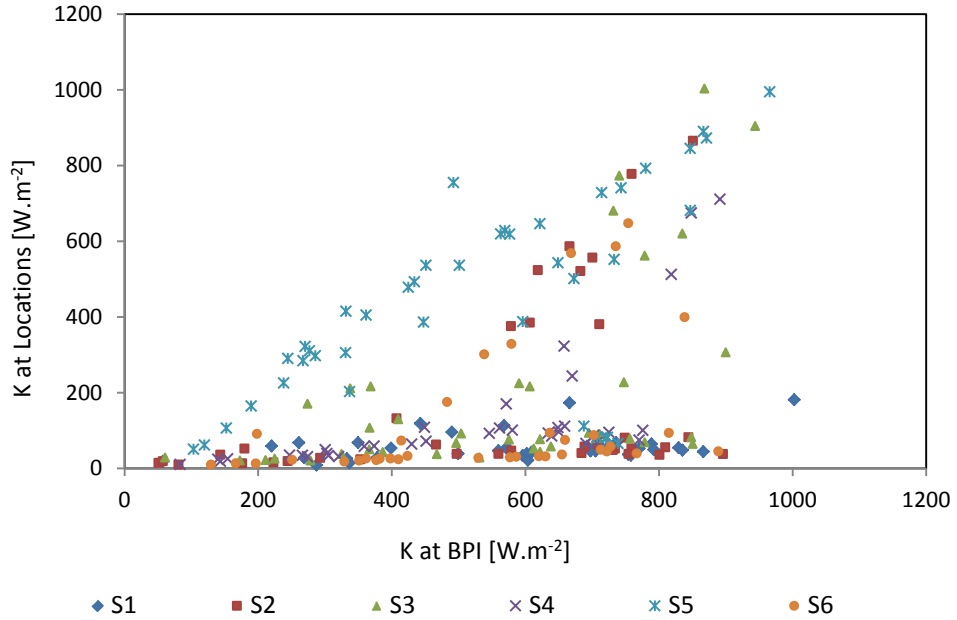


Figure 4-16: Measured solar radiation at the BPI and at the measuring spots (category: Street; S1, S2, S3, S4, S5 and S6)

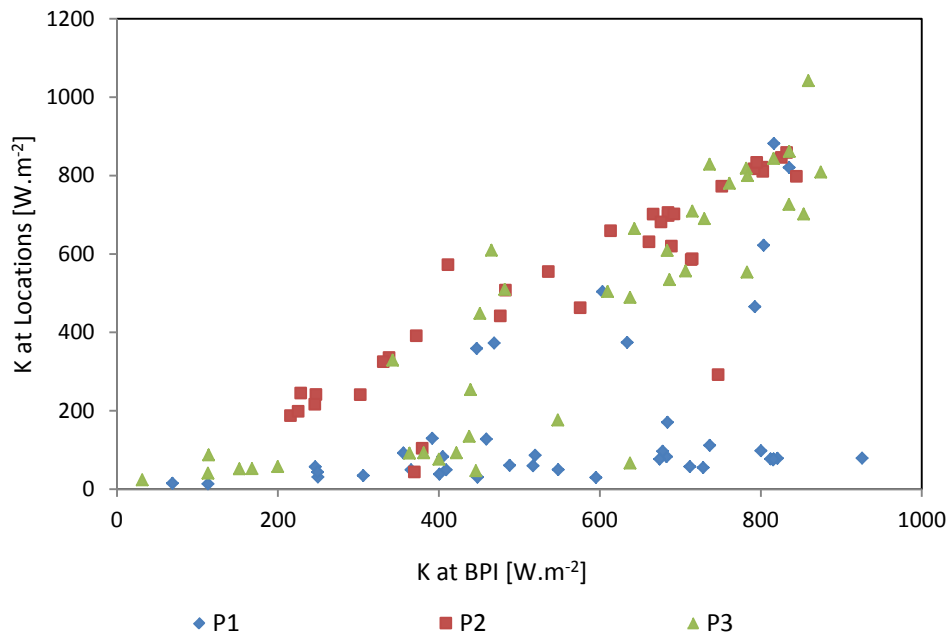


Figure 4-17: Measured solar radiation at the BPI and at the measuring spots (category: Plaza; P1, P2 and P3)

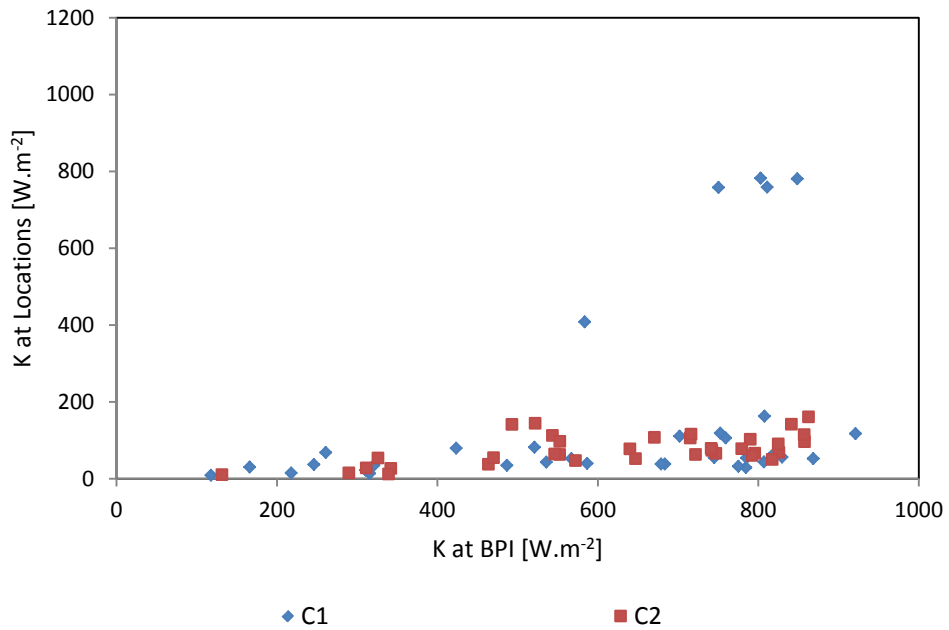


Figure 4-18: Measured solar radiation at the BPI and at the measuring spots (category: Courtyard C1 and C2)

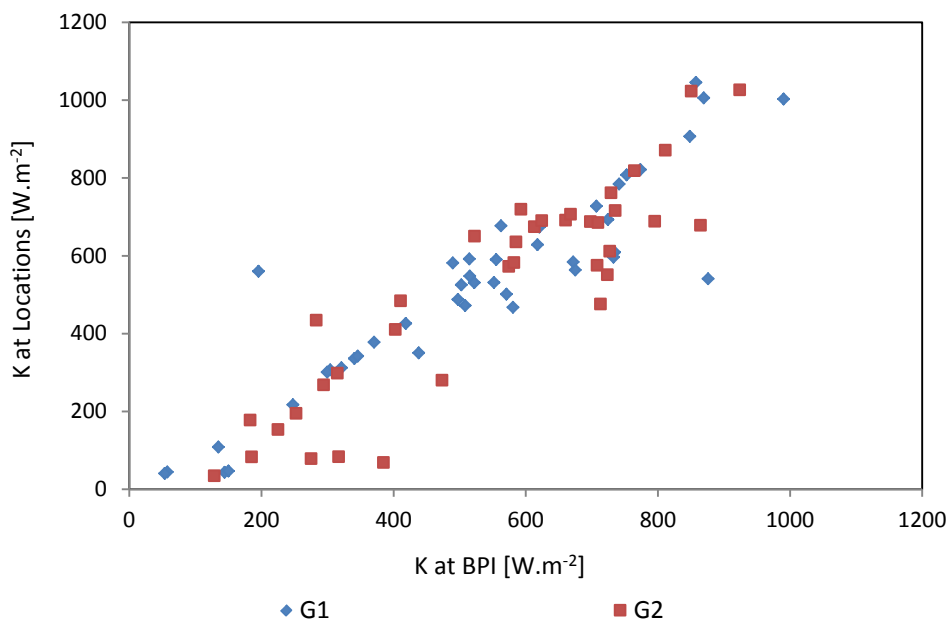


Figure 4-19: Measured solar radiation at the BPI and at the measuring spots (category: Park; G1 and G2)

The relationships between the wind speed at the measurement spots and BPI are depicted in the figures 4-20 to 4-4-23. No significant correlation between them can be observed.

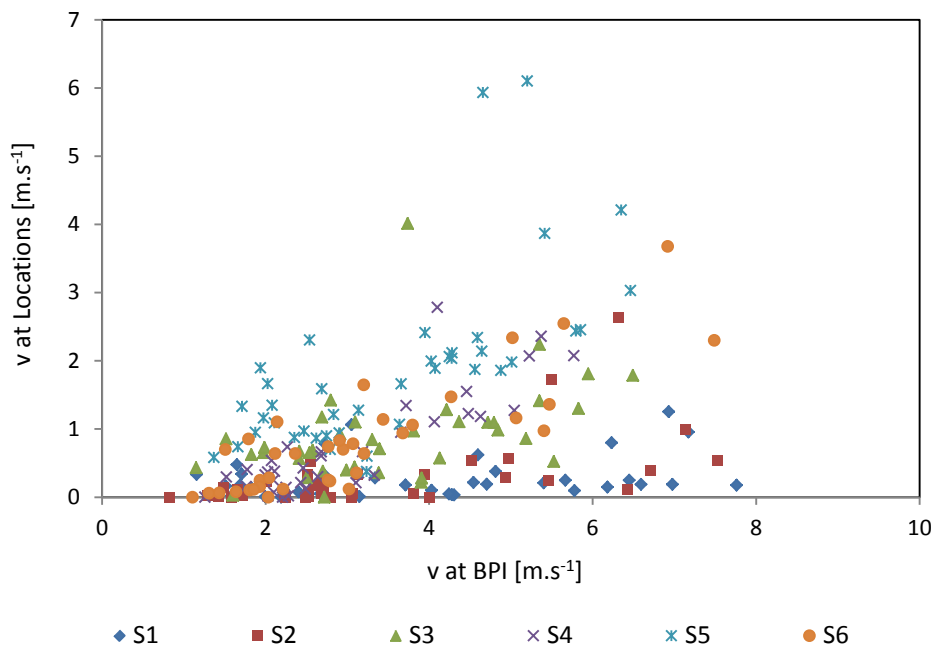


Figure 4-20: Relationship between wind speed at BPI and Streets

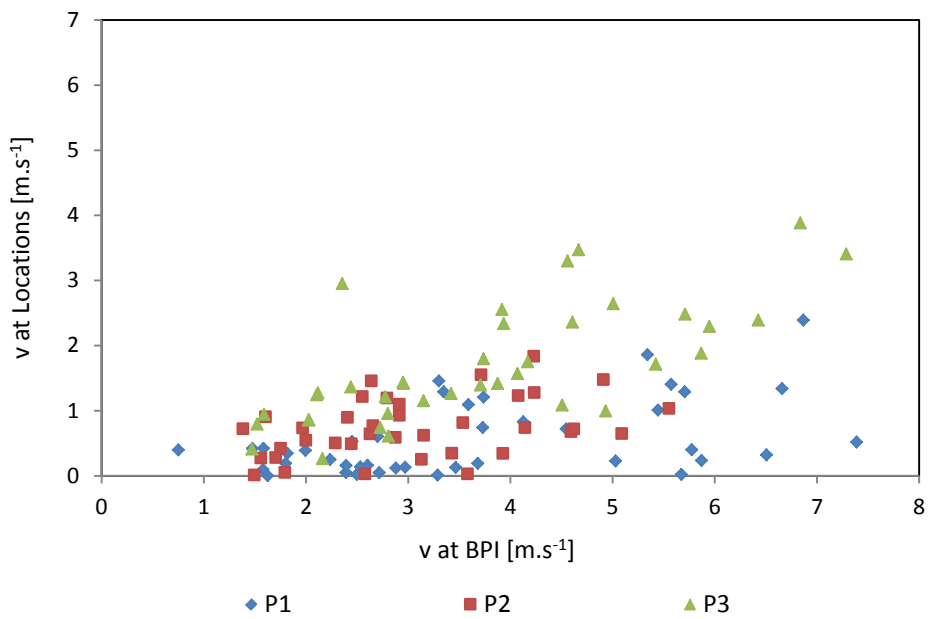


Figure 4-21: Relationship between wind speed at BPI and plazas

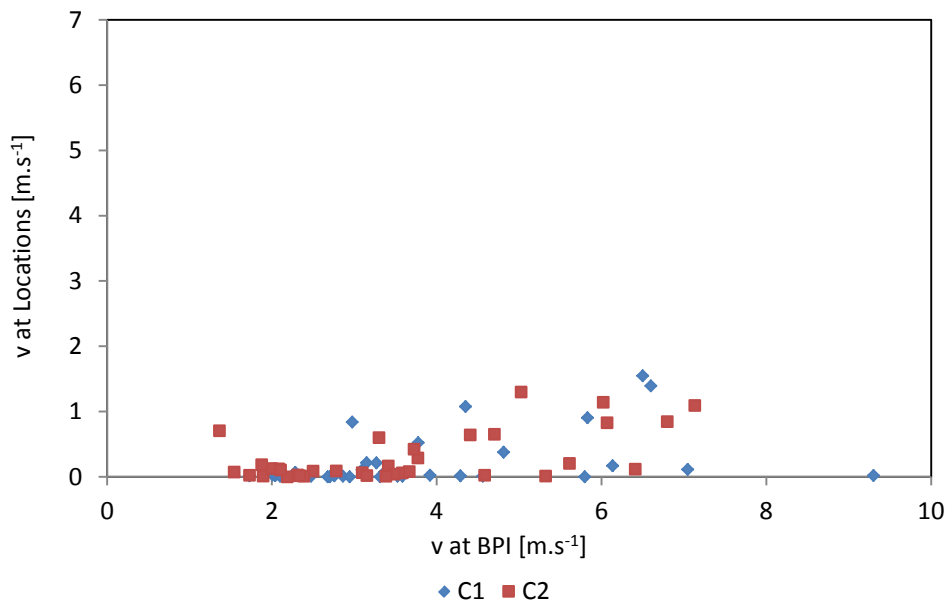


Figure 4-22: Relationship between wind speed at BPI and Courtyards

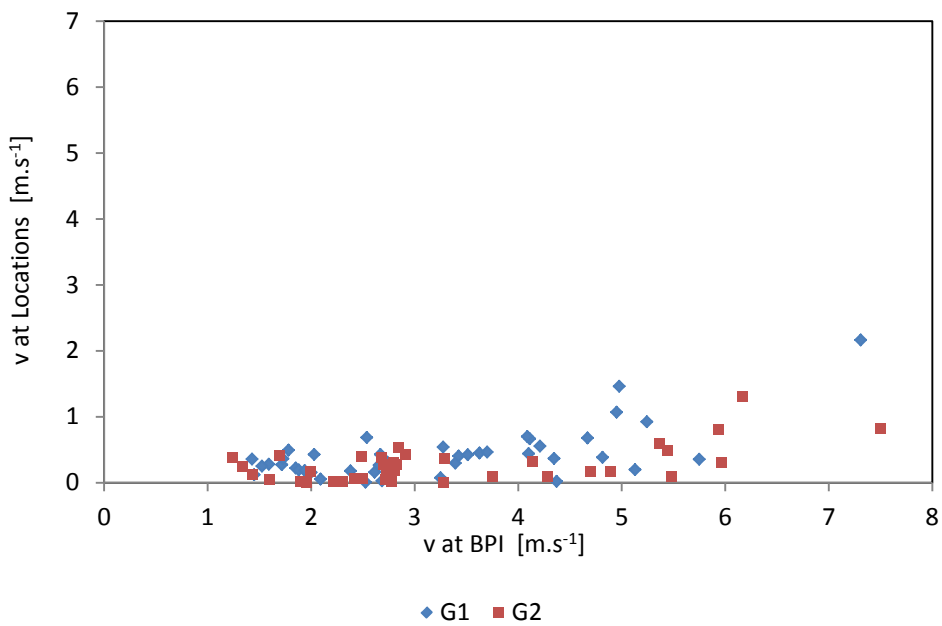


Figure 4-23: Relationship between wind speed at BPI and Parks

Figures 4-24 to 4-27 illustrate the relationship between the absolute humidity at the measurements locations and BPI. In case of absolute humidity, likewise the air temperature, there is a significant correlation between the measurement spots and the BPI,  $R^2 > 0.92$ .



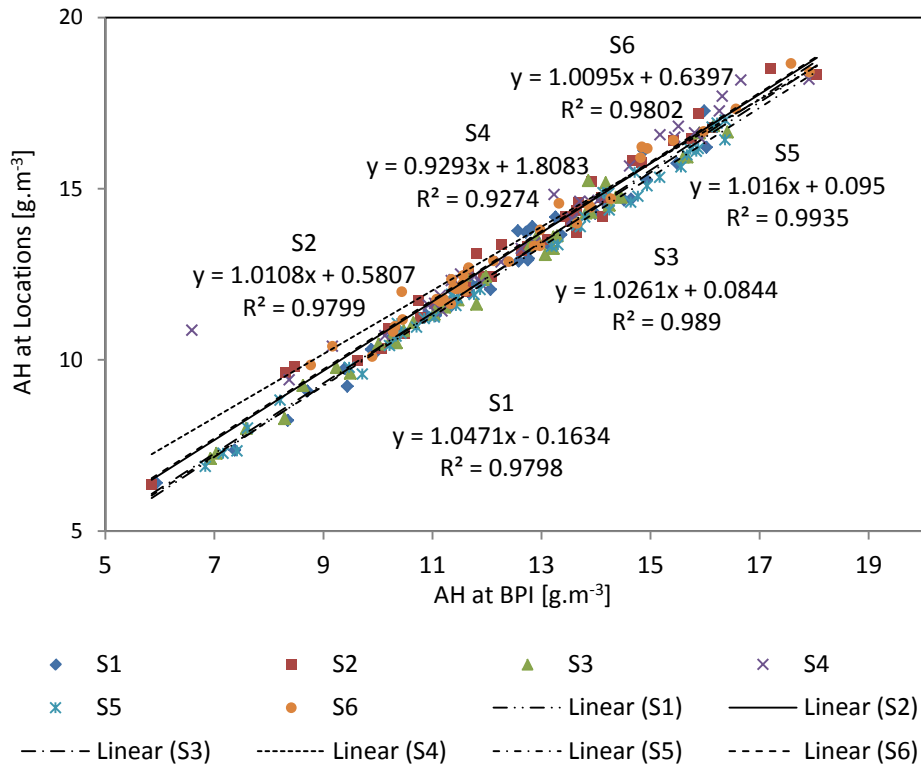


Figure 4-24: Relation between absolute humidity at BPI and streets

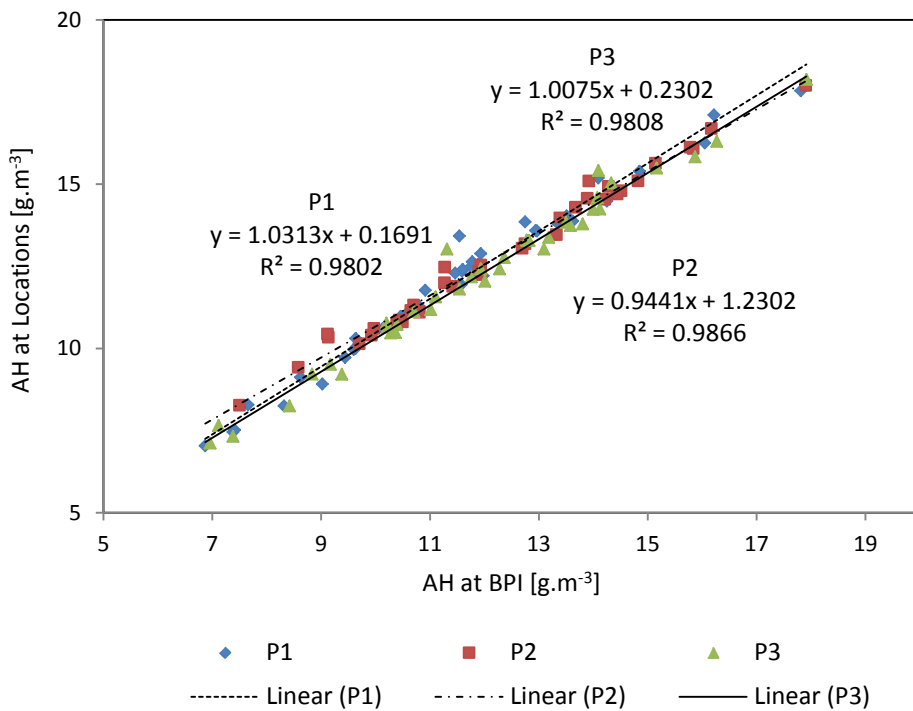


Figure 4-25: Relation between absolute humidity at BPI and plazas

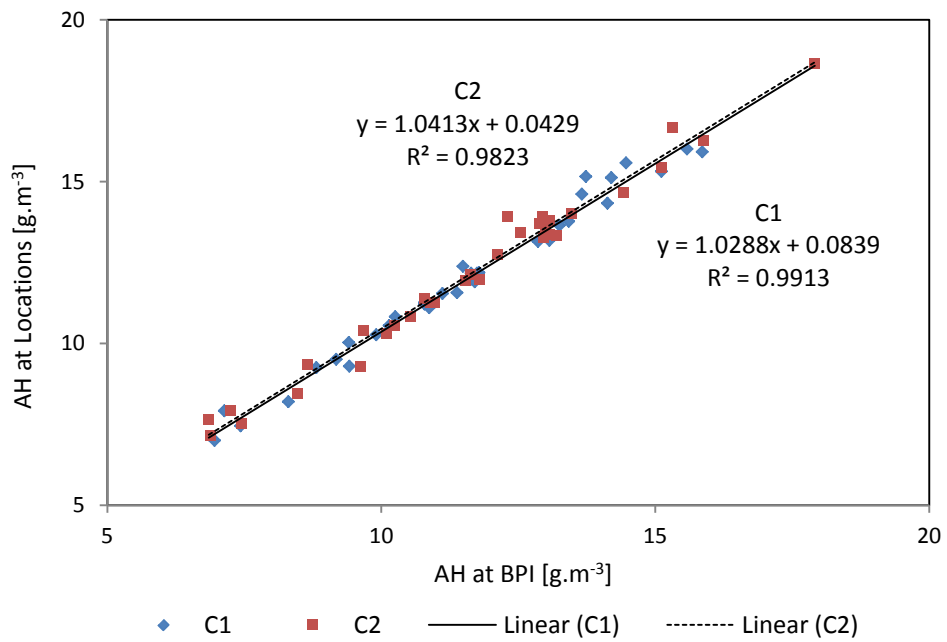


Figure 4-26: Relation between absolute at BPI and courtyards

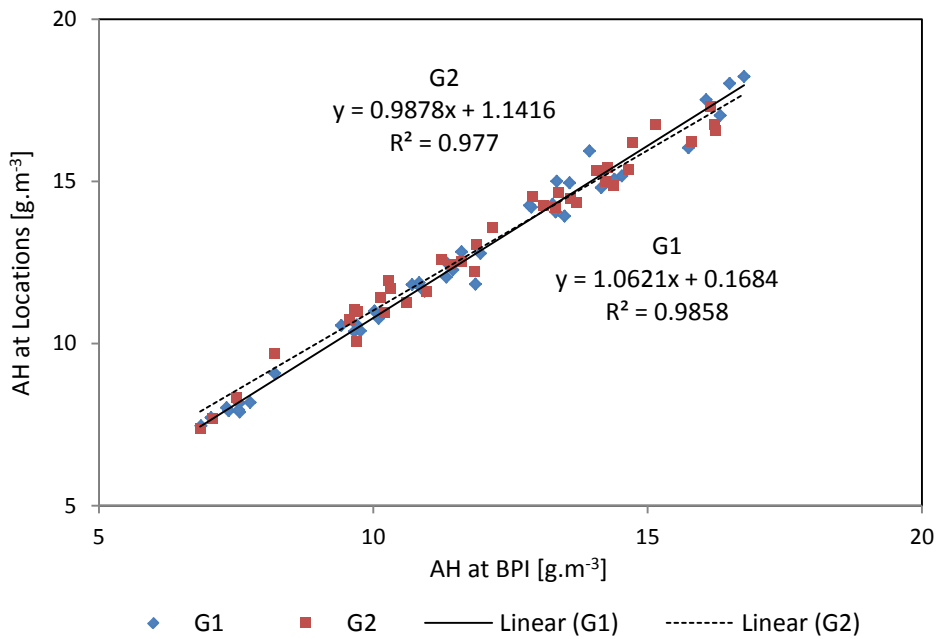


Figure 4-27: Relation between absolute humidity at BPI and parks

### **4.3. Control studies**

The urban micro-climate conditions are influenced by time, meteorological, geographical and urban characteristics simultaneously (Kolokotroni and Giridharan 2008). Therefore, to achieve more reliable results, the above mentioned simultaneous interferences were restricted by categorizing the parameters which were not controllable during the measurements, i.e. sky condition, wind speed and the measuring time due to variation in measurements with time. The effect of the time is studied in section 4.2.1. In the following section the variation of temperature, water vapor and carbon dioxide concentration under controlled/ categorized sky condition and velocity speed is discussed.

#### **4.3.1. Influence of air velocity, sky conditions, and diurnal pattern on temperature**

The mean temperature differences (MW-BPI) for all 13 measurement locations, categorized by the sky conditions, namely clear sky, partly cloudy, and cloudy, are shown in figure 4-28. Likewise figure 4-29 shows the mean temperature differences (MW-BPI) for all 13 measuring spots, categorized according to prevailing wind speeds. Values for wind speed were taken from the reference point and categorized in ranges below  $2.5 \text{ m.s}^{-1}$ , between  $2.5$  and  $5 \text{ m.s}^{-1}$  and between  $5$  and  $10 \text{ m.s}^{-1}$ .

Figure 4-30 shows the temperature differences (MW-BPI) for all 13 locations, categorized into morning (am), afternoon (pm), and night hours after 9 pm (night).

Accordingly, the sky conditions seem to have less effect on the behavior of the temperature at the measurement spots. Results, categorized in different wind conditions, show that when the wind speed is higher, generally, temperature is higher at the measurement spots compared to the reference point (BPI). In general, it can be stated that some locations are more affected (such as C1, C2, S1, and S2) by the wind speed factor than the others (S4, S5, and S6). Besides, the results suggest that closed locations, e.g. courtyards, and locations with higher aspect ratio, are more affected by the wind speed than locations with lower aspect ratio. The data, categorized in morning and afternoon hours, show that during the morning air temperature at measurement spots are higher than the reference point. During afternoon hours, the temperature recorded at the measuring spots is generally lower than that of the reference point.

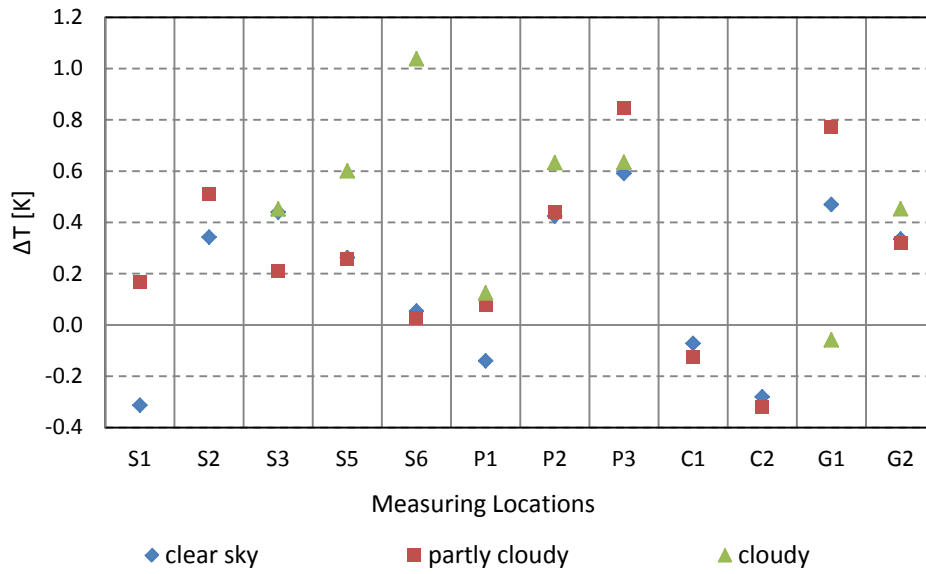


Figure 4-28: Mean temperature differences for all 13 measuring locations, classified by sky condition

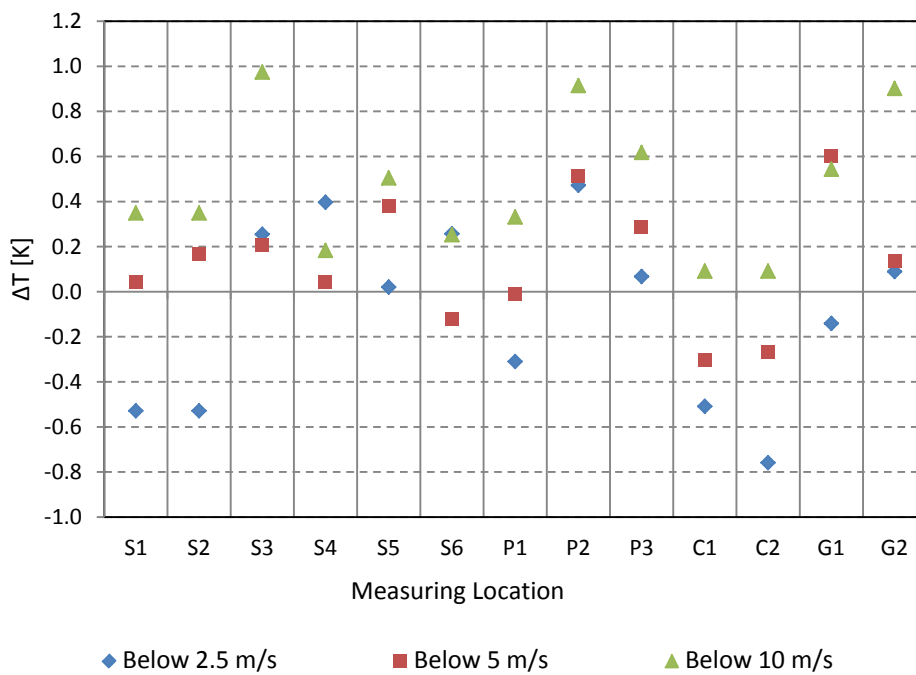


Figure 4-29: Mean temperature differences for all 13 measuring locations, classified by wind speed at BPI

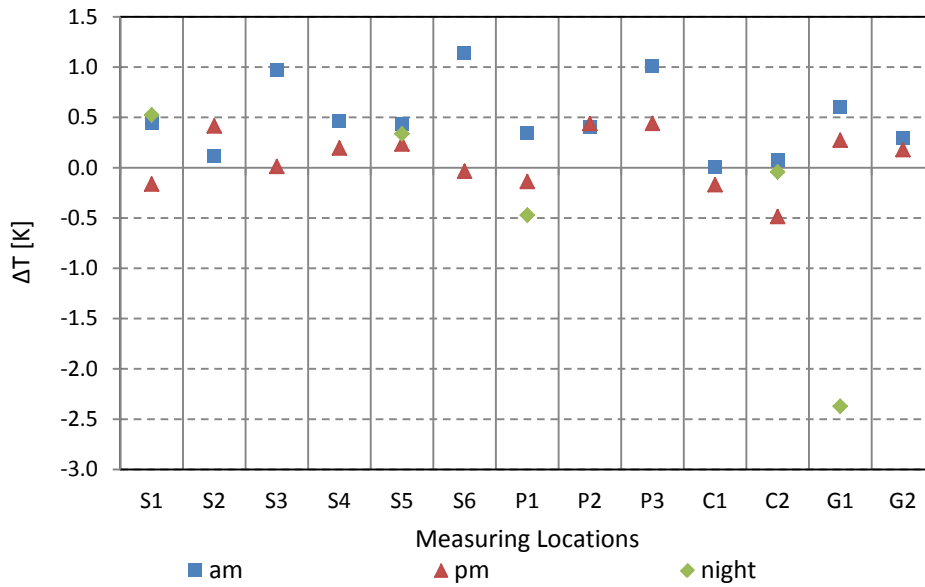


Figure 4-30: Mean temperature differences for all 13 measuring locations classified by the day time

### 4.3.2. Influence of air velocity, sky conditions, and diurnal pattern on water vapor concentration

Mean water vapor concentration differences (MW-BPI) for all 13 measuring locations, categorized by sky conditions, i.e. clear sky, partly cloudy, and cloudy are shown in figure 4-31. Likewise, figure 4-32 shows the mean water vapor concentration differences (MW-BPI) for all 13 measuring locations, categorized according to the prevailing wind speeds.

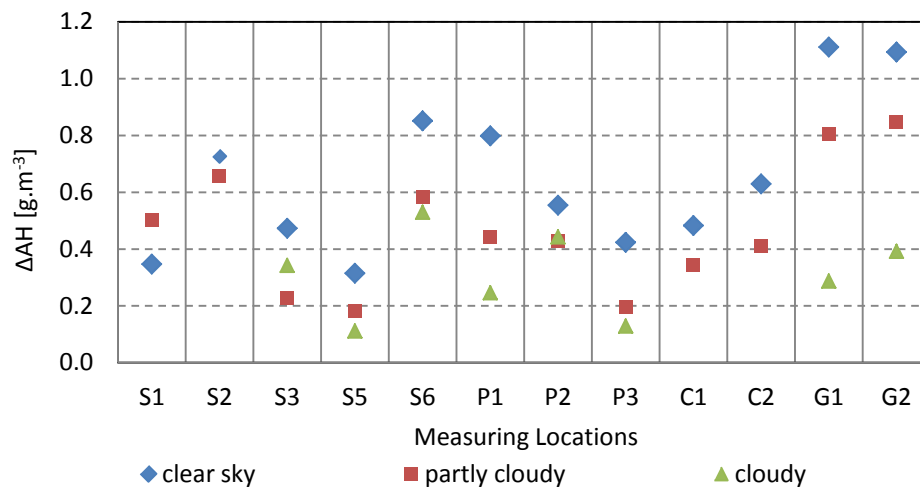


Figure 4-31: Mean water vapor concentration differences (MW – BPI) for all 13 locations classified by sky condition

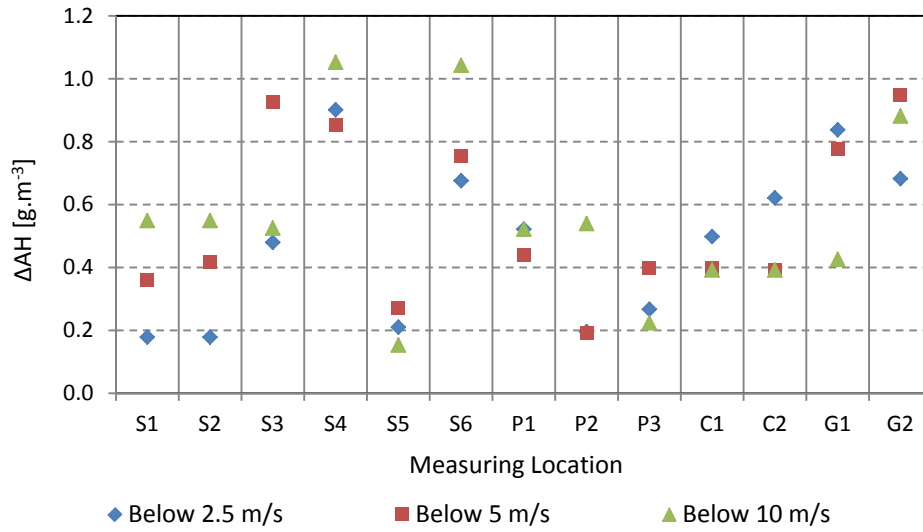


Figure 4-32: Mean water vapor concentration differences (MW – BPI) for all 13 locations classified by wind speed at BPI

### 4.3.3. Influence of air velocity, sky conditions, and diurnal pattern on CO<sub>2</sub>

Figure 4-33 shows the mean CO<sub>2</sub> concentrations for all 13 measuring locations, categorized by the sky conditions, i.e. clear sky, partly cloudy, and cloudy. Likewise, mean CO<sub>2</sub> concentration for all 13 measurement locations categorized according to the prevailing wind speeds are displayed in figure 4-34.

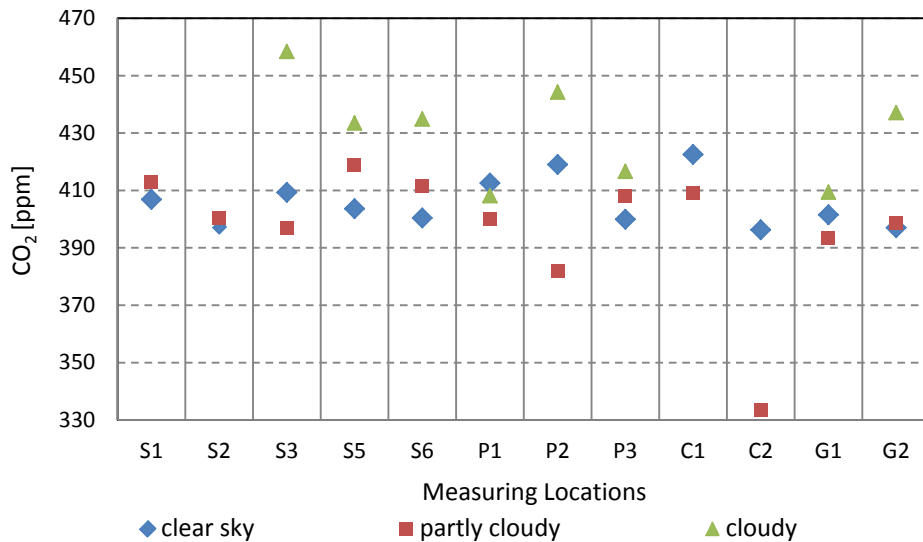


Figure 4-33: Mean CO<sub>2</sub> concentration for all 13 locations classified by wind sky condition

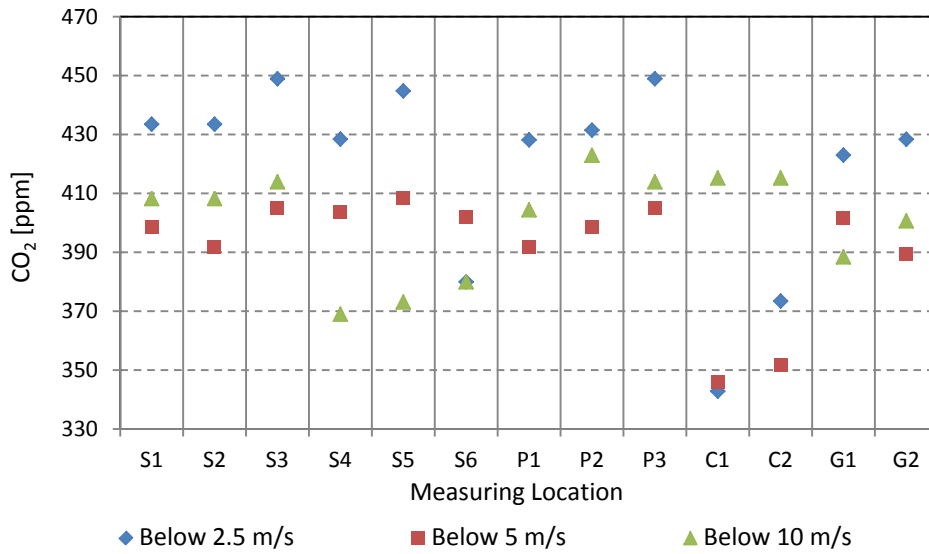


Figure 4-34: Mean CO<sub>2</sub> concentration for all 13 locations classified by wind speed at BPI

#### 4.3.4. Influence of the wind speed above the urban canopy on that of inside the urban canopy

As it can be seen in figure 4-35, by increasing of the wind speed above the urban canopy the absolute wind speed difference (MW-BPI) increases. In lower velocities (below 2.5 m/s) all the locations have almost constant reduction of wind speed within the canopy while in higher velocities (5-10 m/s) there is a considerable difference between locations. In such condition narrow streets (S1 & S2), courtyards (C1 & C2), parks (G1 & G2) plazas and streets with trees (S3 & P1) diminish the wind speed much more than open spaces such as streets and plazas without trees (S5, S6, P2, P3).

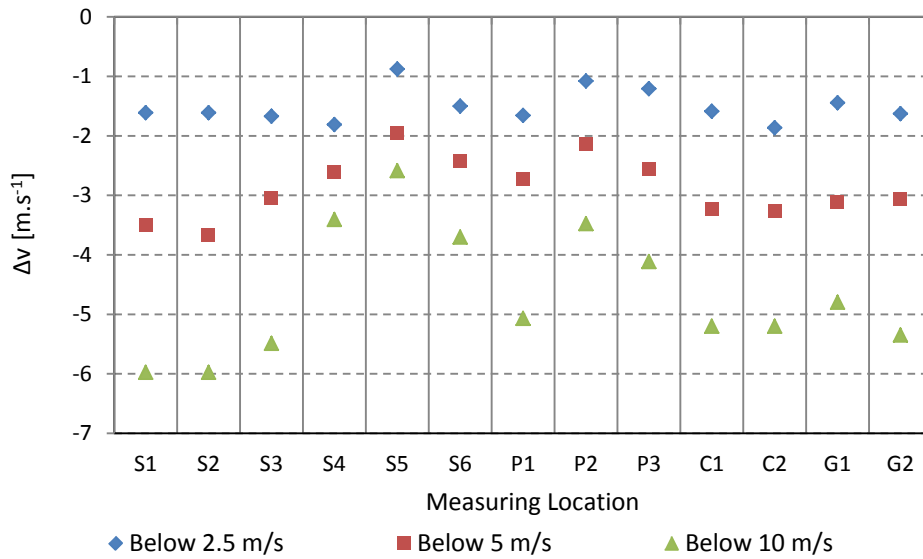


Figure 4-35: Mean wind speed differences (MW-BPI) for all 13 locations classified by wind speed at BPI

#### 4.4. Long time measurements

In addition to the short time measurements, several long-time measurements were performed over a period of 12 hours. In figure 4-36 collected data through long time measurements are shown the temperature difference (MW-BPI) for the locations S1, S5, P1, C2, and G1. As it can be seen, locations with lower SVF tend to keep higher temperature values during the night hours, whereas the park location G1 shows a significant decrease of temperature.

In the case of solar radiation, as it is observed in figure 4-37 locations with high SVF, G1 and S5, show in significant difference with BPI, while other measuring spots, i.e. S1, P1 and C2 depending on the day time and accordingly available magnitude of solar radiation in the upper boundaries show considerable difference with BPI.

Figure 4-38 shows the absolute humidity difference between the measuring spots and BPI. As expected the water vapor concentration in the locations with vegetation is higher during the day but during the night the difference decreases and reaches to the amount of locations without vegetation. It may be caused by higher air temperature and solar radiation during the day.

In case of wind speed as it is shown in figure 4-39 S1 has wider difference with BPI than the other measuring spots and seems to have the least air velocity, but since the wind speed was not the same in all the location during the measuring period reaching to this conclusion may not be true in every condition (regarding the wind speed and direction). Hence, more measurements are needed to validate this result.



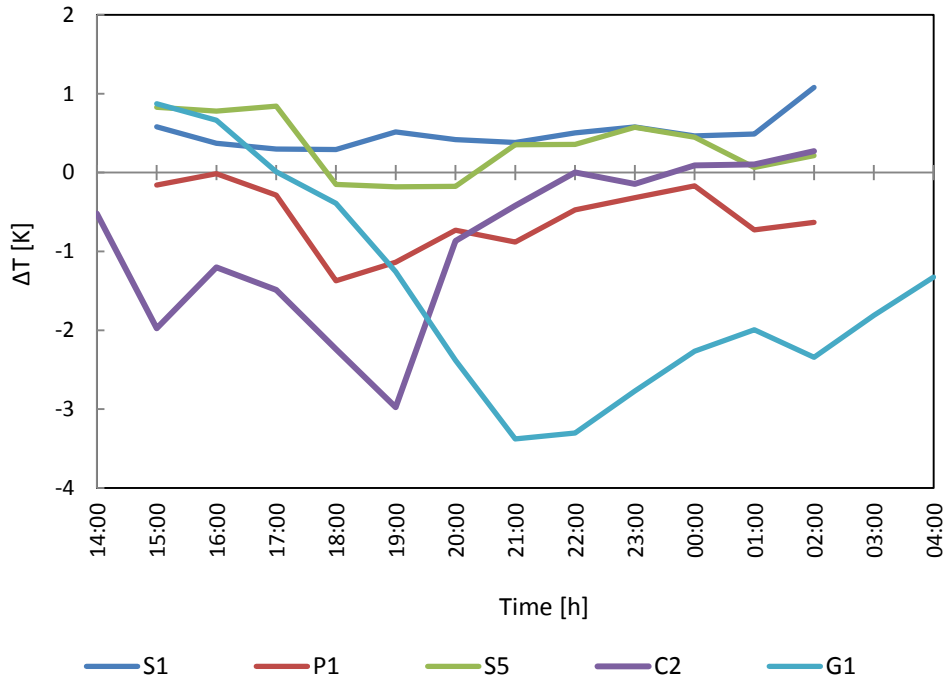


Figure 4-36: The temperature difference (MW-BPI) for the locations S1, S5, P1, C2, and G1 during long measurements.

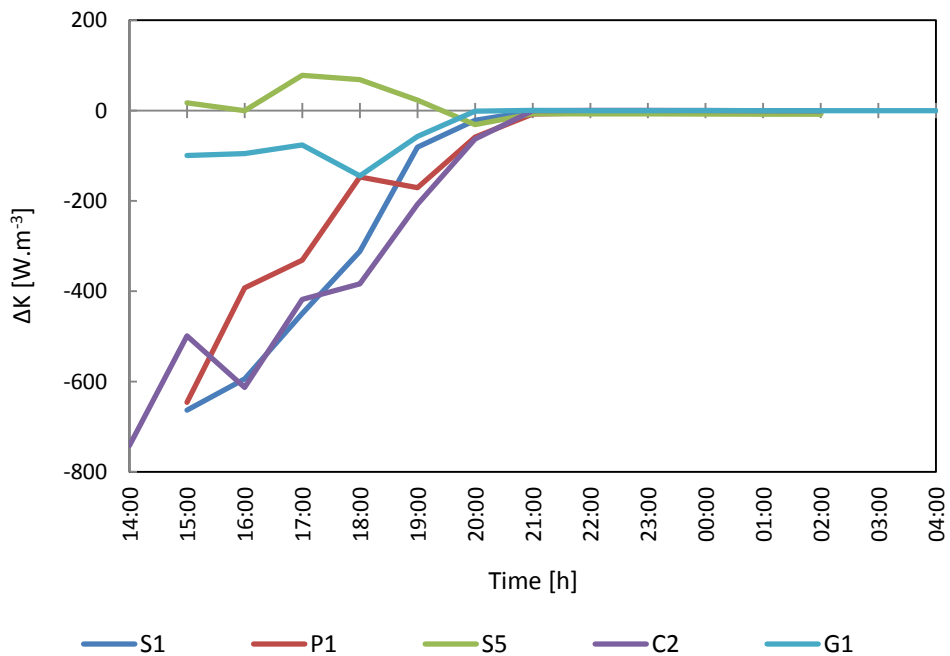


Figure 4-37: Solar radiation differences (MW-BPI) for the locations S1, S5, P1, C2, and G1 during long measurements

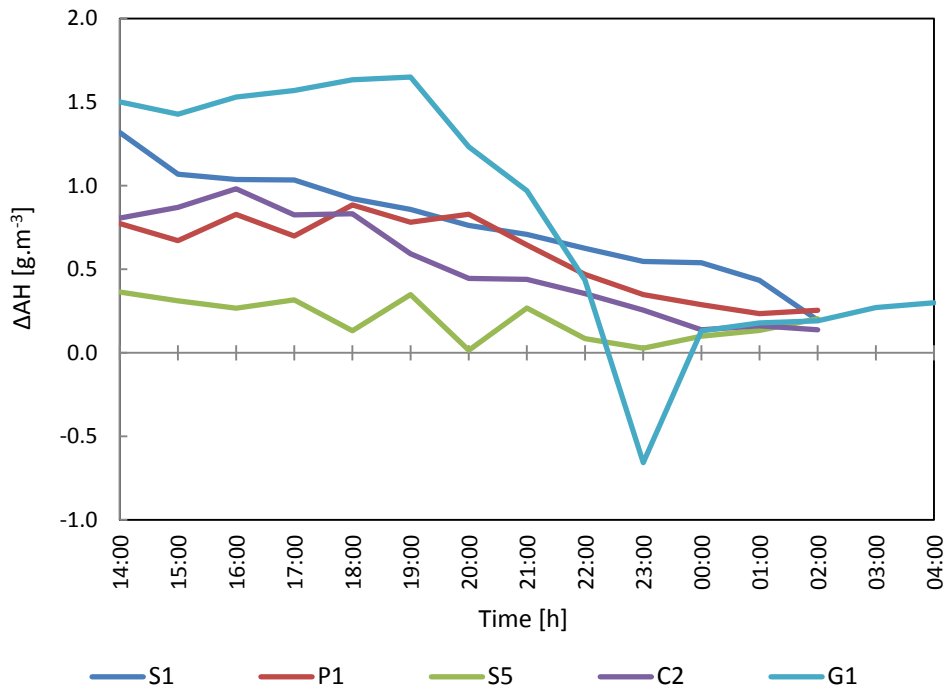


Figure 4-38: Water vapor differences (MW-BPI) for the locations S1, S5, P1, C2, and G1 during long measurements.

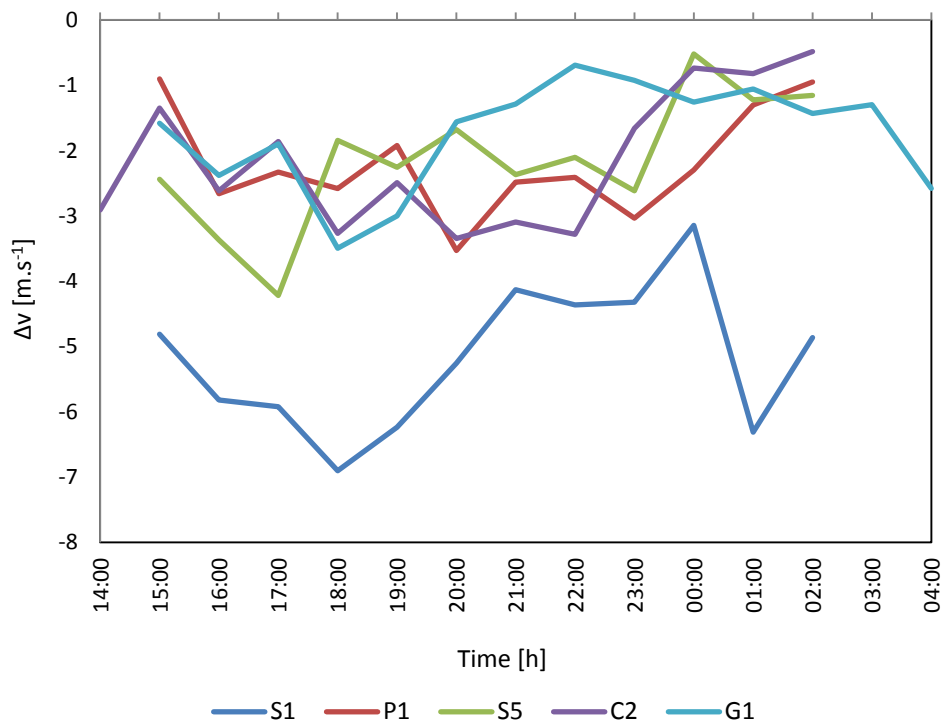


Figure 4-39: Wind speed differences (MW-BPI) for the locations S1, S5, P1, C2, and G1 during long measurements

## 5. Computational Inquiry Results

Complex mechanism prevailing the atmospheric behavior, and the complicated interrelations between an urban fabric and its associated atmospheric/environmental conditions define the microclimatic situations in the very urban area. These are the main reason behind the fact that just by collecting weather data through measurements variation of microclimatic condition in an urban fabric may not be determined (Maleki et al. 2014). In this context, especially the point has to be taken into account that because of complexities involved; on-site measurements are subject to controllable limitations, which, in turn, hamper the achievement of reliable and effective analysis. All these facts reflect the need for an optimized and effective approach, i.e. for micro-climate modeling based on CFD. This is why a main part of this work has been allocated to CFD-modeling to suitable micro-climatic conditions within an urban fabric in the City of Vienna.

In the following sections the required procedure along with the obtained results are discussed.

### 5.1. Adjusting the required input weather data

As mentioned in section 3.3.10, the accuracy of the results of a micro-climate simulation is strongly dependent on the quality of its input data as initial/boundary condition. Hence, the proper input data should be prepared for the present work regarding to the project requirements, based on the available data. Thus, a small area pertaining to BPI and C\*, two available and close stationary weather station in the measuring area, as well as three measuring spots, i.e. C2, P1 and S1, was selected to test and optimize the software for further modeling aims of the project. These weather stations were included due to using their monitored weather data to set the software and to validate the accuracy of the outputs.

The BPI weather station is located on top of a tower above the urban canopy and therefore its view to sky is without any barrier ( $SVF=1$ ). Hence it could be considered as the best receptor to evaluate the ability of the software to predict the solar radiation in the boundary condition. This point was also used as the reference point in investigating the measured data (see section 3.2.2.). According to examine the accuracy of the obtained temperature profile as a result of simulation this point was of vital importance.

The second stationary weather station utilized was the C\*, located inside the urban canopy (for further information see table3-1, and was recording the weather

condition continuously. Its data was used to evaluate the accuracy of the simulation outputs for the urban canopy.

As next step, the geometrical model (input model area) of the defined area, as shown in figure 5-1, was generated based on the map taken from the official website of the city of Vienna and on-site measurements and observations. The grid size for this model selected equal to (5×5×2).

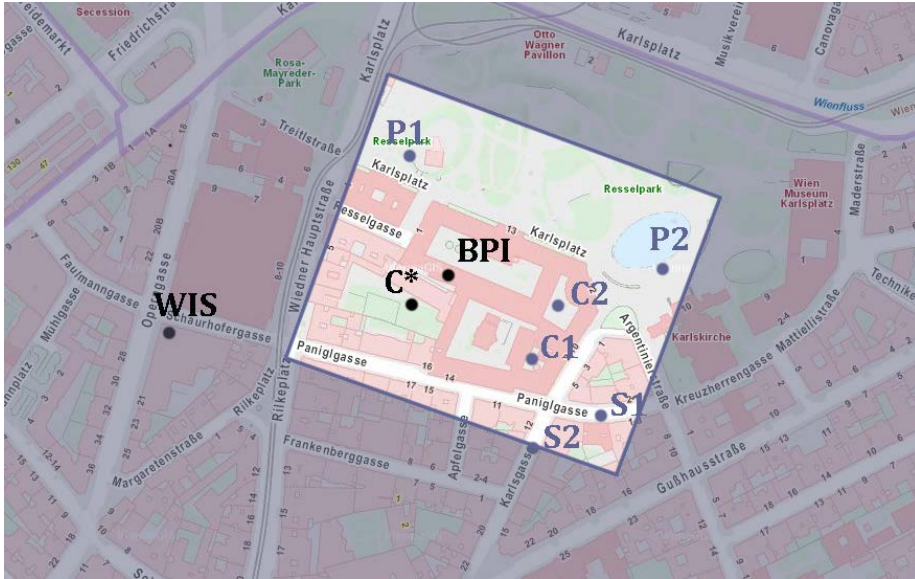


Figure 5-1: Selected area as first model including BPI, C\*, C2, S1 and P1 ([www.wien.at](http://www.wien.at))

In terms of the initial/boundary conditions, since for some settings the exact needed values were not available or the results obtained via those inputs were not satisfying several trial runs were conducted to find the most suitable settings.

To do so, a procedure was defined and based on it some scenarios were defined and according to their outputs further scenarios were developed and conducted till achieving acceptable results. Among these trials, five scenarios displayed the best fitting results which are listed and summarized in table 5-4 and are described by detail in follow as scenarios 0 to IV:

*Scenario 0:* this scenario was the first surveyed trial. It was made using ENVI-met 3.1 and was run through “none-forcing” mode, based on minimum possible initial/boundary condition input variables. Detailed description of primary settings and the method of the collecting and the calculation of the input values are explained in follow:

Date: to avoid the complexity of the simulation of cloudy sky, 22.7.2010 as a sunny day with completely clear sky was selected from the days that long measurements were conducted.

Initial atmospheric temperature: since there was no available weather information for this parameter according to the ENVI-met developer's recommendation the average air temperature in the model area was used for this purpose. To do so, the average air temperature from 4:00 AM to 3:00 AM on the next day (the simulated period), measured at BPI, was calculated and used to set the model.

Wind speed and direction: requirement of the software for this parameter is the horizontal wind speed at 10 m above the ground. Hence, the monitored data via C\* which was at about 7 m above the ground was used to calculate the average wind speed during the simulation interval. But in case of wind direction, the monitored prevailing wind direction at BPI was used.

Relative air humidity: required measuring height for this parameter is 2 m above the ground so the measured relative humidity through MW was used to set this variable.

Roughness length: default value of the software for this parameter in the urban area is 0.1 and according to the manual of the software, software is not significantly sensible to its variation so the default value was not changed for any of the simulation models in this project.

Specific humidity at the top of the model (H=2500 m): as it mentioned before, there was no available weather data in higher atmospheric layers. Thus, the value used by other similar simulation models (regarding to their similarity in the climate type and the air temperature and relative humidity) was considered as first assumption for this parameter.

The first trial simulation, named scenario 0, was run based on aforementioned assumptions as input data. The predicted air temperature by this scenario was compared with the measured data at BPI and C\*. As it can be seen in figures 5-2 and 5-4 the results were poorly fitting with the measurements. Thus, more trial scenarios were made to find the most suitable data for the uncertain inputs which were defined through assumptions in scenario 0.

*Scenario I:* after several trial runs to optimize the setting of the software, the best results was performed by following input data that their associated simulation model was named scenario I;

Wind speed: the wind speed measured at BPI,  $2 \text{ m.s}^{-1}$ , caused a considerable correction in air temperature amplitude. So the measured value at C\* was replaced by the value measured at BPI.

Initial temperature: predicted air temperatures by scenario 0 showed very low values comparing with observed ones so some simulations were run with higher values. Among these trials the one with average air temperature plus 2 K resulted in better fitting predicted air temperature. So for this scenario the average air temperature measured at BPI plus 2 K was used.

Specific humidity: for specific humidity the same procedure as initial temperature was repeated and the obtained results for the air specific humidity along with the air temperature were compared with the measured data. The results, predicted by

using  $8 \text{ g.kg}^{-1}$  as specific humidity ( $H=2500 \text{ m}$ ) were the most satisfying. Thus  $8 \text{ g.kg}^{-1}$  was used for this parameter in scenario I.

Solar adjustments: in some certain location the predictions for the solar radiation flux might be systematically over/under estimated by ENVI-met due to its internal methods for calculation. To correct this error an optional setting, named “solar adjustment”, is provided. In case of Vienna as it is shown in figure 5-3 by the scenario 0 there is an all through overestimation which has been resolved by setting the “solar adjustment” to 0.82 scenario I as well as in other scenarios. Upon applying the solar adjustment the results were improved considerably and the predicted variables were almost matching the measured ones.

*Scenario II*: by conducting calibration runs for the model the preview version of ENVI-met 4.0, released for academic purposes was used especially because of its ability in forcing atmospheric parameters. Thus, in the scenario II the same assumptions pertaining to the input data as the scenario I were applied to preview version for 4.0 to evaluate its accuracy compared to the version 3.1.

*Scenario III*: in this scenario, the possibility of forcing the air temperature and the air relative humidity by version 4.0 was examined. Accordingly, the air temperature and the air relative humidity were added to the input data of version II on an hourly base.

*Scenario IV*: in this scenario instead of hourly air temperature and air relative humidity the maximum and minimum of these variables during the simulated period with their associated time were used for forcing.

Obtained results from simulations were compared with measured weather data at both defined receptors, i.e. at the BPI and at the C\* stations, to achieve the best fitting scenario.

Figure 5-2 and 5-4 show the monitored and simulated air temperatures for the BPI and C\* stations, respectively. Simulations were performed starting from 4:00 h in the morning for a duration of 24 hours. As suggested by the software developer, by each run the first 2-3 h simulation time should be considered as the initialization period, during which the simulation results cannot be taken into account as enough accurate. Thus, by reviewing the results just those belonging to the time period 6:00 h to 4:00 h were considered.

As it can be seen in figures 5-2 to 5-4, the simulated values by all scenarios, except scenario 0, display relatively similar tendency very close to the associated measured data at both receptors BPI and C\*. To evaluate the offset between the modeling results and the values obtained through measurements, three different indicators were defined. First indicator was the index of agreement (d) suggested by (Willmott 1982). Index of agreement is a descriptive measure and can be applied to make cross-comparison between models as a relative and bounded measure. Index of agreement (d) is calculated as follows:

$$d = 1 - \frac{\sum_i^n (s_i - m_i)^2}{\sum_i^n (|s_i| - |m_i'|)^2} \quad 0 \leq d \leq 1 \quad (5-1)$$

where  $s_i' = s_i - \bar{m}$  and  $m_i' = m_i - \bar{m}$ ,  $\bar{m}$  is the mean value of measured variables,  $m_i$  is the measured variable and the  $s_i$  is the simulated ones. The second used indicator was the Root Mean Square Deviation (RMSD) or Root Mean Square error (RMSE), a measure of the differences between outcomes of a model and the associated observed values. RMSE is a good measure to show the accuracy by comparing different predicting errors within a dataset, the lower value indicates the less error in the predicted values. It is calculated using the following formula (Willmott 1982):

$$RMSE = \sqrt{\frac{\sum_{i=1}^n (m_i - s_i)^2}{n}} \quad (5-2)$$

And the third indicator was the “Coefficient of Variation of the Root Mean Square Deviation” CV (RMSE), and is calculated by (Tahmasebi and Mahdavi 2012) :

$$CV(RMSE) = \left( \frac{RMSE}{\bar{m}} \right) \times 100 \quad (5-3)$$

All these indicators were used in each of the modeled scenarios to obtain the offset between the measured values and the simulation results concerning the air temperature and the solar radiations for both, aforementioned receptors. The results are given in tables 5-1 to 5-3.

Indicators pertaining to the air temperature, in each of the scenarios, regarding to the highest  $d$  and the lowest RMSE and CV(RMSE) at BPI and C\* show that the scenario III delivers more realistic result, in comparison with the others. In the same way the outputs of the scenarios I and III, pertaining to the modeled global radiation values, could be approved to the best.

In next step, scenarios I to III were repeated for locations C2, S1, S5 and P1, where long measurements had been conducted, and the same weighting method was used for all cases (tables 5-5 to 5-8). The results also confirmed the scenario III as the best fitting scenario among the all.

The results of evaluation of scenarios show the program overestimates the calculated global solar radiation at the upper boundary and suggests using the number of 0.82 as solar adjustment for the city of Vienna. Likewise, it is suggested to use the wind speed above the urban canopy as the input value for wind speed instead of the wind speed at 10 m above the ground level. Additionally, the results of scenario III showed, utilizing the hourly based forcing to run the simulation model improves the accuracy of the results considerably.

Table 5-1 : *d* and RMSE and CV (RMSE) in simulated calibration scenarios for BPI temperature

Scenarios	0	I	II	III	IV
d	0.50	0.88	0.92	0.95	0.92
CV(RMSE) [%]	11.04	7.84	6.32	4.51	11.04
RMSE [K]	3.15	2.24	1.80	1.29	3.15

Table 5-2: *d* and RMSE and CV (RMSE) in simulated calibration scenarios for BPI solar radiation

Scenarios	0	I	II	III – IV
d	0.98	1.00	0.99	1.00
CV(RMSE) [%]	13.82	5.05	10.44	6.45
RMSE [W.m <sup>-2</sup> ]	73.81	27.00	55.79	34.45

Table 5-3 : *d* and RMSE and CV (RMSE) in simulated calibration scenarios for C\* temperature

Scenarios	0	I	II	III	IV
d	0.67	0.91	0.94	0.97	0.95
CV(RMSE) [%]	9.25	6.89	5.30	3.36	10.04
RMSE [K]	2.64	1.97	1.51	0.96	2.87



Table 5-4: Simulation input data for calibration scenarios (0-I-II-III-IV)

	Scenarios	0	I	II	III	IV
	Envi-met Version	3.1	3.1	4	4	4
<b>Basic Input data</b>	Date	22.7.2010	22.7.2010	22.7.2010	22.7.2010	22.7.2010
	Wind Speed [ $\text{m.s}^{-1}$ ]	0.2	2	2	2	2
	Wind Direction [°]	163	163	163	163	163
	Initial Temperature [K]	301	303	303	303	303
	Solar Adjustment	1	0.82	0.82	0.82	0.82
	Relative Humidity [%]	57	57	57	57	57
	Specific Humidity [ $\text{g Water.kg air}^{-1}$ ]	7	8	8	8	8
<b>LBC type</b>	LBC for T and q	open	open	open	open	open
	LBC for TKE	open	open	open	open	open
<b>Buildings</b>	Heat Transmission Walls [ $\text{W.m}^{-2}\text{K}^{-1}$ ]	0.6	0.6	0.6	0.6	0.6
	Heat Transmission Roofs [ $\text{W.m}^{-2}\text{K}^{-1}$ ]	0.6	0.6	0.6	0.6	0.6
	Albedo Walls	0.2	0.4	0.4	0.4	0.4
	Albedo Roofs	0.2	0.4	0.4	0.4	0.4
<b>Simple Forcing</b>	Max temperature [K]	---	---	---	306.85	306.85
	Time of Max temperature	---	---	---	16:00	16:00
	Min temperature [K]	---	---	---	295.15	295.15
	Time of Min temperature	---	---	---	04:00	04:00
	Max relative humidity [%]	---	---	---	76	76
	Time of Max relative humidity	---	---	---	04:00	04:00
	Min relative humidity [%]	---	---	---	39	39
	Time of Min relative humidity	---	---	---	17:00	17:00
Forcing	---	---	---	Hourly	Min & Max	

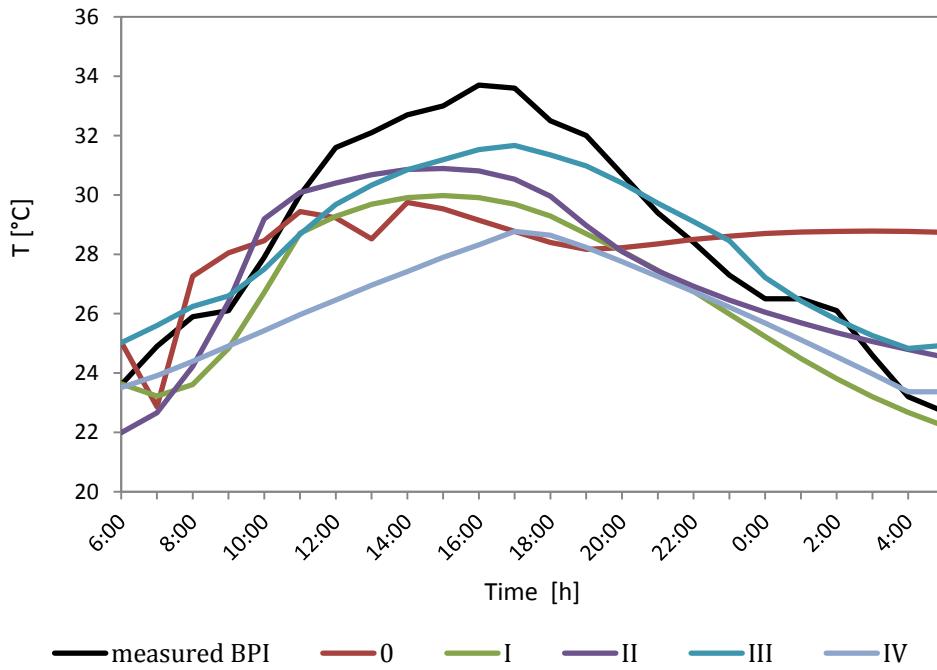


Figure 5-2: Monitored and simulated air temperatures of BPI (scenarios: 0- I-II-III- IV), simulated time period from 06:00 h on 22.07.2010 to 05:00 h on 23.07.2010

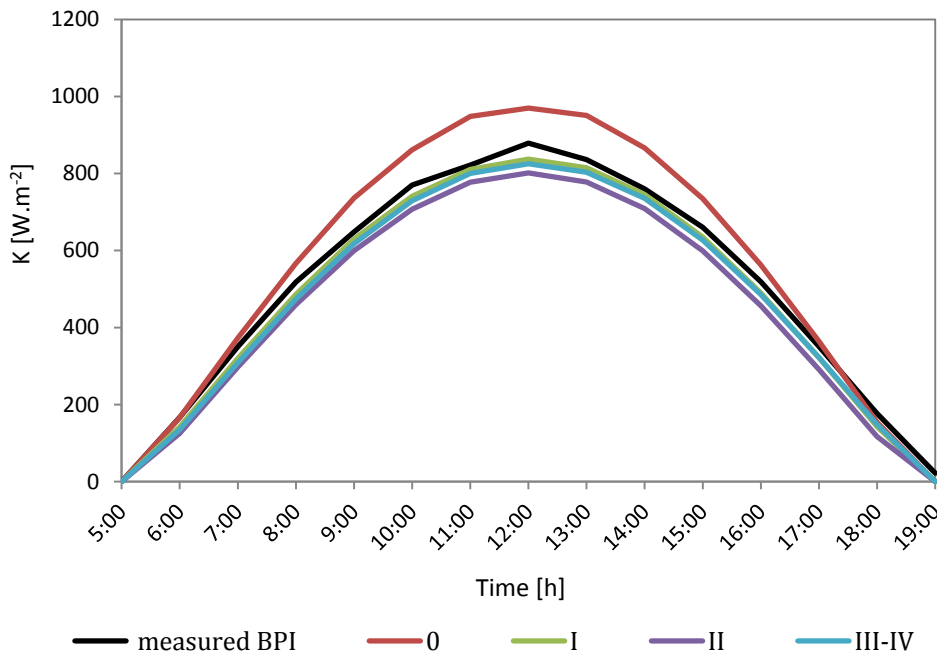


Figure 5-3: Monitored and simulated global radiation of BPI (scenarios: 0- I-II-III- IV), simulated time period from 05:00 h on 22.07.2010 to 05:00 h on 23.07.2010

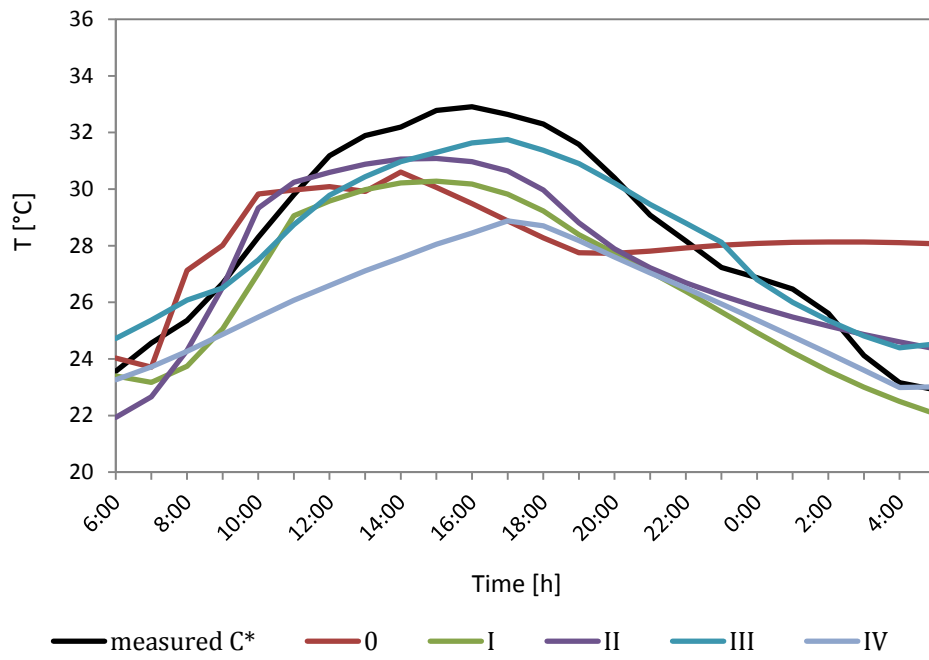


Figure 5-4: Monitored and simulated air temperatures of C\* (scenarios: 0- I-II-III- IV), simulated time period from 06:00 h on 22.07.2010 to 05:00 h on 23.07.2010

Table 5-5:  $R^2$  and RMSE and CV (RMSE) in simulated calibration scenarios for C2 air temperature

Scenarios	I	II	III
d	0.93	0.94	0.98
CV(RMSE)	4.37	3.66	2.44
RMSE [K]	1.24	1.04	0.69

Table 5-6:  $R^2$  and RMSE and CV (RMSE) in simulated calibration scenarios for S1 air temperature

Scenarios	I	II	III
d	0.75	0.78	0.86
CV(RMSE)	8.75	7.49	5.54
RMSE [K]	2.69	2.30	1.70

Table 5-7:  $R^2$  and RMSE and CV (RMSE) in simulated calibration scenarios for S5 air temperature

Scenarios	I	II	III
d	0.63	0.57	0.83
CV(RMSE)	10.55	7.25	5.55
RMSE [K]	3.18	2.18	1.67

Table 5-8:  $R^2$  and RMSE and CV (RMSE) in simulated calibration scenarios for P1 air temperature

Scenarios	I	II	III
d	0.96	0.80	0.93
CV(RMSE)	3.37	5.80	3.56
RMSE [K]	1.00	1.73	1.06

## 5.2. Main Simulation Model Buildup

After receiving satisfying simulation results from the initial model focus was made, as the next step on buildup of a main model. The main model was used to perform simulations, results of which could be considered as describing the variation of micro-climate conditions of the urban fabric of the city of the Vienna in an acceptable realistic way.

To do so, an urban area, shown in figure 5-5 including a part of VUT complex with several courtyards, wide North-South oriented streets, narrow North-South and East-West oriented streets was selected which was supposed to be modeled using ENVI-met. The domain boundaries were defined in a way to include the two available stationary weather stations within the area as well. These weather stations are the BPI weather station (see section 3.2.2) and Vienna inner city weather station named “Wien Innere Stadt” (WIS). The WIS belongs to the central institute for meteorology and geodynamic (ZAMG) and is located at the intersection of a wide and a narrow street, on the terrace of the second floor of a tall building at a height of approximately 9 m from ground level. In the following section the model, its buildup in ENVI-met and the associated simulation approach are described in detail.

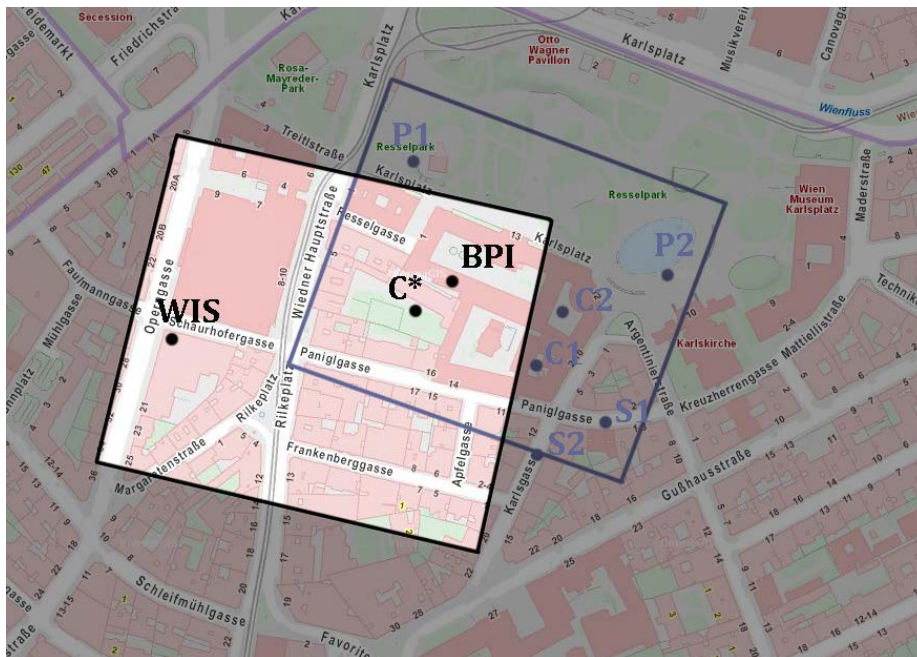


Figure 5-5: Map of the simulated area ([www.wien.at](http://www.wien.at))

### 5.2.1. Domain properties

The size of the model domain is about 76960 m<sup>2</sup> (296 m×260 m), out of which around 42544 m<sup>2</sup> (55%) is occupied by buildings. The mean value of the model buildings compactness (building volume/area) is around 4.85 m. Most of the buildings are considered as old buildings with light colored walls and dark roofs. Pitched roofs comprise 60% of the roof areas. Ground surface is sealed by either asphalt or single stones except for green areas, which consist of soil, and cover 18% of the surface area. There is no vegetation in the streets. Green areas and trees (total number of trees is 71) are mostly inside the courtyards. There is no green roof in the area. Most part of the buildings is either allocated to academic affairs or commercial use. The existing narrow streets within the domain are not supposed to suffer a heavy traffic load. The above mentioned domain, selected as the simulation model, is mapped in figures 5-5 and 5-6.



Figure 5-6: Aerial picture from the simulated area (google. Map)

### 5.2.2. Model setting and sensitivity analysis

Considering the model area and based on the simulation software limitations the finest possible resolution of the model grid could be 3 m for  $\Delta x$  and  $\Delta y$  and 2 m for  $\Delta z$ . Thus, to examine the sensitivity of the simulation results with respect to the grid size, three identical models just with different grid sizes ( $\Delta x$ ,  $\Delta y$ ,  $\Delta z$ ), i.e. (3×3×2), (4×4×2) and (5×5×2), were made. Each of three models was used for a simulation run to simulate a clear and warm summer day (day: 13.07.2011). The weather data collected by WIS, were used as input forcing weather data. The model with 3 m grid size could not be used further, due to the error encountered in the path of simulation, which is traced back to the model complexity and ENVI-met limitations,

so it was ignored. Simulated temperatures for the locations BPI and WIS, were compared with the measured data at those points to evaluate the accuracy of models with 4 m and 5 m grid size, named 4m-w and 5m-w respectively.

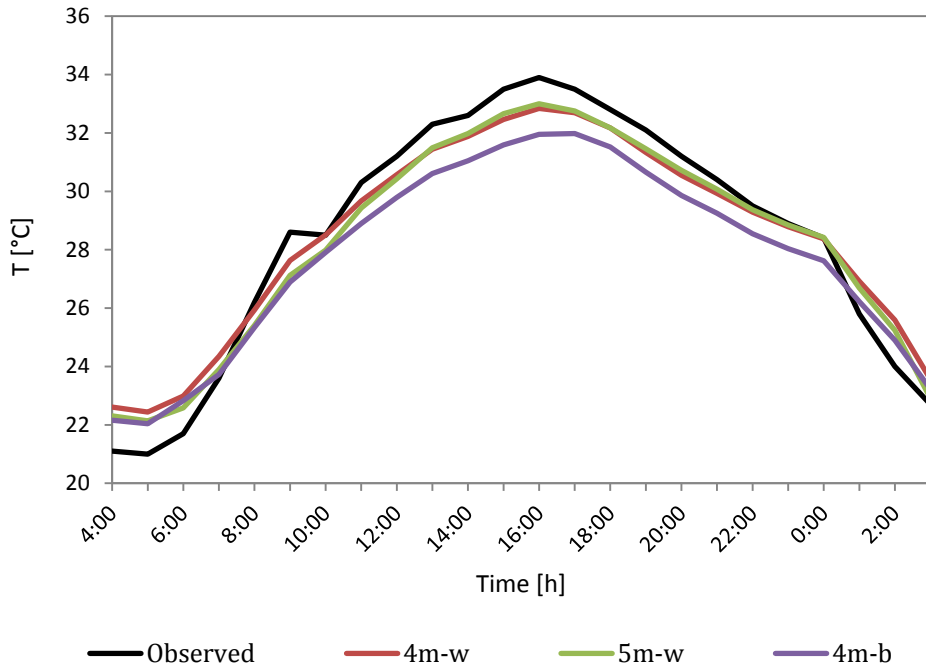


Figure 5-7: Observed and predicted air temperature at WIS, (simulated day: 13.07.2011)

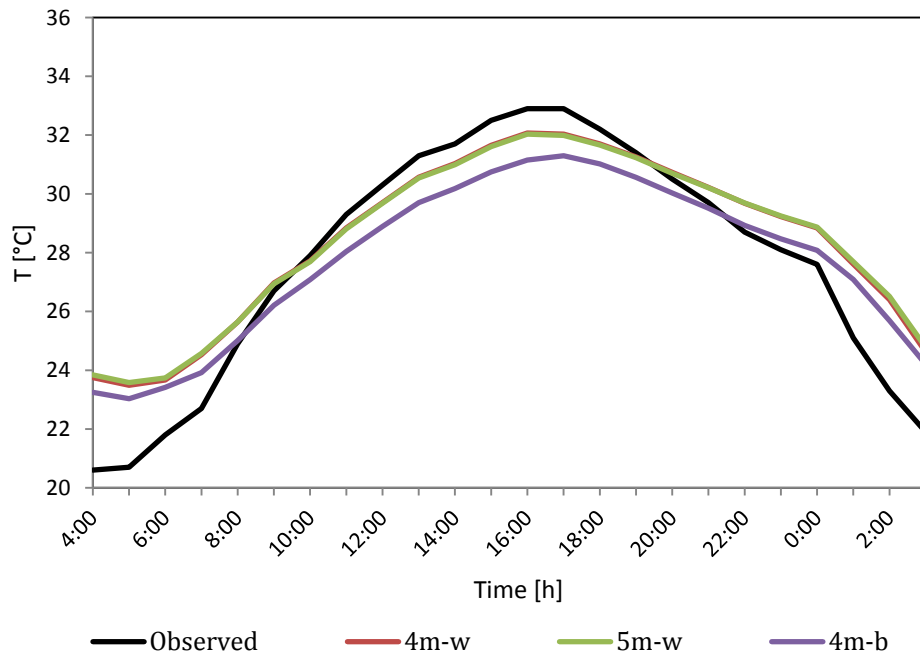


Figure 5-8: Observed and predicted air temperature at BPI, (simulated day: 13.07.2011)

The results of simulations as they are shown in figures 5-6 and 5-7 (4m-w vs. 5m-w) do not display significant difference from each other, but due to having higher resolution and as a result to have more detailed outputs, 4 m grid size was selected for further simulation surveys. As it mentioned before two stationary weather stations are located within the model, i.e. WIS inside the canopy and the BPI above the urban canopy, both close to the boundary of the model. Previous simulations were conducted using the obtained data from WIS as input weather data for forcing. An additional simulation named, 4m-b, based on the weather data monitored at BPI as input data for forcing, using the model with 4 m grid size was performed to evaluate the performance of ENVI-met regarding to the method of collecting the input weather data for forcing. Since the model with 4 m grid size was selected for further simulations the model with 5 m grid size was ignored for this evaluation.

As it mentioned in section 3.3.9, input air temperature/relative humidity for implementing simple forcing were used to generate a 1D-profile for inflow boundary. These data were referred to be valid at a height of 2 m. The associated calculated indicators, shown in table 5-9 (4m-w vs. 4m-b), reveal that using the data measured at higher levels for forcing decrease the accuracy of outputs within the canopy up to 2%, while the outputs for higher levels are not affected significantly and even are improved slightly (less than 0.5%).

Comparison between the results of simulations 4m-w, 5m-w and 4m-b showed the best fitting results for investigating the micro-climate of the present model was obtained from the model with 4 m grid size and forced by the data collected by WIS. To reassure the model validity and to assess the accuracy of the model for other possible days two more simulations were conducted, using the model with 4 m grid size and WIS data for forcing, for two other warm and sunny days (clear sky condition) in June and July 2011. The results showed, as given in table 5-10, a relatively good match between the observed and the predicted air temperatures in the model. The accuracy of the model within the canopy was considerably higher than above the canopy. The reason is assumed to be the lack of the possibility for wind speed and direction forcing by the used ENVI-met version. In the path of the simulation wind speed and direction is considered to be constant. Since the wind direction and speed within the canopy are modified by urban geometry, sudden changes in wind direction and speed are attenuated inside the urban canyons. Therefore the mean value of wind speed or the direction of prevailing wind can be representative for whole simulation period within the canopy and the effect of this simplification is less, comparing with above the urban canopy which is more influenced by the current air velocity. Also the results demonstrate the accuracy of collecting input data affect the outcomes. Since at the moment, ENVI-met is programmed to calculate the inflow profile just based on the input data for one level (2 m), using the data collected in different levels can influence the results significantly.



Table 5-9: Indicators showing the of ENVI-met model performance for different input weather data forcing

Model Name	grid size	Forced by	at BPI			at WIS		
			RMSE	CV	d	RMSE	CV	d
4m-b	4m	BPI-data	1.48	5.33	0.95	1.24	4.35	0.97
4m-w	4m	WIS-data	1.54	5.54	0.95	0.88	3.10	0.99
5m-w	5m	WIS-data	1.59	5.74	0.95	0.78	2.75	0.99

Table 5-10: Indicators showing the ENVI-met model performance in comparison with observed data for different days

Model Name	Date	at BPI			at WIS		
		RMSE	CV	d	RMSE	CV	d
4m-w	13.7.2011	1.54	5.54	0.95	0.88	3.10	0.99
4m-w	12.7.2011	1.09	4.67	0.95	0.73	3.09	0.98
4m-w	22.6.2011	1.67	6.69	0.94	1.02	3.98	0.98

### 5.3. Parametric Analysis

Due to limitations associated with the on-site measurements such as impossibility of changing the pavement type of the area, some of important parameters necessary for the description of the urban micro-climate variation, like the role of pavement type or amount of vegetation, could not have been measured via empirical inquiries. Hence, the effect of those parameters was investigated using numerical simulations. Therefore nine scenarios pertaining to change in vegetation density, materials properties and geometry of the urban fabric were defined:

- Increasing in the amount of vegetation:
  - **V1:** Trees;
  - **V2:** Green roofs;
  - **V3:** Combination of trees and green roof;
- Changing the materials properties:
  - **M1:** Permeable pavements;
  - **M2:** White roofs;
  - **M3:** Light walls;
- Combination of change in materials properties and vegetation density:
  - **VM:** trees and green roofs with permeable pavement;
- Different aspect ratios:
  - **H1:** Lower aspect ratio;
  - **H2:** Higher aspect ratio;

In this way, the simulation results concerning each of the above mentioned scenarios were compared with those of obtained for the base case to depict the effect of each.

To obtain a deeper understanding about the influence of the defined parameters on the micro-climate of different urban spaces, the four following urban spaces were selected in the model:

- “Wiedner Hauptstrasse”, a North-South oriented street
- “Paniglgasse”, an East-West oriented street
- “Apfelgasse”, a North-South oriented street
- Courtyard, a large courtyard surrounded by buildings,

These spaces are shown in figure 5-8 and their properties are described in table 5-11.

Table 5-11: The properties of the locations

location	pavement	vegetation	orientation	SVF
Wiedner Hauptst.	Asphalt	0%	N-S	0.35
Paniglg.	Asphalt	0%	E-W	0.22
Apfelg.	Stone	0%	N-S	0.18
Courtyard	Stone	80%	---	0.11

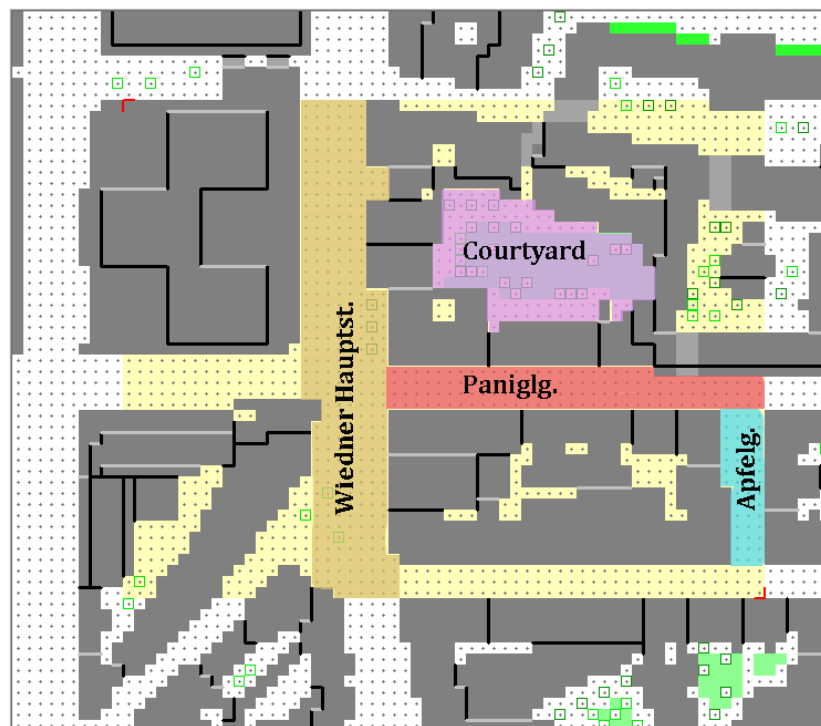


Figure 5-9: Different urban spaces surveyed in the parametric analysis for the Main Model

### 5.3.1. Main Model, Base case

The model described in the section 5.2.1, which was made and set based on the real geometrical and material properties of the urban area, is used as the “Base Case” for the parametric analysis. Simulations were performed for a time period starting of 5:00 h on July 13<sup>th</sup> to 4:00 h on July 14<sup>th</sup> 2011. Sky was considered clear during the simulation and associated weather data obtained from the WIS were used for forcing. Air temperature during this day was fluctuating between 21.5°C and 33.5°C. The average relative humidity was around 52% and the specific humidity was

fluctuating between 10.5 to 12 g.kg<sup>-1</sup>. For this day the average wind speed above the canopy was around 2.5 m.s<sup>-1</sup> and the prevailing wind direction was from South-East to North-West (for further information about input data see appendix B).

To evaluate the results of modifications and study of their effects on micro-climate of the defined areas mean value of the outputs of all the grids inside the defined borders for every area was calculated as represented value for respective urban space. Furthermore the mean value of all the grids once for all the streets and once for the whole area in the core of model except buildings (yellow area in figure 5-8) was calculated. Then the results of every scenario were subtracted from base case (current condition) to show the magnitude of modification done in the weather condition.

Due to variation in characteristics of the locations, as it is seen in figures 5-10 and 5-11, air temperature as well as the specific humidity varies within the model. Likewise, the conclusions of the empirical inquiries in section 4.2.3 have shown that locations with higher SVF are warmer during the day and cooler during the night, reverse is valid for locations having lower SVF. “Wiedner Hauptstrasse” with a SVF of about 0.35 has the highest SVF in the model area and is the warmest during the day and the courtyard with a SVF equal to 0.11 has the least SVF; and that is the coolest location during the day. SVF calculation for “Paniglgasse” and “Apfelgasse” are 0.22 and 0.18 respectively. The SVF mean value for the whole surveyed area (model domain) is about 0.22.

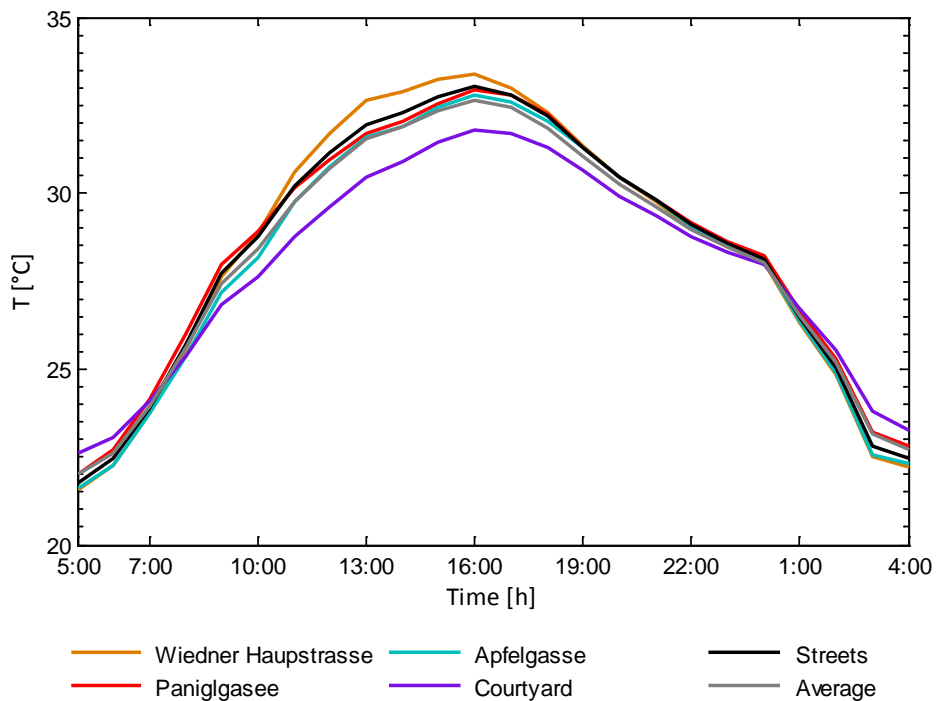


Figure 5-10: Simulated air temperature for defined locations at 1.4 m above the ground level (the base case)

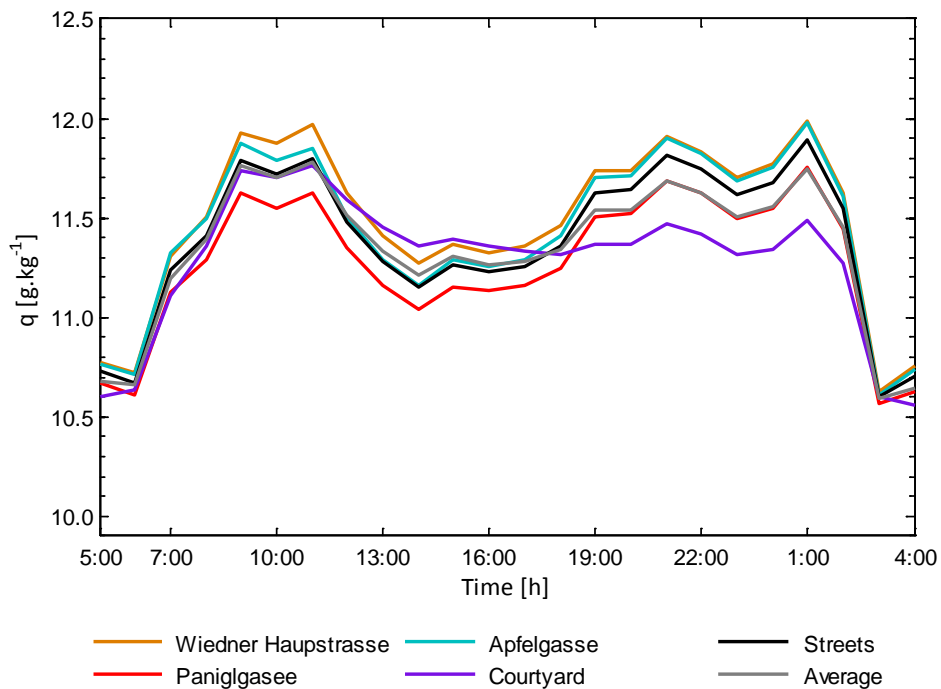


Figure 5-11: Simulated specific humidity for defined locations at 1.4 m above the ground level (the base case model)

### 5.3.2. V1: Vegetation change, trees

In this scenario to increase the amount of the vegetation (with reference to the base case) 100 trees were added to the domain. Most of them were distributed within the streets and a few in the courtyards (courtyards already had some trees). The type of the trees used was Robinia with 12 m height and 7 m crown diameter, for which default properties, defined by the program (for further information see appendix E5), were used. The density of trees in the area has been increased in this way from 21 trees/hectare to 50 trees/hectare. This scenario is shown in figure 5-12.

The results of this simulation are shown in Figure 5-13. It can be seen adding trees has caused an air temperature decrease in the streets of about 0.7 K, and in the whole model area of about 0.5 K. As mentioned in section 2.4, vegetation modifies the micro-climate of the area by shading and evapotranspiration, both these factors are related with solar radiation effect. Since “Wiedner Hauptstrasse” as a wide street and “Paniglgasse” as an East-West street are longer exposed to the solar radiation, therefore by the additional trees their micro-climate is more influenced than that of the “Apfelgasse” which is a narrow North-South street and the courtyard with the lowest SVF.

Besides, measurements done by (Dimitrova et al. 2014) show an average 0.5 K difference in air temperature between streets with and without trees which approves the simulated results in this work.



Figure 5-12: view of the 3D model V1

Likewise, the evapotranspiration via trees has a strong correlation with the solar radiation (see section 3.3.6. vegetation model). It can be seen in figure 5-14 that additional trees caused an increase in the air specific humidity in the model area after sunrise. The most cooled areas have accordingly more water vapor concentration during the day. After the sunset the humidity differences in the whole model area has dropped and stayed steady during the evening and the night.

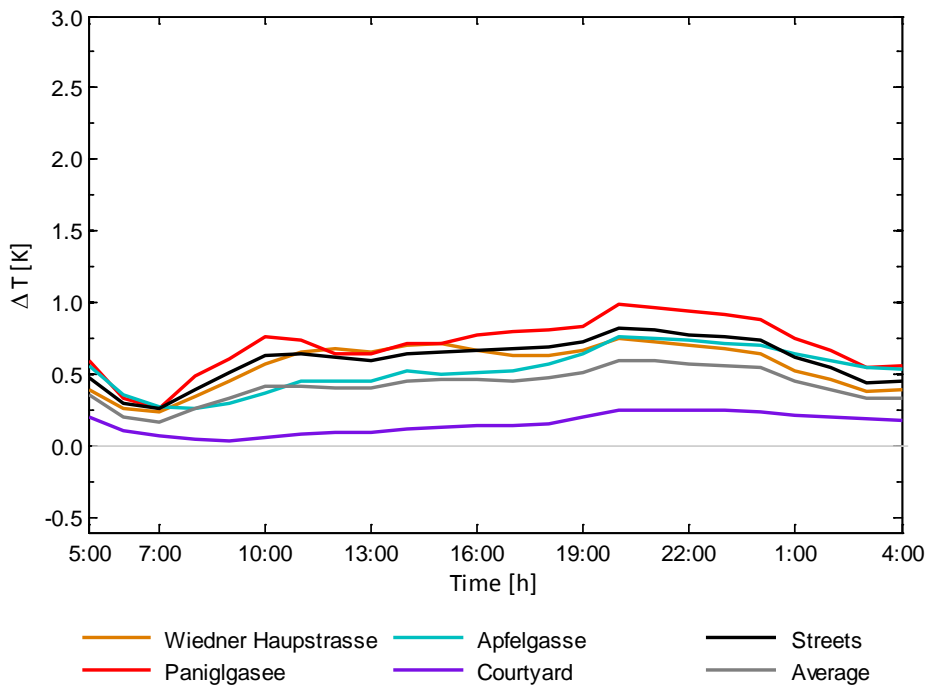


Figure 5-13: Air temperature differences between the base case and V1 (B - V1) at 1.4 m above the ground level

In this scenario the air temperature and the humidity in the courtyard has not been influenced significantly. Because this courtyard was already vegetated in the base case and was already shaded by the trees so no more tree was added to this area.

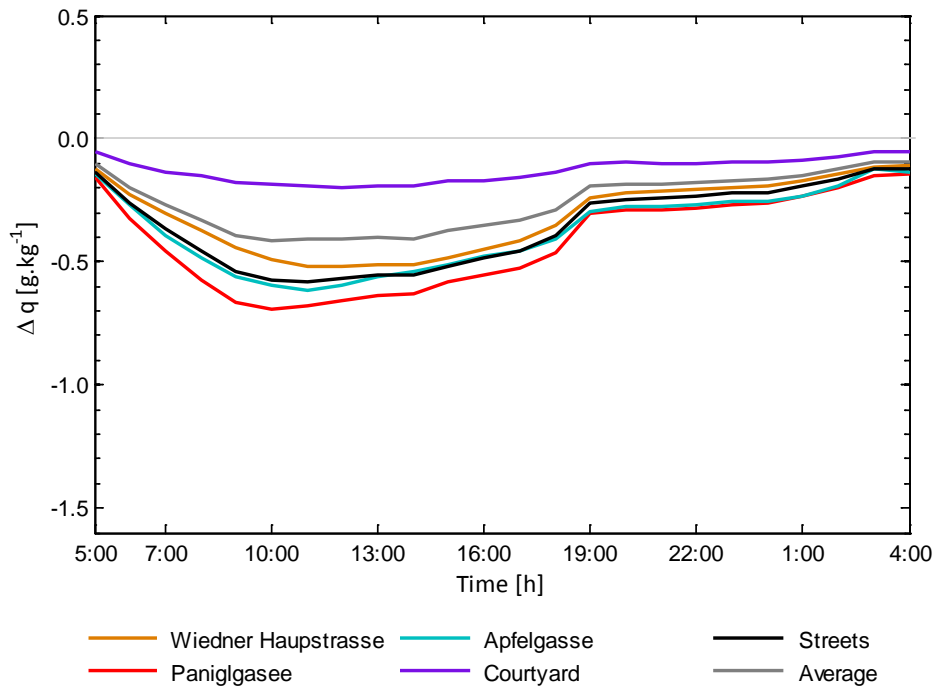


Figure 5-14: Water vapor concentration differences between the base case and the scenario V1 (B - V1) at 1.4 m above the ground level

### 5.3.3. V2: Vegetation change, green roof

In the Base Case, there is no green roof in the model area and most of the roofs are pitched. For this scenario just the capable roofs (flat roofs) were converted to green roof. The roofs were identified using the “Grun dachpotenzial ketoster” (Vienna City Administration n.d.). At the end, green roof was implemented on 60% of the roof areas within the model. By doing this, the selected vegetation type was grass with a height of 18 cm and an albedo of about 0.2. The humidity of the soil is in its maximum possible condition and plants never reach to the stress condition during the simulation interval. The above mentioned scenario is shown in figure 5-15.



Figure 5-15: view of 3D model of scenario V2

Green roofs alter the urban micro-climate via decreasing the surface temperature (Gartland 2008) by shading the roof surface and using the sun energy for evapotranspiration. Thus, the lower surface temperature leads to the lower air temperature. Nevertheless figure 5-16 depicts a slight cooling in the air temperature, about 0.3 K, for this scenario. This may have been caused by the uniformity of buildings height.

The uniform building height decreases the possibility of mixing the air above the canopy with the air inside the canopy. Consequently, in such urban configuration, green roof, which influences the air layer above the roof surface, can hardly affect the pedestrian level. Likewise, in this model as it is illustrated in figure 5-17, the air passing above the buildings has the least interaction with the air within the canopy.

Since all of the roofs were not capable of replacing by green roof. Thus, a homogeneous cooling effect because of the green roofs cannot be expected within the model according to the wind direction scattering and the existing variation in the density of the green roofs; so some areas may be affected more and some other less. Concerning “Wiedner Hauptstrasse” and “Apfelgasse”, this could be the reason why they are swayed more than other locations by the green roof, while the courtyard is not affected considerably.



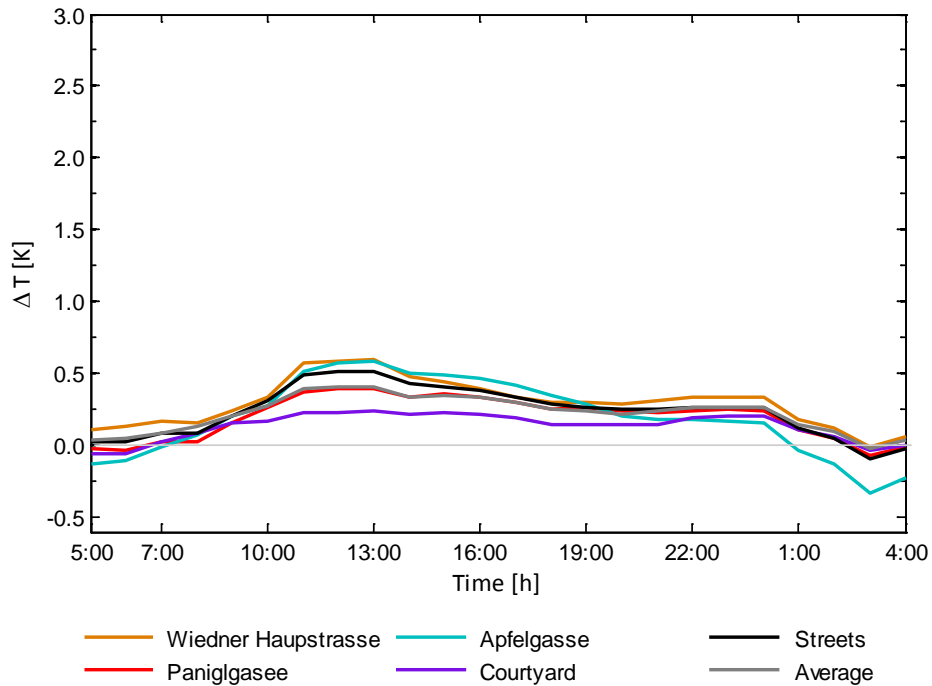


Figure 5-16: Air temperature differences between base case and V2(B – V2) at 1.4 m above the ground level

During the night while the magnitude of the short wave radiation is zero, the long wave radiation heat flux is the major part of the energy balance equation. In the absence of the solar radiation, the urban surfaces including buildings, the ground and plant surfaces emit long wave radiation and lose heat. As mentioned in section 3.3.11, one of the short-comings of ENVI-met is that emitted Long wave radiation by buildings and plants is calculated based on average temperature of surfaces within the model. In terms of the green roof scenario, the covered roof surfaces by the grass were not contributing to the warm up during the day as bare roofs could have done, thus the average surface temperature within the model decreases comparing to the base case model. Consequently the long wave radiation budget has been underestimated within the canopy, where the surface temperature has not changed significantly. Subsequently, the calculated amount of the released heat from the surfaces to the sky was less compared with the base case resulting in higher surface temperatures in the model area and accordingly the higher air temperature. This can be the reason why during early morning, before the sunrise, the air temperature in this scenario was higher than that of as in the base case.

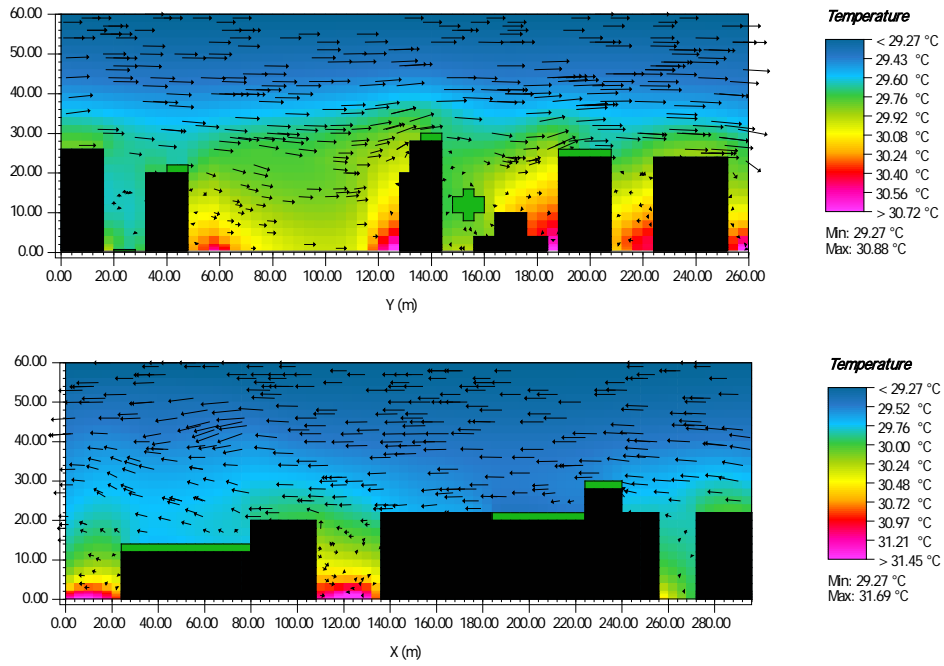


Figure 5-17: Vertical view of wind distribution in the scenario V2

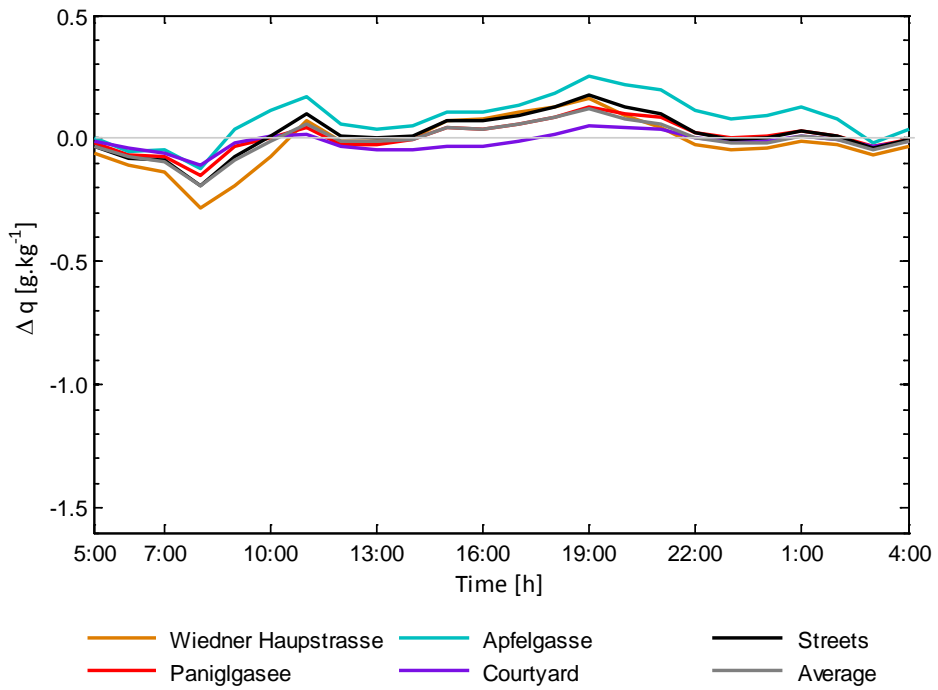


Figure 5-18: Water vapor concentration differences between the base case and the scenario V2(B – V2) at 1.4 m above the ground level

### 5.3.4. V3: Vegetation change, trees and green roof

In previous scenarios, V1 and V2, the effect of increase in amount of the vegetation within the canopy layer (V1) and above it (V2) was surveyed, separately. This scenario, V3, was defined to evaluate the effect of combining the two aforementioned scenarios, V1 and V2, on the urban micro-climate within the model area. To do so, as it is illustrated in figure 5-19, 100 trees with the same pattern as V1 was added to the area, and the green roofs were implemented on all the possible roof like as V2.



Figure 5-19: view of the 3D model after adding the trees and green roofs (scenario V3)

The results showed (figure 5-20) in this scenario the air temperature of all the streets has decreased almost equally, about 1 K. Courtyard as like the first scenario (trees) is not affected significantly due to the aforementioned reasons in section 5.3.2. Comparison among the results of V1, V2 and V3 showed as expected a somehow cumulative effect of V1 and V2 can be considered in scenario V3. This may especially be traced back to the fact that the cooling down mechanism in each of the scenarios V1 and V2 are acting independent from each other in case of the scenario V3 in affecting the air temperature in the model domain. But to come up with a certain conclusion on the interactive influence of these two modifications more measurements and investigations are needed.

In case of specific humidity, as it is shown in figure 5-21, the same discussion can be applied. Besides, a reverse relationship between the air temperature and the specific humidity could be observed, the more reduction in the air temperature the more increase in water vapor concentration in the air, verifying the role of plants in reducing the air temperature through evapotranspiration effect.

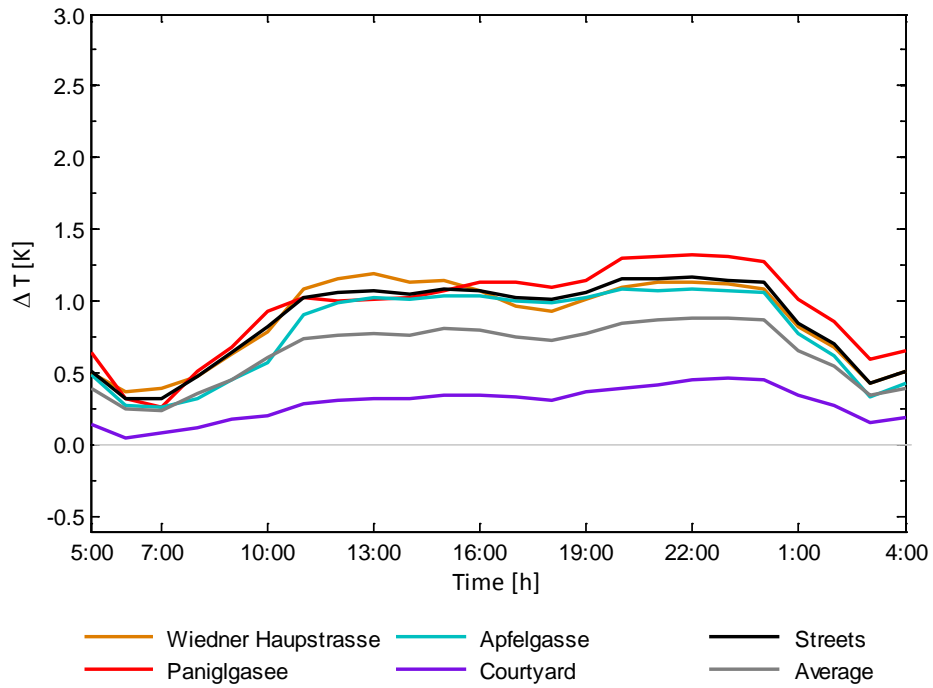


Figure 5-20: air temperature differences between the base case and the model after implementing additional trees and green roof (scenario V3), (B – V3) at 1.4 m above the ground level

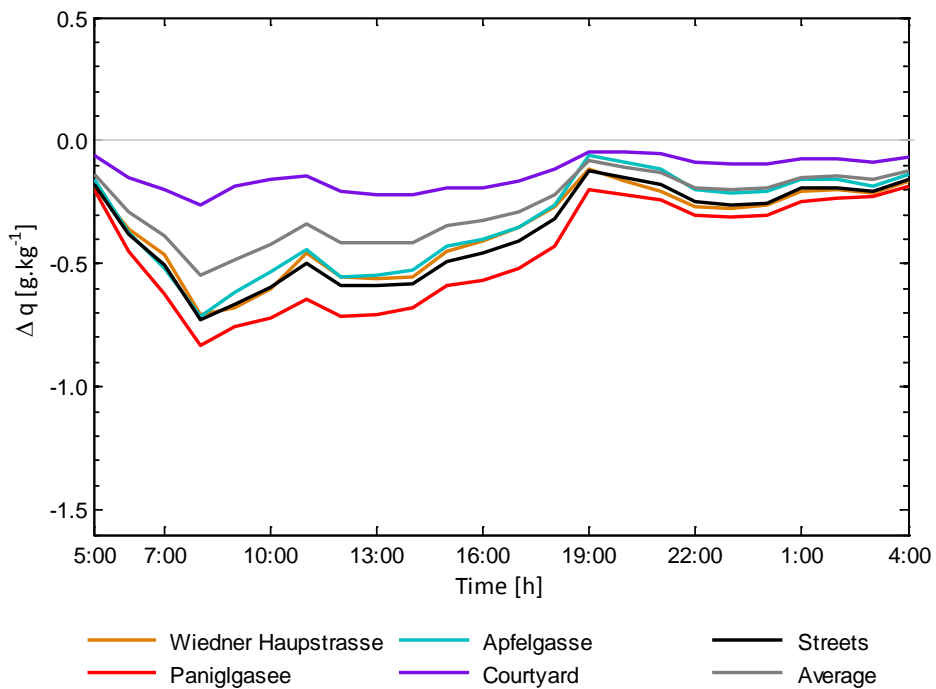


Figure 5-21: Water vapor concentration differences between the base case and the model after implementing additional trees and green roof (scenario V3) (B – V3)

### 5.3.5. M1: Material properties change, permeable pavement

In the main model (in the base case), 18% of the unbuilt area comprises of natural soil, mostly placed inside the courtyards as a constituent of the gardens; and the rest of the surface (i.e. 82%) is sealed (asphalt, stone). In scenario M1 the existing pavements of the narrow streets, all the existing sealed surfaces of the courtyards and the sidewalks of the wide streets have been replaced with a permeable material. For this purpose, pervious concrete, with less water content capacity and more hydraulic conductivity than loamy soil (for more details see Appendix E1) was used. Through this implemented modification the fraction of the permeable surfaces increased to 53% (of the unbuilt space). Figure 5-22 illustrates the scenario M1.

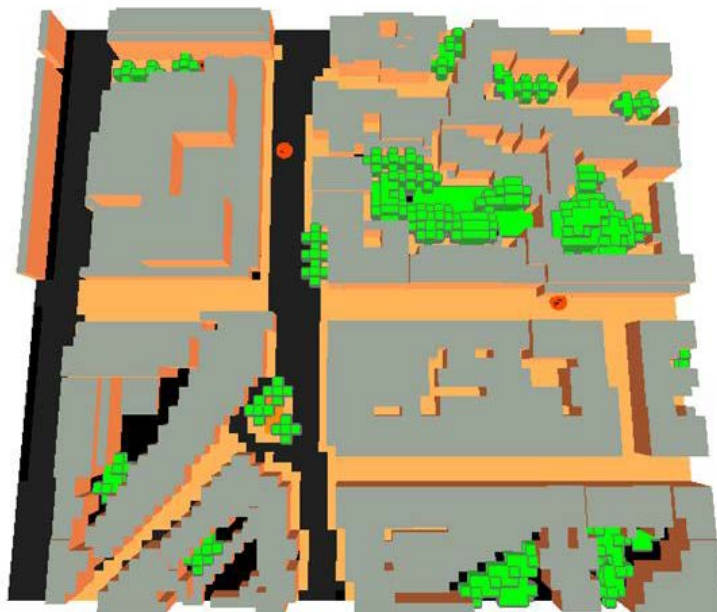


Figure 5-22: view of the 3D model after adding the permeable pavements (scenario M1)

Construction of permeable pavements causes a temperature reduction in the ambient air through evaporation. This means that on hot days with lower relative humidity the cooling effect of evaporation is more significant than it is on cooler days.

Figure 5-23 depicts how the change in the perviousness of the pavements has influenced the air temperature of the area. As it can be seen, the average air temperature in all streets has been decreased 0.3 K to 1.4 K during the simulated time. In “Paniglgasse”, which in this scenario is completely paved by permeable materials, the observed cooling effect was around 1.7 K during the day and around 1 K during the night time. In “Wiedner Hauptstrasse” just the pavement of the sidewalks were changed. As a result the decrease in ambient air temperature was less than that of in “Paniglgasse”, i.e. 1.4 K cooling during the day and about 0.6 K during the night. “Apfelgasse”, which is parallel to “Wiedner Hauptstrasse” but with

less width, shows a similar air temperature difference trend as in case of “Wiedner Hauptstrasse” was observed, but with 0.2 K less cooling although its all of the pavement had been changed.

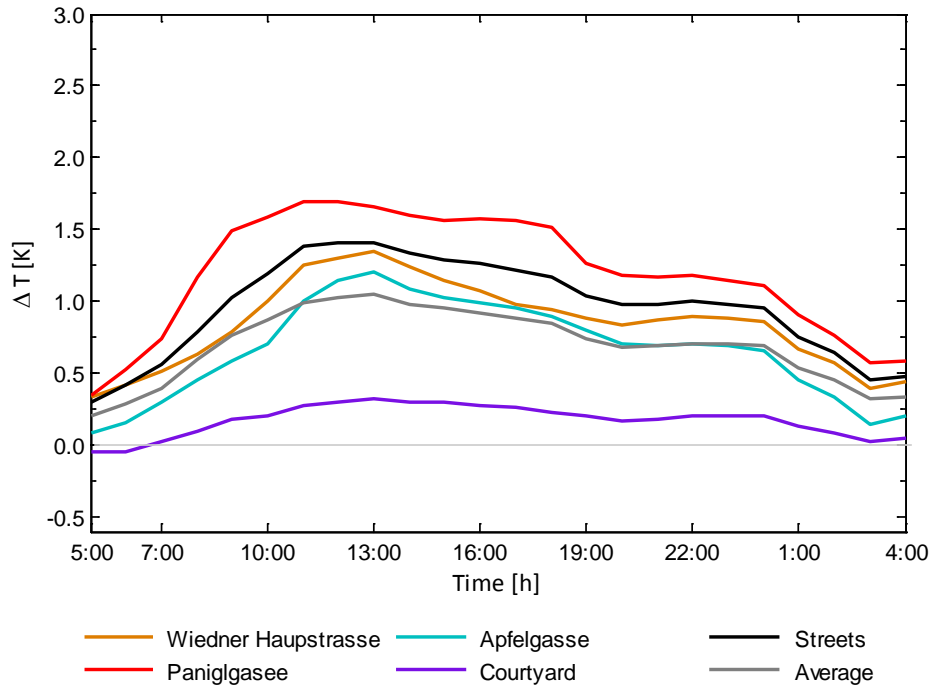


Figure 5-23: Air temperature differences-between the base case and the main model as defined by scenario M1 (B – M1) at 1.4 m above the ground level

Overall air temperature reduction pattern in scenario M1 showed that the cooling effect of permeable pavement integration in an urban fabric is somehow in direct relation to the exposure of the paved areas to the solar radiation. The locations with higher SVF or longer daily exposure time to the solar radiation (due to their orientation), showed more reduction in the ambient air temperature. For example “Wiedner Hauptstrasse” with a higher average SVF comparing to “Apfelgasse” (0.35 vs 0.18) showed more cooling, and “Paniglgasse” having a higher daily exposure time with respect to that of “Wiedner Hauptstrasse” (or that of “Apfelgasse”) showed more cool down as well. The extent of the implemented changes in the area is another effective factor, caused dissimilar changes in the different locations.

As it can be understood from figure 5-24, like the other scenarios (V1, V2, V3), in which the cooling of the ambient air was caused by evaporation, also in this scenario the water vapor concentration in the environment has been increased in a reverse relationship with the associated air temperature reduction. As it is shown in figure 5-23 and 5-24, in the courtyard, which is widely vegetated and the major part of its ground surface is covered by grass (70%), such a small change in the form of

replacing its stone-pavement could not have caused a considerable change in its ambient air temperature and humidity.

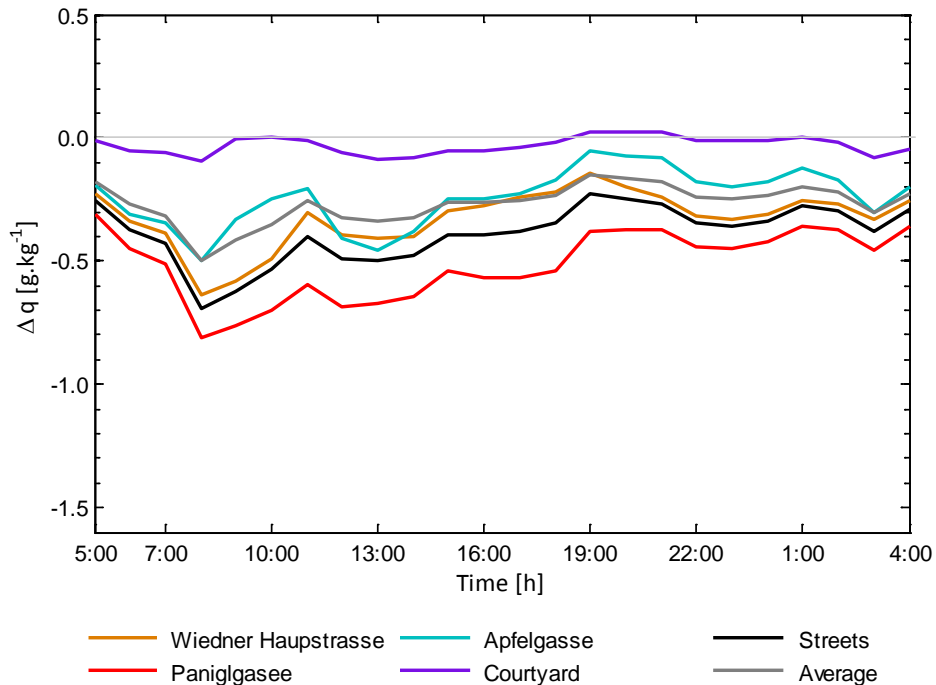


Figure 5-24: Water vapor concentration differences the base case and the main model as defined by scenario M1(B – M1) at 1.4 m above the ground level

### 5.3.6. VM: Combination of scenario V3 and M1 – increasing vegetation and applying impermeable materials

Scenario VM was defined to evaluate the interaction between all the changes modifying the urban micro-climate through evaporation. In order to do so, as it is shown in figure 5-25, scenarios V3 and M1 were combined together to form VM. For this purpose, trees and green roofs were added to the model area in the same pattern as V3 and the existing pavements of the narrow streets, courtyards and the sidewalk of the wide streets was replaced with permeable pavements as like as M1.

Studying of the air temperature changes caused by this scenario, as shown in figure 5-26, revealed the fact that although the observed air temperature difference between VM and the Base Case is the largest among other scenarios, i.e. V1, V2, V3 and M1; while matching the expectations, it did not show a cumulative effect of the mentioned scenarios. The reason could be traced back to the fact that, unlike scenario V3, in this scenario, two types of modifications, i.e. increasing the extent of vegetation (adding trees) and that of permeable pavements, were applied to the canopy layer (within the canopy). Hence it may be concluded, the shades of the

added trees has weakened the cooling effect of the additionally embedded permeable pavements.



Figure 5-25: View of the 3D model after adding more trees and green roof as well as changing the sealing to the permeable pavement (scenario VM)

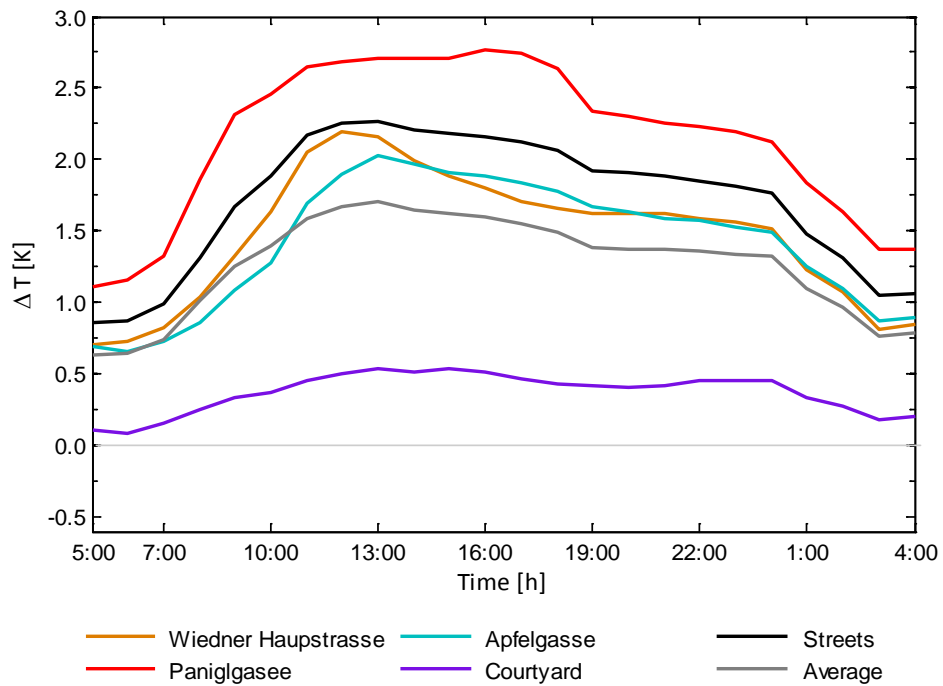


Figure 5-26: Air temperature differences between the base case and the model after adding more trees and green roof as well as changing the sealing to the permeable pavement (scenario VM), (B – VM) at 1.4 m above the ground level



Since all the changes, made in the area, mostly influence the micro-climate via evaporation and partially by shading (in case of trees) consequently, as it is shown in figure 2-27 a significant water vapor concentration increase (up to  $1 \text{ g.kg}^{-1}$ ) was observed in the model domain. The amount of increase in the air specific humidity seemed to be dependent on the extent of the alteration applied, i.e. the more changes applied, the higher increase in the air specific humidity could be noticed in the model domain.

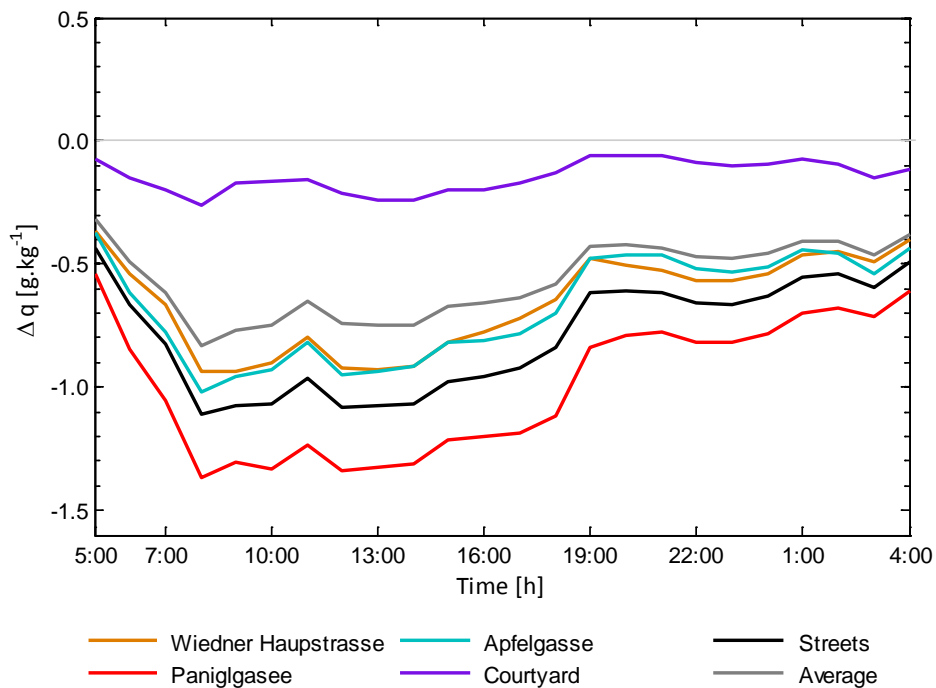


Figure 5-27: Water vapor concentration difference between the base case and the model after adding more trees and green roof as well as changing the sealing to the permeable pavement (scenario VM), (B – VM) at 1.4 m above the ground level

### 5.3.7. M2: Material properties change, white roofs

The aim of defining scenarios M2 and M3 was to evaluate the influence of increasing the reflectivity of the urban surfaces, M2 for roof surfaces and M3 for the walls. In the main model (in the base case) around 60% of the model area was occupied by buildings, whose roofs were in dark colors with a reflectivity of about 0.3 (i.e. the selected reflectivity in ENVI-met for the roof material in the base case was 0.3). To match the above-mentioned goal, as illustrated in figure 5-28, in this scenario all roof materials were replaced with a material having a reflectivity of 0.8. The results of the performed simulations, as it is seen in figure 5-29, revealed a slight effect in

terms of cooling down the ambient air temperature, i.e. the implemented modification has just caused a slight decrease in the air temperature at the pedestrian level. The observed reduction in the air temperature seemed to be somehow identical in all streets (max. cool down of about 0.5 K); however the courtyard and the consideration of an average value for the whole area showed even a less cool down effect.



Figure 5-28: view of the 3D model after increasing the roofs reflections (scenario M2)

Since light-colored roofs reflect the major portion of the incident solar radiation during the day, their surface temperature can be up to 40 K less than that of the dark roofs with a 0.2 to 0.3 reflectivity (Gartland 2008). Therefore the ambient air temperature in the vicinity of light-colored roofs would be less than that of in the vicinity of darker roofs; and due to air movements it can even influence the pedestrian level air temperature, as well (Gaffin et al. 2010). But depending on the wind speed and distribution pattern its impact will vary among different locations, so the cooling effect of light-colored roofs cannot be expected to be identical all through the whole model domain. Thus it can be the reason why in this scenario streets are more affected than the courtyards. On the other hand, during the night when the shortwave radiation in the model energy balance (see equation 2-1) is zero, reflectivity of the building surfaces could not play a role in this regard (under the condition that the emissivity of the surfaces has not been changed, as it was the case here), so it was expected that the ambient air temperature during the night to be either slightly cooler or at least equal to that of as observed in the base case.

Instead, as shown in figure 5-29, at some locations such as “Apfelgasse” even higher temperatures during the night were observed. The reason could be traced back to the existing limitations of ENVI-met by a correct consideration of the long wave radiation contribution in the energy balance for a model in the path of its simulation. As it had already been mentioned in section 5.3.3 (scenario V2),

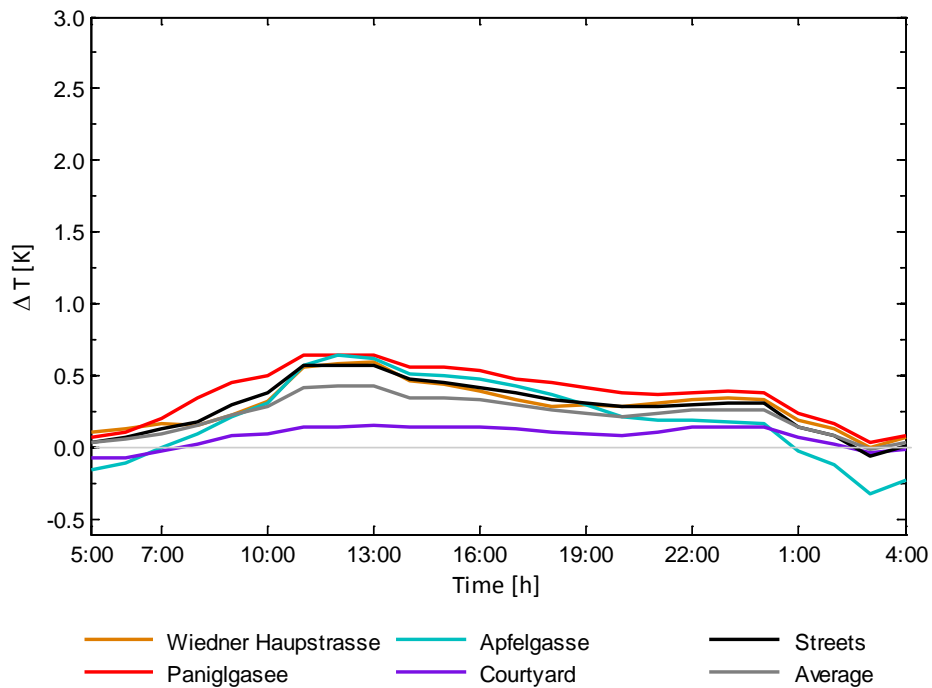


Figure 5-29: Air temperature differences between the base case and the model after increasing roofs reflections (scenario M2), (B – M2) at 1.4 m above the ground level

The results pertaining to changes in the specific humidity are illustrated in figure 5-30. It can be seen that, unlike the air temperature, the water vapor concentration level has not been affected by the applied modifications. Probably because in most part of the area (streets) there is no source for evaporation neither before nor after the applied modifications; so the changes in the air temperature hardly affected the water vapor concentration level at any point. In the case of the surveyed courtyard, despite the fact that it consisted of vegetation to a great extent and accordingly a considerable source for evaporation, no significant change in the air specific humidity could be observed. This observation was expected, since the air temperature in the courtyard was not affected considerably as a result of the change in the roof reflectivity level, which could not have affected the radiation budget inside the canopy at this location. In any case in order to be able to make more clarifications on this issue more surveys in terms of measurements and simulations are necessary.

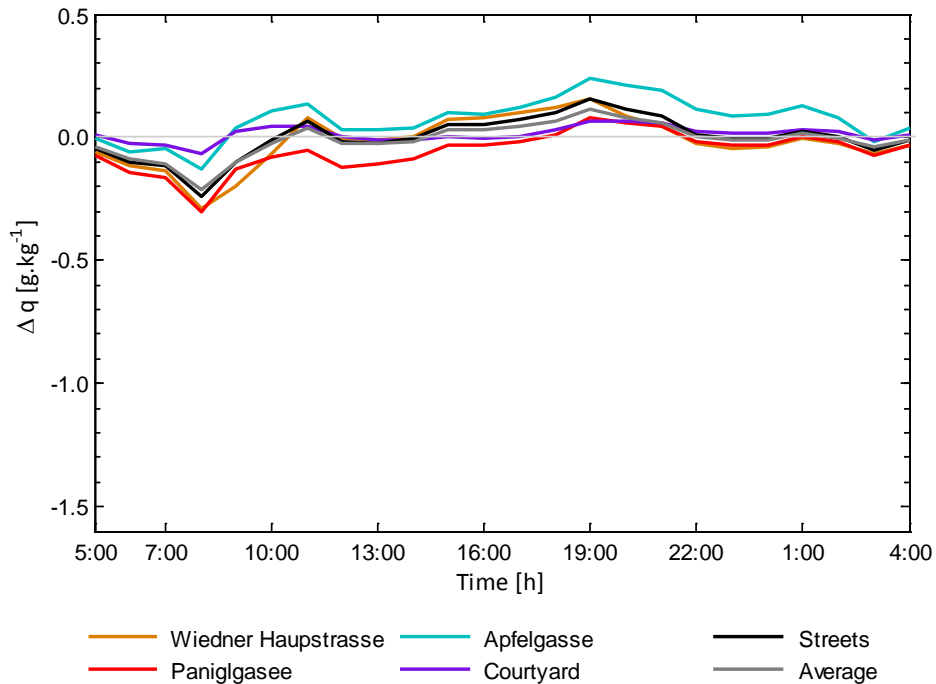


Figure 5-30: Water vapor concentration difference between the base case and the model after increasing roofs reflections (scenario M2), (B – M2) at 1.4 m above the ground level

### 5.3.8. M3: Material properties change, light Walls

The aim of this scenario is to survey the effect of using materials with higher reflectivity for the walls on the urban micro-climate. The total area of the buildings walls in the model domain is about 130400 m<sup>2</sup>. In the real condition their material and color varies in a wide range from the white plaster to the dark grey granite. But for simplification purposes, a material having a reflectivity of 0.4 was assigned to all the buildings in the Base Case. To match the goal of this scenario, as it is shown in figure 3-31, the reflectivity of the walls material was increased to 0.7.

Opaque materials with a higher reflectivity are cooler than the others when they are exposed to the short wave radiation, as they absorb less and accordingly reflect more. Consequently it was expected that their adjacent air temperature to be increased due to more reflected short wave radiation back into the neighboring air space. This fact was confirmed through the results obtained by this scenario. As it can be seen in figure 5-32, the walls with higher reflectivity caused higher air temperature within the canopy. The increase in the reflectivity of the walls resulted an increase in the magnitude of the global radiation inside the urban canopy and accordingly a slight upsurge in the air temperature. The increase in the air temperature is strongly related to the solar radiation thus after the sunset a fast

decrease could be observed, which approached to the value of the air temperature, as observed in the Base Case.



Figure 5-31: view of the 3D model after increasing the walls reflections (scenario M3)

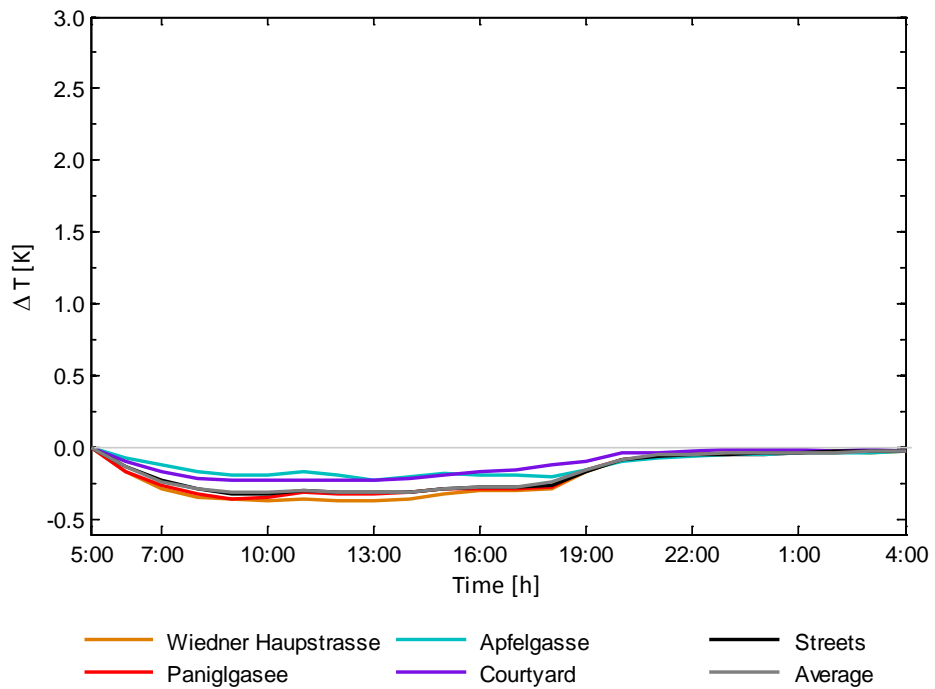


Figure 5-32: Temperature difference between the base case and the model after increasing walls reflections (scenario M3), ( $B - M3$ ) at 1.4 m above the ground level

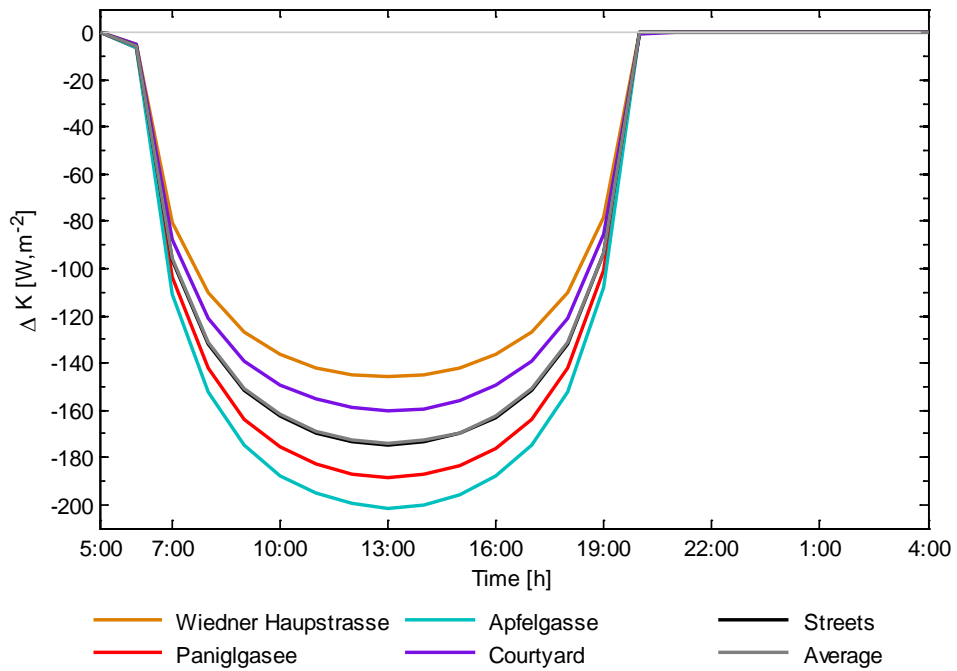


Figure 5-33: Global radiation difference between the base case and the model after increasing walls reflections (scenario M3), (B – M3) at 1.4 m above the ground level

For the air specific humidity, as shown in figure 5-34, changing the walls reflectivity did not have any effect in the streets. But a slight increase in the courtyards during the day was observed. It could be caused by the increase in the short wave radiation budget in the environment, which apparently has stimulated the plants to evapotransprate more resulting in more water vapor release to the environment.

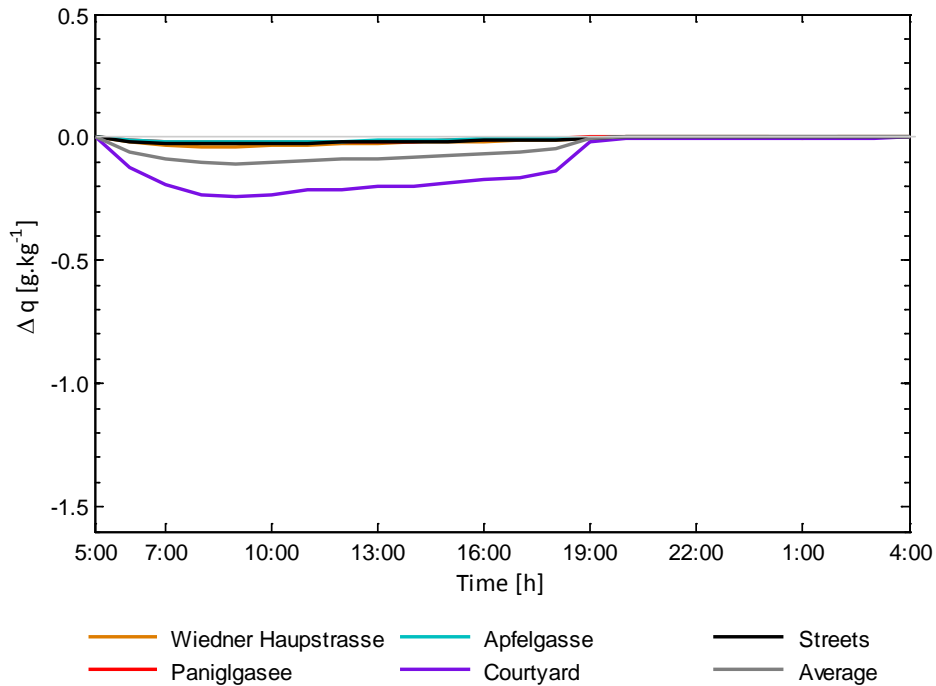


Figure 5-34: Water vapor concentration difference between the base case and the model after increasing walls reflections (scenario M3), (B – M3) at 1.4 m above the ground level

### 5.3.9. H1: Aspect Ratio change, lower aspect ratio

Effect of height of the buildings on the urban micro-climate was the last evaluated parameter in this study (scenarios H1 and H2). To investigate the possible effect, the height of all the buildings was decreased 30%. Such a change in the height of the buildings caused automatically a 30% decrease in the volume of the buildings as well as in the surface area of buildings facades. Figure 5-35 shows a view of the 3D model of above-mentioned scenario H1.

Decreasing the height of the buildings in one hand reduces the amount of the mass in the area and accordingly causes a decrease in the heat storage in the model domain. On the other hand such an act would increase the SVF pertaining to the exposure of the urban surfaces to the solar radiation. The effect of changes in height of buildings (change in SVF) on the amount of solar radiation striking urban surfaces depends on the angle of incident radiation. When the height of sun is low its effect is more significant. But when the sun height increases and incident solar radiation angle become closer to the 90° the effect of buildings height decreases. Thus during the morning and in the afternoon when the height of the sun is low, any reduction in the height of the buildings results in a significant increase in the amount of incident radiation and accordingly increase of the air temperature, but around noon time the effect of the buildings masses is the dominating one, i.e. its decrease causes a slight

drop in the air temperature. Likewise, during the night the higher SVF accelerates the cooling of the ground and the buildings surfaces causing a reduction in the ambient air temperature. The obtained simulation results for this scenario confirmed the above mentioned argumentation. The profile of the air temperature difference between the base case and this scenario (H1) is shown in figure 5-36.



Figure 5-35: view of the 3D model after decreasing the height of buildings to 70% of their current condition (scenario H1)



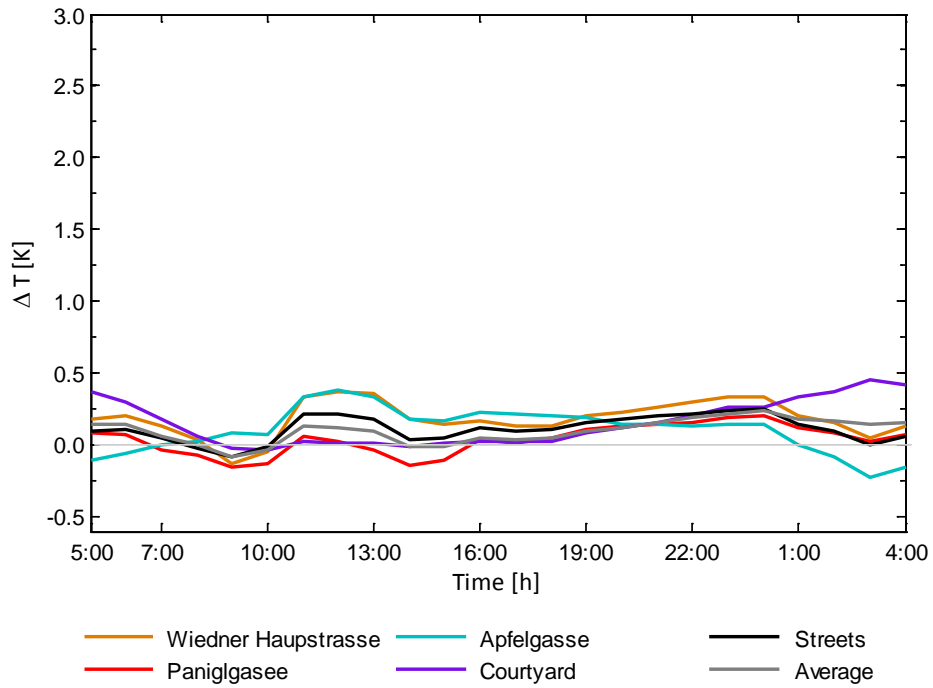


Figure 5-36: Air temperature differences between the base case and the model after decreasing the height of the buildings to 70% of its current condition (scenario H1), (B – H1) at 1.4 m above the ground level

Figure 5-37 illustrates the change in water vapor concentration caused by the recent modification. The water vapor concentration differences, like the air temperature, were fluctuating between below and above the zero during the day and night. The courtyard was the only location with constant increase in the humidity, which could be caused by the existing dense vegetation. Shorter buildings allow the plants to receive more solar radiation and accordingly release more water vapor to the environment resulting in an increase in the specific humidity.

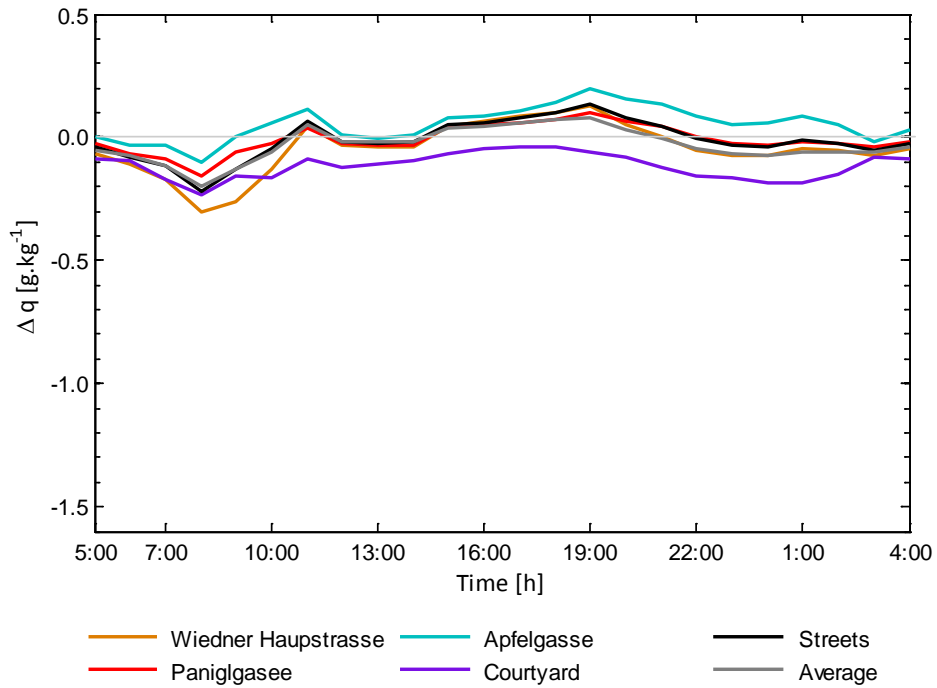


Figure 5-37: Water vapor concentration differences between the base case and the model after decreasing the height of the buildings to 70% of its current condition (scenario H1), (B – H1) at 1.4 m above the ground level

### 5.3.10. H2: Aspect Ratio change, higher aspect ratio

In this scenario by 30% increasing of the height of the buildings, the impact of the higher aspect ratio was investigated. The view of 3D model of this scenario is displayed by figure 5-38.



Figure 5-38: view of the 3D model after increasing the height of buildings up to 30% (scenario H2)

As it is seen in figure 5-39, higher buildings resulted in lower temperature in all the locations during the day. On the contrary during the night the air temperature was increased by about 0.5 K.

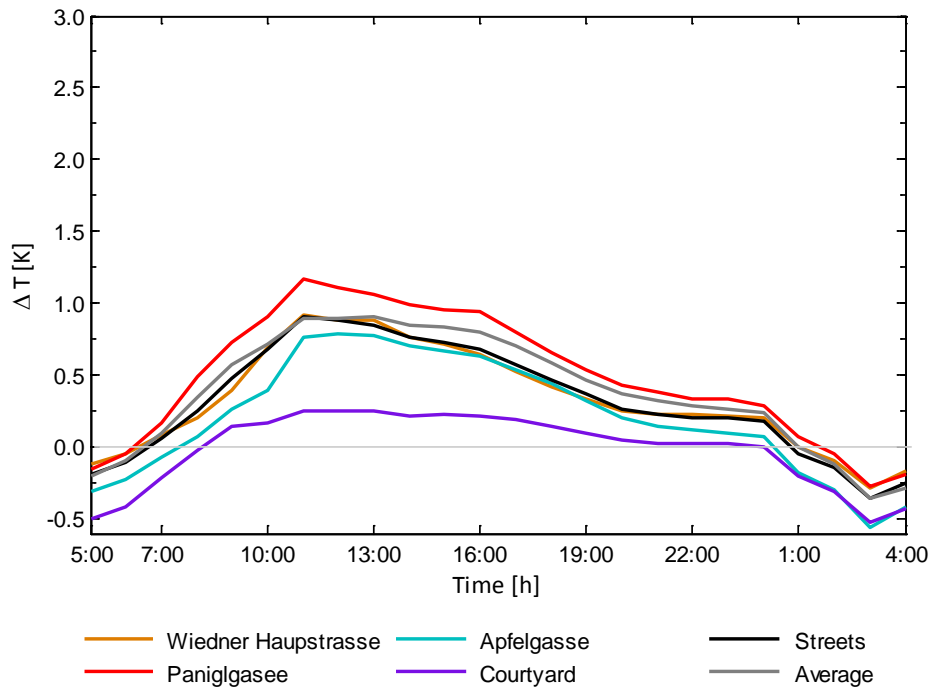


Figure 5-39: Air temperature differences between base case and the model after decreasing the height of buildings to 70% of its current condition (scenario H2), (B – H2) at 1.4 m above the ground level

Air temperature drop during the day can be explained by lower sky view factor induced by higher buildings. During the day higher buildings reduce the amount of the incoming incident solar radiation inside the canyon. Since the solar radiation constitute the major part of the energy of the urban energy balance equation (see section 2.2.1) any reduction in the input radiation heat flux can result in drop in the air temperature. On the other hand higher buildings limit the access of urban surfaces to the sky during the night. This in turn causes trapping of the emitted long wave radiation by the surfaces within the canopy (spaces between the building surfaces), which subsequently avoids the cool down of the associated surfaces during the night.

Based on the simulation results, the courtyard was not affected during the day as much as the canyons probably due to its size and the existing trees. Increasing the height of the buildings by 30% did not cause a big difference in sky view factor and accordingly the magnitude of the incoming solar radiation pertaining to this space. Therefore during the day the temperature was not changed significantly. The results showed that during the night the courtyard became warmer comparing to the base

case. It can be explained by the out-coming long wave radiation model used in ENVI-met. As it mentioned in sections 3.3.11 and 5.3.3 the out-coming long wave radiation heat, which causes the urban surfaces cool down, is calculated based on the average surface temperature within the model area. Higher buildings and accordingly lower sky view factor induce more shaded and cooler surfaces in the whole model domain. As a result the model has calculated less emitted long wave radiation from this space (due to the lower average surface temperature within the model area although courtyard surfaces temperature did not change), which has led to less cool down during the night compared to the base case.

Unlike the air temperature, water vapor concentration did not change considerably, as shown in figure 5-40, because of the aspect ratio change implemented in this scenario. The observed slight reduction in the air specific humidity may be traced back to the fact that the air temperature reduction due to the implemented higher aspect ratio has resulted in less evaporation in the area and accordingly less water vapor concentration.

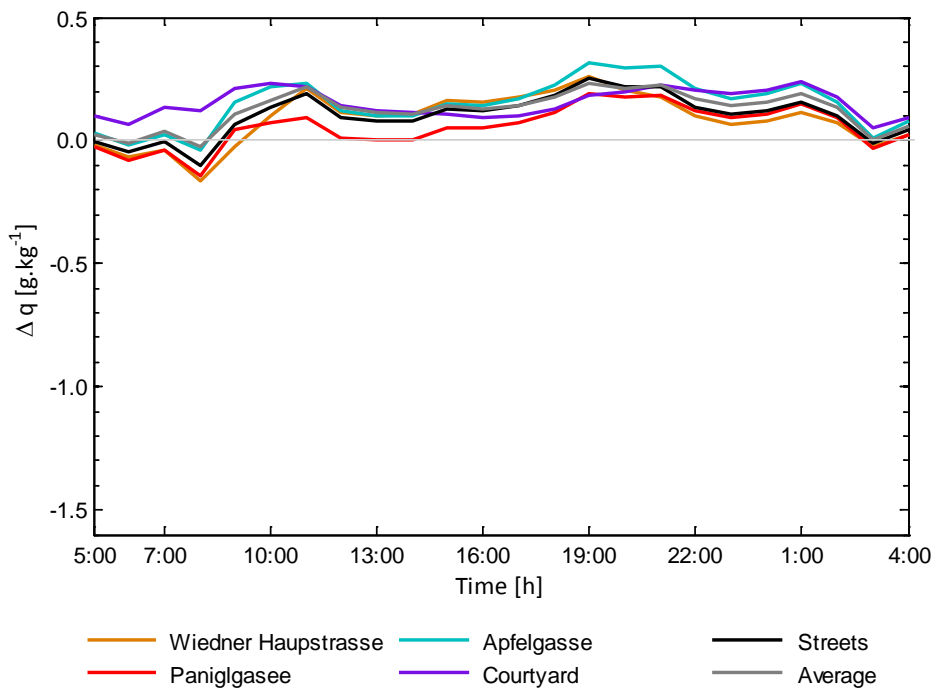


Figure 5-40: Water vapor concentration difference between base case and the model after decreasing the height of buildings to 70% of its current condition (scenario H2), (B – H2) at 1.4 m above the ground level

### 5.3.11. Overview, differences among all scenarios

The courtyards within the model domain either already contained vegetation and permeable pavements or were too small to have them. Hence, the implemented changes were mostly applied to the streets rather than courtyards. Therefore, to have a more detailed analysis about the overall influence of the applied modifications on the urban micro-climate, streets and the whole area were surveyed separately through figures 5-41 and 5-42. As it is seen in figures 5-41 and 5-42, due to above mentioned reason the effect of V1, V3, M1 and VM on the air temperature in the streets (Figure 5-42) was about 0.5 K more than average influence of them on the whole area (Figure 5-41). Another aspect regarding to the scenarios M2, M3, V2, H1 and H2 was that, by all of these scenarios a more homogeneous influence on the air temperature of the model area could be observed. The graphs showed that the scenario VM, which is about the combination of adding more trees and green roof as well as changing the ground surface sealing to the permeable pavement, has affected the air temperature at most, comparing to the other scenarios.

The scenarios M1 and V3 caused approximately equal reduction in the air temperature, but in different hours. The cooling effect of M1 was more during the day, while V3 showed more cool-down in the area during the evening and the night.

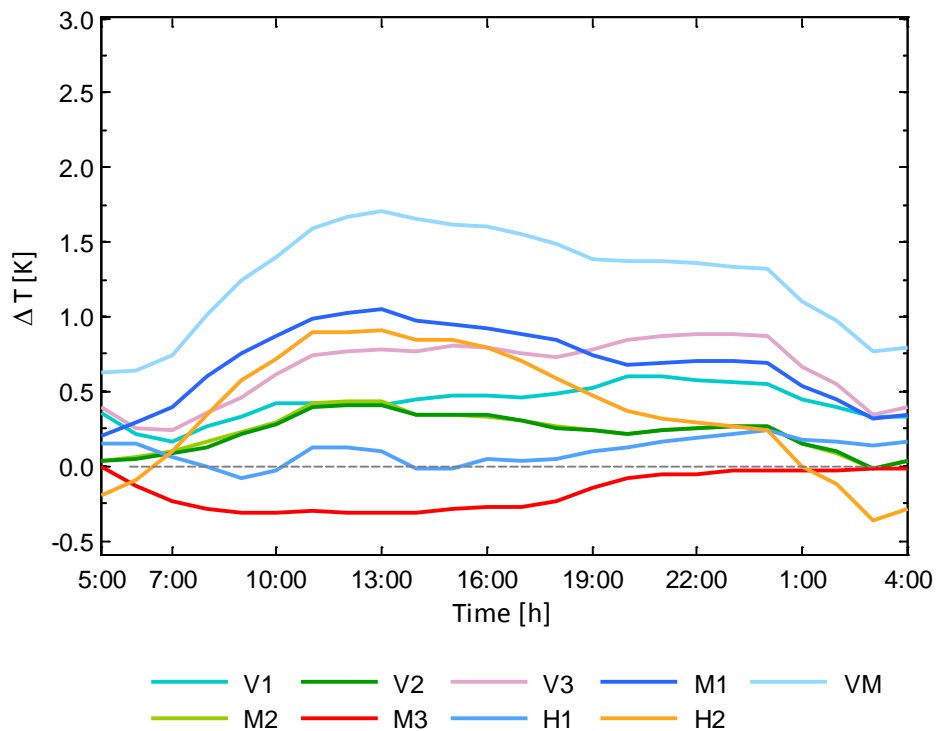


Figure 5-41: Average air temperature differences between scenarios and the base case within the model domain (Base – Scenario)

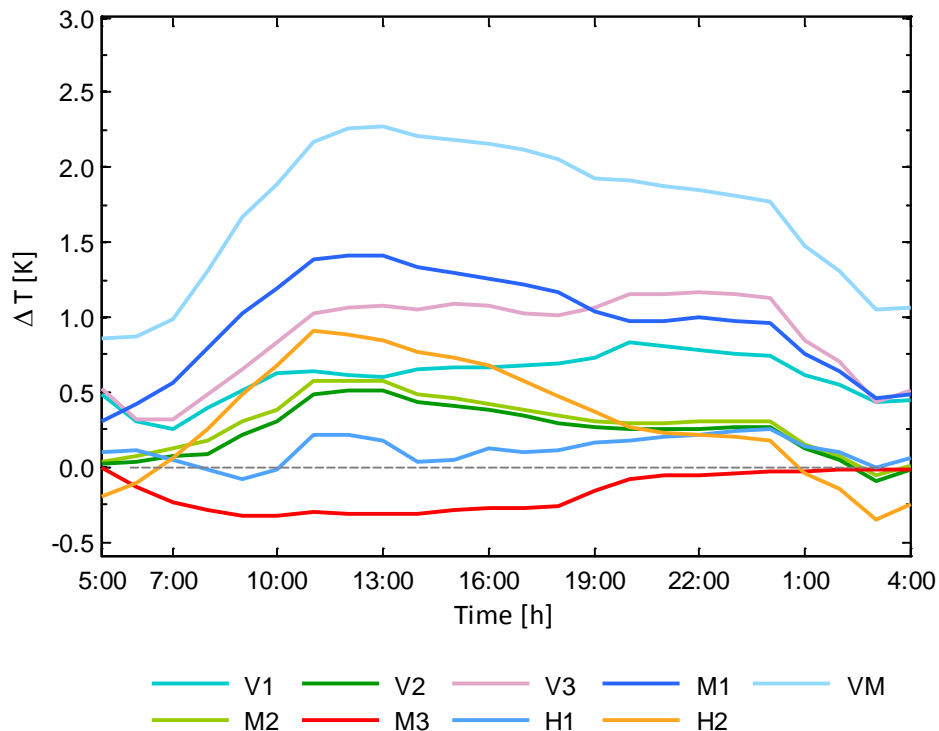


Figure 5-42: Average air temperature differences between scenarios and the base case within the streets (Base – Scenario)

By the scenarios V2 and M2 it was about changes applied on the surface of the roofs, hence their effect on the air temperature within the canopy layer was almost equal and in the same pattern. In any case to get a deeper understanding on how the applied changes through V2 and M2 would affect the microclimatic situation within a model, more measurements and simulations are needed.

In the scenario M3 the effect of walls with higher reflectivity was considered. Based on the achieved results, the scenario M3 showed a unique change in the microclimatic condition in the model domain, through which a slight increase in the air temperature was observed. Due to the modifications applied, an increase of about 0.2 K in the air temperature during the day could be noticed. It was further noticed that this difference (the temperature difference between M3 and the base case) was immediately disappeared after the sunset.

Among the scenarios, H1 caused the least effect on the air temperature (max about 0.2 K reduction), while through H2 (increasing the buildings height) the air temperature was decreased about 1 K during the day. However, during the night air temperature has been increased via H2.

The same method was employed to study the specific humidity changes in all the scenarios in figures 3-44 and 3-45.

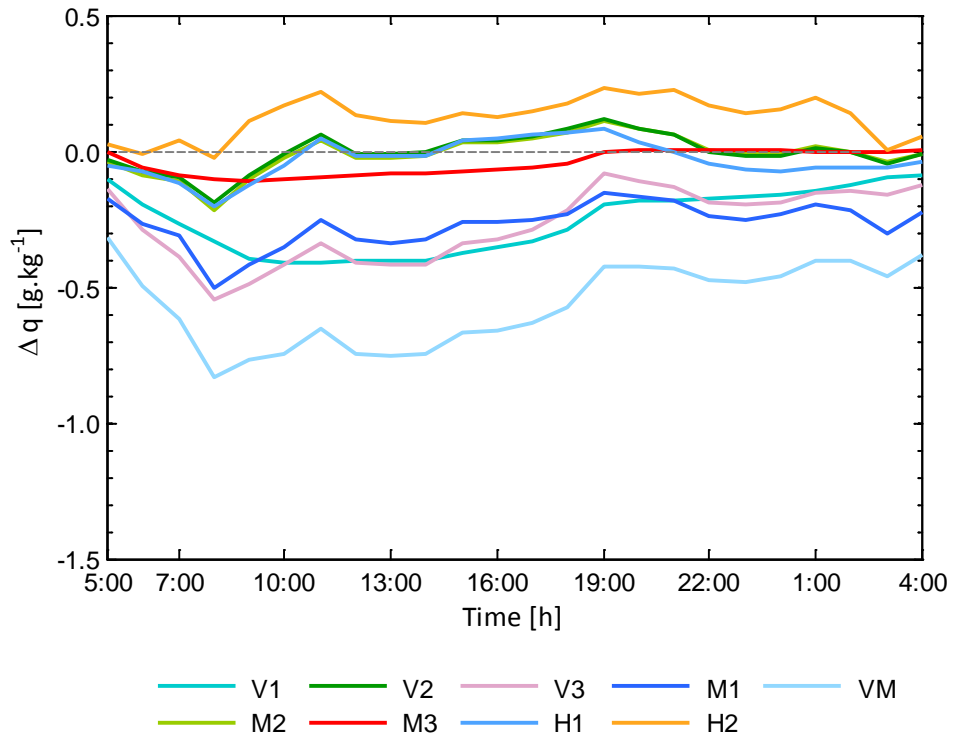


Figure 5-43: Average water vapor concentration differences between scenarios and the base case within the model domain (Base – Scenario)

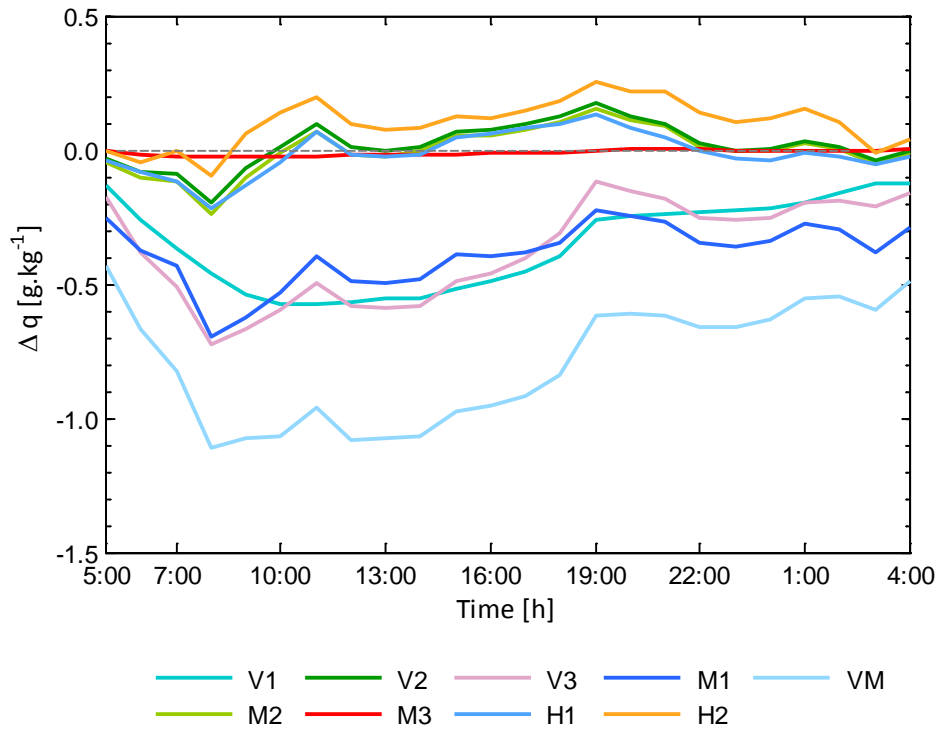


Figure 5-44: Average water vapor concentration differences between scenarios and the base case within the streets (Base – Scenario)

Figure 5-45 shows the average temperature differences between the base case and the scenarios during the 24 hours for every location separately. “Paniglgasse” as an East-West street was the most affected area by the modifications, meanwhile “Wiedner Hauptstrasse” as wider North-South oriented street seemed to be less affected, and “Apfelgasse” (parallel to “Wiedner Hauptstrasse”) was observed to be the street influenced at least. This can be explained by their orientation and exposure duration to the solar radiation. Since by most of the scenarios it was about altering the radiation budget within the canyons, areas with more incoming radiation (in terms of either higher intensities or more exposure time) got more affected by any change applied in the associated radiation factors. On the other hand in scenarios such as V2 (green roof), where the applied modifications had not happened inside the canopy the changes in the air temperature were almost equal throughout the whole areas. Concerning the courtyard, since the applied alterations did not change its properties significantly, so the changes in the results were not considerable and its air temperature was affected the least.



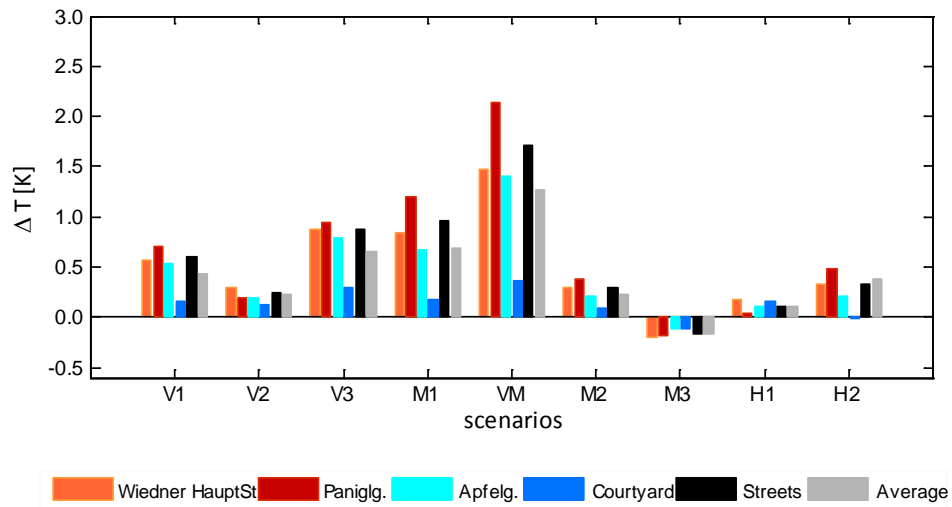


Figure 5-45: Average cooling effect of the evaluated scenarios for every location during 24 hours

Figures 5-46 and 5-47 show the average temperature difference between the current condition (the base case) and the different scenarios for the areas during the day and the night, respectively. The day and the night hours were defined according to the sunrise and sunset times in Vienna in the simulated date, from 5:00 h to 20:00 h was considered as the day and from 21:00 h to 4:00 h as the night. The graphs depict, except M3 and H2, the increase in the reflectivity of the walls and increasing the buildings height, other scenarios have cooling effect in the area during the day as well as the night however the amount of the changes in the temperature varies from day to night. The influence of the implemented modifications during the day was more than night except in H1 (the lower aspect ratio). In case of H2, increase of buildings height, the air temperature variation profile is different than the other scenarios. This is the only case, in which the air temperature has increased during the night in spite of a considerable decrease in that of during the day, although the overall mean value showed that the total reduction in the air temperature was more than its total nocturnal increase.

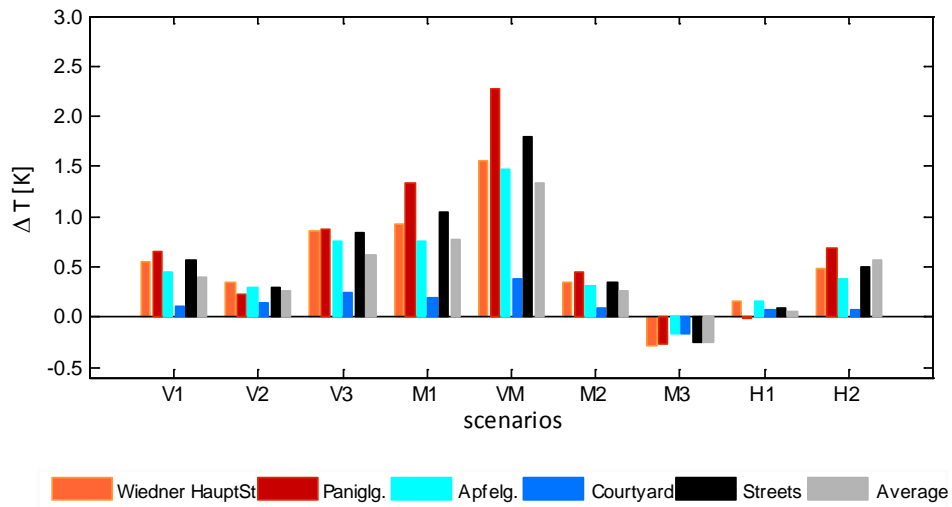


Figure 5-46: Average cooling effect of the evaluated scenarios for every location during the day

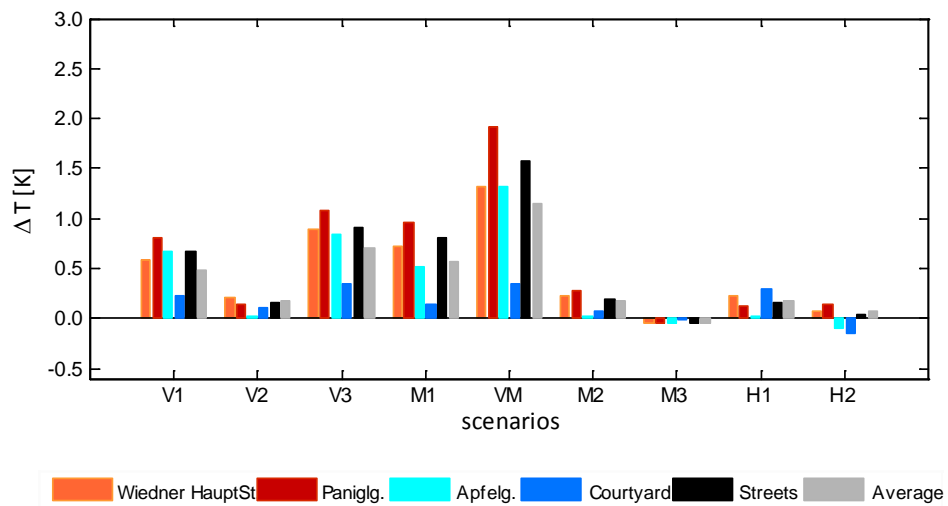


Figure 5-47: Average cooling effect of the evaluated scenarios for every location during the night

By all of the analyzed scenarios the domain micro-climate was affected either by changing the evapotranspiration or by altering the radiation budget within the urban canopy. Addition of more plants as well as more permeable surfaces, in both cases, reduced the air temperature by changing the amount of evaporation of the water (as the associated latent heat is provided by the surroundings which includes the ambient air) from the plants or the ground surface. Hence, any reduction of the air temperature due to evaporation automatically increased the water vapor concentration in the environment. That is why, as it can be seen in figure 5-48 to 5-

50, in the case of the trees, the permeable pavements and their combination, the average water vapor difference between the scenarios and the base case showed an increase of about 1 g/kg. The influence of modifications, which alter the radiation budget in the associated areas, on the humidity depends on the existing local condition. The humidity of locations without any source for evaporation, i.e. plants or permeable pavement, were not affected by such modifications, but that of those locations containing plants or permeable pavements was influenced depending on the alteration of radiation budget. At such locations, reductions in the magnitude of the radiation resulted in the reduction of the humidity as well, and an increase in radiation budget caused a water vapor concentration rise in the area. Higher aspect ratios proved such conditions, in which because of increased shaded areas in the canyon and accordingly the reduction of the magnitude of the incoming radiation the air temperature within the domain was decreased. This reduction in the ambient air temperature led, intern, to a lower water evaporation in the associated environment resulting in a lower air specific humidity.

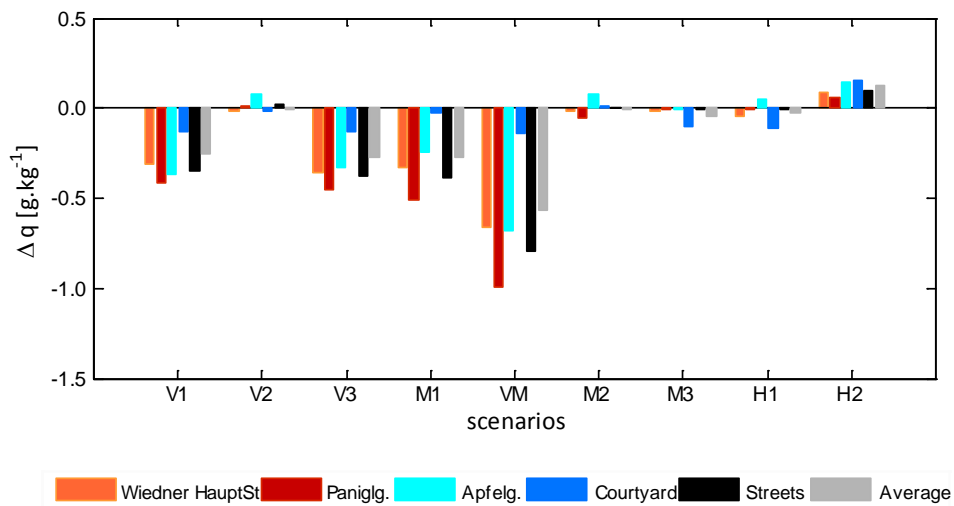


Figure 5-48: Average air specific humidity change for the evaluated scenarios for every location during 24 hours

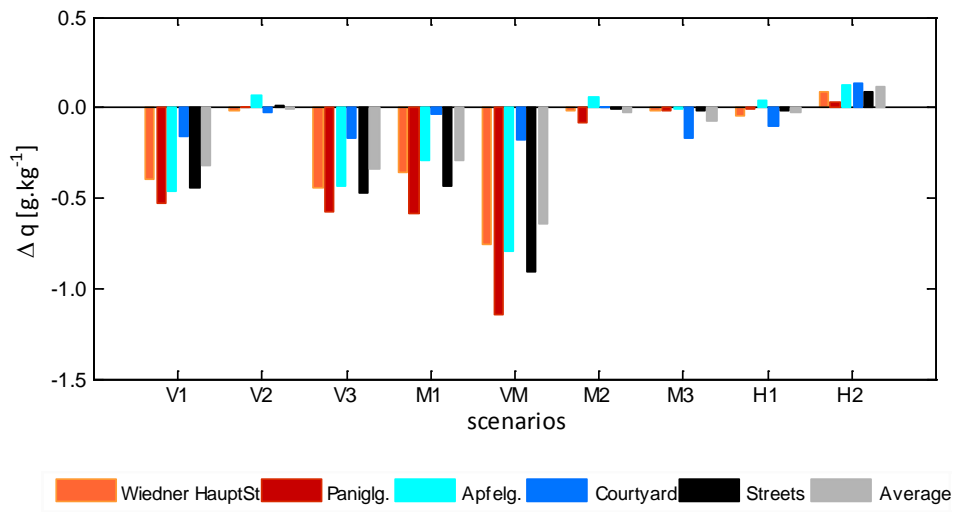


Figure 5-49: Average air specific humidity change for the evaluated scenarios for every location during the day

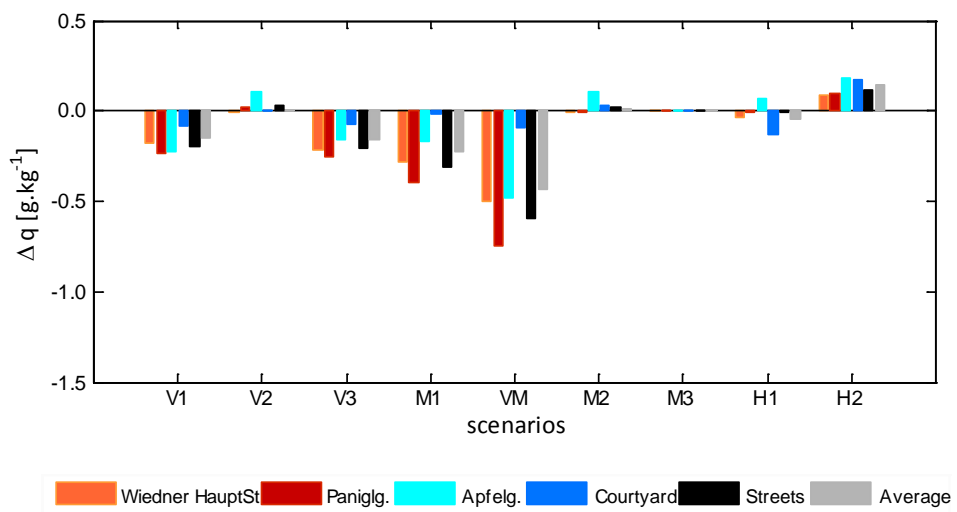


Figure 5-50 Average air specific humidity change for the evaluated scenarios for every location during the night

## 6. Conclusion

This contribution presents the results of a monitoring and modeling study of the urban micro-climate in the city of Vienna. The survey was performed in two parts: empirical and computational inquiries.

For the empirical analysis, required weather data was collected via measurements conducted using mobile traverse method. This data was compared with the obtained weather data from stationary weather stations located inside the investigated area.

Results of the on-site measurements suggested that micro-climatic conditions at different locations vary considerably. Comparison between the (stationary) reference point and the mobile weather station readings showed that within the surveyed area (0.5 km<sup>2</sup>) air temperature varies about 2.5 K. Moreover, these variations appeared to be related to certain characteristic features of the locations (e.g., sky view factor, density of existing vegetation, etc.). Highest temperatures, with about 2 K difference with the reference point, were monitored at open plazas and parks (P3, G1, G2), whereas the shaded courtyards, (C1 and C2) and the streets displayed the lowest temperatures during the day differing from the reference point by around 2.4 K. The readings of the air temperature and solar irradiance showed a significant congruence with the sky view factors. Likewise, trees affected the air temperature (reduced) and humidity (increased) in the area, considerably, while the grass fields and the water bodies showed less impact.

Also, further analyses showed that beside the geometrical and physical properties of an urban fabric, general climate conditions, e.g. sky condition and wind speed, are also affecting the urban microclimate variation within the city. Based on the obtained results, the higher the wind speed above the urban canopy, the greater air temperature differences between the reference point (BPI) and measurement spots should be expected. Likewise, according to the results, the impact of the wind speed on closed locations, e.g. on courtyards and on narrow canyons, is stronger than that of on open spaces/ wider canyons.

Within the context of the computational inquiries a simulation model was generated using a three dimensional urban micro-climate simulation tool, ENVI-met 4.0 (Bruse 1999). This model was used to simulate microclimatic conditions in a part of the city of Vienna including a part of the area, in which the measurements pertaining to the aforementioned empirical study had been done. Adjustment runs showed that the quality of input data and utilizing appropriate weather data can improve the RMSE of the predicted air temperature by about 1.9 K and reach to RMSE=1.29 K, while the simulation model is not considerably sensible to grid size.

The influence of four parameters including the density of vegetation, the extent of permeable pavements, the reflectivity of the roofs/ the walls and the aspect ratio of the canyons, was evaluated in nine scenarios. The results suggested modifications within the urban canopy were more effective in influencing the relevant microclimatic conditions than those implemented to the roof levels.

Likewise, combination of the alterations, which result in lower air temperature, can enhance their cooling effect. As it was shown by the results, the maximum cooling effect, about 2.7 K, was achieved through the scenario VM, increasing vegetation and applying permeable pavement. The numerical simulations also showed that increase in the amount of vegetation, (either within the canyon or above the roofs), in the area of pervious pavements or in the reflectivity of the roof material could cause a decrease in day time and night time air temperature during the hot summer period. On the other hand changes in the canyon aspect ratio could lead to different effects (decrease or increase) on the microclimatic condition during day and night. Also replacing wall materials with those having a higher reflectivity led to a wall surface temperature decrease, while at the same time a slight increase, of about 0.4 K, in the associated ambient air temperature during the day was observed.

Based on the obtained results, it can be concluded that the influence of the above-mentioned parameters on microclimatic conditions is not only dependent on the extent of the applied changes, but is also in direct relation to other characteristic parameters of the location such as the orientation and the aspect ratio of the canyon in the investigated area.

## **7. Outlook**

The urban micro-climate is influenced by the different meteorological, geographical and urban characteristics as well as the human activities in the urban area. The effect of some of these parameters was studied within the context of this work. More simultaneous, on-site measurements, distributed in different locations while taking into account all associated parameters, within a bigger time span can help achievement of a deeper understanding concerning variations in an urban micro-climate.

The urban micro-climate modeling is not only a low cost powerful predicting tool for generating needed weather data along with the optimized associated effective parameters concerning an investigation, but also it can provide more reliable inputs for building performance simulation models. Therefore coupling of urban micro-climate models with building performance simulation codes would enable designers and engineers to achieve better and more effective evaluations and as a result would lead to more accurate and optimized solutions for urban construction projects. On the other hand buildings are one of the input energy resources in urban energy balance equation (see section 2.2) coupling of the two above-mentioned tools can provide more accurate input data for urban micro-climate modeling.

## References

- Akbari, H. 2002. *Shade trees reduce building energy use and CO<sub>2</sub> emissions from power plants*. Environmental Pollution, 116, pp. 119-126.
- Akbari, H., Pomerantz, M., and Taha, H. 2001. *Cool surfaces and shade trees to reduce energy use and improve air quality in urban areas*. Solar Energy, 70(3), pp. 295-310.
- Alduchov, O., and Eskridge, R. 1997. *Improved Magnus form approximation of saturation vapor pressure*. National Oceanic and Atmospheric Administration Eskridge Asheville, NC (United States). National Climatic Data Center.
- Alexandri, E., and Jones, P. 2006. *Sustainable Urban Future in Southern Europe - What about the Heat Island Effect?* ERSA2006, pp. 1-26. Volos.
- Ali Toudert, F. 2005. *Dependence of Outdoor Thermal Comfort on Street Design in Hot and Dry Climate*. Ph.D. Thesis, Freiburg: Freiburg University.
- Ali Toudert, F., and Mayer, H. 2006. *Numerical study on the effects of aspect ratio and orientation of an urban street canyon on outdoor thermal comfort in hot and dry climate*. Building and Environment, 41(2), pp. 94-108.
- Arnfield, A. 2003. Two decades of urban climate research: a review of turbulence, exchanges of energy and water, and the urban heat island. Int. J. Climatol (International Journal of Climatology), 23(1), pp. 1-26.
- Asaeda, T., and Ca, V. 1993. *The subsurface transport of heat and moisture and its effect on the environment: A numerical model*. Boundary-Layer Meteorology, 65(1-2), pp. 159-179.
- Asimakopoulos, D., Asimakopoulos, V., Chrisomallidou, N., Klitsikas, N., Mangold, D., Michel, P., Santamouris, M., Tsangrassoulis, A. 2001. *Energy and Climate in the Urban Built Environment*. (M. Santamouris, Ed.) London: EArthscan.
- Bahrami, M. 2011, 9 6. *Engineering Thermodynamics and Heat Transfer-Natural convection*. Retrieved 10 2, 2013, from <http://www.sfu.ca/~mbahrami/ensc388.html>
- Bird, R., Stewart, W., and Lightfoot, E. 1976. *Transport phenomena* (2. print., corr. ed.). New York: Wiley.
- Bishop, M. 1976. *Focus on earth science*. USA: Merrill.
- Bruse, M. 1999. ENVI-met Model Architecture. Retrieved 1 15, 2013, from <http://www.envi-met.com/>
- Bruse, M. 1999. *Simulating microscale climate interactions in complex terrain with a high-resolution numerical model: A case study for the Sydney CBD Area*. Sydney: International Conference on Urban Climatology & International Congress of Biometeorology.



- Bruse, M. 2004. *Updated overview over ENVI-met 3.0*. Retrieved May 11, 2011, from Envi-met: <http://www.envi-met.info/hg2e/doku.php?id=resources:elib>
- Buyantuyev, A., and Wu, J. 2010. *Urban heat islands and landscape heterogeneity: linking spatiotemporal variations in surface temperatures to land-cover and socioeconomic patterns*. *Landscape Ecology*, 25(1), pp. 17-33.
- Central Institute for Meteorology and Geodynamics (ZAMG). (n.d.). *Klimadaten von Österreich*. Retrieved 9 6, 2012, from [http://www.zamg.ac.at/fix/klima/oe71-00/klima2000/klimadaten\\_oesterreich\\_1971\\_frame1.htm](http://www.zamg.ac.at/fix/klima/oe71-00/klima2000/klimadaten_oesterreich_1971_frame1.htm)
- Chou, P. 1945. *On velocity correlations and the solution of the equations of turbulent fluctuation*.
- Christen, A., and Vogt, R. 2004. *Energy and radiation balance of a central European city*. *International Journal of Climatology*, 24(11), pp. 1395-1421.
- Davidov, B. 1961. *On the statistical dynamics of an incompressible turbulent fluid*.
- De la Flor, F., and Dominguez, S. 2004. *Modelling microclimate in urban environments and assessing its influence on the performance of surrounding buildings*. *energy and Buildings*, 36, pp. 403-413.
- Department of Economic and Social Affairs, Population Division. 2012. *World Urbanization Prospects, the 2011 Revision*. New York: United Nations.
- Dimitrova, B., Vuckovic, M., Kiesel, K., and Mahdavi, A. 2014. *Trees and the microclimate of the urban canyon: A case study*. Proceedings of the 2nd ICAUD International Conference in Architecture and Urban Design. Tirana.
- Dimoudi, A., and Nikolopoulou, M. 2003. *Vegetation in the urban environment: microclimatic analysis and benefits*. *Energy and Buildings*, 35, pp. 69-76.
- Encyclopaedia Britannica. 2013. *Encyclopaedia Britannica*. Retrieved 2013, from <http://www.britannica.com/>
- Erell, E., Paarlmutter, D., and Williamson, T. 2011. *Urban Microclimate- Designing the Space Between the Buildings* 1st ed.. London ;, Washington, DC: Earthscan.
- Florens, E., Eiff, O., and Moulin, F. 2013. *Defining the roughness sublayer and its turbulence statistics*. *Experiments in Fluids*, 54(4), pp. 1–15.
- Fung, W., Lam, K., Nichol, J., and Wong, M. 2008. *Derivation of Nighttime Urban Air Temperatures Using a Satellite Thermal Image*. *Journal of Applied Meteorology and Climatology*. 48. pp. 863–872
- Gaffin, S., Rosenzweig, C., Eichenbaum-Pikser, J., Khanbilvardi, R., and Susca, T. 2010. *A Temperature and Seasonal Energy Analysis of Green, White, and Black Roofs*. New York: Columbia University, Center for Climate Systems Research.
- Gartland, L. 2008. *Heat Islands Understanding and Mitigating Heat in Urban Areas*. London: Earthscan.
- Geerts, B., and Linacre, E. 1997. *Climates and Weather Explained*. Routledge.

- Ghiaus, C., Allard, F., Santamouris, M., Georgakis, C., and Nicol, F. 2006. *Urban environment influence on natural ventilation potential*. Building and Environment, 41(4), pp. 395-406.
- Gidlof-Gunnarsson, A., and Öhrström, E. 2007. *Noise and well-being in urban residential environments: The potential role of perceived availability to nearby green areas*. Landscape and Urban Planning, 83, pp. 115-126.
- Giridharan, R., Ganesan, S., and Lau, S. 2004. *Daytime urban heat island effect in high-rise and high-density residential developments in Hong Kong*. Energy and Buildings, 36(6), pp. 525-534.
- Givoni, B. 1998. *Climate Considerations in Building and Urban Design*. John Wiley and Sons.
- Grimmond, C., Potter, S., Zutter, H., and Souch, C. 2001. *Rapid methods to estimate sky-view factors applied to urban areas*. International Journal of Climatology, 21(7), 903-913.
- Hamada, S., and Ohta, T. 2010. *Seasonal variations in the cooling effect of urban green areas on surrounding urban areas*. Urban Forestry and Urban Greening, 9(1), pp. 15-24.
- Hamilton, I., Davies, M., Steadman, P., Stone, A., Ridley, I., and Evans, S. 2009. *The significance of the anthropogenic heat emissions of London's buildings: A comparison against captured shortwave solar radiation*. Building and Environment, 44(4), pp. 807-817.
- Harlow, F., and Nakayama, P. 1967. *Turbulent transport equations, The Physics of Fluids*.
- Harmel, R., Smith, P., and Migliaccio, K. 2010. *Modifying Goodness-of-Fit Indicators to Incorporate Both Measurement and Model Uncertainty in Model Calibration and Validation*. American Society of Agricultural and Biological Engineers, 53(1), pp. 55-63.
- Huang, G., Zhou, W., and Cadenasso, M. 2011. *Is everyone hot in the city? Spatial pattern of land surface temperatures, land cover and neighborhood socioeconomic characteristics in Baltimore, MD*. Journal of Environmental Management, 92(7), pp. 1753-1759.
- Huang, L., Li, J., Zhao, D., and Zhu, J. 2008. *A fieldwork study on the diurnal changes of urban microclimate in four types of ground cover and urban heat island of Nanjing, China*. Building and Environment, 43(1), 7-17.
- Huang, Y., Akbari, H., Taha, H., and Rosenfeld, H. 1987. *The Potential of Vegetation in Reducing Summer Cooling Loads in Residential Buildings*. Journal of Climate and Applied Meteorology, 26, pp. 1103-1116.
- Huttner, S. 2012. *Further development and application of the 3D microclimate simulation ENVI-met*. Ph.D. Thesis. Johannes Gutenberg University Mainz. Retrieved 4 27, 2013, from <http://ubm.opus.hbz-nrw.de/volltexte/2012/3112/pdf/doc.pdf>

- Ioannis X, T. 2010. *Assessment and energy implications of street air temperature cooling by shade trees in Athens (Greece) under extremely hot weather conditions*. *Renewable Energy*, 35(8), pp. 1866–1869.
- Jones, W., and Launder, B. 1972. *The prediction of laminarization with a two equation model of turbulence*. *Heat and Mass Transfer*.
- Kantzioura, A., Kosmopoulos, P., and Zoras, S. 2011. *Urban surface temperature and microclimate measurements in Thessaloniki*. *Energy and Buildings*, 44, pp. 63-72.
- Kitous, S., Bensalem, R., and Adolphe, L. 2012. *Airflow patterns within a complex urban topography under hot and dry climate in the Algerian Sahara*. *Building and Environment*, 56, pp. 162-175.
- Kolokotroni, M., and Giridharan, R. 2008. *Urban heat island intensity in London: An investigation of the impact of physical characteristics on changes in outdoor air temperature during summer*. *Solar Energy*, 82(11), pp. 986-998.
- Kolokotsa, D., Psomas, A., and Karapidakis, E. 2009. *Urban heat island in southern Europe: The case study of Hania, Crete*. *Solar Energy*, 83(10), pp. 1871-1883.
- Konopacki, S., and Akbari, H. 2001. *Energy Impacts of Heat Island Reduction Strategies in the Greater Toronto Area, Canada*. Lawrence Berkeley National Laboratory, Heat Island Group, Berkeley. Retrieved 10 23, 2011, from [http://www.epa.gov/heatisland/resources/pdf/toronto\\_energysavings.pdf](http://www.epa.gov/heatisland/resources/pdf/toronto_energysavings.pdf)
- Kottek, M., Grieser, J., Beck, C., Rudolf, B., and Rubel, F. 2006. *WORLD MAPS OF KÖPPEN-GEIGER CLIMATE CLASSIFICATION*. Retrieved 10 9, 2013, from <http://koeppen-geiger.vu-wien.ac.at/present.htm>
- Krüger, E., Minella, F., and Rasia, F. 2011. *Impact of urban geometry on outdoor thermal comfort and air quality from field measurements in Curitiba, Brazil*. *Building and Environment*, 46(3), pp. 621-634.
- Lam, K., Ng, S., Hui, W., and Chan, P. 2005. *Environmental quality of urban parks and open spaces in Hong Kong*. *Environmental Monitoring Assess*, 111(1-3), pp. 55-73.
- Li, R., and Roth, M. 2009. *Spatial Variation of the Canopy-Level Urban Heat Island in Singapore*. The seventh International Conference on Urban Climate. Yokohama.
- Liu, J., Ma, F., and Li, Y. 2011. *The Impact of Vegetation on Mitigating Heat Island Intensity in Four Major Cities in China*. *AMR(Advanced Materials Research)*, 260-263, pp. 2935-2939.
- Mahdavi, A., Kiesel, K., and Vuckovic, M. 2013. *A framework for the evaluation of urban heat island mitigation measures*. *Proceedings of SB13 Munich: Implementing Sustainability - Barriers and Chances*. Munich.
- Maleki, A., Kiesel, K., Vuckovic, M., and Mahdavi, A. 2014. *Empirical and Computational Issues of Microclimate Simulation*. In M. Mahendra, E. Neuhold, A. Tjoa, and I. You, *Information and Communication Technology, Lecture Notes in Computer Science*, Berlin Heidelberg: Springer, pp. 78-85.

- Maleki, A., Orehounig, K., Kiesel, K., and Mahdavi, A. 2012. *MONITORING AND MODELING OF THE URBAN MICRO-CLIMATE*. Book of Abstracts of the EURA 2012 International Conference. Vienna.
- Masson, V., Grimmond, C., and Oke, T. 2002, october. *Evaluation of the Town Energy Balance (TEB) Scheme with Direct Measurements from Dry Districts in Two Cities*. JOURNAL OF APPLIED METEOROLOGY, 41, pp. 1011-1026.
- Mirzaei, P., and Haghighat, F. 2010. *Approaches to study Urban Heat Island – Abilities and limitations*. Building and Environment, 45(10), pp. 2192-2201.
- Moriyama, M., and Tanaka, T. 2012. *The Mitigation of UHI Intensity through an Improved Land-Use Plan in the Urban Central Area: Application to Osaka City, Japan*. Journal of Heat Island Institute International, 7(2), 65-71.
- Morway, Z.K., and Gvozdenac, D.D. 2008. *Applied industrial energy and environmental management*. Chichester, West Sussex, U.K. ;, Hoboken, NJ, [Piscataway, NJ]: Wiley;IEEE Press.
- National Renewable Energy Laboratory (NREL). 1995. *Landscaping for Energy Efficiency*. U.S. Department of Energy. The Energy Efficiency and Renewable Energy Clearinghouse (EREC).
- Niachou, K., Livada, I., and Santamouris, M. 2008. *Experimental study of temperature and airflow distribution inside an urban street canyon during hot summer weather conditions. Part II: Airflow analysis*. Building and Environment, 43(0360-1323), pp. 1393 - 1403.
- Offerle, B., Grimmond, C., and Oke, T. 2003. *Parameterization of net All-Wave Radiation for urban areas*. Journal of Applied Meteorology, 42(8), pp. 1157-1173.
- Oke, T. R. 1982. *The energetic basis of the urban heat island*. Quart. J. R. Met. Soc. (Quarterly Journal of the Meteorological Society), 108, pp. 1-24.
- Okeil, A. 2010. *A holistic approach to energy efficient building forms*. Building and Environment, 42(9), pp. 1437-1444.
- Oliveira, S., Andrade, H., and Vaz, T. 2011. *The cooling effect of green spaces as a contribution to the mitigation of urban heat: A case study in Lisbon*. Building and Environment, 46(11), pp. 2186–2194.
- Ooka, R., Chen, H., and Kato, S. 2008. *Study on optimum arrangement of trees for design of pleasant outdoor environment using multi-objective genetic algorithm and coupled simulation of convection, radiation and conduction*. Journal of Wind Engineering and Industrial Aerodynamics, 96(10-11), pp. 1733-1748.
- Peterson, T. C. 2003. *Assessment of Urban Versus Rural In Situ Surface Temperatures in the Contiguous United States: No Difference Found*. Journal of Climate, 16(18), pp. 2942-2952
- Pinho, O., and Orqaz, M. 2000. *The urban heat island in a small city in coastal Portugal*. International Journal of Biometeorology, 44(4), pp. 198-203.

- Priyadarsini, R. 2009. *Urban Heat Island and its Impact on Energy Consumption*. Urban Heat Island and its Impact on Building Energy Consumption. *Advances in Building Energy Research*, 3(1), pp. 261-270.
- Rajagopalan, P., Wong Nyuk, H., and Cheong Kok Wai, D. 2008. *Microclimatic modeling of the urban thermal environment of Singapore to mitigate urban heat island*. *Solar Energy*, 82(8), pp. 727-754.
- Rajasekar, U., and Weng, Q. 2009. *Urban heat island monitoring and analysis using a non-parametric model: A case study of Indianapolis*. *ISPRS Journal of Photogrammetry and Remote Sensing*, 64(1), pp. 86-96.
- Robinson, D. 2011. *Computer modelling for sustainable urban design. Physical principles, methods and applications*. London: Earthscan.
- Robitu, M., Musy, M., Inard, C., and Groleau, D. 2006. *Modeling the influence of vegetation and water pond on urban microclimate*. *Solar Energy*, 80(4), pp. 435-447.
- Rodi, W. 1980. *Turbulence models and their application in hydraulics – a state of the art review*. Karlsruhe University.
- Sanei, N. 2005. *Safety analysis for the design of a core-catcher for a helium cooled fast breeder reactor*. Ph.D. Thesis. Aachen: RWTH.
- Santamouris, M., Papanikolaou, N., Livada, I., Koronakis, I., Georgakis, C., Argigiou, A., and Assimakopoulos, D. 2001. *On the impact of urban climate on the energy consumption of buildings*. *Solar Energy*, 70(3), pp. 201-216.
- Schuss, M. 2011. *Implementation of a predictive simulation-based controller for environmental systems in buildings*. Ph.D. Thesis. Vienna: Vienna university of Technology.
- Shahmohamadi, P., Che-Ani, A., Abdul-Maulud, K., Mohd-Tawil, N., and Abdullah, N. 2011. *The Impact of Anthropogenic Heat on Formation of Urban Heat Island and Energy Consumption Balance*. *Urban Studies Research*, 2011, pp. 1-9.
- Shashua-Bar, L., Hoffman, M., and Tzimir, Y. 2006. *Integrated thermal effects of generic built forms and vegetation on the UCL microclimate*. *Building and Environment*, 41(3), pp. 343-354.
- Shashua-Bar, L., Tzimir, Y., and Hoffman, M. 2004. *Thermal effects of building geometry and spacing on the urban canopy layer microclimate in a hot-humid climate in summer*. *International Journal of Climatology*, 24(13), pp. 1729-1742.
- Shishegar, N. 2013. *Street Design and Urban Microclimate: Analyzing the Effects of Street Geometry and Orientation on Airflow and Solar Access in Urban Canyons*. *Journal of Clean Energy Technologies*, 1, pp. 52-56.
- Spagnolo, J., and Dear, R. 2003. *A field study of thermal comfort in outdoor and semi-outdoor environments in subtropical Sydney Australia*. *Building and Environment*, 38, pp. 721-738

- Spangenberg, J., Shinzato, P., Johansson, E., and Duarte, D. 2008. *Simulation of the influence of vegetation on microclimate and thermal comfort in the city of Sao Paolo*. Brazilian Society of Urban Forest (SBAU), 3(2), pp. 1-19.
- Taha, H. 1997. *Urban climates and heat islands: albedo, evaporation, and anthropogenic heat*. Energy and Buildings, 25, pp. 99-103.
- Tahmasebi, F., and Mahdavi, A. 2012. *Optimization-based simulation model calibration using sensitivity analysis*. Talk: Simulace Budov a Techniky Prostredi - 7. narodni konference s mezinarodni ucasti. Brno: Ceska Technika - nakladatelstvi CVUT.
- Urban Climate Group. University of Gothenburg. Department of Earth Science. 2011. *The SkyViewFactorCalculator*. Gothenburg: University of Gothenburg.
- Vicente-Serrano, S., Cuadrat-Prats, J., and Saz-Sánchez, M. 2005. *Spatial patterns of the urban heat island in Zaragoza (Spain)*. CLIMATE RESEARCH, 30, pp. 61-69.
- Vienna City Administration. (n.d.). Wien. Retrieved 10 8, 2013, from [www.wien.at](http://www.wien.at)
- Willmott, C. 1982. *Some comments on the evaluation of model performance*. Bulletin American Meteorological Society, 63, pp. 1309–1369.
- Yang, F., Lau, S., and Qian, F. 2010. *Summertime heat island intensities in three high-rise housing quarters in inner-city Shanghai China: Building layout, density and greenery*. Building and Environment, 45(1), pp. 115-134.
- Yow, D., and Carbone, G. 2006. *The urban heat island and local temperature variations in Orlando, Florida*. Southeastern Geographer, 46(2), pp. 297-321.

## **Appendices**

## Appendix A-1: Input data to run a simulation using ENVI-met 4.0

Category	Variable	Unit
	start day	DD.MM.YYYY
	start time	HH:MM:SS
	total simulation time	h
	output interval time receptors	m
	output interval time all other files	m
Meteorology: Basic setting	wind speed at 10m height	m/s
	wind direction	deg
	Roughness length at measurement site	m
	initial temperature of atmosphere	K
	specific humidity at 2500m	g/kg
	relative humidity in 2m height	%
Meteorology: simple forcing	hourly temperature	K
	hourly relative humidity	%
Meteorology: Further setting	Adjustment factor for solar radiation	0.5-1.5
	cover of low cloud	octas
	cover of medium cloud	octas
	cover of high cloud	octas
	Turbulence scheme for 1D reference model	diagnostic/ prognostic
	Turbulence scheme for 3D main model	diagnostic/ prognostic
	Upper boundary conditions for TKE and dissipation rate 3D model	open/ closed
	Lateral boundary condition for temperature and humidity	open/ closed
	Lateral boundary condition for temperature and humidity	open/ closed
Model timing	Sun height for switching dt(0) -> dt(1)	deg
	Sun height for switching dt(1) -> dt(2)	deg
	time step t0	s
	time step t1	s
	time step t2	s
	Update Plant Processes	s
	Update Surface Data	s
	Update Radiation/Shadows	s
	Update Flow Field	s



Category	Variable	Unit
Soil and plants	Initial Temperature Upper Layer (0-20 cm)	K
	Initial Temperature Middle Layer (20-50 cm)	K
	Initial Temperature Deep Layer (below 50 cm)	K
	Relative Humidity Upper Layer (0-20 cm)	%
	Relative Humidity Middle Layer (20-50 cm)	%
	Relative Humidity Deep Layer (below 50 cm)	%
	Transpiration model	
	Co2 background level	ppm
Pollutant dispersion	operation mode	
	NO-O3-NO2 chemistry	
	update interval for emission rates	s

**Appendix A2: Required information to build an area input file**

	Variable	Unit
number of grids	x	-
	y	-
	z	-
	nesting	-
grid sizes	dx	m
	dy	m
	dz	m
	telescoping factor	%
	start telescoping after	m
location	latitude	deg
	longitude	deg
Georeference	Co-ordinate of lower left grid x-value	-
	Co-ordinate of lower left grid y-value	-
	reference level above sea level for DEM=0	-
	model rotation out of grid north	-
building	top of building	m
	bottom of building	m
	walls material	-
	roof material	-
vegetation	plant type	-
DEM height	Terrain height	m
soil and surface	soil profile	-
	soil profile for nesting grids	-
sources	source type	-

### Appendix A3: ENVI-met outputs, main data file (Atmosphere)

Field	Unit	Meaning
Flow u	$m.s^{-1}$	Wind speed u-component
Flow v	$m.s^{-1}$	Wind speed v-component
Flow w	$m.s^{-1}$	Wind speed w-component
Wind Speed	$m.s^{-1}$	Total wind speed
Wind Speed change	%	Change of wind speed comp. to inflow
Wind direction	deg	direction of the wind flow relative to geographic north
pressure perturb	Pa	Relative Pressure Perturbation
Pot. Temperature	K	Potential Air temperature
Pot. Temperature (Diff K)	K	Potential Air temp. difference to inflow
Pot. Temperature Change	$K.h^{-1}$	Change of Air Temperature with time
Spec. Humidity	$g.kg^{-1}$	Specific Humidity Air
Relative Humidity	%	Relative Humidity of Air
TKE	$m^2.s^{-2}$	Turbulent Kinetic Energy
Dissipation	$m^3.s^{-2}$	Dissipation of TKE
Vertical Exchange Coef. l.	$m^2.s^{-1}$	Vertical Turbulent exchange coefficient Km
Horizontal Exchange Coef.	$m^2.s^{-1}$	Horizontal Turbulent exchange coefficient Km
Absolute LAD	$m^2.m^{-3}$	Leaf Area Density
Direct SW Radiation	$W.m^{-2}$	Shortwave Direct Radiation
Diffuse SW Radiation	$W.m^{-2}$	Shortwave Diffuse Radiation
Reflected SW Radiation	$W.m^{-2}$	Shortwave Reflected Radiation
Longwave Rad. Environment	$W.m^{-2}$	Longwave Radiation received from the environment
Sky-View-Factor Buildings	-	Sky-View-Factor (only buildings considered)
Sky-View-Factor Bld+ Vegetation	-	Sky-View-Factor (buildings plus vegetation considered)
Temperature Flux	$K.m.s^{-1}$	Temperature flux from vegetation per unit leaf area
Vapor Flux	$(g.kg^{-1}).m.s^{-1}$	Vapor flux from vegetation per unit leaf area
Water on leaves	$g.m^{-2}$	Amount of liquid water on leaves
Wall Temp Cell border x	K	Wall Temperature Wall x-axis

Field	Unit	Meaning
Wall Temp Cell border z	K	Wall Temperature Wall z-axis
Leaf Temperature	K	Temperature of leafs in grid box
Local Mixing Length	m	Mixing length calculated from the TKE-Dissipation
PMV Value	-	PMV value
PPD Value	%	Percentage People Dissatisfied
Mean Radiant Temperature	K	Mean Radiative temperature
Gas/Particle concentration	$\mu\text{g}\cdot\text{m}^{-3}$	Concentration of selected particle or gas in microgram
Gas/Particle source	$\mu\text{g}\cdot\text{s}^{-1}$	Emission rate of particle or gas source in microgram
Deposition velocity	$\text{mm}\cdot\text{s}^{-1}$	Deposition velocity (only at surfaces)
Total Deposited Mass	$\mu\text{g}\cdot\text{m}^2$	Total amount of mass deposited to ground or leaf surface unit area since start
Deposited Mass time averaged	$\mu\text{g}\cdot\text{m}^2\cdot\text{s}^{-1}$ Average	Average Amount of mass deposited per hour
TKE normalized 1D - TKE normalized with 1D profile	$E\cdot E^{-1}_{1D}$	
Dissipation normalized 1D - Dissipation normalized with 1D profile	$E\cdot \epsilon^{-1}_{1d}$	
$K_m$ normalized 1D - Vertical $K_m$ norm. with 1D profile	$K_m\cdot K_m^{-1}_{1D}$	
TKE Mechanical Prod	$K_m\cdot K_m^{-1}_{1D}$	Turbulence Production due to wind shear (tensor deformation)
Stomata Resistance	$\text{m}\cdot\text{s}^{-1}$	Stomata resistance of plant
CO2	$\text{mg}\cdot\text{m}^{-3}$	concentration (if A-gs model used
CO2	ppm	concentration in ppm
Plant CO2 flux	$(\text{mg}\cdot\text{kg}^{-1})\cdot\text{m}\cdot\text{s}^{-1}$	flux per unit leaf area
Div Rlw Temp change	$\text{K}\cdot\text{h}^{-1}$	Temperature change due to longwave flux divergence
Local mass budget	$\mu\text{g}\cdot(\text{s}\cdot\text{m}^3)$	Local pollutant mass budget of grid cell (-: net deposition)

## Appendix A4: ENVI-met outputs, main data file (Surface)

Field	Unit	Meaning
z_topo	m	Absolute height of model ground surface (always 0 in recent version)
T Surface	K	Ground surface temperature
T Surface Diff	K	Difference of ground surface to reference surface
T Surface change	K.h <sup>-1</sup>	Change of ground surface temperature
q Surface	g.kg <sup>-1</sup>	Specific humidity of surface (available vapor)
uv above surface	m.s <sup>-1</sup>	Wind speed at the first grid level above ground surface
Sensible heat flux	W.m <sup>-2</sup>	Sensible heat flux into the air (+: towards air)
Exchange coef. heat	m <sup>2</sup> .s <sup>-1</sup>	Exchange coefficient for heat between surface and air
Latent heat flux	W.m <sup>-2</sup>	Sensible heat flux into the air (+: towards air)
Soil heat flux	W.m <sup>-2</sup>	Heat flux into soil (+: directed towards deeper layers)
Sw direct radiation	W.m <sup>-2</sup>	Direct shortwave radiation reaching ground surface
Sw diffuse radiation	W.m <sup>-2</sup>	Diffuse shortwave radiation reaching ground surface
Lambert factor		Value of Lambert's law for solar angle
Longwave radiation bud.	W.m <sup>-2</sup>	Longwave radiation budget of ground surface
Longwave rad. from vegetation	W.m <sup>-2</sup>	Longwave radiation received from vegetation layers above
Longwave rad. from environment	W.m <sup>-2</sup>	Longwave radiation received from buildings
Water flux	g.m <sup>-2</sup> s <sup>-1</sup>	Water flux from/to the ground surface
Sky-View Factor		Sky View factor for z=0 (buildings only counted)
Building height	m	Height of building top (0 if no building assigned)
Surface albedo		Albedo of ground surface
Deposition speed	mm.s <sup>-1</sup>	Deposition flux of analyzed pollutant component
Mass deposited	µg.m <sup>-2</sup>	Mass deposited at ground surface in µg

### Appendix A5: ENVI-met outputs, main data file (Buildings)

Field	Unit	Meaning
Temperature façade node1 (outside)	K	
Temperature façade node2	K	
Temperature façade node3	K	
Temperature façade node4	K	
Temperature façade node5	K	
Temperature façade node6	K	
Temperature façade node7(inside)	K	
longwave radiation emitted by façade	W.m <sup>-2</sup>	
uvw in front of façade	m.s <sup>-1</sup>	
absorbed direct SW radiation	W.m <sup>-2</sup>	
incoming LW radiation	W.m <sup>-2</sup>	
air temperature in front of façade	K	
sensibile heat transmission coefficient outside	W.m <sup>-2</sup> K <sup>-1</sup>	
longwave energy balance	W.m <sup>-2</sup>	
heat flux through façade	W	
temperature of building (inside)	K	
energy needed to keep T constant	KWh	

### Appendix A6: ENVI-met outputs, main data file (Soil)

Field	Unit	Meaning
T	K	Soil temperature
ete	m <sup>3</sup> .m <sup>-3</sup>	Volumetric Water Content

### Appendix A7: ENVI-met outputs, 1D-Model Model Files (1D- inflow)

Field	Unit	Meaning
u	$m.s^{-1}$	Wind speed u-component
v	$m.s^{-1}$	Wind speed v-component
T	K	Air temperature
q	$g.kg^{-1}$	Specific Humidity Air
Ri	-	Richardson Number
$K_m$	$m^2.s^{-1}$	Exchange Coefficient Impulse
E	$m^2.s^{-2}$	Turbulent Kinetic Energy
$\epsilon\sigma$	$m^3.m^{-2}$	Dissipation of TKE
E_prod		Production of E
E_therm		Thermal E production
E_trans		Transport of E
Km_limit	$m^2.s$	Limit of Km if using E- $\epsilon$ model
L_diag	m	Mixing Length calculated using the diagnostic approach
l_prog	m	Mixing Length calculated from the E/ $\epsilon$ data

## Appendix A8: ENVI-met outputs, receptor files

Field	Unit	Meaning
Date		Date of the model time (String)
Time		Model time of clock at output (String)
Mod Time	(min)	Model time in min since start
z	m	Model height of data
u	$m.s^{-1}$	Wind speed u-component
v	$m.s^{-1}$	Wind speed v-component
w	$m.s^{-1}$	Wind speed w-component
W Speed	$m.s^{-1}$	Total wind speed
W Dir		Wind direction, 0=North, Rotation corrected
T	K	Air temperature
dT/dt	$K.h^{-1}$	Change of Air Temperature with time
q	$g.kg^{-1}$	Specific Humidity Air
q <sub>rel</sub>	%	Relative Humidity Air
K <sub>m·vert</sub>	$m^2.s^{-1}$	Vertical Exchange Coefficient Impulse
K <sub>m·vert.nrm</sub>		Vertical Km normed with logarithmic law
K <sub>m·hor</sub>	$m^2.s^{-1}$	Horizontal Exchange Coefficient Impulse
E	$m^2.s^{-2}$	Turbulent Kinetic Energy
ε	$m^3.s^{-2}$	Dissipation of TKE
TMRT	K	Mean Radiant Temperature
LAD	$m^2.m^{-3}$	Leaf Area Density
T <sub>leaf</sub>	K	Leaf Foliage Temperature (0 if no leaves)
H <sub>leaf</sub>	$W.m^{-2}$	Sensible Heat Flux from Leafs to Air (see remark)
LE <sub>leaf</sub>	$W.m^{-2}$	Latent Heat Flux from Leafs to Air (see remark)
rs	$m.s^{-1}$	Stomata Resistance (0 if no leaves)
CO2	$Mg.m^{-3}$	CO2 Concentration
CO2.flx	$mg.(kg.s)^{-1}$	CO2 Flux at plants (if A-gs model used)
SW.dir	$W.m^{-2}$	Shortwave Direct Radiation (see remark)
SW.dif	$W.m^{-2}$	Shortwave Diffuse Radiation
Press.p	Pa	Pressure Perturbation
mass	$mg.m^{-3}$	Mass concentration
E.mech		Mechanical Production of TKE
R <sub>lw·warming</sub>	K.h	Air temperature change due to longwave flux divergence
SVF.bldg		Sky-View factor (only buildings)



## Appendix B: Sim file for the Base case

```

%---- ENVI-met V4 main configuration file -----
%---- generated with ProjectWizard -----
Fileversion           =4.0
JobID                 =Simulation
% Main data .....
Name for Simulation (Text):      =base
Area Input File to be used      =C:\forced-final\base.in3
Filebase name for Output (Text): =B
Output Directory:              =C:\forced-final\base
Start Simulation at Day (DD.MM.YYYY): =13.07.2011
Start Simulation at Time (HH:MM:SS): =3:00:00
Total Simulation Time in Hours:   =25
Wind Speed in 10 m ab. Ground [m/s] =2.5
Wind Direction (0:N..90:E..180:S..270:W..) =150
Roughness Length z0 at Reference Point [m] =0.1
Initial Temperature Atmosphere [K] =303
Specific Humidity in 2500 m [g Water/kg air] =8
Relative Humidity in 2m [%]      =52
% End main data .....
[OUTPUTTIMING] _____
Output interval main files (min)   =60.00
Output interval log files (min)    =60.00
Include Nesting Grids in Output (0:n,1:y) =0
[SOLARADJUST] _____
Factor of shortwave adjustment (0.5 to 1.5) =0.82

```

[TIMESTEPS] \_\_\_\_\_

Sun height for switching dt(0) -> dt(1) =40.00

Sun height for switching dt(1) -> dt(2) =50.00

Time step (s) for interval 1 dt(0) =1.00

Time step (s) for interval 2 dt(1) =1.00

Time step (s) for interval 3 dt(2) =1.00

[SIMPLEFORCE] \_\_\_\_\_

Hour 00h [Temp, rH] = 301.55, 52.00

Hour 01h [Temp, rH] = 298.95, 62.00

Hour 02h [Temp, rH] = 297.15, 66.00

Hour 03h [Temp, rH] = 293.95, 71.00

Hour 04h [Temp, rH] = 294.25, 72.00

Hour 05h [Temp, rH] = 294.15, 72.00

Hour 06h [Temp, rH] = 294.85, 68.00

Hour 07h [Temp, rH] = 296.75, 65.00

Hour 08h [Temp, rH] = 298.70, 58.00

Hour 09h [Temp, rH] = 300.80, 53.00

Hour 10h [Temp, rH] = 301.65, 50.00

Hour 11h [Temp, rH] = 303.45, 46.00

Hour 12h [Temp, rH] = 304.35, 42.00

Hour 13h [Temp, rH] = 305.45, 39.00

Hour 14h [Temp, rH] = 305.75, 38.00

Hour 15h [Temp, rH] = 306.65, 37.00

Hour 16h [Temp, rH] = 307.05, 36.00

Hour 17h [Temp, rH] = 306.65, 37.00

Hour 18h [Temp, rH] = 305.95, 39.00

Hour 19h [Temp, rH] = 305.25, 42.00

Hour 20h [Temp, rH] = 304.35, 44.00

Hour 21h [Temp, rH] = 303.55, 47.00

Hour 22h [Temp, rH] = 302.65, 49.00

Hour 23h [Temp, rH] = 302.05, 50.00

**Appendix C1: Simulated air temperature for the base case  
[K]**

Hour	Wiedner. HS.	Panigl.	Apfelg.	Courtyard	Streets	All area
4:00	294.8	295.27	294.88	295.95	295.03	295.31
5:00	294.7	295.16	294.77	295.75	294.92	295.16
6:00	295.41	295.84	295.41	296.2	295.59	295.77
7:00	296.92	297.29	296.91	297.26	297.07	297.12
8:00	298.74	299.2	298.53	298.52	298.89	298.79
9:00	300.75	301.13	300.34	299.96	300.85	300.58
10:00	302.02	302.06	301.33	300.77	301.93	301.59
11:00	303.74	303.31	302.9	301.9	303.37	302.92
12:00	304.85	304.11	303.91	302.76	304.3	303.85
13:00	305.77	304.85	304.77	303.59	305.12	304.69
14:00	306.02	305.19	305.06	304.03	305.43	305.03
15:00	306.4	305.7	305.59	304.59	305.91	305.5
16:00	306.55	306.09	305.93	304.96	306.2	305.79
17:00	306.16	305.92	305.73	304.86	305.96	305.57
18:00	305.43	305.38	305.19	304.43	305.35	305.01
19:00	304.48	304.45	304.45	303.78	304.46	304.19
20:00	303.59	303.63	303.63	303.07	303.62	303.39
21:00	302.9	302.97	302.94	302.51	302.94	302.76
22:00	302.18	302.29	302.22	301.94	302.24	302.1
23:00	301.64	301.78	301.68	301.49	301.71	301.6
0:00	301.19	301.35	301.24	301.11	301.28	301.19
1:00	299.47	299.81	299.51	299.89	299.63	299.69
2:00	298.01	298.44	298.05	298.69	298.21	298.35
3:00	295.68	296.34	295.73	296.94	295.98	296.29
4:00	295.38	295.94	295.45	296.39	295.63	295.87

**Appendix C2: Simulated air temperature for the V1 [K]**

Hour	Wiedner. HS.	Panigl.	Apfelg.	Courtyard	Streets	All area
4:00	294.39	294.65	294.29	295.74	294.53	294.93
5:00	294.3	294.56	294.21	295.55	294.44	294.8
6:00	295.15	295.51	295.05	296.09	295.29	295.56
7:00	296.68	297.03	296.63	297.19	296.81	296.95
8:00	298.39	298.71	298.27	298.47	298.49	298.52
9:00	300.29	300.52	300.04	299.92	300.34	300.25
10:00	301.44	301.29	300.96	300.71	301.3	301.17
11:00	303.08	302.57	302.44	301.82	302.73	302.5
12:00	304.17	303.46	303.46	302.66	303.68	303.44
13:00	305.11	304.2	304.32	303.49	304.52	304.28
14:00	305.32	304.47	304.53	303.91	304.78	304.58
15:00	305.68	304.98	305.09	304.46	305.25	305.03
16:00	305.88	305.31	305.42	304.82	305.53	305.32
17:00	305.53	305.12	305.2	304.71	305.28	305.11
18:00	304.8	304.57	304.62	304.27	304.66	304.53
19:00	303.81	303.61	303.8	303.58	303.73	303.67
20:00	302.84	302.64	302.87	302.82	302.79	302.79
21:00	302.17	302	302.19	302.26	302.13	302.16
22:00	301.48	301.35	301.48	301.69	301.46	301.53
23:00	300.96	300.86	300.96	301.24	300.95	301.04
0:00	300.55	300.47	300.53	300.87	300.54	300.64
1:00	298.94	299.06	298.86	299.67	299.01	299.24
2:00	297.54	297.77	297.45	298.48	297.66	297.95
3:00	295.3	295.79	295.18	296.75	295.54	295.96
4:00	294.99	295.38	294.91	296.21	295.18	295.54

**Appendix C3: Simulated air temperature for the V2 [K]**

Hour	Wiedner. HS.	Panigl.	Apfelg.	Courtyard	Streets	All area
4:00	294.7	295.31	295.03	296.03	295.03	295.28
5:00	294.59	295.18	294.9	295.81	294.9	295.12
6:00	295.28	295.87	295.51	296.26	295.56	295.72
7:00	296.75	297.27	296.92	297.24	296.99	297.03
8:00	298.58	299.17	298.46	298.43	298.8	298.66
9:00	300.51	300.97	300.14	299.8	300.64	300.37
10:00	301.69	301.8	301.05	300.6	301.62	301.31
11:00	303.16	302.94	302.38	301.67	302.88	302.52
12:00	304.26	303.71	303.33	302.53	303.79	303.44
13:00	305.17	304.45	304.18	303.35	304.61	304.28
14:00	305.54	304.85	304.56	303.81	305	304.69
15:00	305.96	305.34	305.1	304.36	305.5	305.15
16:00	306.15	305.75	305.46	304.74	305.82	305.45
17:00	305.82	305.62	305.31	304.67	305.62	305.27
18:00	305.13	305.13	304.84	304.28	305.06	304.76
19:00	304.18	304.19	304.16	303.63	304.19	303.95
20:00	303.3	303.39	303.42	302.93	303.37	303.17
21:00	302.59	302.74	302.76	302.36	302.69	302.52
22:00	301.85	302.05	302.04	301.75	301.98	301.84
23:00	301.3	301.53	301.51	301.29	301.44	301.33
0:00	300.86	301.11	301.08	300.91	301.01	300.92
1:00	299.29	299.7	299.54	299.78	299.51	299.54
2:00	297.89	298.39	298.18	298.63	298.16	298.25
3:00	295.69	296.41	296.06	296.97	296.07	296.31
4:00	295.32	295.95	295.68	296.39	295.65	295.83

**Appendix C4: Simulated air temperature for the V3 [K]**

Hour	Wiedner. HS.	Panigl.	Apfelg.	Courtyard	Streets	All area
4:00	294.3	294.63	294.39	295.81	294.51	294.9
5:00	294.2	294.52	294.28	295.6	294.4	294.76
6:00	295.04	295.52	295.13	296.15	295.27	295.52
7:00	296.53	297.03	296.64	297.18	296.75	296.88
8:00	298.26	298.69	298.21	298.4	298.41	298.43
9:00	300.12	300.45	299.89	299.78	300.2	300.12
10:00	301.23	301.13	300.75	300.57	301.1	300.98
11:00	302.65	302.28	301.99	301.61	302.34	302.18
12:00	303.69	303.11	302.92	302.45	303.24	303.08
13:00	304.58	303.83	303.74	303.27	304.04	303.91
14:00	304.88	304.16	304.04	303.71	304.38	304.26
15:00	305.25	304.62	304.55	304.24	304.82	304.69
16:00	305.48	304.95	304.89	304.61	305.12	304.99
17:00	305.19	304.79	304.73	304.53	304.93	304.82
18:00	304.5	304.28	304.2	304.12	304.34	304.28
19:00	303.46	303.3	303.42	303.41	303.4	303.41
20:00	302.49	302.33	302.54	302.67	302.46	302.54
21:00	301.77	301.66	301.86	302.09	301.78	301.89
22:00	301.05	300.97	301.13	301.48	301.07	301.21
23:00	300.52	300.47	300.6	301.02	300.56	300.72
0:00	300.1	300.07	300.18	300.65	300.15	300.32
1:00	298.65	298.8	298.73	299.54	298.78	299.03
2:00	297.33	297.58	297.43	298.41	297.51	297.8
3:00	295.25	295.74	295.39	296.78	295.55	295.94
4:00	294.87	295.28	295.02	296.2	295.12	295.47

**Appendix C5: Simulated air temperature for the M1 [K]**

Hour	Wiedner. HS.	Panigl.	Apfelg.	Courtyard	Streets	All area
4:00	294.51	294.99	294.85	296.02	294.78	295.15
5:00	294.37	294.81	294.69	295.8	294.62	294.96
6:00	294.99	295.31	295.25	296.24	295.17	295.48
7:00	296.4	296.55	296.61	297.23	296.51	296.72
8:00	298.11	298.03	298.08	298.42	298.1	298.19
9:00	299.96	299.64	299.75	299.78	299.82	299.82
10:00	301.02	300.47	300.63	300.56	300.74	300.72
11:00	302.49	301.61	301.9	301.62	301.99	301.93
12:00	303.55	302.42	302.76	302.46	302.89	302.82
13:00	304.42	303.19	303.56	303.27	303.71	303.64
14:00	304.78	303.59	303.97	303.73	304.09	304.05
15:00	305.25	304.14	304.56	304.29	304.62	304.55
16:00	305.48	304.51	304.94	304.68	304.94	304.87
17:00	305.18	304.36	304.78	304.6	304.74	304.69
18:00	304.49	303.87	304.29	304.2	304.18	304.16
19:00	303.6	303.18	303.65	303.57	303.42	303.45
20:00	302.75	302.45	302.93	302.9	302.64	302.71
21:00	302.03	301.8	302.25	302.33	301.96	302.07
22:00	301.28	301.11	301.51	301.73	301.24	301.39
23:00	300.75	300.63	300.99	301.28	300.73	300.9
0:00	300.33	300.24	300.58	300.91	300.32	300.5
1:00	298.8	298.9	299.05	299.76	298.88	299.15
2:00	297.44	297.67	297.71	298.6	297.57	297.9
3:00	295.28	295.76	295.58	296.91	295.52	295.97
4:00	294.94	295.35	295.24	296.34	295.15	295.53

**Appendix C6: Simulated air temperature for the VM [K]**

Hour	Wiedner. HS.	Panigl.	Apfelg.	Courtyard	Streets	All area
4:00	294.12	294.2	294.23	295.86	294.21	294.7
5:00	293.99	294.05	294.08	295.64	294.06	294.53
6:00	294.68	294.68	294.75	296.12	294.72	295.13
7:00	296.1	295.97	296.18	297.1	296.08	296.38
8:00	297.7	297.34	297.67	298.27	297.58	297.78
9:00	299.43	298.81	299.25	299.62	299.18	299.33
10:00	300.38	299.6	300.05	300.4	300.04	300.19
11:00	301.69	300.66	301.21	301.44	301.2	301.33
12:00	302.66	301.42	302.01	302.26	302.04	302.18
13:00	303.61	302.14	302.74	303.05	302.85	302.98
14:00	304.03	302.48	303.09	303.51	303.22	303.38
15:00	304.51	302.99	303.68	304.05	303.73	303.88
16:00	304.75	303.32	304.05	304.45	304.04	304.19
17:00	304.45	303.18	303.89	304.39	303.84	304.02
18:00	303.77	302.74	303.41	304	303.29	303.52
19:00	302.86	302.11	302.78	303.36	302.54	302.8
20:00	301.97	301.33	302	302.66	301.71	302.02
21:00	301.28	300.71	301.35	302.09	301.06	301.39
22:00	300.59	300.06	300.65	301.49	300.39	300.74
23:00	300.08	299.59	300.15	301.03	299.9	300.26
0:00	299.68	299.23	299.75	300.66	299.51	299.87
1:00	298.24	297.97	298.26	299.55	298.15	298.59
2:00	296.94	296.8	296.95	298.41	296.9	297.38
3:00	294.87	294.97	294.86	296.76	294.93	295.52
4:00	294.53	294.57	294.55	296.19	294.57	295.08



**Appendix C7: Simulated air temperature for the M2 [K]**

Hour	Wiedner. HS.	Panigl.	Apfelg.	Courtyard	Streets	All area
4:00	294.7	295.23	295.04	296.04	295.01	295.29
5:00	294.59	295.09	294.92	295.82	294.88	295.12
6:00	295.28	295.73	295.51	296.27	295.52	295.71
7:00	296.75	297.09	296.91	297.28	296.94	297.02
8:00	298.58	298.85	298.43	298.49	298.71	298.63
9:00	300.52	300.67	300.12	299.87	300.55	300.35
10:00	301.7	301.56	301.02	300.67	301.55	301.3
11:00	303.18	302.66	302.32	301.75	302.8	302.5
12:00	304.26	303.46	303.27	302.61	303.72	303.42
13:00	305.17	304.21	304.15	303.43	304.54	304.26
14:00	305.55	304.63	304.55	303.89	304.95	304.68
15:00	305.96	305.14	305.09	304.44	305.45	305.15
16:00	306.16	305.55	305.45	304.82	305.78	305.46
17:00	305.83	305.44	305.3	304.73	305.58	305.27
18:00	305.14	304.93	304.82	304.32	305.01	304.74
19:00	304.18	304.03	304.15	303.68	304.15	303.95
20:00	303.3	303.25	303.41	302.98	303.33	303.17
21:00	302.59	302.6	302.75	302.4	302.65	302.52
22:00	301.84	301.91	302.03	301.8	301.94	301.84
23:00	301.29	301.39	301.5	301.34	301.4	301.33
0:00	300.85	300.97	301.07	300.96	300.97	300.92
1:00	299.28	299.57	299.53	299.82	299.48	299.54
2:00	297.88	298.27	298.17	298.66	298.13	298.26
3:00	295.68	296.3	296.05	296.97	296.04	296.3
4:00	295.31	295.85	295.67	296.4	295.62	295.83

**Appendix C8: Simulated air temperature for the M3 [K]**

Hour	Wiedner. HS.	Panigl.	Apfelg.	Courtyard	Streets	All area
4:00	294.8	295.27	294.88	295.95	295.03	295.31
5:00	294.7	295.16	294.77	295.75	294.92	295.16
6:00	295.58	296	295.48	296.29	295.72	295.9
7:00	297.2	297.55	297.03	297.42	297.3	297.36
8:00	299.08	299.52	298.7	298.73	299.18	299.07
9:00	301.11	301.48	300.53	300.19	301.17	300.89
10:00	302.39	302.4	301.52	301	302.25	301.9
11:00	304.1	303.62	303.06	302.12	303.67	303.22
12:00	305.22	304.43	304.1	302.98	304.61	304.16
13:00	306.14	305.17	304.99	303.82	305.43	305
14:00	306.38	305.5	305.26	304.24	305.74	305.34
15:00	306.72	305.99	305.77	304.78	306.19	305.78
16:00	306.85	306.37	306.12	305.13	306.47	306.06
17:00	306.46	306.2	305.92	305.01	306.23	305.84
18:00	305.71	305.65	305.39	304.55	305.61	305.25
19:00	304.65	304.6	304.6	303.87	304.62	304.34
20:00	303.67	303.71	303.72	303.1	303.7	303.47
21:00	302.96	303.03	303.01	302.54	303	302.81
22:00	302.22	302.34	302.28	301.96	302.29	302.15
23:00	301.67	301.82	301.73	301.5	301.75	301.63
0:00	301.22	301.39	301.28	301.12	301.31	301.22
1:00	299.5	299.84	299.54	299.9	299.66	299.72
2:00	298.03	298.47	298.08	298.71	298.23	298.38
3:00	295.71	296.36	295.76	296.95	296	296.31
4:00	295.4	295.96	295.47	296.41	295.65	295.89

**Appendix C9: Simulated air temperature for the H1 [K]**

Hour	Wiedner. HS.	Paniglg.	Apfelg.	Courtyard	Streets	All area
4:00	294.64	295.2	294.99	295.58	294.94	295.16
5:00	294.52	295.08	294.87	295.38	294.82	295.01
6:00	295.21	295.77	295.47	295.9	295.48	295.62
7:00	296.79	297.32	296.91	297.08	297.02	297.06
8:00	298.7	299.27	298.5	298.46	298.91	298.79
9:00	300.88	301.28	300.25	299.98	300.93	300.66
10:00	302.07	302.19	301.26	300.8	301.94	301.62
11:00	303.41	303.25	302.57	301.88	303.15	302.79
12:00	304.48	304.09	303.53	302.75	304.08	303.73
13:00	305.41	304.88	304.43	303.58	304.94	304.59
14:00	305.84	305.33	304.88	304.04	305.39	305.04
15:00	306.26	305.8	305.42	304.58	305.86	305.51
16:00	306.38	306.05	305.7	304.93	306.08	305.74
17:00	306.03	305.91	305.51	304.84	305.86	305.53
18:00	305.3	305.33	304.98	304.4	305.24	304.96
19:00	304.28	304.34	304.26	303.69	304.3	304.09
20:00	303.36	303.5	303.48	302.95	303.44	303.27
21:00	302.63	302.82	302.8	302.35	302.74	302.6
22:00	301.88	302.13	302.09	301.73	302.02	301.91
23:00	301.31	301.59	301.54	301.23	301.47	301.38
0:00	300.86	301.15	301.1	300.84	301.03	300.95
1:00	299.26	299.69	299.51	299.56	299.49	299.51
2:00	297.85	298.35	298.13	298.32	298.11	298.18
3:00	295.63	296.31	295.95	296.48	295.98	296.15
4:00	295.25	295.87	295.6	295.97	295.57	295.71

**Appendix C10: Simulated air temperature for the H2 [K]**

Hour	Wiedner. HS.	Panigl.	Apfelg.	Courtyard	Streets	All area
4:00	294.95	295.45	295.21	296.51	295.25	295.53
5:00	294.82	295.31	295.08	296.25	295.11	295.36
6:00	295.46	295.88	295.64	296.61	295.7	295.86
7:00	296.83	297.12	296.98	297.47	297.01	297.02
8:00	298.54	298.71	298.46	298.54	298.64	298.44
9:00	300.35	300.4	300.07	299.81	300.37	300.01
10:00	301.33	301.15	300.94	300.6	301.25	300.87
11:00	302.82	302.14	302.14	301.65	302.46	302.02
12:00	303.97	303	303.12	302.51	303.42	302.95
13:00	304.89	303.79	303.99	303.34	304.27	303.78
14:00	305.25	304.2	304.36	303.81	304.66	304.18
15:00	305.68	304.75	304.92	304.36	305.18	304.66
16:00	305.9	305.15	305.3	304.74	305.52	304.99
17:00	305.63	305.12	305.19	304.67	305.38	304.87
18:00	305.01	304.72	304.75	304.28	304.88	304.42
19:00	304.15	303.91	304.13	303.68	304.09	303.72
20:00	303.34	303.2	303.43	303.02	303.35	303.02
21:00	302.67	302.59	302.8	302.48	302.71	302.44
22:00	301.95	301.95	302.1	301.91	302.03	301.81
23:00	301.42	301.45	301.58	301.47	301.51	301.33
0:00	300.99	301.06	301.17	301.11	301.1	300.95
1:00	299.47	299.74	299.69	300.09	299.67	299.69
2:00	298.1	298.49	298.35	299	298.35	298.47
3:00	295.96	296.61	296.29	297.46	296.33	296.65
4:00	295.55	296.13	295.87	296.82	295.88	296.15

**Appendix D1: Simulated specific humidity for the base case [g.kg<sup>-1</sup>]**

Hour	Wiedner. HS.	Paniglg.	Apfelg.	Courtyard	Streets	All area
4:00	10.82	10.718	10.81	10.64	10.774	10.724
5:00	10.772	10.671	10.761	10.599	10.727	10.68
6:00	10.718	10.614	10.717	10.633	10.673	10.661
7:00	11.309	11.131	11.328	11.11	11.236	11.195
8:00	11.509	11.287	11.497	11.36	11.415	11.394
9:00	11.926	11.625	11.875	11.734	11.792	11.766
10:00	11.873	11.551	11.788	11.701	11.723	11.706
11:00	11.973	11.627	11.848	11.764	11.799	11.784
12:00	11.626	11.347	11.504	11.59	11.483	11.516
13:00	11.41	11.159	11.288	11.457	11.28	11.334
14:00	11.271	11.042	11.164	11.36	11.156	11.216
15:00	11.372	11.156	11.291	11.397	11.265	11.304
16:00	11.322	11.136	11.257	11.36	11.229	11.268
17:00	11.356	11.159	11.294	11.33	11.26	11.278
18:00	11.461	11.25	11.409	11.312	11.361	11.339
19:00	11.736	11.503	11.701	11.372	11.63	11.536
20:00	11.735	11.525	11.716	11.37	11.643	11.542
21:00	11.912	11.687	11.9	11.467	11.816	11.687
22:00	11.836	11.622	11.822	11.419	11.745	11.625
23:00	11.7	11.498	11.685	11.316	11.614	11.504
0:00	11.769	11.551	11.754	11.338	11.676	11.553
1:00	11.991	11.751	11.977	11.485	11.89	11.744
2:00	11.629	11.445	11.612	11.272	11.551	11.45
3:00	10.629	10.567	10.612	10.601	10.602	10.597
4:00	10.753	10.631	10.741	10.559	10.701	10.648

## Appendix D2: Simulated specific humidity for the V1 [g.kg<sup>-1</sup>]

Hour	Wiedner. HS.	Paniglg.	Apfelg.	Courtyard	Streets	All area
4:00	10.943	10.876	10.952	10.696	10.909	10.826
5:00	10.894	10.828	10.902	10.654	10.861	10.782
6:00	10.944	10.94	10.987	10.735	10.937	10.859
7:00	11.611	11.589	11.724	11.248	11.601	11.463
8:00	11.885	11.86	11.983	11.513	11.873	11.726
9:00	12.371	12.287	12.437	11.914	12.33	12.159
10:00	12.367	12.246	12.383	11.886	12.298	12.118
11:00	12.49	12.305	12.465	11.957	12.377	12.193
12:00	12.145	12.005	12.097	11.786	12.051	11.923
13:00	11.924	11.796	11.848	11.65	11.833	11.734
14:00	11.786	11.671	11.707	11.549	11.707	11.62
15:00	11.856	11.739	11.804	11.571	11.782	11.678
16:00	11.774	11.69	11.737	11.528	11.716	11.622
17:00	11.769	11.685	11.751	11.484	11.714	11.608
18:00	11.816	11.716	11.818	11.449	11.757	11.628
19:00	11.974	11.806	11.997	11.475	11.891	11.729
20:00	11.958	11.817	11.989	11.468	11.889	11.725
21:00	12.128	11.978	12.176	11.569	12.057	11.869
22:00	12.043	11.904	12.087	11.519	11.978	11.801
23:00	11.898	11.768	11.936	11.409	11.837	11.672
0:00	11.961	11.814	12.006	11.43	11.893	11.717
1:00	12.159	11.987	12.214	11.571	12.083	11.891
2:00	11.772	11.643	11.806	11.345	11.714	11.574
3:00	10.743	10.716	10.734	10.654	10.727	10.693
4:00	10.862	10.777	10.877	10.612	10.823	10.74

### Appendix D3: Simulated specific humidity for the V2 [g.kg<sup>-1</sup>]

Hour	Wiedner. HS.	Paniglg.	Apfelg.	Courtyard	Streets	All area
4:00	10.879	10.734	10.809	10.648	10.803	10.756
5:00	10.834	10.69	10.761	10.607	10.759	10.714
6:00	10.828	10.682	10.768	10.675	10.753	10.737
7:00	11.443	11.208	11.371	11.17	11.327	11.292
8:00	11.793	11.435	11.618	11.468	11.61	11.584
9:00	12.121	11.658	11.835	11.75	11.863	11.853
10:00	11.946	11.548	11.675	11.693	11.71	11.72
11:00	11.9	11.58	11.675	11.745	11.701	11.726
12:00	11.635	11.372	11.444	11.622	11.472	11.525
13:00	11.423	11.185	11.249	11.502	11.28	11.348
14:00	11.27	11.047	11.113	11.405	11.143	11.219
15:00	11.298	11.113	11.181	11.426	11.194	11.262
16:00	11.241	11.096	11.151	11.391	11.157	11.229
17:00	11.252	11.099	11.158	11.344	11.164	11.221
18:00	11.332	11.163	11.227	11.296	11.234	11.256
19:00	11.574	11.373	11.451	11.32	11.456	11.418
20:00	11.643	11.424	11.501	11.327	11.516	11.46
21:00	11.865	11.6	11.701	11.428	11.718	11.628
22:00	11.86	11.596	11.705	11.419	11.722	11.625
23:00	11.746	11.495	11.603	11.33	11.617	11.525
0:00	11.808	11.542	11.661	11.346	11.673	11.568
1:00	11.999	11.721	11.85	11.476	11.858	11.736
2:00	11.653	11.435	11.532	11.274	11.542	11.457
3:00	10.693	10.601	10.628	10.632	10.644	10.64
4:00	10.782	10.633	10.7	10.567	10.707	10.662

### Appendix D4: Simulated specific humidity for the V3 [g.kg<sup>-1</sup>]

Hour	Wiedner. HS.	Paniglg.	Apfelg.	Courtyard	Streets	All area
4:00	11.007	10.914	10.967	10.702	10.951	10.861
5:00	10.96	10.867	10.919	10.66	10.904	10.818
6:00	11.074	11.065	11.089	10.78	11.053	10.95
7:00	11.774	11.752	11.845	11.308	11.744	11.583
8:00	12.212	12.121	12.211	11.623	12.141	11.943
9:00	12.606	12.379	12.489	11.92	12.457	12.252
10:00	12.473	12.27	12.323	11.856	12.32	12.127
11:00	12.431	12.274	12.288	11.91	12.294	12.121
12:00	12.179	12.063	12.055	11.794	12.068	11.929
13:00	11.968	11.863	11.834	11.678	11.868	11.75
14:00	11.824	11.724	11.692	11.583	11.736	11.632
15:00	11.819	11.744	11.717	11.589	11.755	11.646
16:00	11.73	11.703	11.657	11.554	11.688	11.593
17:00	11.707	11.681	11.646	11.494	11.665	11.564
18:00	11.73	11.677	11.667	11.429	11.675	11.557
19:00	11.848	11.704	11.76	11.415	11.75	11.618
20:00	11.901	11.742	11.803	11.415	11.796	11.65
21:00	12.118	11.925	12.018	11.517	11.997	11.818
22:00	12.104	11.924	12.021	11.509	11.995	11.814
23:00	11.975	11.806	11.901	11.41	11.873	11.7
0:00	12.033	11.853	11.963	11.432	11.927	11.744
1:00	12.196	12	12.135	11.557	12.085	11.894
2:00	11.827	11.677	11.772	11.345	11.74	11.596
3:00	10.843	10.796	10.799	10.692	10.81	10.757
4:00	10.918	10.818	10.877	10.624	10.859	10.77



### Appendix D5: Simulated specific humidity for the M1 [g.kg<sup>-1</sup>]

Hour	Wiedner. HS.	Paniglg.	Apfelg.	Courtyard	Streets	All area
4:00	11.054	11.038	11.006	10.654	11.034	10.904
5:00	11.002	10.98	10.952	10.613	10.98	10.857
6:00	11.053	11.066	11.03	10.684	11.048	10.931
7:00	11.696	11.645	11.673	11.167	11.667	11.509
8:00	12.145	12.095	11.996	11.452	12.111	11.894
9:00	12.51	12.384	12.206	11.738	12.415	12.182
10:00	12.365	12.253	12.037	11.7	12.258	12.057
11:00	12.278	12.225	12.057	11.772	12.197	12.037
12:00	12.017	12.032	11.91	11.65	11.972	11.842
13:00	11.817	11.829	11.741	11.543	11.775	11.674
14:00	11.67	11.683	11.541	11.439	11.636	11.542
15:00	11.669	11.697	11.54	11.448	11.656	11.563
16:00	11.598	11.7	11.507	11.413	11.624	11.528
17:00	11.6	11.727	11.518	11.372	11.64	11.53
18:00	11.681	11.79	11.58	11.33	11.708	11.571
19:00	11.88	11.886	11.757	11.351	11.855	11.687
20:00	11.934	11.9	11.787	11.348	11.889	11.708
21:00	12.155	12.061	11.983	11.444	12.083	11.868
22:00	12.155	12.062	11.998	11.427	12.092	11.865
23:00	12.031	11.944	11.884	11.329	11.974	11.754
0:00	12.081	11.973	11.933	11.348	12.015	11.788
1:00	12.246	12.108	12.098	11.483	12.167	11.941
2:00	11.896	11.818	11.781	11.289	11.848	11.669
3:00	10.958	11.024	10.915	10.681	10.981	10.897
4:00	11.004	10.989	10.939	10.608	10.989	10.874

### Appendix D6: Simulated specific humidity for the VM [g.kg<sup>-1</sup>]

Hour	Wiedner. HS.	Paniglg.	Apfelg.	Courtyard	Streets	All area
4:00	11.188	11.273	11.191	10.712	11.215	11.045
5:00	11.135	11.214	11.135	10.67	11.16	10.995
6:00	11.261	11.458	11.333	10.781	11.341	11.154
7:00	11.972	12.188	12.105	11.308	12.064	11.814
8:00	12.446	12.653	12.519	11.619	12.528	12.224
9:00	12.86	12.929	12.832	11.902	12.868	12.533
10:00	12.773	12.884	12.714	11.868	12.79	12.454
11:00	12.767	12.859	12.664	11.918	12.763	12.437
12:00	12.551	12.686	12.457	11.805	12.563	12.26
13:00	12.337	12.483	12.224	11.7	12.356	12.085
14:00	12.183	12.351	12.081	11.599	12.222	11.961
15:00	12.187	12.373	12.11	11.596	12.24	11.975
16:00	12.098	12.339	12.068	11.558	12.185	11.926
17:00	12.076	12.344	12.077	11.502	12.179	11.912
18:00	12.103	12.37	12.108	11.443	12.2	11.917
19:00	12.21	12.342	12.178	11.434	12.246	11.961
20:00	12.238	12.316	12.176	11.427	12.251	11.964
21:00	12.439	12.464	12.365	11.526	12.431	12.12
22:00	12.401	12.437	12.344	11.506	12.404	12.098
23:00	12.268	12.313	12.221	11.415	12.277	11.984
0:00	12.307	12.333	12.263	11.432	12.309	12.012
1:00	12.453	12.448	12.418	11.56	12.442	12.149
2:00	12.081	12.122	12.066	11.364	12.094	11.856
3:00	11.122	11.283	11.15	10.751	11.195	11.058
4:00	11.154	11.24	11.173	10.671	11.191	11.027

**Appendix D7: Simulated specific humidity for the M2  
[g.kg<sup>-1</sup>]**

Hour	Wiedner. HS.	Paniglg.	Apfelg.	Courtyard	Streets	All area
4:00	10.879	10.788	10.81	10.631	10.819	10.759
5:00	10.834	10.742	10.762	10.59	10.774	10.717
6:00	10.832	10.759	10.774	10.657	10.777	10.751
7:00	11.448	11.292	11.377	11.141	11.352	11.306
8:00	11.801	11.59	11.623	11.428	11.655	11.61
9:00	12.123	11.753	11.837	11.712	11.894	11.867
10:00	11.943	11.635	11.681	11.655	11.737	11.733
11:00	11.893	11.681	11.716	11.716	11.732	11.743
12:00	11.633	11.469	11.473	11.586	11.502	11.541
13:00	11.421	11.265	11.258	11.465	11.302	11.36
14:00	11.266	11.128	11.123	11.368	11.162	11.231
15:00	11.297	11.189	11.192	11.392	11.213	11.272
16:00	11.243	11.17	11.163	11.361	11.178	11.238
17:00	11.256	11.174	11.173	11.324	11.187	11.233
18:00	11.339	11.242	11.244	11.283	11.259	11.272
19:00	11.578	11.424	11.461	11.305	11.473	11.424
20:00	11.646	11.47	11.508	11.307	11.53	11.461
21:00	11.868	11.642	11.706	11.406	11.73	11.626
22:00	11.863	11.639	11.709	11.393	11.733	11.621
23:00	11.743	11.531	11.598	11.297	11.621	11.515
0:00	11.808	11.581	11.66	11.318	11.68	11.561
1:00	11.998	11.75	11.85	11.451	11.863	11.728
2:00	11.652	11.465	11.531	11.249	11.547	11.451
3:00	10.695	10.638	10.632	10.609	10.655	10.639
4:00	10.783	10.664	10.702	10.548	10.714	10.659

**Appendix D8: Simulated specific humidity for the M3  
[g.kg<sup>-1</sup>]**

Hour	Wiedner. HS.	Paniglg.	Apfelg.	Courtyard	Streets	All area
4:00	10.82	10.718	10.81	10.64	10.774	10.724
5:00	10.772	10.671	10.761	10.599	10.727	10.68
6:00	10.738	10.626	10.727	10.756	10.689	10.72
7:00	11.339	11.147	11.343	11.303	11.259	11.282
8:00	11.545	11.306	11.516	11.591	11.442	11.498
9:00	11.963	11.645	11.895	11.978	11.819	11.874
10:00	11.908	11.569	11.805	11.937	11.748	11.808
11:00	12.002	11.644	11.863	11.98	11.821	11.878
12:00	11.652	11.364	11.52	11.8	11.504	11.607
13:00	11.432	11.177	11.301	11.654	11.3	11.419
14:00	11.29	11.059	11.177	11.556	11.175	11.296
15:00	11.389	11.17	11.301	11.581	11.28	11.377
16:00	11.337	11.146	11.264	11.532	11.242	11.333
17:00	11.369	11.166	11.297	11.492	11.269	11.336
18:00	11.471	11.254	11.411	11.45	11.369	11.386
19:00	11.738	11.503	11.702	11.387	11.631	11.54
20:00	11.734	11.524	11.715	11.373	11.642	11.54
21:00	11.911	11.685	11.899	11.468	11.814	11.685
22:00	11.835	11.621	11.821	11.42	11.744	11.623
23:00	11.7	11.497	11.684	11.318	11.614	11.503
0:00	11.769	11.55	11.754	11.34	11.676	11.552
1:00	11.992	11.751	11.977	11.487	11.89	11.744
2:00	11.629	11.445	11.612	11.273	11.551	11.45
3:00	10.629	10.567	10.612	10.602	10.602	10.597
4:00	10.753	10.63	10.741	10.559	10.7	10.647

### Appendix D9: Simulated specific humidity for the H1 [g.kg<sup>-1</sup>]

Hour	Wiedner. HS.	Paniglg.	Apfelg.	Courtyard	Streets	All area
4:00	10.881	10.741	10.805	10.731	10.81	10.772
5:00	10.836	10.698	10.758	10.688	10.766	10.73
6:00	10.824	10.681	10.752	10.729	10.754	10.736
7:00	11.478	11.221	11.36	11.28	11.354	11.31
8:00	11.815	11.443	11.601	11.594	11.632	11.596
9:00	12.184	11.686	11.869	11.888	11.923	11.892
10:00	12.001	11.577	11.733	11.863	11.767	11.763
11:00	11.925	11.586	11.732	11.851	11.733	11.734
12:00	11.661	11.373	11.493	11.712	11.5	11.532
13:00	11.451	11.19	11.292	11.564	11.307	11.353
14:00	11.307	11.071	11.153	11.458	11.177	11.232
15:00	11.325	11.113	11.21	11.465	11.215	11.264
16:00	11.259	11.084	11.171	11.408	11.169	11.22
17:00	11.268	11.099	11.184	11.372	11.179	11.217
18:00	11.361	11.177	11.267	11.348	11.262	11.268
19:00	11.609	11.4	11.506	11.431	11.495	11.457
20:00	11.685	11.457	11.559	11.453	11.562	11.508
21:00	11.909	11.641	11.763	11.589	11.769	11.69
22:00	11.886	11.621	11.739	11.573	11.752	11.674
23:00	11.773	11.523	11.632	11.483	11.647	11.574
0:00	11.842	11.581	11.699	11.52	11.712	11.63
1:00	12.036	11.766	11.894	11.67	11.902	11.807
2:00	11.681	11.468	11.562	11.421	11.576	11.511
3:00	10.703	10.607	10.633	10.679	10.654	10.655
4:00	10.797	10.648	10.712	10.648	10.724	10.69

### Appendix D10: Simulated specific humidity for the H2 [g.kg<sup>-1</sup>]

Hour	Wiedner. HS.	Paniglg.	Apfelg.	Courtyard	Streets	All area
4:00	10.838	10.741	10.78	10.541	10.775	10.697
5:00	10.793	10.696	10.733	10.502	10.73	10.657
6:00	10.783	10.697	10.737	10.566	10.721	10.673
7:00	11.345	11.171	11.304	10.974	11.243	11.154
8:00	11.67	11.43	11.533	11.242	11.514	11.42
9:00	11.948	11.579	11.72	11.524	11.729	11.656
10:00	11.776	11.476	11.567	11.472	11.586	11.54
11:00	11.761	11.535	11.615	11.543	11.606	11.568
12:00	11.51	11.34	11.385	11.447	11.387	11.383
13:00	11.309	11.159	11.186	11.335	11.203	11.223
14:00	11.161	11.038	11.061	11.249	11.076	11.109
15:00	11.207	11.106	11.139	11.287	11.138	11.164
16:00	11.169	11.085	11.113	11.269	11.11	11.141
17:00	11.182	11.084	11.121	11.232	11.116	11.135
18:00	11.255	11.139	11.183	11.181	11.178	11.165
19:00	11.478	11.314	11.387	11.185	11.379	11.304
20:00	11.532	11.35	11.423	11.174	11.423	11.328
21:00	11.733	11.501	11.599	11.24	11.599	11.463
22:00	11.739	11.499	11.61	11.212	11.607	11.456
23:00	11.633	11.407	11.512	11.127	11.509	11.364
0:00	11.689	11.444	11.564	11.131	11.557	11.397
1:00	11.874	11.605	11.747	11.248	11.733	11.55
2:00	11.557	11.353	11.455	11.093	11.448	11.314
3:00	10.655	10.596	10.605	10.551	10.616	10.592
4:00	10.728	10.606	10.66	10.464	10.659	10.593

## Appendix E1: Database of soil type in ENVI-met

ID	Description	ns	nfc	nwilt	matpot	hydro-lf	C <sub>p</sub>	b	waerme-lf
0	Default Soil (Loam)	0.451	0.24	0.155	-0.478	7	1.212	5.39	0
SD	Sand	0.395	0.135	0.0068	-0.121	176	1.463	4.05	0
BS	Smashed brick	0.395	0.135	0.0068	-0.121	176	2	4.05	0
PS	Pervious Concrete	0.395	0.135	0.0068	-0.121	176	2	4.05	0
LS	Loamy Sand	0.41	0.15	0.075	-0.09	156.3	1.404	4.38	0
SL	Sandy Loam	0.435	0.195	0.114	-0.218	34.1	1.32	4.9	0
SO	Silt Loam	0.485	0.255	0.179	-0.786	7.2	1.271	5.3	0
LE	Loam	0.451	0.24	0.155	-0.478	7	1.212	5.39	0
TS	Sandy Clay Loam	0.42	0.255	0.175	-0.299	6.3	1.175	7.12	0
TL	Silty Clay Loam	0.477	0.322	0.218	-0.356	1.7	1.317	7.75	0
LT	Clay Loam	0.476	0.325	0.25	-0.63	2.5	1.225	8.52	0
ST	Sandy Clay	0.426	0.31	0.219	-0.153	2.2	1.175	10.4	0
TO	Clay	0.482	0.367	0.286	-0.405	1.3	1.089	11.4	0
TF	Peat	0.863	0.5	0.395	-0.356	8	0.836	7.75	0
ZB	Cement Concrete	0	0	0	0	0	2.083	0	1.63
MB	Mineral Concrete	0	0	0	0	0	1.75	0	2.33
AK	Asphalt (with Gravel)	0	0	0	0	0	2.214	0	1.16
AB	Asphalt (with Basalt)	0	0	0	0	0	2.251	0	0.9
GR	Granite	0	0	0	0	0	2.345	0	4.61
BA	Basalt	0	0	0	0	0	2.386	0	1.73
WW	Water	0	0	0	0	0	0	0	0

ID	Description	ns	nfc	nwilt	matpot	hydro-lf	C <sub>p</sub>	b	waerme-lf
BR	Brick	0	0	0	0	0	2	0	1
CC	Mineral concrete wet	0	0	0	0	0	1.75	0	2.33
WD	Wood Planks	0	0	0	0	0	0.454	0	0.9

ID: the two-digit ID which links the soils with the profile data in PROFILES.DAT

ns: Volumetric water content at saturation in [m<sup>3</sup>.m<sup>-3</sup>]

nfc: Volumetric water content at field capacity in [m<sup>3</sup>.m<sup>-3</sup>]

nwilt: Volumetric water content at wilting point (for the vegetation model) in [m<sup>3</sup>.m<sup>-3</sup>]

matpot: Matrix Potential at saturation in [m]

hydr: Hydraulic conductivity at saturation in [10<sup>-6</sup>.m.s<sup>-1</sup>]

C<sub>p</sub>: Volumetric Heat Capacity in [10<sup>6</sup>.J.m<sup>-3</sup>.K<sup>-1</sup>]

b: Clapp & Hornberger Constant

waerme-lf: Heat Conductivity of the material in [W.m<sup>-1</sup>.K<sup>-1</sup>]



**Appendix E2: Database of soil profile in ENVI-met**

ID	0	ST	PP	LO	SD	WW	KK	KG	GG	GS	G2	
<b>Description</b>	Default Un sealed Soil	Asphalt Road	Pavement (Concrete), used/ dirty	Loamy Soil	Sandy Soil	Deep Water	Brick road (red stones)	Brick road (yellow stones)	Dark Granit Pavement	Granit Pavement (single stones)	Granit shining	
<b>z0-length</b>	0.015	0.01	0.01	0.015	0.05	0.01	0.01	0.01	0.01	0.01	0.01	
<b>albedo</b>	0.2	0.2	0.4	0	0	0	0.3	0.5	0.3	0.4	0.8	
<b>emissivity</b>	0.98	0.9	0.9	0.98	0.9	0.96	0.9	0.9	0.9	0.9	0.9	
<b>soil profile</b>	1	LE	AB	ZB	LE	SD	WW	BR	BR	GR	GR	GR
	2	LE	AB	ZB	LE	SD	WW	BR	BR	GR	GR	GR
	3	LE	AB	ZB	LE	SD	WW	BR	BR	SD	GR	GR
	4	LE	AB	ZB	LE	SD	WW	SD	SD	LE	GR	GR
	6	LE	AB	SD	LE	SD	WW	LE	LE	LE	GR	GR
	8	LE	AB	LE	LE	LE	WW	LE	LE	LE	MB	LE
	10	LE	AB	LE	LE	LE	WW	LE	LE	LE	LE	LE
	20	LE	AB	LE	LE	LE	WW	LE	LE	LE	LE	LE
	30	LE	AB	LE	LE	LE	WW	LE	LE	LE	LE	LE
	40	LE	LE	LE	LE	LE	WW	LE	LE	LE	LE	LE
	50	LE	LE	LE	LE	LE	WW	LE	LE	LE	LE	LE
	100	LE	LE	LE	LE	LE	WW	LE	LE	LE	LE	LE
	150	LE	LE	LE	LE	LE	WW	LE	LE	LE	LE	LE
	200	LE	LE	LE	LE	LE	WW	LE	LE	LE	LE	LE
	250	LE	LE	LE	LE	LE	WW	LE	LE	LE	LE	LE
	300	LE	LE	LE	LE	LE	WW	LE	LE	LE	LE	LE
350	LE	LE	LE	LE	LE	WW	LE	LE	LE	LE	LE	
400	LE	LE	LE	LE	LE	WW	LE	LE	LE	LE	LE	
450	LE	LE	LE	LE	LE	WW	LE	LE	LE	LE	LE	

ID	WC	PC	PG	PL	PD	TB	PS	AR	BA	WD	
<b>Description</b>	Wet Concrete TEST	Photocat Test	Concrete Pavement Gray	Concrete Pavement Light	Concrete Pavement Dark	Terre battue (Smashed brick)	Pervious concrete	Asphalt road with red coating	Basalt Brick Road	Wood Planks	
<b>z0-length</b>	0.01	0.01	0.01	0.01	0.01	0.01	0.01	0.01	0.01	0.01	
<b>Albedo</b>	0.4	0.4	0.5	0.8	0.2	0.8	0.6	0.5	0.8	0.8	
<b>Emissivity</b>	0.9	0.9	0.9	0.9	0.9	0.9	0.9	0.9	0.9	0.9	
<b>Soil profile</b>	1	CC	ZB	ZB	ZB	ZB	BS	PS	AB	BA	WD
	2	CC	ZB	ZB	ZB	ZB	BS	PS	AB	BA	WD
	3	CC	ZB	ZB	ZB	ZB	BS	PS	AB	BA	WD
	4	CC	ZB	ZB	ZB	ZB	SD	PS	AB	BA	WD
	6	SD	SD	SD	SD	SD	LS	LS	AB	BA	WD
	8	LE	LE	LE	LE	LE	LS	LS	AK	SD	WD
	10	LE	LE	LE	LE	LE	LE	LE	AB	LE	WD
	20	LE	LE	LE	LE	LE	LE	LE	AB	LE	SD
	30	LE	LE	LE	LE	LE	LE	LE	AB	LE	LS
	40	LE	LE	LE	LE	LE	LE	LE	AB	LE	LE
	50	LE	LE	LE	LE	LE	LE	LE	LE	LE	LE
	100	LE	LE	LE	LE	LE	LE	LE	LE	LE	LE
	150	LE	LE	LE	LE	LE	LE	LE	LE	LE	LE
	200	LE	LE	LE	LE	LE	LE	LE	LE	LE	LE
	250	LE	LE	LE	LE	LE	LE	LE	LE	LE	LE
	300	LE	LE	LE	LE	LE	LE	LE	LE	LE	LE
350	LE	LE	LE	LE	LE	LE	LE	LE	LE	LE	
400	LE	LE	LE	LE	LE	LE	LE	LE	LE	LE	
450	LE	LE	LE	LE	LE	LE	LE	LE	LE	LE	

### Appendix E3: Database of materials in ENVI-met

ID	Description	Default thickness	Absorption	Transmission	Reflection	Emissivity	specific heat	Thermal conductivity	Density
B1	Brick: aerated	0.3	0.6	0	0.4	0.9	840	0.3	1000
B2	Brick: burned	0.3	0.6	0	0.4	0.9	650	0.44	1500
B3	Brick: reinforced	0.3	0.6	0	0.4	0.9	840	1.1	1920
B4	Brick: cp900	0.3	0.6	0	0.4	0.9	900	0.3	1000
B5	Brick: cp1000	0.3	0.6	0	0.4	0.8	1000	0.3	1000
B6	Brick: white	0.3	0.3	0	0.7	0.9	840	0.3	1000
C1	Concrete: heavyweight	0.3	0.7	0	0.3	0.9	840	1.3	2000
C2	Concrete: lightweight	0.3	0.7	0	0.3	0.9	840	0.2	620
C3	Concrete: hollow block	0.3	0.7	0	0.3	0.9	840	0.86	930
C4	Concrete: filled block	0.3	0.7	0	0.3	0.9	840	0.85	1260
C5	Concrete: cast dense	0.3	0.7	0	0.3	0.9	840	1.9	2500
C6	Concrete: cp900	0.3	0.7	0	0.3	0.9	900	0.85	1260
C7	Concrete: cp1000	0.3	0.7	0	0.3	0.8	1000	0.85	1260
C8	Concrete: Ref0.55	0.3	0.45	0	0.55	0.9	840	0.85	1260
C9	Concrete: Ref0.8	0.3	0.2	0	0.8	0.9	840	0.85	1260
MH	Masonry: heavyweight	0.3	0.65	0	0.35	0.9	840	0.9	1850
G1	Heat protection glass	0.03	0.05	0.9	0.05	0.9	750	1	2500
G2	Plexiglas	0.02	0.05	0.9	0.05	0.9	1500	0.19	1180
G3	foamed glass	0.25	0.7	0	0.3	0.9	840	0.052	140
G4	clear float glass	0.02	0.05	0.9	0.05	0.9	750	1.05	2500
G5	glass brick surface	0.25	0.2	0.7	0.1	0.9	840	1.4	2500

---

ID	Description	Default thickness	Absorption	Transmission	Reflection	Emissivity	specific heat	Thermal conductivity	Density
R1	Roofing: tile	0.05	0.5	0	0.5	0.9	800	0.84	1900
R2	Roofing: terracotta	0.05	0.5	0	0.5	0.9	840	0.81	1700
AL	Aluminum	0.03	0.1	0	0.9	0.18	880	203	2700
Cu	Copper	0.03	0.1	0	0.9	0.2	390	384	8600
IR	Iron	0.02	0.4	0	0.6	0.25	530	72	7900
ST	Steel	0.02	0.2	0	0.8	0.1	4800	45	800
PV	PVC	0.02	0.3	0	0.7	0.9	1470	0.19	1200
PC	Concrete, Photoactive	0.3	0.53	0	0.3	0.95	1000	1.3	1300
O2	Air	0.01	0	1	0	0.96	1006	0.025	1.2041
So	soil	0.3	0.95	0	0.05	0.98	1500	0	2700

**Appendix E4: Database of wall/roof type in ENVI-met**

ID	Description	Material			Thickness		
		outer	middle	inner	outer	middle	inner
SU	PVC Sun Sail	PV	PV	PV	0.02	0.02	0.02
PC	Concrete Wall, Photoactive	PC	C2	C2	0.1	0.1	0.1
C1	Concrete Wall (heavy)	C1	C1	C1	0.1	0.1	0.1
C2	Concrete wall (light weight)	C2	C2	C2	0.1	0.1	0.1
C3	Concrete wall (hollow block)	C3	C3	C3	0.1	0.1	0.1
C4	Concrete wall (Filled block)	C4	C4	C4	0.1	0.1	0.1
C5	Concrete Wall (cast dense)	C5	C5	C5	0.1	0.1	0.1
C6	Concrete Wall cp900	C6	C6	C6	0.1	0.1	0.1
C7	Concrete Wall cp1000	C7	C7	C7	0.1	0.1	0.1
C8	Concrete roof Ref0.55	C8	C8	C8	0.1	0.1	0.1
C9	Concrete roof Ref0.8	C9	C9	C9	0.1	0.1	0.1
G1	Heat Protection Glass (one layered)	G1	G1	G1	0.01	0.01	0.01
G2	Plexiglas (one layered)	G2	G2	G2	0.01	0.01	0.01
G3	Foamed Glass (one layered)	G3	G3	G3	0.01	0.01	0.01
G4	Clear Float glass (one layered)	G4	G4	G4	0.01	0.01	0.01
G5	Glass Bricks (one layered)	G5	O2	G5	0.02	0.02	0.02
AL	Aluminum (single layer)	Al	Al	Al	0.01	0.01	0.01
CU	Copper (single layer)	Cu	Cu	Cu	0.01	0.01	0.01
IR	Iron (single layer)	IR	IR	IR	0.01	0.01	0.01
ST	Steel (one layer)	ST	ST	ST	0.02	0.02	0.02
B1	Brick wall (aerated)	B1	B1	B1	0.15	0.15	0.15

ID	Description	Material			Thickness		
		outer	middle	inner	outer	middle	inner
B2	Brick wall (burned)	B2	B2	B2	0.15	0.15	0.15
B3	Brick wall (reinforced)	B3	B3	B3	0.15	0.15	0.15
B4	Brick wall cp900	B4	B4	B4	0.15	0.15	0.15
B5	Brick wall cp1000	B5	B5	B5	0.15	0.15	0.15
R1	Roofing: Tile	R1	R1	R1	0.1	0.1	0.1
R2	Roofing: Terracotta	R2	R2	R2	0.1	0.1	0.1
GH	Heat protection glass (one air layer)	G1	O2	G1	0.5	0.5	0.5
So	soil	so	so	so	0.2	0.1	0.1
B6	Brick wall (white)	B6	B6	B6	0.15	0.15	0.15

## Appendix E5: Database 3D plants in ENVI-met

ID	Description	Plant type	Leaf type	Albedo	rs_min	Height	Width	Depth	cell size	xy_cells	z_cells	LAD	RAD
5	amerikanische Gleditschie	0	1	0.18	0	6	5	2.8	1	5	6	2	0.1
6	amerikanische Gleditschie	0	1	0.18	0	10	7	0.8	1	7	10	2	0.1
B5	Gemeine Esche	0	1	0.18	0	20	11	1.2	1	11	20	1	0.1
BB	Biergartenbaum	0	1	0.2	0	20	11	10	1	11	20	2	1
A4	Gr. Robinie	0	1	0.18	0	22	13	3.5	1	13	22	0.8	0.1
A3	kl. Robinie	0	1	0.18	0	12	7	1.5	1	7	12	0.5	0.1
B2	Blutbuche	0	1	0.18	0	25	15	1.4	1	15	25	1.5	0.1
DB	doofer Baum	0	1	0.5	0	15	11	8	1	11	15	2.5	1
B3	Stieleiche	0	1	0.18	0	25	15	1.5	1	15	25	1.8	0.1
B1	Rotbuche	0	1	0.18	0	25	21	1.4	1	21	25	1.3	0.1
B8	Feld-Ulme	0	1	0.18	0	20	19	1.6	1	19	20	1	0.1
A9	Feldahorn	0	1	0.18	0	12	9	3	1	9	12	2	0.1
B6	Gold-Ulme	0	1	0.18	0	10	5	0.6	1	5	10	0.7	0.1
4	Gr. Robinie	0	1	0.18	0	22	13	3.5	1	13	22	2	0.1
A5	amerikanische Gleditschie 1	0	1	0.18	0	15	11	0.8	1	11	15	0.5	0.1
A6	amerikanische Gleditschie 2	0	1	0.18	0	10	7	0.8	1	7	10	0.3	0.1
B4	Hainbuche	0	1	0.18	0	20	15	1.5	1	15	20	1.7	0.1
B1	Rotbuche	0	1	0.18	0	25	21	1.4	1	21	25	2	0.1
B2	Blutbuche	0	1	0.18	0	25	15	1.4	1	15	25	2	0.1
3	Kl. Robinie	0	1	0.18	0	12	7	1.5	1	7	12	2	0.1
KB	komischer Baum	1	1	0.25	0	3	3	2	1	3	3		1
C1	Lärche	0	2	0.18	0	25	11	2.5	1	11	25	0.5	0.1

ID	Description	Plant type	Leaf type	Albedo	rs_min	Height	Width	Depth	cell size	xy_cells	z_cells	LAD	RAD
A2	Sommerlinde	0	1	0.18	0	25	15	1.3	1	15	25	1.3	0.1
A7	Spitzahorn	0	1	0.18	0	15	7	3.45	1	7	15	1.5	0.1
C4	Fichte	0	2	0.18	0	25	13	1.3	1	13	25	0.5	0.1
B9	Palme	0	1	0.18	0	6	5	1	1	5	6	0.5	0.1
B8	Platane	0	1	0.18	0	30	21	1.5	1	21	30	1.1	0.1
C2	Kiefer	0	2	0.18	0	25	11	2	1	11	25	0.7	0.1
B7	Sandbirke	0	1	0.18	0	6	7	1.4	1	7	6	0.9	0.1
C3	Weißtanne	0	2	0.18	0	30	11	1.5	1	11	30	0.7	0.1
A1	Winterlinde	0	1	0.18	0	20	13	1.3	1	13	20	1	0.1
2	Sommerlinde	0	1	0.18	0	25	15	1.3	1	15	25	1	0.1
7	Spitzahorn	0	1	0.18	0	15	7	3.45	1	7	15	2	0.1
A8	Bergahorn	0	1	0.18	0	30	21	2	1	21	30	1.3	0.1
1	Winterlinde	0	1	0.18	0	20	13	1.3	1	13	20	1	0.1
CC	Hasel-Tree	0	1	0.6	0	15	5	2	1	5	15	1	0.1
JU	Judas Tree	0	1	0.6	0	5	3	2	1	3	5	0.8	0.1
PW	Palm Washingtonia	0	1	0.6	0	5	3	2	1	3	5	0.8	0.1
PI	Pine Tree	0	2	0.8	0	4	5	2	1	5	4	2	0.1
AC	Acacia	0	1	0.6	0	2	3	2	1	3	2	1	0.1
TA	Tamarix Gallica	0	1	0.6	0	2	3	2	1	3	2	0.8	0.1
PR	Prunus Avium	0	1	0.6	0	5	3	2	1	3	5	1	0.1
W3	kl. Robinie-winter	0	1	0.1	0	12	7	1.5	1	7	12	0.3	0.1
R3	Kl. Robinie dense	0	1	0.18	0	12	7	1.5	1	7	12	3	0.1



# Curriculum Vitae

## I. Personal Data

Name: Maleki Gavgani  
First name: Aida  
Date of Birth: September 1, 1977  
Place of Birth: Tabriz, Iran  
Marital Status: Single  
Nationality: Iranian  
Address: Forsthausgasse 2,  
Vienna 1200  
Tel.: 00436503705035  
E-mail: Ida.maleki@gmail.com

## II. Educational Background

Oct. 2009 – Jul. 2014 Building physics and Building ecology Institute, Vienna university of technology, Vienna – Austria, running for Ph.D. in Architecture  
  
Thesis: „Monitoring and modeling of the urban micro-climate of Vienna “  
  
Fields of specialization:  
- Urban microclimate  
- Urban Heat Islands,

Sep. 1996 - Feb. 2003 Sahand university of technology, Tabriz – Iran  
Degree: M.Sc. in Architecture  
  
Thesis: „Design of Astronomy Research Center of Maragheh “

Sep. 1988 - Jun.1995 High school diploma,  
Farzanegan highschool, Tabriz – Iran (under supervision of  
Exceptional Talent Organization of Iran)

Sep. 1983 - Jun 1987 Primary School in Tabriz - Iran

### **III. Key Qualifications**

More than 9 years of progressive working experience as an architect in Iran and in Austria in the following fields:

- Construction detailed design;
- Virtual design (architectural design);
- Effective natural factors in sustainable designs;
- Rural dwelling typological investigation;
- Urban micro-climate simulation;
- Statistical survey/ monitoring concerning urban heat Island;
- Building thermal performance simulation;
- Curriculum design, E-learning,
- Administrative affairs (office management);

Lecturing experiences:

In parallel to my role in administrative/ managerial affairs, from Feb. 2003 to Sep. 2009 active as a lecturer at faculty of architecture and applied art, Tabriz Islamic Art university in Tabriz, Iran,

Delivered courses: Elementary Architecture Design 1, Geometry 2, Applied Geometry, Architectural Design1, Building & Construction Workshop 2,

### **IV. Professional Experiences**

Sep. 2011 – Jul. 2014    Building physics and building ecology Institute, Vienna university of technology, Vienna, Austria

Main areas of responsibility:

- Working as a scientific assistant (Ph.D. student), thesis: "Monitoring of micro-climates of Vienna",
- Working as a project assistant, UHI project, funded by EU

Jan. 2005 – Sep. 2009    Tabriz Islamic Art university, Tabriz, Iran

Main areas of responsibility:

- Researcher: virtual museum of historical buildings of Tabriz;
- Researcher: effective natural factors on locating historical city of Tabriz;
- Researcher: typology of rural dwelling of East Azerbaijan province of Iran;
- Head of "supervising & evaluation office";
- Head of "talented students leading" office;
- Manager of educational affairs (administrational office) of University;
- Lecturer,

## **V. Languages Skills**

Persian - native speaker;  
Azarbayjani - native speaker;  
English - fluent in speaking and writing,

## **VI. Computer Skills**

MS-Office including MS-Word, MS-Excel and MS-Power point;  
AutoCAD, Photoshop, TAS, Designbuilder, ODEON, AnTherm, Dialux, Envi-met; MATLAB

## **VII. Publications and Presentations**

Aida Maleki, Kristina Kiesel, Milena Vuckovic, and Ardeshir Mahdavi. "Empirical and Computational Issues of Microclimate Simulation." In *Information and Communication Technology, Lecture Notes in Computer Science*, by MadeSudiana Mahendra, ErichJ Neuhold, AMin Tjoa and Ilsun You, 78-85. Berlin Heidelberg: Springer, 2014

Aida Maleki, Kristina Orehounig, Ardeshir Mahdavi, "Monitoring and modeling of the urban micro-climate in Vienna", Eura Conference 2012, Urban Europe challenge to meet urban future, Vienna, Austria, Sep 2012;

Aida Maleki, Kristina Orehounig, Ardeshir Mahdavi, "Monitoring and modeling of the urban micro-climate", 1<sup>st</sup> International Conference on Architecture & Urban Design, EPOKA University , Tirana, Albania, April 19-21 2012;

Aida Maleki, Pardis Alizadeh, "A framework for the online Architectural design learning Studio", (Persian), 2<sup>nd</sup> national conference of E-learning of Iran, Zahedan, Iran. November 2007;

Pardis Alizadeh, Aida Maleki, „Internal evaluation as an instrument for the improvement of higher education quality case study: Architectural department of Tabriz Islamic Art University“, the 2007 APQN AGM Conference, Kuala Lumpur, Malaysia, February, 2007;

Pardis Alizadeh, Aida Maleki, "Transforming Project-Based courses to Blended Learning Environment: Case study Architectural foundation courses", 6th International conference on multimedia and ICTs in education, Seville, Spain, Nov. 2006, (virtual presentation);

Aida Maleki, Pardis Alizadeh „Sustainable development by building conservation, case study: Faculty of urbanism& architecture, Tabriz Islamic Art University“, 11th International seminar forum UNESCO on University and heritage: documentation for conservation and development new heritage strategy for the future, Florence, Italy, Sep. 2006, (poster presentation);

Pardis Alizadeh, Aida Maleki, „Web-based curriculum for foundation courses in architecture, Case study: courses of elementary architecture design 1, material & construction workshop“, (Persian), 1<sup>st</sup> national conference of electronic learning, Zanjan, Iran, May 2006, (presentation);

Parvin Ghaemmaghmi, Aida Maleki, Pardis Alizadeh, „Creating sustainable work environment in historic fabrics, case study: Tabriz Islamic Art University“, 8th international conference on human habitat, Mumbai, India, Jan. 2006, (presentation);